Spring 5-5-2023

# Performance of Helical Piles Retrofitted with a Novel Collar Vane Under Lateral and Torsional Loads

Juan Sebastian Carvajal Munoz
*University of Maine*, sebastian.carvajal@maine.edu

# PERFORMANCE OF HELICAL PILES RETROFITTED WITH A NOVEL COLLAR VANE UNDER LATERAL AND TORSIONAL LOADS

By

Juan Sebastian Carvajal-Munoz

B.Sc., University of Antioquia, 2020

A THESIS

Submitted in Partial Fulfillment of the

Requirements for the Degree of

Master of Science

(in Civil Engineering)

The Graduate School

The University of Maine

May 2023

Advisory Committee:

Aaron P. Gallant, Associate Professor of Civil and Environmental Engineering, University of Maine, Advisor

Keith A. Berube, Associate Professor of Mechanical Engineering Technology, University of Maine

Aaron S. Bradshaw, Associate Professor of Civil and Environmental Engineering, University of Rhode Island

# PERFORMANCE OF HELICAL PILES RETROFITTED WITH A NOVEL COLLAR VANE UNDER LATERAL AND TORSIONAL LOADS

By Juan Sebastian Carvajal-Munoz

Thesis Advisor: Dr. Aaron P. Gallant

An Abstract of the Thesis Presented
in Partial Fulfillment of the Requirements for the
Degree of Master of Science
(in Civil Engineering)
May 2023

Helical piles are lightweight deep foundations designed to support both compressive and uplift loads by mobilizing the shear strength of soil adjacent to helical plates that are welded to an extendable shaft. Helical piles are relatively inexpensive, can be installed quickly utilizing non-specialized equipment, and they are suitable for a wide range of soil conditions. However, helical piles are precluded from many applications due to their inability to support substantial lateral and torsional loads. To overcome this limitation, a novel easy-to-install Collar Vane (CV) is implemented to augment the geotechnical lateral and torsional capacity of helical piles.

The Collar Vane consists of four steel fins welded to a hollow steel collar that wraps around the helical pile shaft. The Collar Vane is structurally coupled to the helical pile via flanges near the helical pile head to transfer lateral and torsional loads through the CV blades to the soil. Two different Collar Vanes prototypes were manufactured, a 'two-piece' Collar Vane (CV2), tested in 2021 and based on the results of this prototype, a 'one-piece' Collar Vane (CV1) was manufactured and tested in 2022. Both prototypes were installed and tested in two different well-characterized soil conditions: medium-stiff cohesive soil and homogeneous dense sand soil.

This thesis presents the field results of an instrumented full-scale helical pile with the Collar Vane subjected to monotonic lateral, monotonic torsional, cyclic lateral and cyclic torsional loads. Displacements and loads were monitored using string potentiometers and load cells, respectively. Strain gauges installed to measure deformations facilitated the computation of the bending moment. The cyclic loading procedure consisted of approximately 1000 cycles at 0.125 Hz to evaluate the effect of cyclic loads on the helical pile which is envisioned to be implemented to support lightweight transportation structures.

The study revealed that the Collar Vane significantly increases the lateral and torsional geotechnical resistance of helical piles. The increase in capacity is associated with the increment in the effective diameter attributed to the mobilization of geotechnical resistance in the upper soil profile. Moreover, strain gauge data suggest that Collar Vane reduces the amount of bending moment on the helical pile shaft by limiting the lateral displacement, reducing the need for a larger diameter pile shaft and hence, making possible a more efficient pile design. In addition, the measured torsional capacity was compared with predicted values using different well-known methodologies. Additionally, the Collar Vane was subjected to different cyclic loading ratios and it was found that the Collar Vane head stiffness degraded as the number of load cycles increased, the accumulated displacement was significant in the first 100 cycles, and a simple approach was proposed to determine the accumulated displacement in function of the number of cycles.

Finally, a numerical analysis is performed using FEM software to validate field torsional results, and a finite difference program, to compare an standard drilled shaft foundation element to the Collar Vane lateral response. Moreover, an example design of a roadside sign structure is shown to demonstrate the applicability of the Collar Vane.

# DEDICATION

I dedicate this work to my family, who has been a constant source of support and encouragement during the challenges of this journey.

# ACKNOWLEDGEMENTS

Finally, I would like to express my gratitude to my family and close friends. They have all been a constant source of encouragement throughout my life, and without them, this thesis would not have been possible.

# TABLE OF CONTENTS

# LIST OF TABLES

# LIST OF FIGURES

# CHAPTER 1

# INTRODUCTION

## 1.1    General Introduction

A helical pile (also referred to as anchor piles or screw piles) is a lightweight deep foundation element composed of a central shaft that is made from round or square steel sections with one or more plates (helixes) that are welded to the shaft. Helical piles (HPs) efficiently generate geotechnical compressive and uplift resistance by mobilizing the shear strength of soil adjacent to the helical plates and can be used as tower foundations or secure moorings. Helical piles are installed by applying an axial force (crowd) and rotating the shaft of the pile by a drive head adding extensions as necessary to allow them to reach great depth and thus, increase their versatility. The use of mechanical torque reduces the amount of noise, vibration, and damage to adjacent structures compared to traditional foundation elements. Furthermore, installation is relatively non-intrusive, less cumbersome, and appreciably less expensive (Perko, 2009).

Due to their economical and performance advantages, helical piles may be implemented as an alternative to support lightweight transportation infrastructure (e.g. sign structures, noise walls, etc.). However, state Departments of Transportation (DOTs) may be hesitant to adopt this technology due, in part, to the limited understanding and uncertainty regarding helical pile's performance under torsional and lateral loading. Although the axial capacity of helical piles is well-understood (Adams & Klym, 1972; Cerato & Victor, 2008; Klym *et al.*, 1986; Livneh & El Naggar, 2008; Bradshaw *et al.*, 2022) helical piles are not designed to resist torsional loads and only a few studies considered their lateral performance: Perko (2003) observed that the helical pile lateral capacity is dependent on the strength of the shaft and the nearby soil conditions, Prasad & Rao (1996) conducted tests on scale models with different numbers of helices and it was found that the lateral capacity increased with embedment depth, shear strength of soil, and the number of helical

plates. It was found that the capacity of helical piles was 1.2-1.5 times the capacity of a single straight pile without helices. However, Elkasabgy & El Naggar (2019) performed a full-scale helical pile test and reported that in large-diameter helical piles, the helical helices did not contribute to the pile lateral capacity. Nevertheless, there are instances where large geotechnical torsional resistances are required and HPs cannot be readily implemented to support torsional loads. The lateral and torsional resistance of helical piles needs to be addressed so that their versatility and economic efficiencies can be extended to more applications.

To overcome the helical pile's limitation to support lateral and torsional loads, a novel easy-to-install Collar Vane is coupled to the helical pile head to increase its lateral and torsional geotechnical resistance. The Collar Vane consists of four steel fins welded to a hollow steel collar that wraps around, but does not interact with, the helical pile shaft. The Collar Vane is structurally coupled to the helical pile via flanges near the pile head to transfer lateral and torsional loads through the vane to the soil. This study presents the field results of a full-scale helical pile instrumented with strain gauges tested with different geometries of Collar Vanes, installed in cohesive and cohesionless soil, and subjected to monotonic and cyclic, lateral and torsional loads.

## 1.2   Research Motivation and Objectives

In recent years, the popularity of helical piles has increased thanks to their inexpensive cost, quick installation with ubiquitous equipment, ability to be installed in areas of limited access, and capacity to support loads immediately after installation. However, they are precluded from many applications due to their inability to resist substantial lateral and torsional loads. These limitations can be addressed by implementing the Collar Vane since it increases the effective diameter attributed to the mobilization of geotechnical resistance in the upper soil profile. With this new technology, state DOTs will be able to implement

an efficient and cost-effective method of foundation elements to support lightweight transportation infrastructure.

The main objective of this project is to advance more efficient foundation alternatives for lightweight transportation structures or to augment existing foundations for reuse or life extension typically supported by conventional, more expensive, and intrusive, foundation alternatives. The specific objectives of this study are to: (i) present the novel Collar Vane, demonstrate how it is coupled into the helical pile and how it is installed into the ground; (ii) analyze the response of different Collar Vane geometries on the performance of helical piles in different soil materials; (iii) illustrate the advantages that the Collar Vane can provide to helical piles when subjected to lateral and torsional loads; (iv) demonstrate that the torsional capacity of the Collar Vane can be predicted using simple tractable models; (v) study the performance of the Collar Vane under cyclic loads.

## 1.3   Thesis Organization

This thesis is structured in the following main parts:

Chapter 2 briefly describes literature relating to the main research. This is aimed to provide a basic background regarding helical piles, lightweight structures, and conventional design methods used to predict pile capacities. Topics reviewed are helical pile performance, applications, axial capacity, and lateral capacity; loaded structures in marine and transportation industries and, well-established approaches used to predict the lateral and torsional capacity of conventional piles.

Chapter 3 will discuss the testing methodology. The Collar Vanes are presented. Soil subsurface investigations and soil characteristics at the Hubbell Power Systems Inc test site are shown. Load testing equipment and procedures implemented in this study are also presented.

Chapter 4 presents the monotonic lateral and torsional results of the helical pile with the Collar Vane in both, cohesive and granular soil sites. Lateral load vs Displacements,

Torque vs Rotation, and bending moment profiles are shown with a detailed analysis and interpretation of the load test results.

Chapter 5 focuses on the cyclic lateral and torsional tests performed in both soil conditions. Interpretations of the cyclic load test are presented.

Chapter 6 shows the numerical analysis focused to validate field results and demonstrate the usage of numerical methods to predict the torsional response of the helical pile with the Collar Vane. A comparison between the Collar Vane and a standard foundation element is also presented using a finite difference program. Moreover, an example design of a roadside sign structure is shown to demonstrate the applicability of the Collar Vane.

Chapter 7 ends the research by presenting a summary of the objectives and drawing conclusions from the results and analysis. Furthermore, recommendations for future research are also considered.

# CHAPTER 2

# BACKGROUND

## 2.1 Helical Piles

Helical piles, also known as screw piles, are lightweight deep foundation elements that are screwed into the ground and efficiently generate geotechnical compressive and uplift resistance by mobilizing the shear strength of soil adjacent to helical plates (helices) that are welded to an extendable shaft. The shaft diameter varies between 60 and 114 mm, whereas the helical plates are between 150 and 400 mm. Single or multiple (up to six) helices may be used depending on the soil condition and amount of load required. Helical piles can be designed to resist a variety of axial loads ranging from 200 to 900 kN. Typical helical pile components are shown in Figure 2.1(a). The pitch of the helical plate is 7.62 cm meaning that the pile advances into the soil this amount every shaft revolution (approximately 30 cm every four revolutions) while intended to reduce the soil disturbance. The amount of helical plates per helical pile is limited to the shaft torque installation capacity required to advance the shaft into the soil.

The helical pile capacity depends on the configuration of its components: the shaft length and diameter as well as the specific arrangement of the number, diameter, $D$, spacing to diameter ratio, $(S/D)$, and embedment depth to diameter ratio, $(H/D)$ of the helices. All of these factors can significantly increase the pile's ultimate capacity. In addition to choosing a trustworthy method to predict the helical pile performance, designing helical piles requires taking loading criteria into account.

Helical piles, in certain conditions, are an attractive alternative over conventional deep foundation elements due to its wide range of load capacity, ability to be loaded immediately after installation and relatively inexpensive cost.
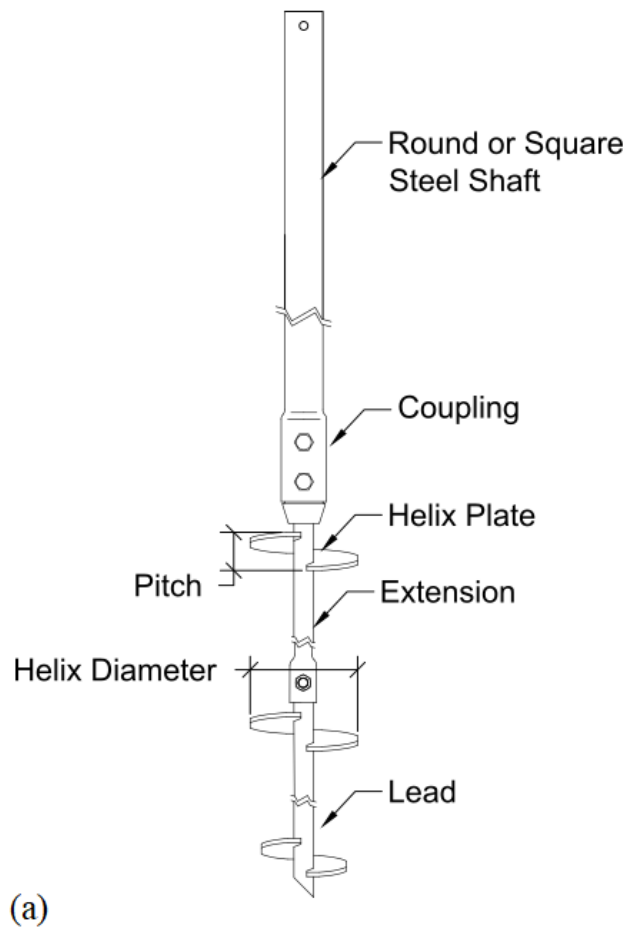
Figure 2.1: Helical pile: (a) basic components and (b) installation at Hubbell Power Systems Inc. Centralia, MO.

### 2.1.1 Installation

Helical piles are quick and simple to install, utilizing non-specialized equipment that is ubiquitous in the United States construction industry, eliminating the need for a specialty contractor. Measurements of torque acquired during installation provide an immediate indication and verification of geotechnical capacity using a torque indicator Figure 2.1(b). The torque motor used for helical pile installations produces a torque between 6 to 100 kN-m. To avoid overstressing, it is recommended that the maximum torque produced by a hydraulic torque motor is lower than the maximum installation torque capacity of the helical pile.

Helical piles are installed in relatively shallow depths up to 6 m. The lead section is the first element to enter the soil. Typically it has one or multiple helical plates as shown in Figure 2.1(a). The helical extension or the extension without helical plates is used to advance the lead section to the deeper stratum into the ground. A hollow circular or square steel shaft is then added to the extension. A constant crowd should be applied while rotating the helical pile to ensure that the helical pile is advancing into the ground. Failure in providing an adequate crowd can lead to soil augering affecting helical pile tensile resistance. Torque values should be recorded at select intervals to estimate torque-to-capacity values using the installation torque as an indicator of soil strength (Perko, 2009).

### 2.1.2 Applications

Helical piles have been in use for more than 180 years. In 1838, an Irish engineer, Alexander Mitchell, designed a helical pile for moorings in England to support the Maplin Sands Lighthouse. In 1851, a helical pile lighthouse was built as the Bridgeport Harbor Lighthouse in Bridgeport Beacon, Connecticut. The original helical piles were installed using eight 6 m long torque bars with a force of 32 to 40 men. Hydraulic torque motors were developed in the 1960s making the helical pile installation smoother and faster becoming the favored product to support tensile forces in the electric utility industry for tie-down anchors on transmission towers and guy wires on utility poles.

Helical piles are ideal for structures subjected to tension or compression forces. Figure 2.2 shows some examples of structures having a combination of these loads: structures supporting foundation for bridge abutments, column bases, concrete slabs; failed foundation restoration; retaining walls tie-back anchors; support batter piers; wind loading structures such as sound walls, billboards, communication towers; permanent or temporary foundation structural shoring; pipeline and pumping equipment supports and a variety of uses in the electric utility industry. Furthermore, helical piles are a desirable alternative in

wetland areas that are environmentally sensitive because of the installation equipment's minimal weight and low soil disturbance. Helical piles in commercial construction have unlimited potential: they can be installed in limited access areas or inside existing buildings without vibration and low noise to support where new loads are planned.



Figure 2.2: Helical piles usage: (a) installed inside existing buildings; (b) pile foundation; (c) retaining wall tie-back anchor; (d) installed in extreme weather (Courtesy of Hubbell Power Systems Inc.).

### 2.1.3 Axial Capacity

There are several names for helical foundation systems such as screw piles, helical anchors, helical piles, and helical piers, but they all essentially refer to the same system. The differences between these systems depend on their design. Typically, the terms helical piers and helical piling refers to shallow foundations and deep foundation systems, respectively. Helical anchor elements are helical piles subjected to tension or uplift loads.

When determining the theoretical load capacity of helical piles is common to use two different methods: the cylindrical shear method (CSM) and the individual bearing method (IBM) as shown in Figure 2.3. Each technique has its own analytical approximations and simplifications proposed by many researchers (Mitsch & Clemence, 1985; Elkasabgy & El Naggar, 2015; Zhang, 1999; Narasimha *et al.*, 1993) including correction factors that depend on the assumed method of analysis and the intended usage of the proposed structure. The suitability of each approach depends on the size and spacing between the helices. When the helical plates are relatively close to each other, it can be assumed that helical plates will create a shearing surface of the soil between the plates (Hoyt & Clemence, 1989). The capacity is given by the sum of the cylindrical shear surface between the uppermost and the lowermost helical plates and the bearing resistance of the lowermost helical plate in compression, or the uppermost in tension plus the shaft resistance as shown in Figure 2.3(a). If the helical plates are relatively far apart along the shaft pile, it is considered that the sum of each helical plate resistance plus the addition of the shaft resistance gives the pile's total ultimate capacity as shown in Figure 2.3(b).

It is not well established what distance between the helical plates creates either condition. Instead, it depends on their size, configuration, and soil condition. Several studies have been conducted to describe the parameters necessary to adopt either method (Lutenegger, 2009, 2011a; Rao *et al.*, 1991). In practice, both approaches are frequently used to evaluate the capacity, and the pile capacity is determined by the lesser of the two values. The three main load transfer mechanisms used in both methods are: skin friction, between the soil and the pile shaft; bearing resistance, provided by the surface area beneath the helical plates, and the soil-to-soil shearing surface at the edge of a mobilized cylindrical soil mass.
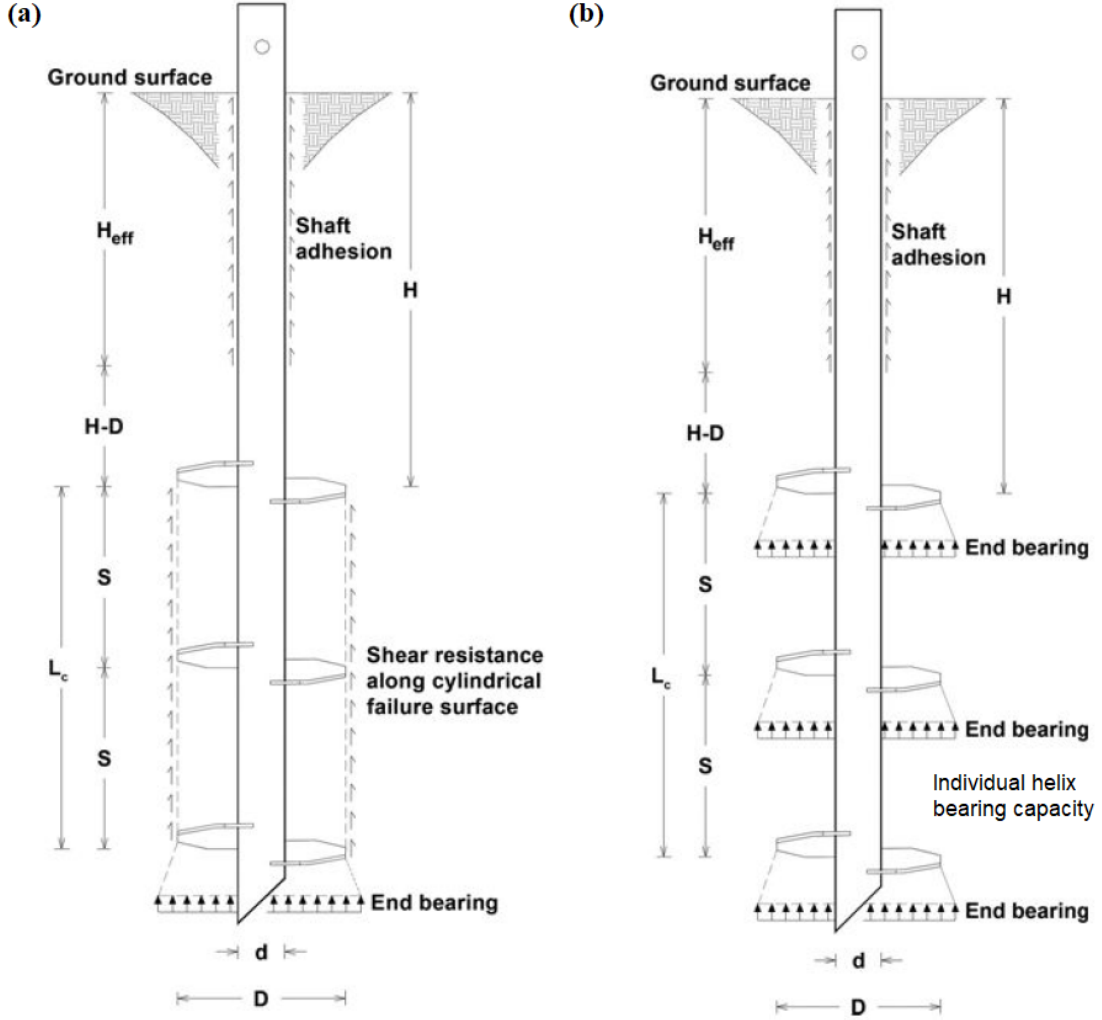
Figure 2.3: Helical pile failure models: (a) cylindrical shear model (CSM) and (b) individual bearing model (IBM) (Elkasabgy & El Naggar, 2015).

### 2.1.3.1 Compressive Individual Plate Bearing Method

Conventional foundation analysis methods like original Terzaghi's general (Terzaghi, 1943) and modified (Meyerhof, 1951) bearing capacity formula have evolved into helical pile design by incorporating modifications to take into account the slenderness of the pile foundation and the individual helical elements. The modified bearing capacity formula is

$$q_{\text{ult}} = cN_cS_cd_c + q'N_qS_qd_q + \frac{1}{2}\gamma BN_\gamma S_\gamma d_\gamma \tag{2.1a}$$

where, $c$, is soil cohesion; $q'$, the effective vertical stress at bearing depth; $\gamma$, the soil unit weight; $B = D$, the width of the bearing element; and $N_c, N_q, N_\gamma$ are Meyerhof's bearing capacity factors depend on soil friction angle, $\phi$:

$$N_c = \cot \phi (N_q - 1) \tag{2.1b}$$

$$N_q = e^{\pi \tan \phi} \tan^2 \left( 45 + \frac{\phi}{2} \right) \tag{2.1c}$$

$$N_\gamma = (N_q - 1) \tan(1.4\phi) \tag{2.1d}$$

$S_c, S_q, S_\gamma$ are shape factors dependent upon the geometry of the helical element:

$$S_c = 1 + \left( \frac{N_q}{N_c} \frac{B}{L} \right) \tag{2.1e}$$

$$S_q = 1 + \left( \frac{B}{L} \right) \tan \phi \tag{2.1f}$$

$$S_\gamma = 1 - 0.4 \left( \frac{B}{L} \right) \tag{2.1g}$$

$d_c, d_q, d_\gamma$, are depth factors dependent upon the location of the helical element below grade

$$d_c = 1 + 0.4K \tag{2.1h}$$

$$d_q = 1 + 2K \tan \phi (1 - \sin \phi)^2 \tag{2.1i}$$

$$d_\gamma = 1 \tag{2.1j}$$

$$K = \tan^{-1} \left( \frac{H}{B} \right) \tag{2.1k}$$

11

where, $H$, is the length above the top helical plate; $L$, is the embedded length; and $K$, is a scaling parameter.

Typically, helical piles have a large length-to-plate diameter ratio, $H/B$, the ratio of $B/L$ is equal to one, and the scaling parameter, $K$, approaches a value of $\pi/2$. Therefore, Equation (2.1a) can be simplified to

$$q_{\text{ult}} = cN_c' + q'(N_q' - 1) + \frac{1}{2}\gamma D N_\gamma' \tag{2.2a}$$

Since $K$ and $B/L$ are constant, the bearing capacity factors only depend on the frictional angle and can be grouped as

$$N_c' = N_c S_c d_c \tag{2.2b}$$

$$N_q' = N_q S_q d_q \tag{2.2c}$$

$$N_\gamma' = N_\gamma S_\gamma d_\gamma \tag{2.2d}$$

where, $D$, is the helix diameter; $N_c'$, is the combined cohesion factor; $N_q'$ is the combined surcharge factor; and $N_\gamma'$, is the combined self-weight term.

Since is generally assumed that the angle of internal friction is equal to zero for undrained loading conditions. More simplifications can be made to Equation (2.2a) for the case of cohesive soils. Skempton (1951) found that the bearing capacity factors are close to the constant values of $N_c' = 9$; $N_q' = 1$; and $N_\gamma' = 0$. For helical piles, the cohesion $c$ can be taken as the undrained shear strength, $s_u$. Thus, the ultimate bearing capacity for helical piles in fine-grained materials is

$$q_{\text{ult}} = 9s_u \tag{2.3}$$

The individual plate bearing capacity analysis for compressive analysis assumes an idealized uniform pressure distribution under each helical plate and shaft friction along the

top pile shaft section as shown in Figure 2.3(b). The total bearing capacity is the sum of each helical plate bearing capacity plus the effective shaft resistance over the pile length:

$$P_{\mathrm{u}} = \sum_n q_{\mathrm{ult}} A_n + \alpha s_u H(\pi d) \tag{2.4}$$

where, $P_{\mathrm{u}}$, is the sum of each bearing capacity of $n^{\mathrm{th}}$ helical plate and the shaft: $A_n$, is the area of the $n^{\mathrm{th}}$ helical bearing plate; $\alpha$, is equal to the unit shaft resistance; $s_u$, is the undrained shear strength of soil along the shaft; $H$, is the length of the helical pile shaft above the top helix; and $d$, is the helical pile shaft diameter.

### 2.1.3.2 Compressive Cylindrical Shear Method

When multiple plates are present and the spacing to plate diameter $(S/D)$ starts to decrease, it will be likely thar each helical plate influence zone starts to overlap with each other as shown in Figure 2.3(a). The soil mass within the plates will create a cylindrical failure with a diameter equal the diameter of the helical plate (Rao & Prasad, 1993) that is assumed to be mobilized once the helical pile is loaded. Therefore, the ultimate bearing capacity of the helical pile under compression based on the cylindrical shear method is equal to the sum of the bearing capacity of the lead helix, adhesion along the shaft, and shear resistance along the cylindrical failure surface (Mooney *et al.*, 1985).

$$P_{\mathrm{u}} = q_{\mathrm{ult}} A_1 + s_u(n-1)s\pi D_{\mathrm{avg}} + \alpha s_u H(\pi d) \tag{2.5}$$

where, $A_1$, is the area of the bottom helix; $s_u$, is the soil shear strength; $H$, is the length of shaft above the top helix; $d$, is the diameter of the pile shaft; $D_{\mathrm{avg}}$, is equal to average helix diameter; $n$, is the number of helices; $\alpha$, is the adhesion factor; and $s$, is the distance between the helices.

The adhesion factor, $\alpha$ is multiplied by the undrained shear strength and the pile shaft surface area to compute the shear resistance along the pile shaft. Ghaly & Clemence (1998) estimated the adhesion factor as

$$\alpha = \frac{2}{3} s_u \tag{2.6}$$

The 2/3 factor accounts for the reduced friction of the bare steel shaft with the soil. Other reduction factors may be used depending on other shaft surface treatments. Using residual shear strength parameters may be more appropriate to estimate adhesion factors because the soil immediately adjacent to the helical pile shafts experience high disturbance during installation.

### 2.1.3.3 Uplift Capacity

The load transfer mechanism between the helical plates and pile shaft is assumed to be the same for both compressive and tensile loading (Narasimha Rao *et al.*, 1989; Lutenegger, 2009; Rao & Prasad, 1993). Hence, the theoretical ultimate bearing capacity is equivalent for both compressive and tensile loading for deep installations. However, it should be noted that the adhesion induced below the pile toe under uplift conditions may result in a slight increment in the pile capacity that is usually neglected for design purposes.

### 2.1.3.4 Installation Torque-Capacity Relations

Helical piles are installed by applying a torque to the pile head and a crowd which is a vertical pressure that allows the helical plates to advance into the soil. The torque is applied by a drive head or torque motor mounted in a boom truck, skid steer, or modified excavator as shown in Figure 2.2(a) and (d). The applied torque can be measured using a torque indicator as shown in Figure 2.1(b).

Empirical relationships between installation torque and pile capacity have been extensively used in the helical pile industry. The torque required to install the pile is directly related to the strength of the soil, and thus the capacity of the pile (Livneh & El Naggar, 2008).

Hoyt & Clemence (1989) found an empirical relationship between the installation torque value, $T$, in the last meter and the ultimate capacity of the pile, $q_u$.

$$q_u = K_t T \tag{2.7}$$

where $K_t$ is a correlation factor that depends on the shaft diameter:

- Square and cylindrical shafts less than 89 mm: $K_t = 33 \text{ m}^{-1}$.

- 89 mm diameter cylindrical shafts: $K_t = 23 \text{ m}^{-1}$.

- 219 mm diameter cylindrical shaft: $K_t = 10 \text{ m}^{-1}$.

The authors (Hoyt & Clemence, 1989) found that the ultimate pile capacity does not depend on soil type or helix plate configuration. Furthermore, Narasimha Rao *et al.* (1989) found that increasing torque installation value is directly related to the pile ultimate capacity, and an increasing shaft diameter reduces the $K_t$ factor. This is consistent with the findings made by Hoyt & Clemence (1989). However, Narasimha Rao *et al.* (1989) found that different anchors with different helix plate spacing and different shaft sizes have an influence on the pile ultimate capacity: The $K_t$ factor was found to increase with an increasing number of helix plates ($S/D$ is decreasing).

The uplift capacity of helical piles using torque-based correlations is influenced by the helical pile geometry. The magnitude of this influence may depend on pore pressure generation and the strain-softening induced by the helical pile installation. Therefore, the $K_t$ factor may have uncertainty and potential error when being used to predict the uplift capacity. However, for specific pile geometries and soil conditions, it is expected to have reliable $K_t$ values from a limited number of field load tests.

### 2.1.4 Lateral Capacity of Piles

Lateral analysis can be subdivided into two categories: rigid and flexible analysis. The rigid analysis is performed in relatively short piles where the pile length is less than about 10 times the shaft diameter. These piles have been used to support lightweight structures such as light poles, signs, and sound walls. Flexible piles are generally used in structures

that require significant axial capacity and some lateral capacity. In the analysis of flexible piles, the pile's structural stiffness and the interaction with the soil are taken into account using loading-deflection $(p-y)$ curves (Perko, 2009).

### 2.1.4.1 Rigid Piles

According to Broms (1964b), a rigid pile fails when the applied horizontal load, $P$, exceeds the ultimate lateral resistance of the soil. The deformation of rigid piles embedded in cohesive soils is shown in Figure 2.4.
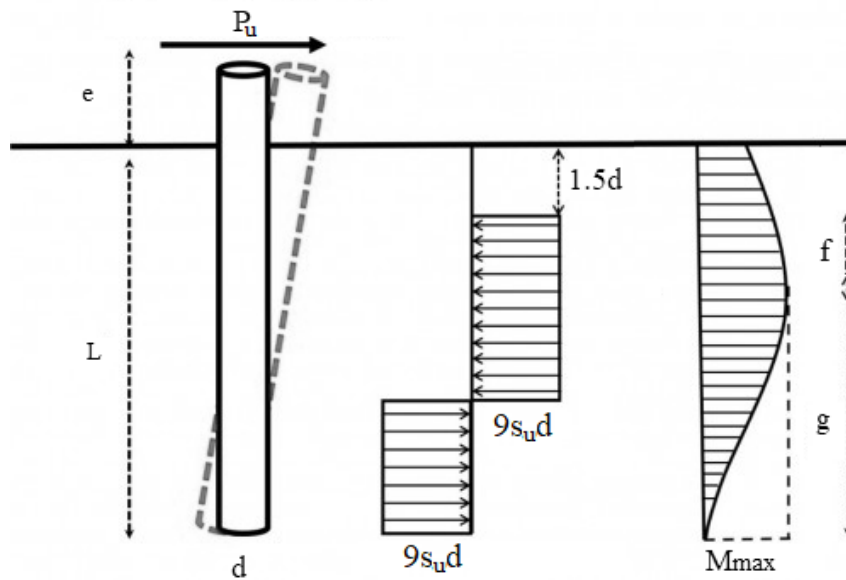


Figure 2.4: Stresses on free-head rigid pile embedded in cohesive soils (Broms, 1964b).

The maximum lateral earth pressure is calculated as

$$P_{\max} = 9s_u d \tag{2.8a}$$

To obtain the maximum horizontal load $P_u$, the integration of the shear forces in the upper and lower portion of the pile yields

$$M_{\max} = P(e + 1.5d + \frac{1}{2}f) \tag{2.8b}$$

16

$$M_{\text{max}} = 9s_u d \left(\frac{g}{2}\right)^2 \qquad (2.8\text{c})$$

$$L = 1.5d + f + g \qquad (2.8\text{d})$$

Finally, the maximum horizontal load $P_u$ is correlated with $f, d$ and $s_u$ as:

$$P_u = 9s_u df \qquad (2.8\text{e})$$

where $f, g, d, e$ and $L$ are defined in Figure 2.4. Based on equations 2.8(b-e), the maximum horizontal load $P_u$ and the maximum bending moment $M_{\text{max}}$ can be determined.

For grained soils, Broms (1964a) assumed a triangular stress soil distribution along the pile shaft as shown in Figure 2.5.
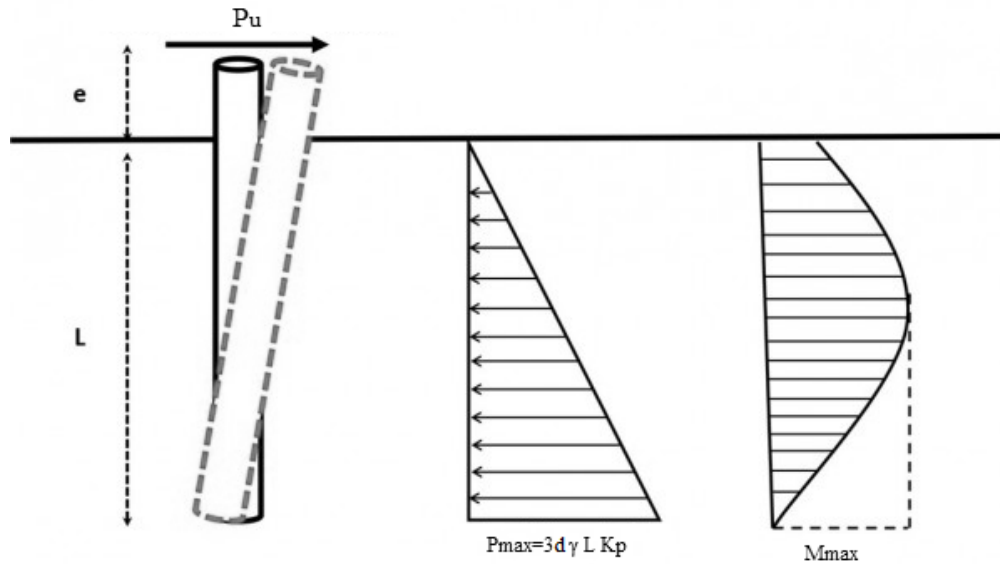


Figure 2.5: Stresses on free-head rigid pile embedded in cohesionless soils (Broms, 1964a).

The maximum developed earth pressure at the bottom of the pile is equal to:

$$P_{\text{max}} = 3d\gamma L K_p \qquad (2.9\text{a})$$

The maximum horizontal load $P_u$ that a pile can carry before soil failure in the closed-form solution given by:

17

$$P_u = \frac{\gamma d L^3 K_p}{2(e+L)} \tag{2.9b}$$

Where, $\gamma$ is the unit weight of soil, and $K_p$ is the passive earth pressure coefficient.

### 2.1.4.2 Flexible Piles

For the long pile analysis, the pile's structural stiffness is also taken into account and it will fail once the maximum bending capacity is exceeded. The problem of laterally loaded piles is related to the problem of a beam resting on an elastic foundation. Most of the numerical solutions involve the concept of modulus of subgrade reaction. This is based on Winkler's assumption of the soil modeled as closely spaced independent elastic springs (Hetényi, 1946). The author gives the differential equation for a beam-column fully embedded in an elastic medium which provides a linear relationship between the pile deflection and the soil response.

Figure 2.6 shows the response of flexible piles subjected to external forces and their corresponding mathematical relationship based on Euler-Bernoulli beam theory. However, there are some limitations in the application of the equations: the beam is assumed to have a uniform cross-section and made of a homogeneous and isotropic material; the beam is fully embedded in a single layer of soil and the soil must have a uniform modulus of subgrade reaction. However, Hetenyi's formulation formed the basis for the $p-y$ curves. Reese & Matlock (1956) presented a solution that assumes a modulus of subgrade reaction that increases with depth. This method was expanded to the $p-y$ method (Reese $et\ al.$, 2005) which assigns nonlinear springs along the pile shaft. Several full-scale tests have been conducted to calibrate the current $p-y$ curves used in standard engineering practice. A wide range of models has been recommended by the American Petroleum Institute (API) (API, 2000).

The equilibrium equation for a fully embedded beam-column element is

$$E_p I_p \frac{d^4 y}{dx^4} + P_x \frac{d^2 y}{dx^2} - p - w = 0 \tag{2.10}$$
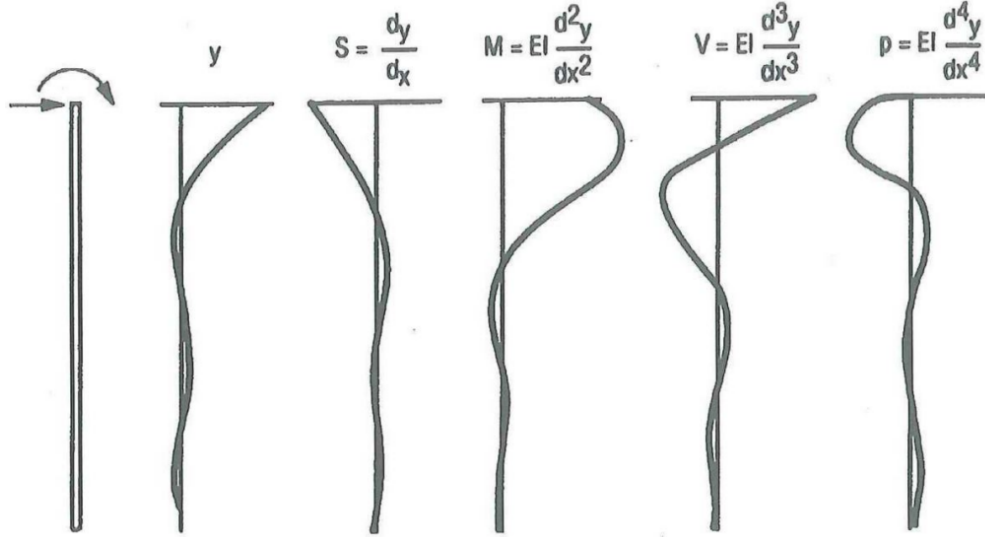
Figure 2.6: Response of a laterally loaded pile (Reese *et al.*, 2005).

where, $E_pI_p$ = bending stiffness of the pile, $y$ = lateral deflection of the pile, $P_x$ = axial load on the pile, $p$ is the lateral soil reaction per unit length of the pile in the function of deflection value, $y$, and $w$ is load distribution along the shaft length (Vega-Posada *et al.*, 2020).

Shear capacity in the transversal direction in the pile shaft is represented by:

$$V = E_pI_p\frac{d^3y}{dx^3} \qquad (2.11)$$

the bending moment in the pile or shaft:

$$M = E_pI_p\frac{d^2y}{dx^2} \qquad (2.12)$$

the slope of deflection diagram calculation:

$$S = \frac{dy}{dx} \qquad (2.13)$$

The reaction of the soil will be presented according to:

$$p = E_{py}y \qquad (2.14)$$

where $E_{py}$ is the spring constant for the soil spring model.

The lateral capacity in flexible piles depends on the pile's structural capacity and the tolerated deflection or rotation at the pile head. If the pile has a considerable structural capacity, failure will be associated with a large displacement. Different interpretation criteria are available to limit the displacement value in function of the pile diameter, pile head rotation limit, or absolute pile head displacement. Chen & Lee (2010) compiled a different lateral capacity interpretation criteria as shown in Table 2.1.

Table 2.1: Different lateral capacity interpretation criteria (Chen & Lee, 2010).

| Method | Type | Definition of interpreted failure load | Symbol |
|---|---|---|---|
| Manoliu *et al.* (1985) | Mathematical Model | Load is equal to inverse slope $(1/m)$ of line $s/p = ms + c$ | $Q_H$ |
| McNulty (1956) | Displacement limitation | Load at 6 mm pile head displacement | $Q_{6mm}$ |
| Walker & Cox (1966) | Displacement limitation | Load at 13 mm pile head displacement | $Q_{13mm}$ |
| City of New York (1981) | Displacement limitation | Load at 25 mm pile head displacement | $Q_{25mm}$ |
| Pyke (1984) | Displacement limitation | Load at 5%D pile head displacement | $Q_{5\%D}$ |
| Briaud (1984) | Displacement limitation | Load at 10%D pile head displacement | $Q_{10\%D}$ |
| Broms (1964b) | Displacement limitation | Load at 20%D pile head displacement | $Q_{20\%D}$ |
| Davidson (1982) | Rotation limitation | Load at 2° head slope | $Q_{2°}$ |
| Ivey & Dunlap (1969) | Rotation limitation | Load at 5° head slope | $Q_{5°}$ |
| Slack & Walker (1970) | Graphical Construction | Load at change in slope on a log-log load-displacement plotabajo | $Q_{S\&W}$ |
| Hirany & Kulhawy (1988) | Graphical Construction | Failure is based on variation of apparent depth of rotation with load | $Q_L$ |

The different criteria shown in Table 2.1 are also represented in a load-deflection curve performed by Bierschwale *et al.* (1981). The interpreted lateral capacities vary from 189 to 882 kN with approximately a ratio of 4.7 times between the maximum and minimum failure criteria. Moreover, Trombly (2006) suggest that the allowable lateral capacity of a pile is half the load that causes 25 mm of deflection. These different interpretations can be found using commercial software such as LPile by applying successively incremental loads until an error message is obtained.
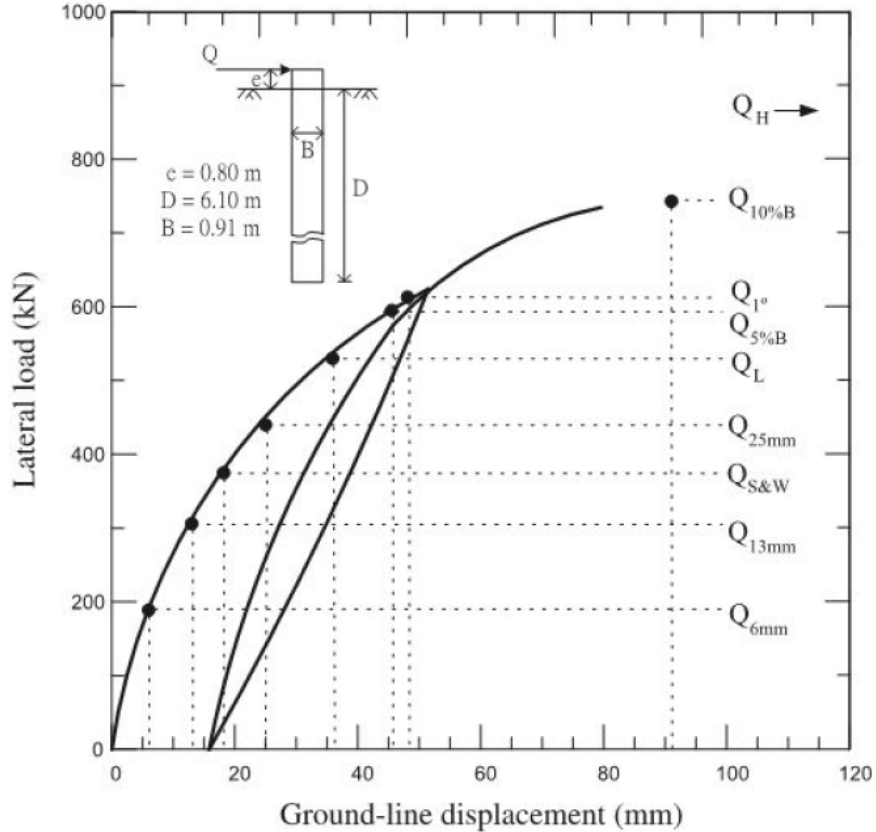
Figure 2.7: Load-deflection curve with different lateral capacity interpretations (Chen & Lee, 2010).

### 2.1.4.3   Helical Piles

Lateral loads in helical piles may be transferred by the supported structures because for a variety of reasons such as wind loading, axial load eccentricities, or seismic loads. Puri *et al.* (1984) performed mathematical models based on Matlock and Reese's nonlinear $p - y$ type analysis on helical piles and compared the results with previously published full-scale lateral load tests and found that: (i) lateral resistance is controlled by the mechanical properties of the shaft for depths of pile's embedment greater than three to five times the critical stiffness factor (2 to 3 m for commonly manufactured helix foundations in stiff clay); (ii) helical anchor pile can develop significant resistance to lateral loads and that capacity can be validly estimated using nonlinear p-y type analysis. Prasad & Rao (1996) studied the lateral capacity of helical piles embedded in clays using small-scale piles. The

ratio of length to helical plate diameter varied from 12 to 18. It was found that the presence of the helical plate increases the lateral capacity of the helical plate by around 1.2 to 1.5 times of the piles without plates. Perko (2003) performed a computer analysis to determine the lateral strength of helical piles in different soil conditions. A 76.2 mm O.D. pile was tested and it was found that the lateral capacity depends on the shaft strength near the surface. The force required to displace the pile 12.7 mm was between 13 to 27 kN.

Due to the slenderness of the pile shaft, helical piles do not provide high lateral resistance compared to pile foundations with large diameters. The role of the HP helices providing lateral resistance is negligible according to Zhang (1999). Similar observations were reported by Puri *et al.* (1984) using scale anchors where he concluded that helices had a negligible effect on the lateral behavior when the embedded length is more than 3 to 5 the stiffness factor $R = (E_p I/K)^{0.25}$ (i.e., flexible pile) where, $E_p$ is Young's modulus of the pile; $I$ is the pile moment of inertia; and $K$ is the subgrade modulus (67 times the undrained shear strength) meaning that the resistance is governed mainly by the shaft diameter (Sakr, 2009). Hoyt (2007) compiles different methods to increase the lateral capacity of helical piles.
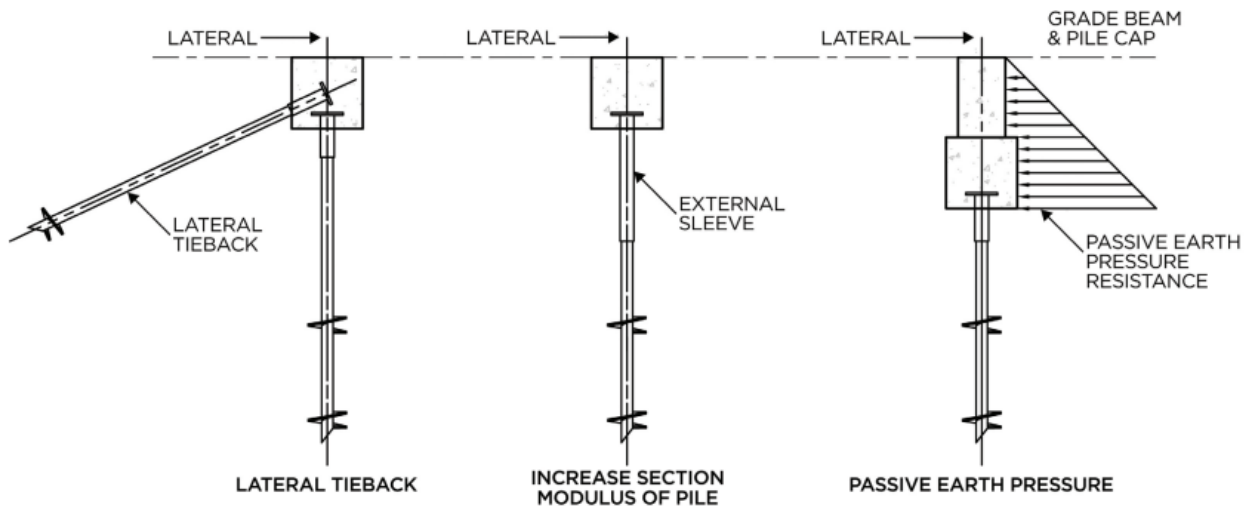


Figure 2.8: Methods to increase helical pile lateral capacity (Hoyt, 2007).

Figure 2.8 shows several approaches to increase the helical pile lateral capacity. The first approach is to install a lateral tieback at the helical pile cap. The applied lateral force would mobilize the lateral tieback in tension. The second approach is to place an external sleeve over the pile shaft to increase the stiffness or moment of inertia at the top where the maximum bending moments are occurring. The other option is using concrete by pre-drilling a hole at sufficient depth to meet the lateral load requirements.

## 2.2   Laterally Loaded Structures

Several types of foundation systems are used to support a wide variety of structures in different conditions. Pile-supported structures in marine environments are subject to a variety of loading sources, intensities, and frequencies such as berthing and mooring forces, wind, waves, storm surges, and current forces. Moreover, transportation structures such as bridge piers, excavation supports, and traffic signs are subjected to different types of loads.

### 2.2.1   Lightweight Marine Structures

Pile-supported structures in marine environments such as piers, pipelines, and walkways are subject to a variety of loading sources, intensities, and frequencies. Helical anchor technology, which was initially developed for the marine environment to anchor oil pipelines to the ocean floor, has established itself as a reliable and environmentally responsible substitute for conventional mushroom, deadweight, and pile anchors for boat owners and marine construction, and the civil engineering industry. Helix mooring anchors are often installed into the seabed by work boats equipped with drill rigs or by divers using submersible tools and torque-reducing devices. The anchors are then installed into good-bearing soil and then the line is connected to the anchor head. Moreover, helix anchors allow marine life to live undisturbed in the places where they are placed and have little effect on delicate ecosystems (Vito & Cook, 2011).

Figure 2.9: Helical anchors in marine structures (Alpha Anchor & Pile Ltd, 2014).

Since the middle of the 19th century, helical anchors have been employed in shallow offshore applications to support mooring anchors, offshore lighthouses, and oceanfront piers in many parts of the world (Lutenegger, 2011b). Morgan (1944) described the use of double-helix and triple-helix screw piles with helical plates of 2.1 and 2.4 m diameter coupled to a 0.9 m diameter shaft to carry a jetty in Scotland. Wilson (1950) also discussed the installation of single-helix screw piles with 2.4 m diameter helical plates mounted on a 0.9 m diameter shaft to hold the jetty at Newport. In both cases, the installation was carried out using electric capstans attached to the top of the pile shaft measuring power to estimate the installation torque. Numerical modeling has been also employed to study the performance of anchor piles for marine structures: Spagnoli & Gavin (2015) performed 48 simulations of screw piles using PLAXIS 3D to compare the uplift capacity with torque-based methods with scope to demonstrate the viability of the use of helical piles as a novel foundation system for offshore structures. Ghazavi *et al.* (2022) considers helical piles as a potential substitution for driven piles in offshore applications. The author performed numerical simulations to study the effects of tapered helices and

24

inter-helix spacing in homogeneous and in-homogeneous soil profiles on the compression capacity. Spagnoli (2017) and Spagnoli *et al.* (2018) presented a sensitivity analysis on the performance of helical piles for offshore structures.

Helical piles have been in use in marine and onshore structures for many years ago. However, the development of other foundation techniques in the 20th century caused a decline in the use of helical piers (Perko, 2009). It recently made a reappearance and is now more often employed in a variety of situations, particularly in marine structures (Khazaei & Eslami, 2017) as shown in Figure 2.9. Some researchers have even considered the application of helical piles to support offshore wind turbines (Byrne & Houlsby, 2015; Lin *et al.*, 2022) as tripods or jackets, or other multi-footing structures, will be required if turbines grow in size or are installed in deeper water where the footing uplift capacity becomes the crucial design criterion for these configurations.

Additionally, the anchor pile is widely used in marine aquaculture. Its uplift resistance capacity determines the safety performance of the marine aquaculture structure. Kong *et al.* (2022) presented the effects of cyclic loads such as wind, waves, and currents in the marine environment on the uplift resistance capacity of anchor piles. It was found that the increase in the loading amplitude reduces the stiffness of the soil and hence the uplift capacity. Gui *et al.* (2021); Cortes-Garcia *et al.* (2019) investigated the effects of the initial tension, angle, pile diameter, embedded depth, and pile configuration on the uplift resistance capacity of anchor piles under oblique loading.

### 2.2.2   Transportation Structures

In general, transportation structures are subjected to different kinds of loads such as high wind velocity, seismic loads, traffic loads, or wave loads. The most common structures for transportation supporting structures are driven piles, jacked piles, and drilled shafts that are used to support: bridge abutments, bridge piers, pedestrian bridges; temporary

excavation support, permanent retaining walls; noise barrier walls, embankment stabilization; light poles and traffic signals.

Besides the vertical loads on a bridge pier, lateral loads from traffic, braking, and wind loads can act on them. Bridge abutments are subjected to lateral earth pressures that also act as a lateral load. They can be supported on a single foundation system or on groups of foundation systems such as drilled shafts or micro piles. Micropiles may be suitable for quick bridge foundation installations. Although they are small in diameter, they can carry surprisingly high loads with small deflections.

Lateral earth pressures generated behind temporal or permanent retaining structures can be supported using different types of deep foundation systems. Helical tieback anchors are used in conjunction with a variety of earth retaining systems such as sheet piles and soldier piles when more lateral strength is required. Tieback anchors are installed to the interior of the retaining wall with the purpose of increasing the stiffness of the wall and keeping it from bowing or leaning in the future.

Lateral loads on sound walls, traffic signals, and signs, are most commonly caused by wind action and these are typically resisted by a single element or occasionally a group of piles or small-diameter pile shafts. Helical piles are a quick and reliable foundation method that have been used to support transportation structures like street lighting, highway signage, or tiebacks for retaining walls.

## 2.3   Design Methods for Lateral and Torsional Loading

When designing structures, it is essential to consider the structural properties of the pile itself and the potential effects of external loading acting on them. This section presents the methodologies used to calculate the loads acting on a structure and estimate the torsional capacities.

### 2.3.1  Lateral Loading

Estimating the response of piles subjected to lateral loads can be achieved using advanced methods such as finite element analysis (FEA) and finite element methods (FEM). These approaches can account for the effects of lateral loads on single or group piles, and simulate complex soil behavior and pile-soil interaction. Several examples of such software are PLAXIS, GRLWEAP, and LPile. These programs offer extensive features and capabilities to analyze and design pile foundations subjected to lateral loads, ensuring that the final design is safe and efficient.

### 2.3.1.1  $p - y$ Curve Method

The lateral deflection of the pile occurs when a lateral load is applied to the top of a pile. It is necessary for the reactions produced in the soil to satisfy the equations of static equilibrium and to be consistent with deflections. Additionally, because no pile is entirely rigid, the amount of pile bending must be consistent with soil reaction and the stiffness of the pile. Thus, this problem is generally called a soil-structure-interaction problem.

To calculate pile deflections, the resistance of the soil must be known. There are different approaches that help to compute the resistance of the soil to pile movement. The $p - y$ method is the preferred method to design piles since is possible to consider: (i) multiple layers of soils; (ii) it can be modeled a non-linear interaction between the soil and the pile shaft; (iii) the flexural rigidity of the pile shaft can be varied along the length of shafts; and (iv) degradation of flexural rigidity of a drilled shaft under loading can be modeled. A number of $p - y$ curves have been proposed for different types of soils as shown in Table 2.2 by several researchers. The curves available for clay and sand are based on a significant number of carefully conducted tests in these conditions. Finite difference numerical algorithms have been used to solve the governing differential Equation (2.10), as in the commonly available commercial software programs such as LPile.

Table 2.2: Recommended criteria for $p-y$ curves in different soils

| Soil Type and Condition | Reference |
| --- | --- |
| Soft Clay Below the Water Table | Matlock (1970) |
| Stiff Clay Below the Water Table | Reese & Welch (1975) |
| Stiff Clay Above the Water Table | Reese *et al.* (1975) |
| Sands | Reese *et al.* (1974) |
| Weak Rock | Reese (1997) |

Figure 2.10 shows a $p-y$ curve for a single element in a particular depth in a deep foundation element. A linear displacement- soil reaction occurs in point a when an external force is applied. A nonlinear stress-strain behavior will occur by increasing the load until it reaches point b and ultimately, the soil will reach the ultimate resistance $p_u$ in point c.
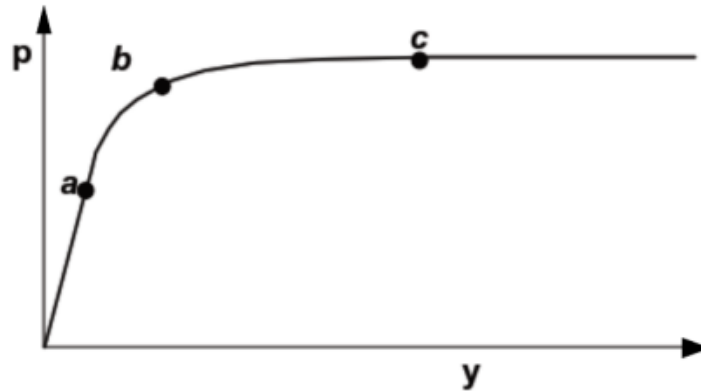


Figure 2.10: $p-y$ curve for a single element (Li & Yang, 2017).

In flexible piles analysis, the pile when subjected to lateral loads will exhibit a flexural rotation response rather than a rigid rotation. The simplest method to perform the lateral analysis is using software applications such as LPile. This software uses discrete elements to solve conventional $p-y$ methods of analysis. The user is able to choose between built-in $p-y$ curves or user-input $p-y$ curves and specify the geometry and structural properties of the pile shaft and the external loads applied at the pile head. The software calculates the bending moment, shear forces, and soil resistance in the function of depth. The program will show an error if the lateral capacity exceeds the ultimate resistance of the

28

pile. The lateral capacity of a helical pile must be determined using an iterative approach because the program cannot solve it directly by setting increasing loads at once. The $p - y$ method's software analysis is generally simple to use and gives results rapidly. This allows the user the opportunity to explore different variables and their potential effects on the design very easily. It is possible to investigate differences in the type of loading, magnitude, and location of the load as well as subsurface conditions such as soil or rock layer depth, thickness, density, and strength. In order to determine the potential sensitivity of the findings to such inputs, the parametric study of input parameters should be a part of the study of deep foundations utilizing the $p - y$ approach.

The $p - y$ curves are not defined only by the type of soil. Pile cross-sectional shape and dimensions, interface friction angle between soil and pile, pile bending stiffness, and pile head conditions also have an influence on the curves. Ashour & Norris (2000) found that in uniform sand deposits using stiff piles results in stiffer $p - y$ curves, it was also found that testing two piles with the same width but one with a circular cross-section and the other one with a square cross-section will result in different $p - y$ curves where the square cross-section had a stiffer response. The limitations to such models include the subsurface conditions type of soil, rock, and groundwater conditions; foundation characteristics foundation type, shape, and size; and loading conditions: static, cyclical, and loading rate.

### 2.3.1.2   Finite Element Model

Nowadays, a lot of structures are being developed with higher computing complexity than before, where traditional analytical calculation techniques would take too long. The finite element method computes approximate solutions to differential equations through the use of nodes that connect the structure's pieces.

PLAXIS 3D is a three-dimensional finite element software that uses advanced material modeling that helps to perform accurate three-dimensional analysis of deformation and stability in geotechnical engineering and rock mechanics (Brinkgreve *et al.*, 2013). These

advanced material models have specific features such as stress-dependency of stiffness, and strain-hardening/softening which help the user to simulate the behavior of soils and rocks more realistically.
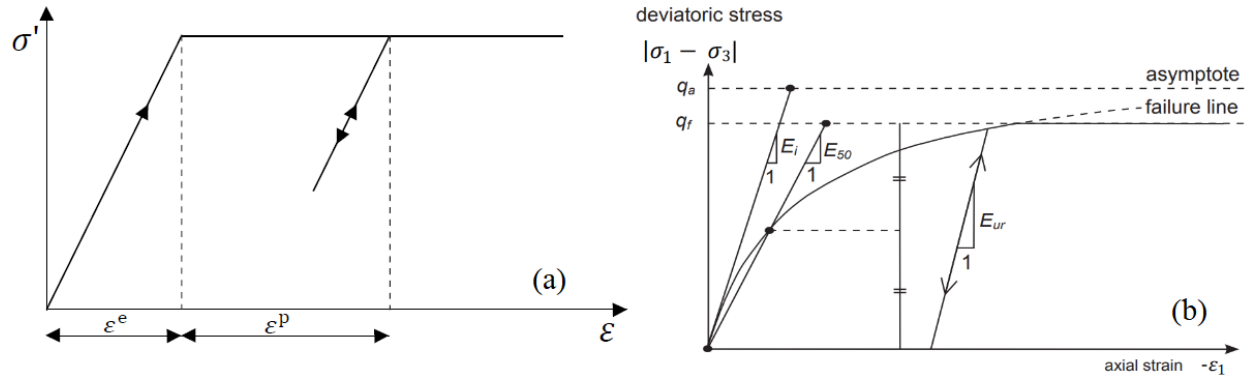


Figure 2.11: (a) Mohr-Coulomb for an elastic and perfectly plastic model; (b) Hardening Soil elastoplastic model (Brinkgreve *et al.*, 2013).

One of the constitutive models included in the software is the linear elastic perfectly-plastic Mohr-Coulomb (MC) model (Figure 2.11a), which involves five input parameters: $E$ and $\nu$ for soil elasticity; $\phi$ and $c$ for soil plasticity and $\psi$ as an angle of dilatancy (Brinkgreve *et al.*, 2013). This Mohr-Coulomb model represents a 'first-order' approximation of soil or rock behavior. Due to this constant stiffness, computations tend to be relatively fast and one obtains a first estimate of deformations. A more advanced model is the Hardening Soil (HS) model (Figure 2.11b). This model is an advanced elastoplastic constitutive model used to simulate both stiff and soft soil behavior. It relates stiffness parameters to stress levels and simulates plastic strain development under compressive loading (Brinkgreve *et al.*, 2013). HS takes into account three stiffness parameters: plastic straining due to primary deviatoric loading, $E_{50}^{\text{ref}}$; plastic straining due to primary compression, $E_{\text{oed}}^{\text{ref}}$; elastic unloading/reloading, $E_{\text{ur}}^{\text{ref}}$. In many practical cases is appropriate to set $E_{\text{ur}}^{\text{ref}} = 3E_{50}^{\text{ref}}$. When the soil is subjected to deviatoric loading, the soil shows a decrease in stiffness, and simultaneously irreversible plastic strains develop. The relationship between stress and axial strain is well represented by a hyperbolic curve as shown in Figure 2.11(b).

### 2.3.2   Torsional Loading

Structures such as offshore wind turbine foundations, traffic signal poles, and mast arm traffic signs are often supported by pile foundations. These structures are usually subjected to lateral loads of considerable magnitude from wind actions or waves. Besides the lateral loads, significant torsional forces can be transferred to the foundation piles due to the eccentricity of these lateral loads.

Figure 2.12 shows typical torque-twist angle responses during torsional load tests of drilled shafts and jacked piles. The plots, in general, show that the torsional displacements have three characteristic regions: an initial elastic region, a sharply curving transition, and a flattening tendency final region where the pile capacity was fully mobilized.

The failure criteria in torsional loading have different interpretations by several based on the amount of rotation or the rate of shear stresses observed under loading conditions. Hu *et al.* (2006) performed several torsional tests in sands using centrifuge tests to analyze drilled shaft's behavior under hurricane extreme events in Florida. Florida Department of Transportation (FDOT) uses 15° of rotation as a failure criterion for traffic sign supports based on serviceability requirements. Moreover, Li *et al.* (2017) extrapolated the torque-rotation behavior beyond the measurements using the hyperbolic curve fit technique to calculate the torsional resistance and suggested failure has occurred when the rate of shear stress increase with rotation is zero (i.e., $dT/d\theta = 0$) (Dutt & O'Neill, 1983). This might be associated with large twist angles, which might be not achievable in load tests. Finally, Zhang & Kong (2006) proposed a failure criterion expressed as the sum of the elastic torsional deformation of the shaft and the toe twist angle at which the toe torsional resistance is mobilized.

The methods to compute the torsional capacity are based on the estimation of the skin friction between the pile and the soil.

Pile capacity, $Q_u$, is commonly estimated as the sum of the shaft and base capacities, as follows:
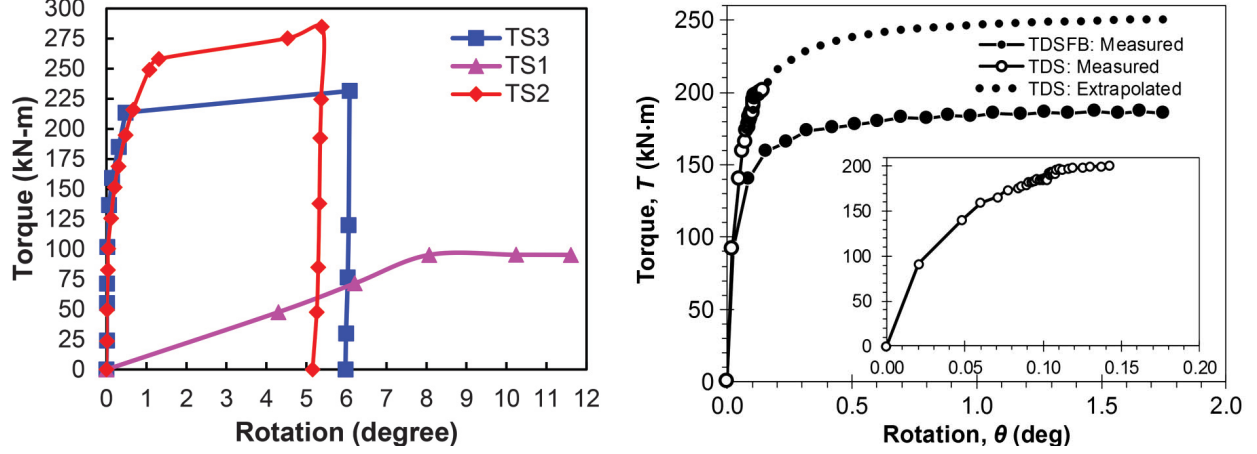
Figure 2.12: Typical torque-twist angle responses during torsional loads (Thiyyakkandi *et al.*, 2016; Li *et al.*, 2017).

$$Q_u = Q_s + Q_b \tag{2.15}$$

where, $Q_s$, is the side capacity and $Q_b$, tip capacity. The side and tip capacity for a cylindrical element may be expressed as

$$Q_s = \int f_s dA_s = \frac{1}{2}\pi D^2 \int_0^L f_s(z)dz \tag{2.16a}$$

$$Q_b = f_s A_b = \frac{1}{12}\pi D^3 f_s \tag{2.16b}$$

where, $f_s$ is the unit shear resistance and $D$ the diameter of the shaft. Several methods are available in the literature for estimating the unit shear resistance.

### 2.3.2.1 $\alpha$-method - Cohesive Soils

The $\alpha$-method was proposed by (Tomlinson, 1957) is based on the adhesion factor, $\alpha$, developed using full-scale load test in cohesive soils. The adhesion factor is an empirical value related to the undrained shear strength and is derived from drilled shaft load test. More rigorous studies by Randolph & Murphy (1985) and Semple & Rigden (1984) proposed that $\alpha$ is not only influenced by the undrained shear strength but also by the mean effective overburden stress, $\sigma'_v$; the overconsolidation ratio, $OCR$; the effective stress

32

friction angle, $\phi'$; the pile width, $D$; and the pile length, $L$. However, the approach is used due to its simplicity and the unit shear resistance $f_s$ can be taken as:

$$f_s = \alpha s_u \tag{2.17}$$

where the adhesion factor $\alpha$ has been proposed by different authors and can be taken as shown in Table 2.3. O'Neil *et al.* (1999) recommended values for $\alpha$ for drilled shafts in clay; Coleman & Arcement (2002) studied four methods for the design of auger cast piles in mixed soil conditions and defined failure criteria for interpreting load test results.

Table 2.3: Unit skin friction ($f_s$) prediction methods for cohesive soils considered in this study.

| Method | Equation |
|---|---|
| 1. O'Neil *et al.* (1999) | $f_s = \alpha s_u$ |
| | $\alpha = \begin{cases} 0.55 & \text{for } \frac{s_u}{p_a} \leq 1.5 \\ 0.55 - 0.1\left(\frac{s_u}{p_a} - 1.5\right) & \text{for } 1.5 \leq \frac{s_u}{p_a} \leq 2.5 \end{cases}$ |
| 2. Coleman & Arcement (2002) | $f_s = \alpha s_u$ |
| | $\alpha = 56.192 s_u^{-1.0162}$ |
| | recommended that $0.35 \leq \alpha \leq 2.5$ |
| 3. Salgado (2010) | $f_s = \alpha s_u$ |
| | $\alpha = 0.4\left[1 - 0.12\ln\left(\frac{s_u}{p_a}\right)\right]$ |
| 4. Loehr *et al.* (2011) | $f_s = \alpha s_u$ |
| | $\alpha = \frac{5.19}{\sqrt{s_u}} \leq 1.0; s_u$ in kPa |

Note: $p_a$, atmospheric pressure.

### 2.3.2.2 $\beta$-method - Cohesionless Soils

For the purpose of calculating shaft friction for piles in sand, different methods published in the literature are used to calculate $\beta$ coefficients. The notion is that Equation (2.18) can be used at any position to determine the unit friction along the pile's surface.

$$f_s = \beta \sigma_v' \tag{2.18}$$

where $f_s$ is the unit shaft friction, $\sigma'_{vo}$ is the vertical effective stress, and $\beta$ can be expressed as

$$\beta = K \tan \phi' \tag{2.19}$$

where $K$ is the lateral earth pressure coefficient and $\phi'$ is the internal friction angle of the soil.

The $\beta$-coefficient varies depending on factors such as grain angularity, density, soil gradation, and mineralogical composition. Table 2.4 shows a general range of $\beta$-coefficients that can be predicted from fundamental soil types using data compiled by Fellenius (2008). However, the $\beta$-coefficients are subject to large variations from the values displayed in Table 2.4. As seen in Figure 2.13, Rollins *et al.* (2005) conducted uplift static loading tests to calculate the beta-coefficients at ultimate resistance. The value of the $\beta$-coefficient is higher when the embedment length is low and as the embedment length increases the coefficient starts to decrease considerably.

Table 2.4: Approximate ranges of $\beta$-coefficients

| Soil Type | $\phi'$ | $\beta$ |
|---|---|---|
| Clay | 25 - 30 | 0.15 -0.35 |
| Silt | 28 - 34 | 0.25 - 0.50 |
| Sand | 32 - 40 | 0.30 - 0.90 |
| Gravel | 35 - 45 | 0.35 - 0.80 |

### 2.3.2.3   CPT-Based Methods

The torsional capacity of a drilled shaft can be approximated using empirical correlations with the results of some field tests such as the standard penetration test (SPT) or the cone penetration test (CPT). Since CPT probes were performed in this study, a list of CPT-based methods is explained below to estimate the skin friction value, $f_s$ based on
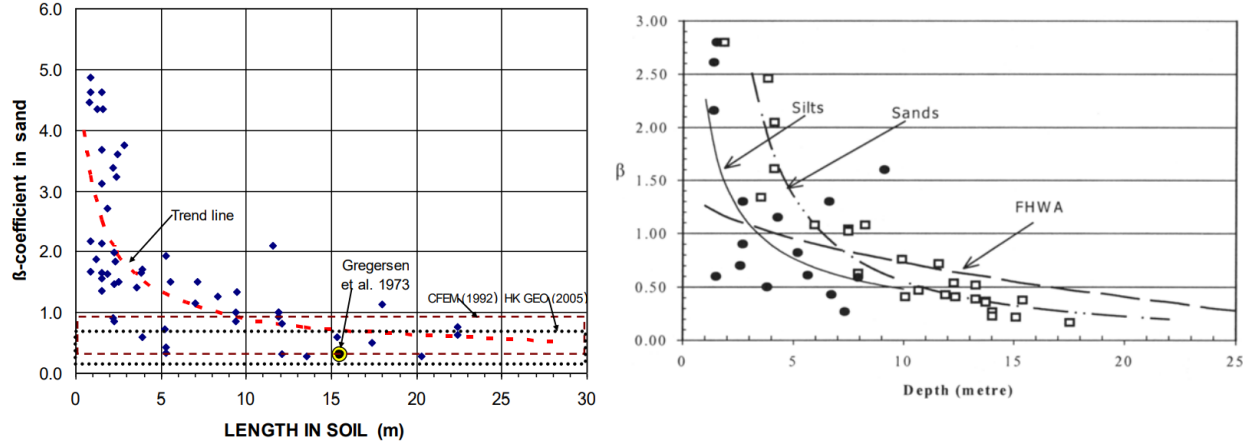
Figure 2.13: $\beta$-coefficients versus embedment length for piles embedded in sand (Fellenius, 2017; Coleman & Arcement, 2002).

correlations with the CPT tip resistance $q_c$. In this section, methods proposed by Bustamante & Gianeselli (1982), Alsamman (1995) and Aoki & Velloso (1975) is presented.

One of the first direct methods based on the CPT which is known as the Laboratoire Central des Ponts et Chaussées (LCPC) method developed by Bustamante & Gianeselli (1982) is based on a large number of full-scale loading tests to correlate the point and skin friction resistance with the cone resistance $q_c$ measured with the CPT and predict the bearing capacity of deep foundations. The 197 full-scale load tests, of which 55 were performed on drilled shafts, constitute the base of the LCPC method. The diameter of the shaft range from 0.42 to 1.50 meters. Testing was done at 48 different locations with a wide range of soil types, including clay, silt, sand, gravel, peat, and weathered rock. The skin friction using the LCPC method can be computed as

$$f_s = \frac{1}{\alpha} q_c \qquad (2.20)$$

where $q_c$ is the cone tip resistance from CPT and $\alpha$ the friction coefficient which depends on the type of soil and pile shown in Table 2.6.

Note: Second values in parentheses corresponds to maximum limit unit skin friction, $f_s$, for piles with careful execution or minimum disturbance of soil during installation.

Table 2.5: Unit skin friction ($f_s$) prediction methods for cohesionless soils considered in this study.

| Method | Equation |
|---|---|
| 1. Touma & Reese (1974) | $f_s = K\sigma'_v \tan\phi' \leq 239.4 \text{ kPa}$ $$K = \begin{cases} 0.7 & \text{for } z \leq 7.6\text{m} \\ 0.6 & \text{for } 7.6 \text{ m} < z \leq 12.2 \text{ m} \\ 0.5 & \text{for } z > 12.2 \text{ m} \end{cases}$$ |
| 2. O'Neil $et\ al.$ (1999) | $f_s = \beta\sigma'_v$ $$\beta = \begin{cases} \frac{N_{60}}{15}(1.5 - 0.245\sqrt{z}) & \text{for } N_{60} < 15 \\ 1.5 - 0.245\sqrt{z} & \text{for } N_{60} \geq 15 \end{cases}$$ |
| 3. Zelada & Stephenson (2000) | $f_s = \beta\sigma'_v$ $$\beta = \begin{cases} \frac{N_{60}}{15}(1.2 - 0.196\sqrt{z}) & \text{for } N_{60} < 15 \\ 1.2 - 0.196\sqrt{z} & \text{for } N_{60} \geq 15 \end{cases}$$ recommended that $0.2 \leq \beta \leq 0.96$ |
| 4. Coleman & Arcement (2002) | $f_s = \beta\sigma'_v$ $\beta = 10.716z^{-1.2982}$ recommended that $0.2 \leq \beta \leq 2.5$ |
| 5. Stuedlein $et\ al.$ (2014) | $f_s = \beta\sigma'_v$ $$\beta = \begin{cases} 1.5 & \text{for } z \leq 6.0 \text{ m} \\ \left[\frac{\log_{10}(\frac{z}{275})}{1.5}\right]^4 & \text{for } 6.0 \text{ m} < z \leq 24.0 \text{ m} \\ 0.25 & \text{for } z > 24.0 \text{ m} \end{cases}$$ |
| 6. FHWA (2018) | $f_s = \beta\sigma'_v$ $\beta = (1 - \sin\phi')\text{OCR}^{\sin\phi'}\tan\phi' \leq K_p \tan\phi'$ $\text{OCR} = \frac{\sigma'_p}{\sigma'_v}$ $\frac{\sigma'_p}{p_a} = 0.47(N_{60})^m$ $$m = \begin{cases} 0.6 & \text{for clean quartz sand} \\ 0.8 & \text{for silty sand up to sandy silt} \end{cases}$$ |

Note: $N_{60}$, SPT blow count adjusted for 60% energy efficiency; $z(m)$ = Pile length

* Category:

– IA Plain bored piles, mud bored piles, hollow auger bored piles, type I micropiles, cast-in-place screwed piles, piers and barrettes.

Table 2.6: Friction coefficient, $\alpha$ (Bustamante & Gianeselli, 1982).

| Soil type | $q_c$ (MPa) | Coefficient $\alpha$ | | | | Maximum Limit $f_s$ (MPa) | | | | | |
|---|---|---|---|---|---|---|---|---|---|---|---|
| | | Category* | | | | | | | | | |
| | | I | | II | | I | | II | | III | |
| | | I A | I B | II A | II B | I A | I B | II A | II B | III A | III B |
| Soft clay and mud | $< 1$ | 30 | 30 | 30 | 30 | 0.015 | 0.015 | 0.015 | 0.015 | 0.035 | - |
| Moderately compact clay | 1 to 5 | 40 | 80 | 40 | 80 | 0.035 (0.08) | 0.035 (0.08) | 0.035 (0.08) | 0.035 | 0.08 | $\geq 0.12$ |
| Silt and loose sand | $\leq 5$ | 60 | 150 | 60 | 120 | 0.035 | 0.035 | 0.035 | 0.035 | 0.08 | - |
| Compact to stiff clay and compact silt | $> 5$ | 60 | 120 | 60 | 120 | 0.035 (0.08) | 0.035 (0.08) | 0.035 (0.08) | 0.035 | 0.08 | $\geq 0.20$ |
| Soft chalk | $\leq 5$ | 100 | 120 | 100 | 120 | 0.035 | 0.035 | 0.035 | 0.035 | 0.08 | - |
| Moderately compact sand and gravel | 5 to 12 | 100 | 200 | 100 | 200 | 0.08 (0.12) | 0.035 (0.08) | 0.08 (0.12) | 0.08 | 0.12 | $\geq 0.20$ |
| Weathered to fragmented chalk | $> 5$ | 60 | 80 | 60 | 80 | 0.12 (0.15) | 0.08 (0.12) | 0.12 (0.15) | 0.12 | 0.15 | $\geq 0.20$ |
| Compact to very compact sand and gravel | $\geq 12$ | 150 | 300 | 150 | 200 | 0.12 (0.15) | 0.08 (0.12) | 0.12 (0.15) | 0.12 | 0.15 | $\geq 0.20$ |

– IB Cased bored piles, driven cast piles.

– IIA Driven precast piles, prestressed tubular piles, jacked concrete piles.

– IIB Driven metal piles and jacked metal piles.

– IIIA Driven grouted piles and driven rammed piles.

– IIIB High pressure grouted piles with diameters > 250 mm and micropiles grouted under high pressure.

Another CPT-based method is the one developed by Aoki & Velloso (1975) which consists of a method to estimate the bearing capacity of different piles based on the results from dynamic penetration tests. The skin friction using Aoki and Velloso method can be computed as

$$f_s = \frac{\alpha}{F_2} q_c \tag{2.21}$$

where $\alpha$ is the resistance factor depending on the type of soil as shown in Table 2.7 and $F_2$ is a correction factor depending on the type of pile as shown in Table 2.8.

Table 2.7: $\alpha$ values for Aoki and Velloso's method.

| Soil | $\alpha$ (%) |
|------|------|
| Sand | 1.4 |
| Silty sand | 2.0 |
| Silty clayey sand | 2.4 |
| Clayey sand | 3.0 |
| Clayey silty sand | 2.8 |
| Silt | 3.0 |
| Sandy silt | 2.2 |
| Sandy clayey silt | 2.8 |
| Clayey silt | 3.4 |
| Clayey sandy silt | 3.0 |
| Clay | 6.0 |
| Sandy clay | 2.4 |
| Sandy silty clay | 2.8 |
| Silty clay | 4.0 |
| Silty sandy clay | 3.2 |

Alsamman (1995) evaluated the cone penetration test as an alternative for calculating the axial capacity of drilled shafts and to develop procedures that are based on CPT resistance to calculate the side and tip capacity of drilled shafts. The results of 48 load

38

Table 2.8: $F_2$ values for Aoki and Velloso's method.

| Type of pile | $F_2$ value |
|---|---|
| Franki | 5.0 |
| Steel | 3.5 |
| Precast concrete | 3.5 |
| Drilled shafts | 6-7 |

tests in cohesive soils, 16 load tests in cohesive soils, and 31 load tests in mixed soils are all included in the database of 95 full-scale drilled shaft load tests. The influence of geometry, construction procedure, type of bearing layer, and cone type on predicted capacity was considered to propose an improved CPT design procedure for drilled shafts.

Table 2.9: Unit skin friction ($f_s$) prediction methods using CPT-based methods.

| Method | Equation |
|---|---|
| 1. LCPC method Bustamante & Gianeselli (1982) | $f_s = \frac{q_c}{\alpha_{LCPC}}$ <br> $\alpha_{LCPC}$, friction coefficient: function of pile type, soil type, and $q_c$ |
| 2. Aoki & Velloso (1975) method | $f_s = \frac{\alpha}{F_2} q_c$ <br> $F_2$=3.5 for steel piles <br> $\alpha$ (resistance factor) =1.4% (sand) and 6% (clays) |
| 3. UIUC method Alsamman (1995) | Cohesive Soil: <br> $f_s = 0.023(q_c - \sigma_v) \leq 86$ kPa <br> Sand or Silty Sand: <br> $f_s(\text{kPa}) = \begin{cases} 0.015q_c & \text{for } q_c \leq 4800 \text{ kPa} \\ 0.0012q_c + 67 \leq 96 & \text{for } q_c > 4800 \text{ kPa} \end{cases}$ |
| 4. Doan & Lehane (2021) | $f_s = (f_t/f_c)0.008p_a(I_c)^{1.6}(q_c/p_a)^{0.8}$ <br> $f_t/f_c = \begin{cases} 1 & \text{for Cohesive Soil} \\ 0.8 & \text{for Sand} \end{cases}$ |

Doan & Lehane (2021) made a compilation of the findings from a recently created database of static load tests conducted in 37 locations around the world using 68 instrumented drilled shafts and auger cast-in-place piles in sands, sand mixes, silt mixtures,

and clays. The authors demonstrated that the LCPC-2012 (Frank, 2017) method was the most accurate approach to estimating the shaft and tip resistance. Furthermore, the authors proposed a new CPT approach that involves the soil behavior type index ($I_c$) in the formulation.

Several authors have shown that CPT methods have much higher reliability (Nadim *et al.*, 2020; Phoon & Retief, 2016; Schneider *et al.*, 2008). Since the CPT test has the ability to eliminate user subjectivity and facilitate the automation of pile capacity calculations directly from recorded data.

A summary of the CPT-based methods considered in this study is presented in Table 2.9. Methods are taken from technical literature documents and referenced.

## 2.4    Cyclically Loaded Foundations

Lateral cyclic loads on vertical piles are commonly generated by wind, waves, variable overloads, or thermal dilatation. The cyclic loading test can be characterized by four parameters: the maximum applied cyclic load, $P_c$, the load variation amplitude, $\Delta P$, the number of cycles, $N$, and the frequency, $f$.
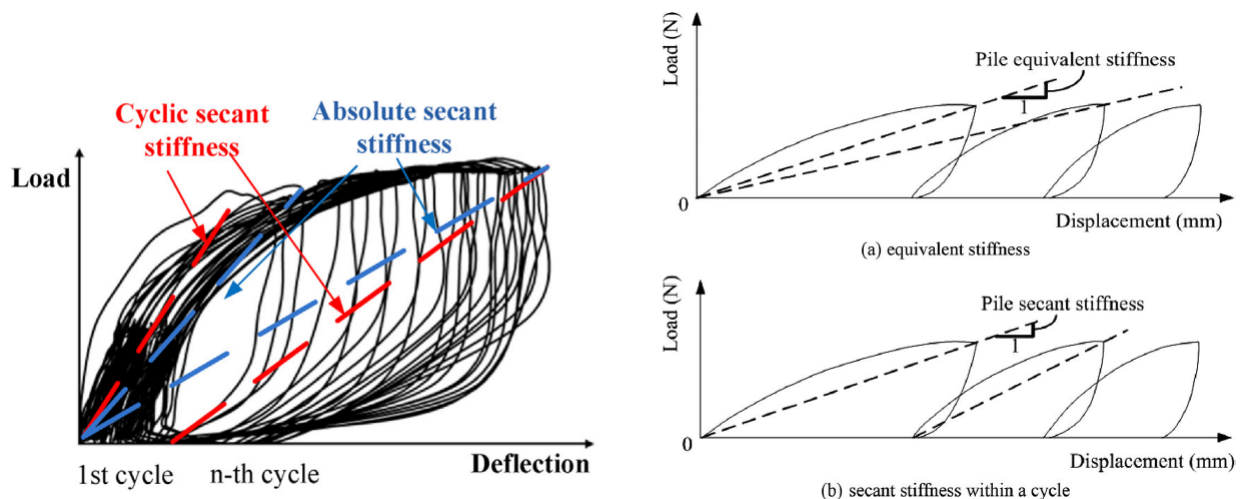


Figure 2.14: Cyclic load-displacement response and definition of pile head equivalent stiffness and secant stiffness (Liao *et al.*, 2018; Chiou *et al.*, 2018).

The rate of loading (i.e., the frequency) has significant effects on the time-dependent performance Rosquoet *et al.* (2007). A typical cyclic load-displacement plot is presented in Figure 2.14. It observed that as the load increases, an increment in displacement occurs, and once the peak cyclic load is achieved ($P_{c,max}$), the load decreases to a minimum cyclic load, and a permanent pile head displacement is recorded. The load then increases again following a 'hysteresis loop'. When the number of cycles increases, the peak displacement tends to accumulate making the hysteresis loop shift along the displacement axis. The figure also depicts the stiffness of the soil-pile system. The first definition is called the equivalent stiffness which is defined as the slope from the peak load point to the origin after each cycle. This type of stiffness shows the accumulation of lateral displacement due to loading cycles. The second type of stiffness is called secant stiffness, which is defined as the secant slope from the beginning to the peak point on the load-deflection curve for a cycle. This type of stiffness describes the lateral pile-soil stiffness (Chiou *et al.*, 2018).

Cyclic laterally loaded pile design is often investigated using a combination of calculations performed under static conditions to find pile head displacements and rotations and then modified to take into account the effects of cyclic loading using degradation laws Garnier (2013). The relationship between the lateral displacement and loading cycles is usually expressed. Several authors have suggested empirical formulations to express the lateral cyclic response for constant-amplitude cyclic loading for the accumulated displacement response $y_N$ after the $N^{\text{th}}$ load cycle as a function of the cyclic number $N$ and the response corresponding to the first load cycle $y_1$, which can be expressed by Equations (2.22)-(2.24).

$$y_N = y_1(1 + b\ln(N)) \qquad (2.22)$$

In recent studies, the expression used to predict this accumulated displacement has been proposed in terms of logarithmic function as shown in Equation (2.22) (Garnier, 2013; Hansen *et al.*, 2013; Li *et al.*, 2010; Lin & Liao, 1999; Peralta, 2010; Rosquoët *et al.*, 2013;

Verdure *et al.*, 2003; Chiou *et al.*, 2018) or a power law as Equation (2.23) (Hansen *et al.*, 2013; Klinkvort & Hededal, 2013; Little & Briaud, 1988; Long & Vanneste, 1994; Peralta, 2010) being the most commonly applied where $b$ and $\alpha$ are model parameters (Li *et al.*, 2014).

$$y_N = y_1 N^\alpha \tag{2.23}$$

Based on the centrifuge test, Bienen *et al.* (2012) proposed an extension of Equation (2.22) that predicts the accumulation of pile head displacement just in terms of the number of cycles:

$$y_N = y_1 \left[ 1 + 0.05 \frac{N-1}{N} \ln\left(\frac{N}{2} + 1\right) \right] \tag{2.24}$$

Different values of $b$ and $\alpha$ used in Equations (2.22) and(2.23) are presented in Table 2.10 and 2.11, respectively. The soil and loading conditions, the type, and the scale of the test were the main determinants of the values of $b$ and $\alpha$ which were seen to range from 0.02 to 0.25, and from 0.062 to 0.120, respectively.

Table 2.10: Value of $b$ in the literature, modified from Rosquoët *et al.* (2013); Li *et al.* (2015)

| Test | Soil | Pile | $N_{max}$ | $b$ | Reference |
|------|------|------|-----------|-----|-----------|
| 1g model | Dry sand | Stiff | 10000 | 0.2 | Hettler (1981) |
| Centrifuge | Dry sand | Stiff | 5 | 0.18–0.25 | Bouafia (1995) |
| In situ | Sand | Flexible | 100 | 0.02–0.24 | Lin & Liao (1999) |
| In situ | Clay and sand | Flexible | 10000 | 0.087 | Hadjadji (1993) |
| Centrifuge | Dense dry sand | Flexible | 50 | 0.04–0.18 | Verdure *et al.* (2003) |
| Centrifuge | Dry sand | Flexible | 500 | 0.12 | Reese (1986) |
| Centrifuge | Dry sand | Flexible | 40 | 0.04–0.07 | Rosquoet *et al.* (2007) |
| Centrifuge | Dense dry sand | Stiff | 1000 | 0.17–0.25 | Li *et al.* (2010) |
| 1g model | Dry sand | Flexible | 1000 | 0.21 | Peralta (2010) |
| Centrifuge | Sand | Flexible | 10000 | 0.17-0.23 | Chiou *et al.* (2018) |
| In situ | Stiff clay | Flexible | 10000 | 0.08-0.12 | This study |

Table 2.11: Value of $\alpha$ in different studies (Li *et al.*, 2015)

| Test | Soil | Pile | $N_{max}$ | $\alpha$ | Reference |
|------|------|------|-----------|----------|-----------|
| In situ | Loose, medium | Flexible | 40 | 0.062–0.086 | Little & Briaud (1988) |
| 1g model | Medium, dense | Flexible | 10000 | 0.12 | Peralta (2010) |

## 2.5 Summary

A helical pile is a foundation element composed of a central shaft that is made from round or square steel sections with one or more plates welded to the shaft. Helical piles generate geotechnical compressive and uplift resistance by mobilizing the shear strength of soil adjacent to helical plates. Helical piles are installed by applying an axial force and rotating the shaft of the pile by a drive head Perko (2009).

Helical piles are used to support building, deck, and tower foundations; tie-back anchors; pipeline and utility tie-downs. The axial capacity can be computed using both the individual plate bearing and the cylindrical shear methods. The lowest capacity between the two should then be used as the estimated capacity. There are also capacity correlations based on the torque installation measurements that only depend on the helical pile diameter.

It has been proven that the lateral capacity of helical piles depends on the shaft diameter and the length of the pile. The lateral loads for design can be addressed using widely used $p - y$ methods that are commonly available in commercial software.

The torsional capacity of piles is based on $\alpha$ methods, for cohesive soils; $\beta$ methods, for granular material; or CPT-based methods. The latter provides a better since capacity calculations are made directly from measured data without user subjectivity. A list of different methodologies to calculate skin friction is given.

Cyclic loading has four characteristic parameters that influence the global stiffness of the soil-pile system. These effects are taken into account by defining two different

approaches that relate the maximum load and displacement after each cycle to describe how the soil-pile system is being affected by the cyclic load.

# CHAPTER 3

# COLLAR VANE FIELD TESTING METHODS AND DETAILS

## 3.1   Introduction

Helical piles (HPs) are well-suited to resist both compressive and tensile axial loads and can be an attractive foundation option because they are relatively inexpensive, utilize non-specialized equipment, and are efficient to install. However, they are precluded from many applications due to their inability to resist substantial lateral and torsional loads. To overcome this limitation, a novel easy-to-install Collar Vane (CV), which is envisioned to increase the effective diameter attributed to the mobilization of geotechnical resistance in the upper soil profile, is incorporated to enhance the lateral and torsional capacity of helical piles. The Collar Vane consists of four steel fins welded to a hollow steel collar that wraps around the helical pile shaft that can accommodate multi-directional lateral and torsional loads to minimize movement of the helical pile. The Collar Vane is structurally coupled to the helical pile via flanges near the pile head to transfer lateral and torsional loads through the CV to the soil. Two different CV prototypes were designed and manufactured by Hubbell Power Systems Inc. and tested in two different soil conditions under monotonic and cyclical loads.

### 3.1.1   Two-Piece Collar Vane (CV2)

A two-piece Collar Vane (CV2) consists of four blades extending from a half-hollow cylinder section. This Collar Vane prototype was manufactured in 2021 and consists of two half-tubular sections that fit together around the HP shaft. Both half-sections can be fastened through the holes using bolts along the CV2 tubular section ("hollow collar"). The nine different two-piece CV geometries tested are shown in Figure 3.1. The CV2 with diameters 0.3 and 0.6 m was manufactured using A36 grade steel (minimum yield strength 250 MPa) whereas the 0.9 m diameter was manufactured using 80-grade steel (minimum

45

yield strength 550 MPa). The CV top portion consists of a prismatic section with a tapered section at the bottom with an angle of 45° allowing a simple and smooth installation process when the CV is being pushed into the ground.



(a) CV2 1-1    (b) CV2 2-1    (c) CV2 3-1

(d) CV2 1-2    (e) CV2 2-2    (f) CV2 3-2

(g) CV2 1-3    (h) CV2 2-3    (i) CV2 3-3

Figure 3.1: Two-piece Collar Vane (CV2) geometries.

This Collar Vane has the particularity of being composed of two half-tubular sections with an O.D. of 115 mm and a thickness of 7 mm. Figure 3.2(a) shows how one section of the CV is composed of three blades (right side in the figure), which is also connected to the helical plate top flange and loading arm, whereas the one side blade (left side in the figure) is only connected to the hollow collar and not directly to the top flange. As a result, the movement of these blades under torsional loads is not going to be uniform. This prototype

was designed to have more control over the protection of the strain gauges located on the pile during the installation. The strain gauges outside the CV section were protected using the strain gauge covers, whereas the strain gauges within the CV section were protected using fiberglass tape as shown in Figure 3.1(i). Moreover, this Collar Vane has the advantage to be coupled into already installed foundation elements giving the possibility to retrofit foundation systems.
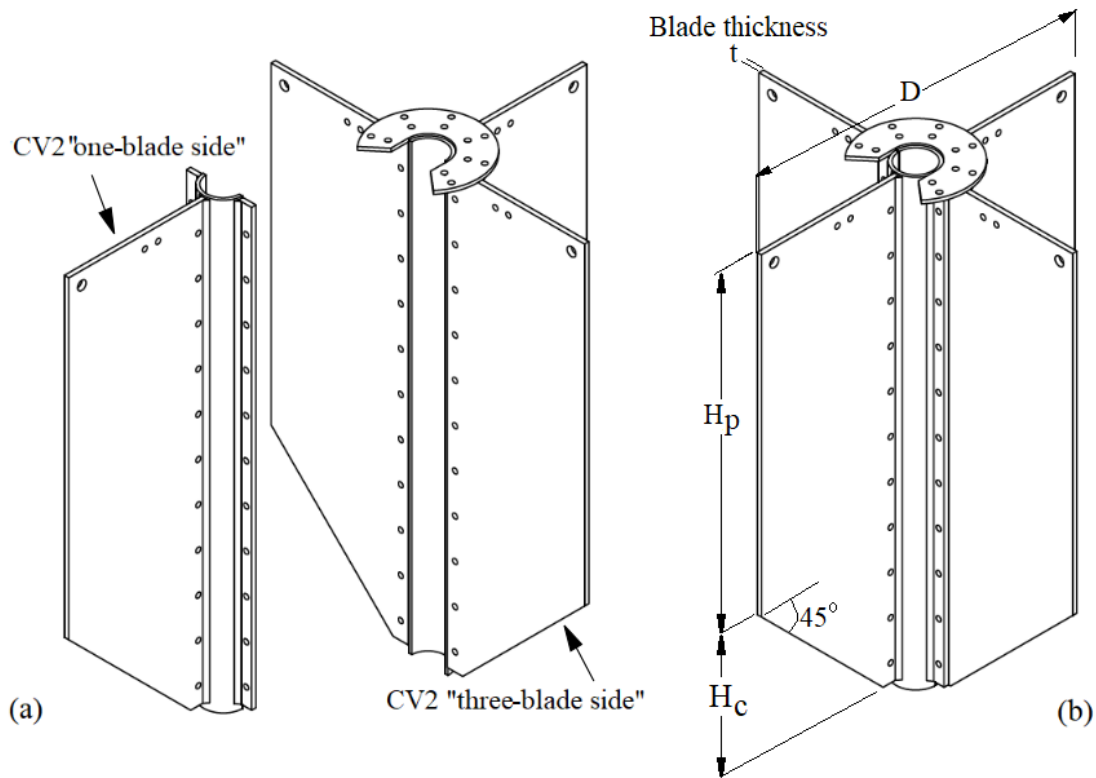


Figure 3.2: Two-piece Collar Vane (CV2) sides: (a) exploded view of the two pieces and (b) final position (Hubbell Power Systems Inc.)

The installation of the CV is relatively quick and not cumbersome. Figure 3.3 shows the HP and the two-piece CV installation sequence. Figure 3.3(a) depicts that the HP is installed applying a clockwise turning torque and a crowd at the pile head while a rate of penetration of 76 mm per revolution to reduce soil disturbance; Figure 3.3(b) shows the CV sections being fastened around the HP shaft using bolts. It is observed that the three-blade side is welded to half the tubular section whereas the other half consists of a
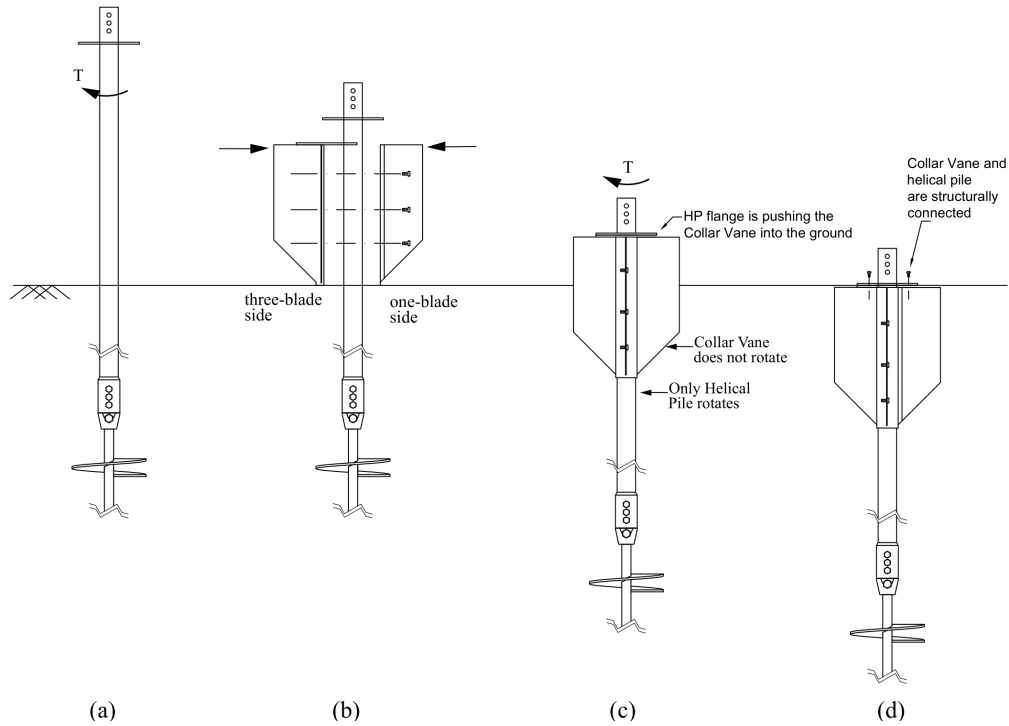
Figure 3.3: Two-piece Collar Vane installation sequence: (a) helical pile is installed; (b) Two-piece Collar Vane sections are connected around the HP shaft; (c) Collar Vane does not rotate while being pushed into the ground; (d) The Collar Vane is pushed into its final position and then locked off.

one-blade side; Figure 3.3(c) HP installation resumes with the CV placed at the HP head. The HP shaft is free to spin whereas the Collar Vane is being pushed into the ground without rotating. To reduce friction and wear during the CV installation, an anti-friction coating was applied to the CV-HP top flanges and the interior of the CV tubular sections. Also, strain gauges within the CV were protected using fiberglass tape; Figure 3.3(d) shows the Collar Vane in its final position at the ground surface and being structurally connected using bolts at the HP top flange.

### 3.1.2   One-Piece Collar Vane (CV1)

The one-piece Collar Vane (CV1) consists of four blades extending from a hollow cylinder section. It was manufactured (and tested in 2022) with the objective of improving the CV2 torsional performance. The CV1 was manufactured using 80-grade steel

48

(minimum yield strength 250 MPa). Unlike the CV2, this CV has four blades welded to the CV shaft to have a more uniform response between the blades when subjected to torsional loads. The thickness of the 0.6-diameter CV was increased from 6.35 to 9.52 mm to increase the cross-sectional area of the blades based on the results of the CV2. A total of four CV1 geometries were manufactured as shown in Figure 3.4.



(a) CV1 2-2

(b) CV1 3-2

(c) CV1 2-3

(d) CV1 3-3

Figure 3.4: One-piece Collar Vane (CV1) geometries.

The installation of the one-piece Collar Vane is similar to the CV2: instead of placing the CV at the end of the HP shaft installation, this element is placed after installing the HP extensions and before connecting the HP shaft to the extensions as shown in Figure 3.5(a) Thus, the sequence shown in Figure 3.3(b) during CV2 installation is no longer needed making the installation is smoother and faster. The shaft is then connected to the

extension's coupling through the CV as shown in Figure 3.5(b). The CV installation resumes by imposing the crowd and torque to the helical pile. Just like the CV2, the CV1 does not rotate in the ground when applying the torque to the helical pile. The top helical pile flange is in contact with the CV flange pushing it into the ground as shown in Figure 3.5(c). Finally, the helical pile and the CV are connected structurally through the flange using bolts.
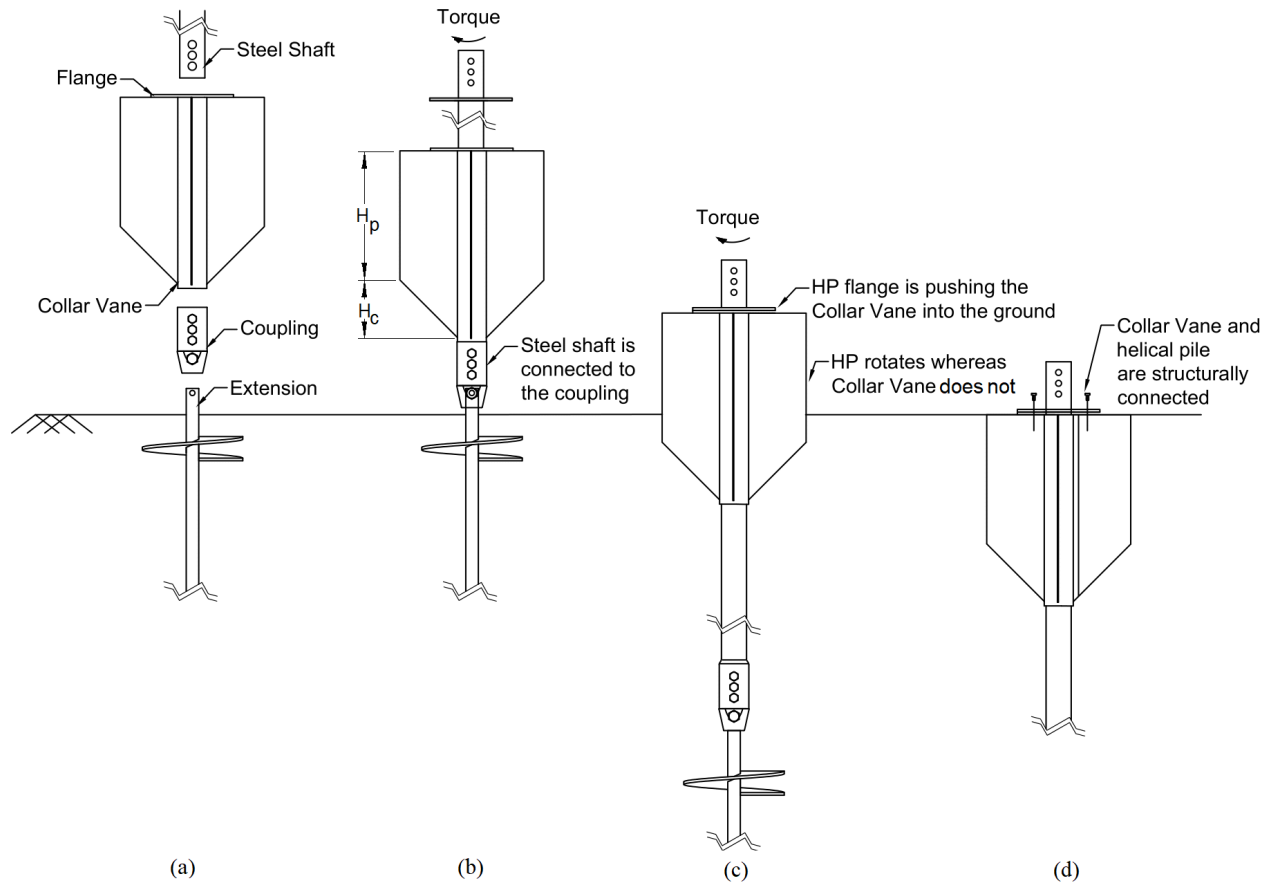


Figure 3.5: One-piece Collar Vane installation sequence: (a) Collar Vane is placed after installing the extension; (b) steel shaft is connected to the extension after being passed through the CV; (c) Collar Vane does not rotate while being pushed into the ground and; (d) the Collar Vane is pushed into its final position and then locked off.

Table. 3.1 shows the nine Collar Vanes geometries tested in this study. The increase in the CV thickness in the CV1 2-2 and 2-3 was made after testing the CV2. The height of the conic section remains constant when the diameter is the same. The conic height, $H_c$, for the diameters 0.30, 0.61, and 0.91 m are 0.06, 0.21, and 0.36 m, respectively.

50

Table 3.1: Collar Vane dimensions.

| Collar Vane No. | Thickness, $t$ (mm) | Diameter, $D$ (m) | Height prism. section, $H_p$ (m) | Total Height, $H_T = H_p + H_c$ (m) |
|---|---|---|---|---|
| CV2 1-1 | 6.35 | 0.30 | 0.30 | 0.36 |
| CV2 1-2 | 6.35 | 0.30 | 0.61 | 0.66 |
| CV2 1-3 | 6.35 | 0.30 | 0.91 | 0.97 |
| CV2 2-1 | 6.35 | 0.61 | 0.30 | 0.51 |
| CV2 2-2 | 6.35 | 0.61 | 0.61 | 0.81 |
| CV2 2-3 | 6.35 | 0.61 | 0.91 | 1.12 |
| CV2 3-1 | 12.7 | 0.91 | 0.30 | 0.66 |
| CV2 3-2 | 12.7 | 0.91 | 0.61 | 0.97 |
| CV2 3-3 | 12.7 | 0.91 | 0.91 | 1.27 |
| CV1 2-2 | 9.52 | 0.61 | 0.61 | 0.81 |
| CV1 2-3 | 9.52 | 0.61 | 0.91 | 1.12 |
| CV1 3-2 | 12.7 | 0.91 | 0.61 | 0.97 |
| CV1 3-3 | 12.7 | 0.91 | 0.91 | 1.27 |

**Note**: CV2 stands for two-piece Collar Vane, manufactured in 2021; and CV1 stands for single-piece Collar Vane, manufactured in 2022.

Collar Vane nomenclature depends on the type of Collar Vane: CV1, for the one-piece Collar Vane; and CV2, for the two-piece Collar Vane. The following two digits represent the diameter, $D$, and the prismatic height, $H_p$, respectively. For instance, CV2 2-3 stands for a two-piece CV with a diameter of 2 (2 ft) and a prismatic height of 3 (3 ft).

The torsional resistance of the Collar Vane is based on the in-situ vane shear test. When the CV is placed into the ground, the blades shear the soil on a circumscribing cylinder, mobilizing an isotropic undrained shear strength of clay uniformly over this surface of rotation when maximum torque is achieved. The maximum torque, $T_u$, can be defined as the algebraic sum of the torque value imposed by the prismatic, and the conic (tapered) portions $T_p$ and $T_c$, respectively Menzies & Merrifield (1980).

$$T_u = T_p + T_c \tag{3.1}$$

$$T_p = \frac{\pi}{2} D^2 H_p s_u \tag{3.2}$$

$$T_c = \frac{\pi}{6} D^2 H_c s_u \tag{3.3}$$

Where, $D$, $H_p$, and $H_c$ are the CV diameter, prismatic section, and conic section height, respectively; $s_u$ is the undrained shear strength. The maximum torque capacity can be estimated using Equation (3.1), which indicates that the torque depends on the in-situ undrained shear strength of the soil and the CV geometry.

## 3.2 Location and Subsurface Conditions

The geotechnical site investigations were performed at Hubbell Power System Inc. testing area in Centralia, MO. Figure 3.6 shows an aerial view of the test site locations which consists of the cohesive soil location, labeled as (a) and (b); and the granular soil location, labeled as (c) in the figure. A detailed description of the test pile and reaction pile locations are shown in Figures 3.23 and 3.24.

### 3.2.1 Subsurface Investigation

Subsurface explorations included geotechnical borings, Field Shear Vane Test (FSVT), Standard Penetration Tests (SPT), and Cone Penetration Tests (CPT). The field investigation consisted of site observation, subsurface exploration, and sampling, as well as field testing and visual classification of the soils encountered in accordance with ASTM specifications. Subsurface exploration and sampling were conducted to define the soil profile and to obtain disturbed representative samples of the various soils encountered for the laboratory investigation for index parameters.
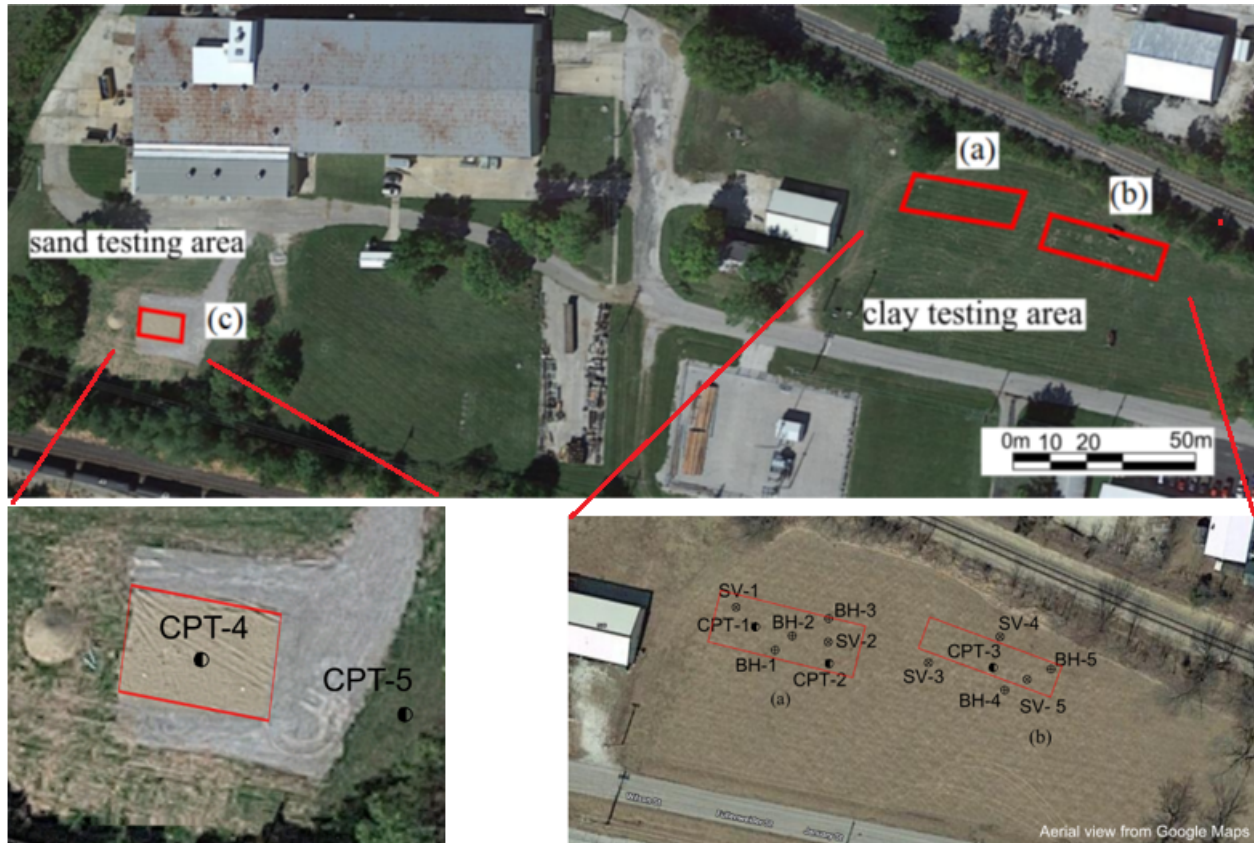
Figure 3.6: Top: aerial view of the test site location in Centralia, MO. with geographical coordinates of test site: 39° 12' 52.6104" N, 92° 08' 32.1504" W. (Google Earth, 2023). Bottom: subsurface investigation locations.

A total of five 2.6-m depth boreholes labeled from BH-1 to BH-5 were completed with a CME 55 truck-mounted drill rig equipped with 82.55 mm I.D. hollow stem augers, as shown in Figure 3.7(a), in accordance with ASTM D6151 and ASTM D1452. Samples were taken at depths of 0.3, 0.9, 1.5, and 2.1 m using hollow stem augers to permit convenient access to the soil below the auger. Figure 3.23 shows the location of the five boreholes performed in the test site location described in Figures 3.6(a-b) in the cohesive soil testing location.

Furthermore, the field testing program included the Standard Penetration Test conducted in accordance with ASTM D1586. In this test, during the Split Spoon sampling procedure, a 50.8 mm inch O.D. (34.93 mm I.D.) 609 mm long standard Split Spoon was driven into the soil through a depth of 0.45 m by a 63.5 kg weight dropped from a distance of 0.76 m. The penetration resistance, 'N', was recorded as the number of blows, from the

Figure 3.7: (a) CME-55 Truck Mounted Drill and; (b) Kubota SVL 75-2 equipped with a Geoprobe 20CPT.

falling weight, required to drive the sampler through the final 0.3 m. Boring log results are detailed in Appendix B Section B.1. For convenience, the nomenclature shown in the geotechnical report is represented by different initials in this study keeping the same numbering (i.e., BH-2 is the same as SB-2). Recovered cohesive samples were tested, when possible, using a calibrated pocket penetrometer. The values from this test were considered an approximate measure of the consistency of the cohesive soils.

FSVT were carried out in addition to SPT testing. The five FSVT tests (SV-1 to SV-5 shown in Figure 3.23) were performed in accordance with ASTM D8121, which measured the undrained shear strength of fine-grained soils. The test places a 4-bladed vane into the soil followed by rotation by a calibrated handle, measuring the torque required to shear the soil. FSVT testing equipment consists of a Humboldt H-4227 inspection kit. FSVT results are detailed in Appendix B Section B.2. For convenience, the nomenclature shown in the

geotechnical report is represented by different initials in this report keeping the same numbering (i.e., SV-2 is the same as VS-2). The report also shows that two different reports for the same location: the first boring (i.e., VS-2), made on August 11th, 2022, shows the peak undrained shear strength, whereas the second boring (i.e., VS-2A), made on September 20th, shows the peak undrained shear strength and the remolded undrained shear strength after applying 25 revolutions, (according to the inspection kit user's manual) zeroing out the scale, and turning the instrument as slowly as possible taking the minimum value recorded. Some of the peak values reported on the second day of soil exploration exceed the value of 13 which is the maximum gauge value that the FSVT kit can measure. These values are not taken into account for this study since they are not a direct measurement from the FSVT kit.

When utilizing the CPT at the site for soundings, a Geoprobe 20CPT rig featuring 196 kN of downforce to effectively push CPT tooling with sufficient force was used in accordance with ASTM D5778. The CPT press is mounted on a Kubota skid steer for small, lightweight access as shown in Figure 3.7(b). The CPT utilizes the wireless NOVA CPT test cone tooling to enable quick, effective, and safe site characterization. CPT investigation determines the in-situ subsurface stratigraphy and estimates geotechnical soil parameters by measuring cone tip pressure, sleeve friction, and pore pressure. The CPT system collects data continuously and in real time, having the capability for on-site interpretation of logs. CPT soil parameter is used to identify soil types, calculate geotechnical parameters, correlate SPT blow counts, and estimate undrained shear strength, relative density, coefficient of lateral stress, and soil friction angles. A total of five 12-m deep cone penetration tests (CPT-1 to CPT-5) were performed in the testing plan. The first three (CPT-1 to CPT-3) were made in the cohesive soil location as shown in Figure 3.23 whereas the remaining two (CPT-4 and CPT-5) were performed in the granular soil location (Figure 3.24). CPT results are detailed in Appendix B Section B.3. It is noted that the same probe location is presented in two reports. The first report starts from a

depth below 0.9 m since the geotechnical exploration contractor pushed a blind dummy point to avoid damage to the CPT probe. However, the second report shows the results from the ground surface to a depth of 0.9 m to obtain the full soil profile characterized.

### 3.2.2 Laboratory Testing

Disturbed samples from borings BH-2 and BH-5 (Figure 3.23) were recovered with a split-spoon sampling tool for soil index testing (ASTM D2216) and Atterberg limits testing (ASTM D4318) as detailed in Appendix B Section B.4. The samples were taken in glass jars to retain moisture as much as possible.

Dry Sieve Analysis and USCS Classification (ASTM D6913 and D2487) were performed for samples taken from the granular material location (e.g., sand test pit). Sieves sizes ranging in mesh size from 4.75 mm down to 0.075 mm were used and stacked in a Gilson Model SS-8R mechanical shaker for ten minutes. Mass of soil retained on each sieve was recorded and the percent passing values calculated. From this analysis, the grain size distribution is shown in Figure 3.8.

From the particle size distribution presented in Figure 3.8. USCS classification can be determined based on ASTM D2487. The coefficient of uniformity and coefficient of curvature values are shown along with other properties from the sand test pit. Estimation of the minimum and maximum dry unit weight are carried out following ASTM D4253 specifications. Table 3.2 presents a summary of the sand soil properties.

The sand in the test pit is a medium size material with a uniformity coefficient of 3.27, an effective diameter of 0.21 mm, a specific gravity of 2.66 and water content of 3%.

### 3.2.3 Sand Test Pit

Since the testing site at Hubbell was composed mostly of fine-grained materials, it was necessary to dig a large hole and backfilled it with granular material to perform the test in these conditions. The test pit consisted of a 9.1 m (L) x 6.1 m (W) x 2.4 m (H) dug hole backfilled with nine layers of sand.
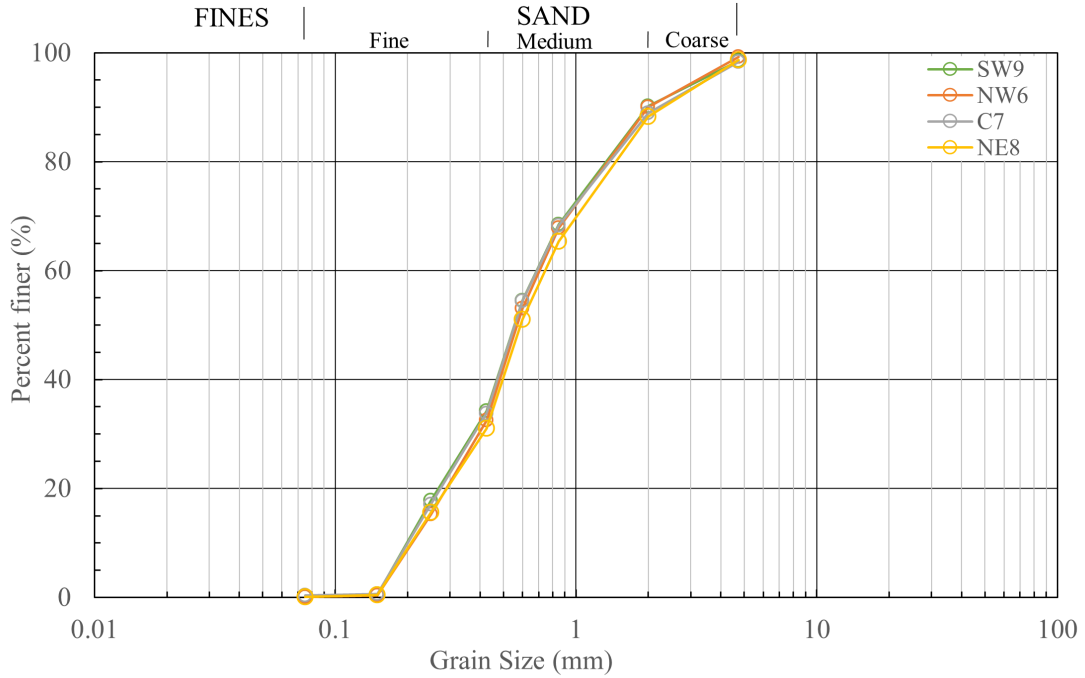
Figure 3.8: Grain size distribution determined from samples from sand test pit.

Table 3.2: Physical properties of sand used in the test.

| | |
|---|---|
| Effective grain size, $D_{10}$ (mm) | 0.21 |
| Average grain size, $D_{50}$ (mm) | 0.57 |
| Uniformity coefficient, $C_u$ | 3.27 |
| Coefficient of curvature, $C_c$ | 1.11 |
| Maximum dry unit weight, $\gamma_{d_{\max}}$ (kN/m$^3$) | 18.53 |
| Minimum dry unit weight, $\gamma_{d_{\min}}$ (kN/m$^3$) | 16.54 |
| Maximum void ratio, $e_{\max}$ | 0.58 |
| Minimum void ratio, $e_{\min}$ | 0.41 |
| Specific gravity, $G_s$ | 2.66 |
| Coarse to medium sand (%) | 66 |
| Fine sand (%) | 34 |
| Classification (USCS) | SP |
| Water content, $W_c$ (%) | 3 |

Figure 3.9: Sand test pit construction sequence.

Figure 3.9 depicts the construction sequence of the sand test pit, showed in Figure 3.6(c), where the first step was to remove the top layer to level the terrain and start digging the hole with heavy equipment as shown in Figure 3.9(b). The sand was placed in layers of 0.2 to 0.3 m and compacted with a vibrator between each lift as shown in Figure 3.9(c-d). Furthermore, a layer of gravel material was placed outside the test pit with the purpose of facilitating the helical pile installation equipment as shown in Figure 3.9(e-f).

### 3.2.4    Interpreted Soil Profiles

The results obtained from the subsurface investigation and laboratory testing are compiled in this section. The depth is presented from the ground surface. The two locations are on a relatively flat surface.

### 3.2.4.1    Cohesive Soil Test Site
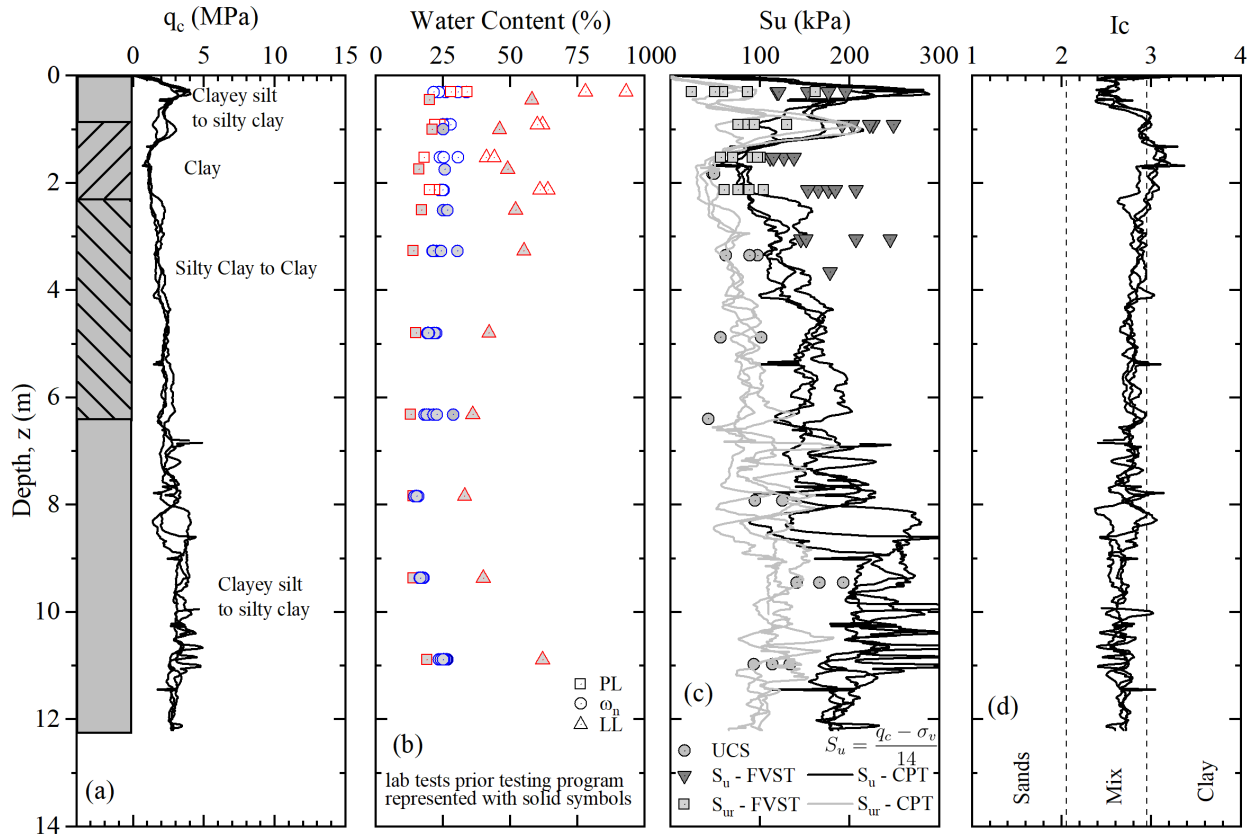


Figure 3.10: Typical soil profile and soil strength characteristics at the cohesive test site: (a) tip resistance; (b) index properties; (c) undrained shear strength; (d) soil behavior type index.

In general, the cohesive soil profile consisted of over-consolidated clayey silt to silty clay. The near-surface soils were desiccated to a depth of 0.5 m and formed a very stiff layer, as indicated by a high $q_c$ in Figure 3.10(a). From a depth of 1 m to approximately 2 m, the clay is medium to a very stiff consistency. A 4-m thick layer of stiff to very stiff clayey silt to silty clay is found about 2.2-6.2 m below ground surface followed by a 6 m thick layer of

very stiff silty clay layer. Groundwater was not encountered in any of the borings while drilling. The average unit weight of the clay layer, clayey silt to silty clay layer, and silty clay layer are 17.5, 18.5, and 19 kN/m$^3$, respectively, based on CPT correlations (Robertson & Cabal, 2010). Index properties are shown in Figure 3.10(b) where closed symbols are laboratory tests performed before this project whose results overlap with laboratory results from this study. In general, results show the water content is close to the plastic limit. The undrained shear strength, $s_u$, is shown in Figure 3.10(c), and the values obtained from unconfined compressive strength (UCS) tests were 50-166 kPa, which is lower than the estimated values from CPT soundings (100-250 kPa). This can be attributed to a possible reduction in strength and stiffness when the soil structure is altered due to sampling. The intact $s_u$ measurements vary between 111-249 kPa with an average value of 171 kPa. Whereas the remolded undrained shear strength, $s_{ur}$, varies between 24-162 kPa with an average value of 76 kPa. Using CPT it is possible to obtain $s_{ur}$ since sleeve friction values are often similar to the remolded undrained shear strength of fine-grained soils (Robertson, 2009). The site exploration shows a relatively uniform variation of layering and soil properties across the CPT soundings. The soil behavior index is shown in Figure 3.10(d) labeled as the East location for the clayey testing site. The soil profile is then classified as a silt mixture and a clay. The three CPT soundings made throughout the site location show a homogeneous soil profile.

### 3.2.4.2   Granular Soil Test Site

Two CPT soundings were performed in the location. CPT-4 was pushed in the middle of the sand pit and CPT-5 outside of it as shown in Figure 3.11. CPT-4 shows that the first layer is composed of a 2.3 m thick layer of sand with a relative density, $D_r$, between 55-78% and an angle of friction, $\phi'$, between 39-42° according to CPT correlations (Jamiolkowski *et al.*, 2003; Kulhawy & Mayne, 1990). A more detailed description of the sand properties is shown in Table 3.2. The following layer is composed of a 4 m layer of
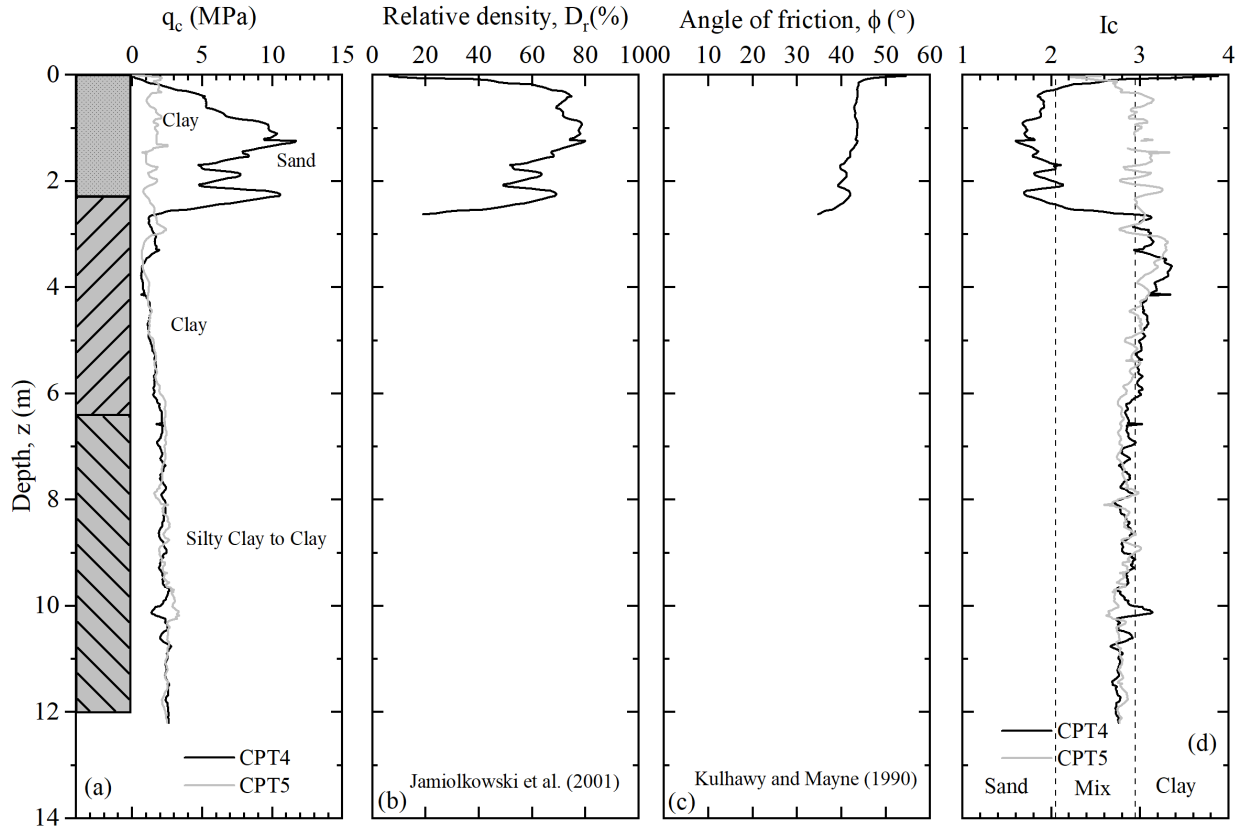
Figure 3.11: Soil profile and soil strength characteristics at the granular test site: (a) tip resistance; (b) relative density; (c) angle of friction and; (d) soil behavior type index.

clay according to the soil behavior index shown in Figure 3.11(d) and a 6 m thick layer of mixed silts. CPT-5 was performed as a 'control' probe. Results from this probe are similar to the soundings made on the cohesive soil testing area.

## 3.3 Lateral and Torsional Testing Details

The following section describes the development, and assembly of the monotonic and cyclic test equipment implemented for this project.

### 3.3.1 Overview of Equipment

The test setup for lateral loading was developed in accordance with ASTM D3966. The test equipment consists of a test pile under lateral loads applied from a hydraulic jack that

is connected to a reaction pile. However, the torsional loading test does not have a standard method, a detailed testing frame and loading procedure are explained subsequently.

To measure displacements and loads, it was necessary to implement string potentiometers, load cells, and a pressure transducer whose calibration process is detailed in Appendix A. Load cells were placed at the same loading point to avoid eccentric measurements, the string potentiometer was mounted on a reference beam to provide an independent measurement of displacement. The detailed description of the equipment used is detailed in the following section.

### 3.3.2   Mechanical and Electrical Equipment

#### 3.3.2.1   Hydraulic Cylinders

To apply the loads to the testing pile it was necessary to implement hydraulic jacks to the testing frame. A total of three different models of jacks were implemented. Two Maverick Tie Rod 300-2016 hydraulic cylinders (Figure 3.26), with a piston stroke of 410 mm and a capacity of 42 kN (29 kN when retracting) kN each, were implemented in a parallel configuration to apply the lateral force in the cohesive test site while in the granular material, a 600 kN Enerpac RCH-606 Single-Acting hollow plunger hydraulic cylinder (Figure 3.27) was used. For the torsion test, two Dalton TR3-2030 Hydraulic cylinders (Figure 3.28), with a piston stroke of 760 mm and a capacity of 16 kN (29 kN when retracting) each were used. The properties of the tie-rods cylinder are: maximum hydraulic pressure of 20,680 kPa and an effective cylinder area of 14 cm$^2$ (5.08 cm bore and 2.85 cm rod). The hollow plunger hydraulic has a piston stroke of 153 mm and a hole diameter of 5.38 cm, maximum hydraulic pressure of 68,947 kPa, and cylinder effective area advance 82.3 cm$^2$.

#### 3.3.2.2   Hydraulic Pumps

To apply the forces to the hydraulic cylinders it is required to use a hydraulic pump to pressurize the hydraulic fluid in the cylinders. A foot-operated Enerpac PAT1105N air

pump was used, as shown in Figure 3.12, to convert the pneumatic pressure from an air compressor into hydraulic pressure. This foot pump has an operating pressure of 69,000 kPa and air consumption of 0.34 (m³/min) at 280-880 kPa. To maintain the pressure at a constant value, a single-acting hand pump cylinder was also implemented in the testing frame. The hand pump utilized has a maximum operating pressure of 69,000 kPa suited to apply small increments of pressure to the cylinder.



Figure 3.12: Enerpac PAT1105N foot pump (front) and Power Team P159 hand pump (back).

### 3.3.2.3 Strain Gauges

Strain gauges were used to measure the bending strain produced by the lateral force in the test pile shaft. This strain is measured through the change in resistance induced by the deformation of the strain gauges. As the strain gauge deforms, the wires in the strain gauge also deform. This causes a change in resistance and thus a change in voltage over the gauge. The change in resistance is related to the strain as $\varepsilon = \frac{\Delta R/R}{G}$. Where, $G$, is the gauge factor. Therefore, the ratio of the variance in the resistance over the gauge factor

indicates the strain on the surface to which the gauge is bonded. This change in resistance can be converted into an electrical signal, which can then be converted to digital values.

The strain gauges used were a Micro-Measurements EA-00-250BF-350/E. The gauge series 250BF is a general-purpose gauge with a high-resistance grid. The "EA" series stands for a gauge with a constantan foil in combination with a tough, flexible, polyimide backing (i.e., adequately high strain sensitivity which is relatively insensitive to strain level and temperature). Class "E" consists of a protective encapsulation of polyimide film approximately 0.025 mm (0.001 in) thick (Micro-Measurements, 2021). 350 stands for the resistance in ohms, higher gauge resistance is preferable so it reduces the heat generation and also has the advantage of decreasing lead-wire resistance effects (i.e., reducing unwanted signal variations). The gauge factor, $G$, at 24°C is 2.060 ± 0.5 %

To install strain gauges successfully, extreme care and precision are required since they are sensitive devices. A chemically clean surface is crucial, and therefore, the installation process involves several steps. First, the surface is degreased using isopropyl alcohol to eliminate oils, greases, organic contaminants, and soluble chemical residues. The next step involves abrading the surface with fine sandpaper to eliminate any loose adherents, such as rust, paint, and oxides, and to create a suitable bonding surface. A conditioner is then applied to accelerate the cleaning process. To position the strain gauge accurately, it is held with cellophane tape and aligned over the pile. A strain gauge catalyst is applied before the cyanoacrylate adhesive to ensure a creep-free and fatigue-resistant bond. After curing the thin coat, the adhesive is spread over the gauge installation area, and the gauge is bonded by applying firm thumb pressure for a minimum of one minute, using a clean gauze sponge. Finally, the tape is peeled slowly and steadily off the surface while keeping the strain gauge intact, as illustrated in Figure 3.13(a).

The round steel shaft was instrumented with electrical strain gauges at eight locations along the outer surface of the pile shaft bonding two gauges at each location using a half-Wheatstone bridge configuration Figure 3.13(b). This configuration was chosen to
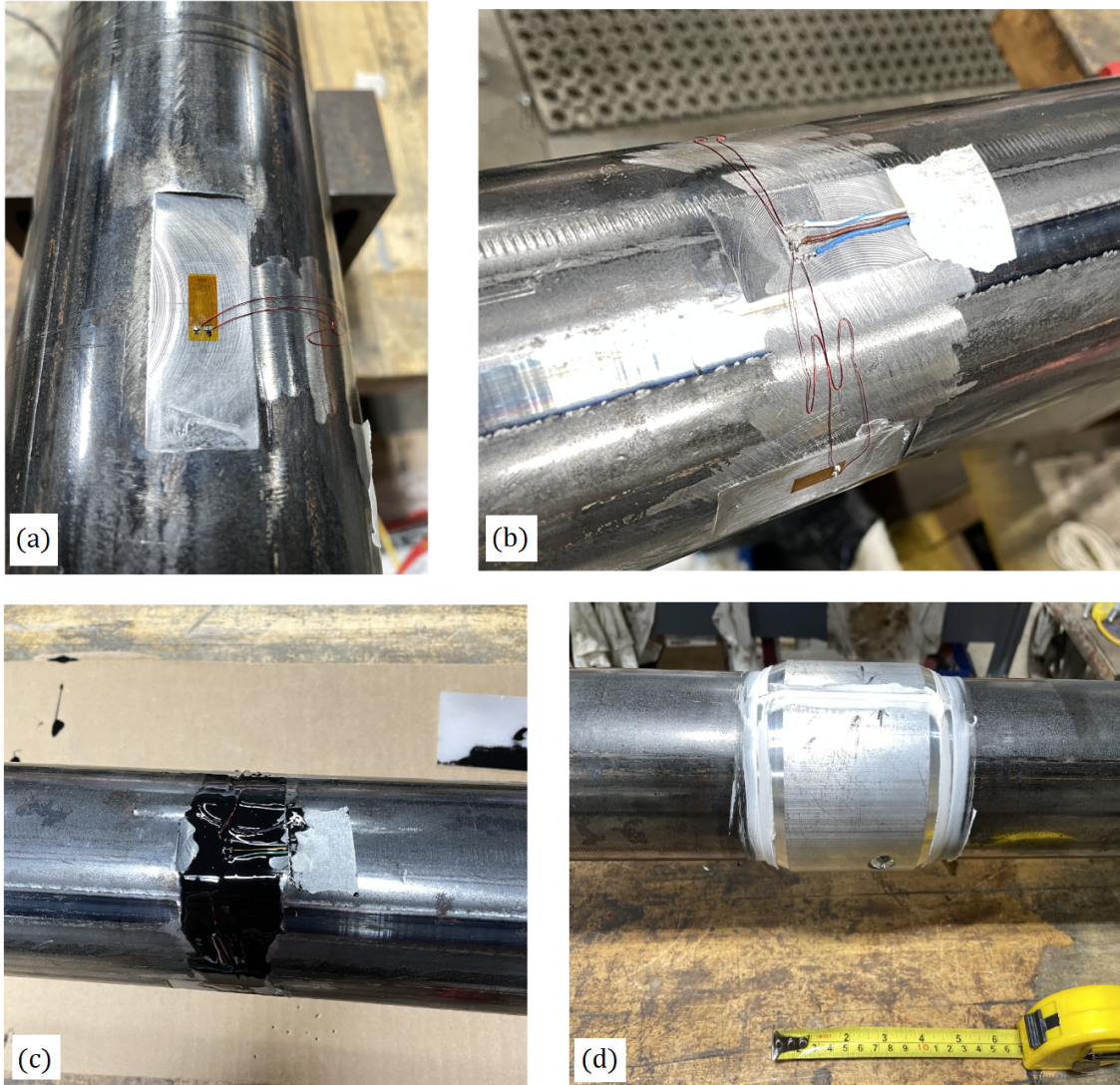
Figure 3.13: Strain gauges: (a) bonding (b) wiring, (c) coating, and (d) protection.

compensate for temperature and axial strain effects. Two sets of strain gauges were installed on the opposite sides of the pile at each location being placed every 0.15 to 0.31 m along the pile shaft. To prevent damage to the strain gauges and wires, a water-resistant protective coating was used to protect them from environmental conditions as shown in Figure 3.13(c). Furthermore, covers were used to protect the strain gauges during the installation. Figure 3.13(d) shows the cover used which consisted of two hollow half-cylinder aluminum pieces that fit together to form a continuous barrier around the shaft at the gauge location. The covers were 100 mm in length and 5 mm in thickness. To fasten the

strain gauge covers to the shaft, holes were drilled through the shaft and cover, and a flat socket head screw was run through the drilled holes and then, bolted at its ends. Since the cover was bolted, this configuration did not change the stiffness of the shaft. Figure 3.22(e) shows the locations of the strain gauges (SG-1 to SG-8) from the helical pile top flange.

### 3.3.2.4  Pressure Transducer

Pressure transducers are commonly used in pile loading testing to measure the load exerted on the pile during a loading test. The pressure transducer is attached to the manifold shown in Figure 3.14 with the purpose of having a backup device to measure pressure (or load) in the pile loading test. The model used is an Omega PX359-5KG5V with serial number: 050819D803 shown in Figure 3.14. The maximum pressure this pressure transducer can read is 34,474 kPa. The pressure transducer has an output voltage of 0 to 5 Vdc, an accuracy value $\pm 1.0\%$ and, a repeatability $\pm 0.25\%$ BSL (Best Straight Line) (Omega Engineering Inc., 2021).
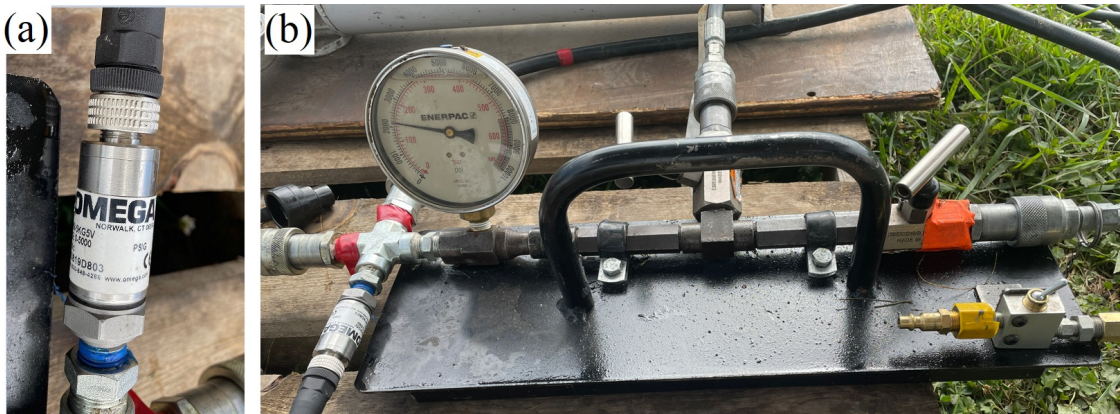


Figure 3.14: (a) Omega PX359-5KG5V pressure sensor and (b) pump manifold.

### 3.3.2.5  Load Cells

Three load cells were implemented in this project, two of them were LCM Systems STA-4 S-Type as shown in Figure 3.15(a) with serial numbers 17662038 and 17649090. These load cells can read up to 50 kN and are designed to accept standard spherical
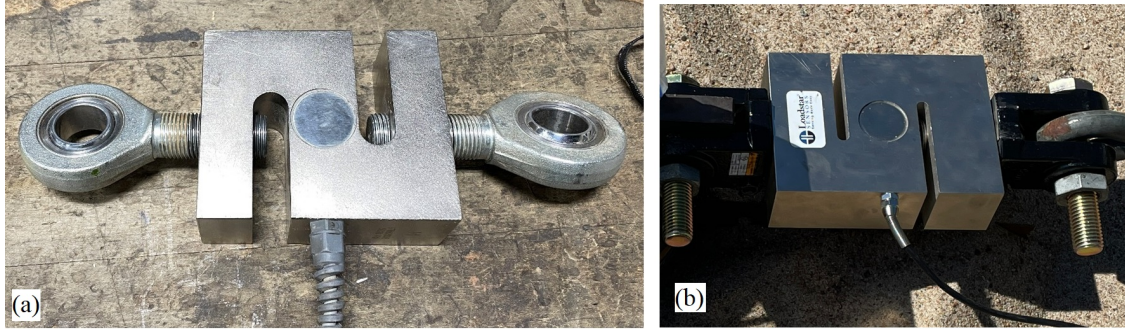
Figure 3.15: Load cells: (a) 50 kN LCM systems and (b) 177 kN RAS1.

rod-end bearings at each end. Thus, the STA-4 series load cell is ideal for measuring both tensile and compressive forces. The load cell has an excitation voltage of 10 Vdc, an output of 2 mV/V at rated load ±0.1%, proof load of 150 % of the capacity, and can safely handle an overload of 300% (LCM Systems, 2021). The other load cell was a RAS1-40KS-S S-Type as shown in Figure 3.15(b) with a capacity of 177 kN and an accuracy of ±0.02%,

### 3.3.2.6 String Potentiometers

Three different models of string potentiometers were used to measure linear position using a miniature steel cable and a spring-loaded spool. The string potentiometers used are shown in Figure 3.16.
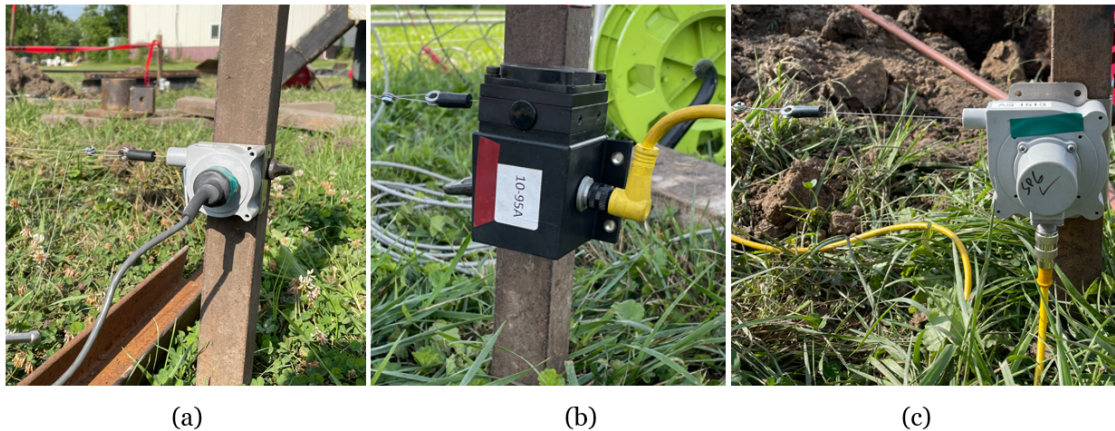


Figure 3.16: String potentiometers: (a) SP2-25; (b) PT1DC-10 and; (c) SGD-80-3.

The string potentiometer shown in Figure 3.16(a) is a TE SP2-25 with a full stroke (FS) of 635 mm of displacement, an output voltage of 10 Vdc, a sensor accuracy (% of FS):

67

0.25, and a repeatability (% of FS): 0.02; Figure 3.16(b) is a TE PT1DC-10 with a range of 254 mm with Output Signal: 0 – 10 Vdc, sensor accuracy (% of FS): 0.15, a repeatability (% of FS): 0.02 and; Figure 3.16(c) is a TE SGD-80-3 with a range of 2,032 mm with Output Signal: 0 – 10 Vdc, sensor Accuracy (% of FS): 0.35, repeatability (% of FS): 0.02, cycle life >250,000.

String potentiometers were implemented to read the pile displacements under lateral load and CV displacements under torsional load. For the lateral test, the string potentiometer was placed at the same level as the test load setup in the opposite side. Thus, every time the load is applied the string potentiometer wire is extended. Likewise, for the torsional test, four string potentiometers were used in this test and were installed at the loading arm ends and the CV blade tips (Figure 3.28).

### 3.3.2.7   DAQ System and Power Supply

A DC power supply was required to provide an electrical input to the string potentiometers and the pressure transducer. An Acopian DB15-15 power supply was utilized and housed in a custom case which allowed the Data Acquisition (DAQ) System to record pile loads, displacements, and deformations. The DAQ System collects output voltages from the devices and converts the analog samples into digital numeric values that can be manipulated by a computer. The DAQ System implemented was a NI cDAQ-9184 chassis with 4-slot for input modules. One NI-9205 module and three NI-9219 modules were used. The NI-9205 module is a 16-channel differential Voltage Input Module used to measure the string potentioemters input voltages and the NI-9219 module is a 4-channel C-Series Universal Analog Input Module. This module is used for multipurpose testing: the strain gauges, load cells, and the pressure transducer were connected to this module. Each channel of this module is individually selectable, so it is possible to perform a different measurement type on each channel. The power supply generated the 15 VDC
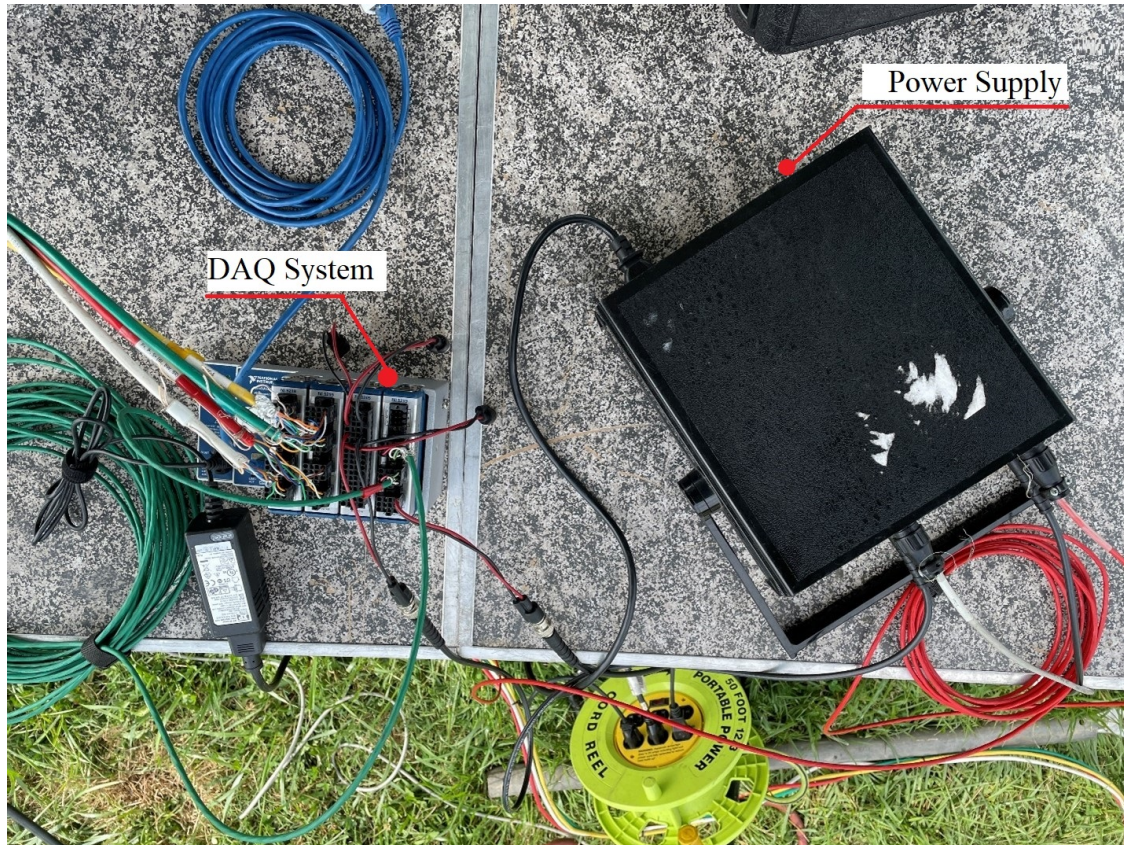
Figure 3.17: Data Acquisition (DAQ) and power supply setup. DAQ is an NI cDAQ-9184 shown on the left and the power supply on the right side.

excitation voltage for the string Potentiometers. Figure 3.17 shows the power supply and DAQ System implemented in this project.

Since the modules used to measure the sensors are a computer-based DAQ system, it is necessary to use a software to receive and save the data from the DAQ system. LabVIEW is a software environment for applications that require testing and measurement with rapid access to hardware and data insights. It has a huge library of digital signal processing (DSP), statistical, mathematical, and mathematical functions that allow the program to convert measurements from sensors, and transducers to numbers in computer memory that can be displayed on graphs or text. Figure 3.18 shows the LabVIEW customized graphical user interface set with a sampling rate of 100 Hz.
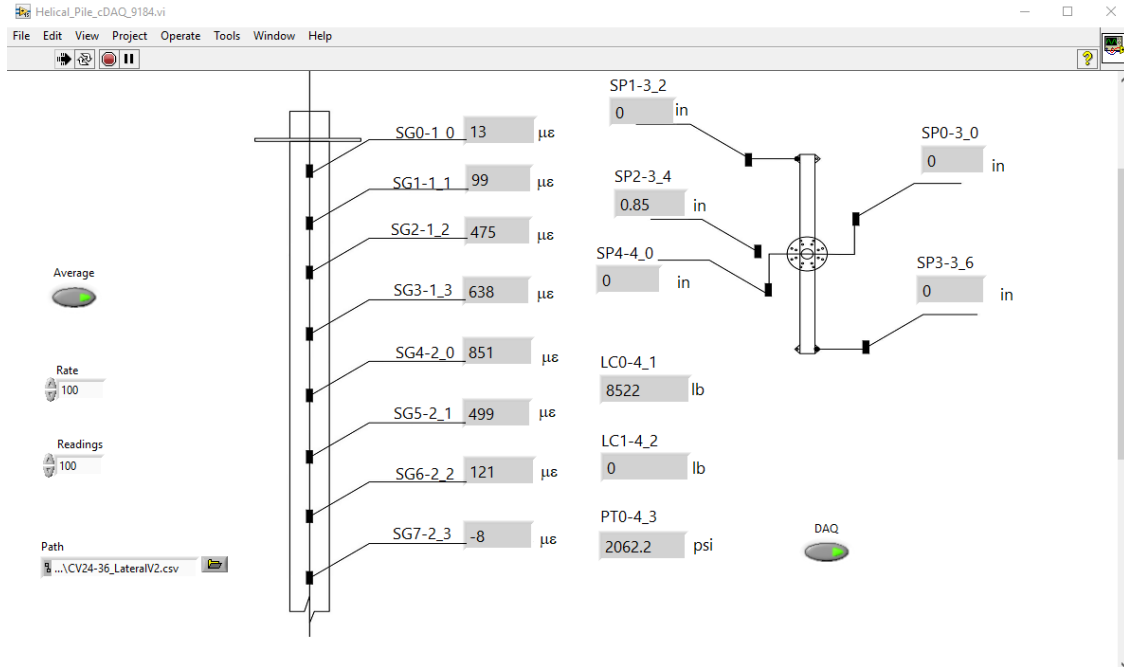
Figure 3.18: LabVIEW front panel graphical user interface.

### 3.3.2.8 Hydraulic Pressure Controller

In a typical pump-jack system, due to the confined nature of the system and the relative incompressibility of hydraulic fluid, the hydraulic pump would supply an increasing pressure to the line resulting in an inability to generate a cyclical pressure required for the cyclic tests.

A Tescom ER5K control system manufactured by Emerson Process Management was implemented to perform cyclic loads. The electro-pneumatic pressure regulator is rated for a maximum hydraulic pressure of 69,000 kPa. The regulator controls the amount of pressure applied to the cylinders by controlling the flow from the hydraulic pump to the cylinders. Figure 3.19(a) shows the PG1204S hydraulic pump used to supply pressure to the cylinders and the Tescom ER5K, shown in Figure 3.19(b), used to regulate the hydraulic pressure. The actuator regulator is a complete pressure control system equipped with an internal pressure transducer that monitors the internal pressure in the flow line. When going from low to high pressures, the exhaust vent is closed allowing the system to build pressure and once the user-predetermined pressure is reached, the regulator's exhaust

70
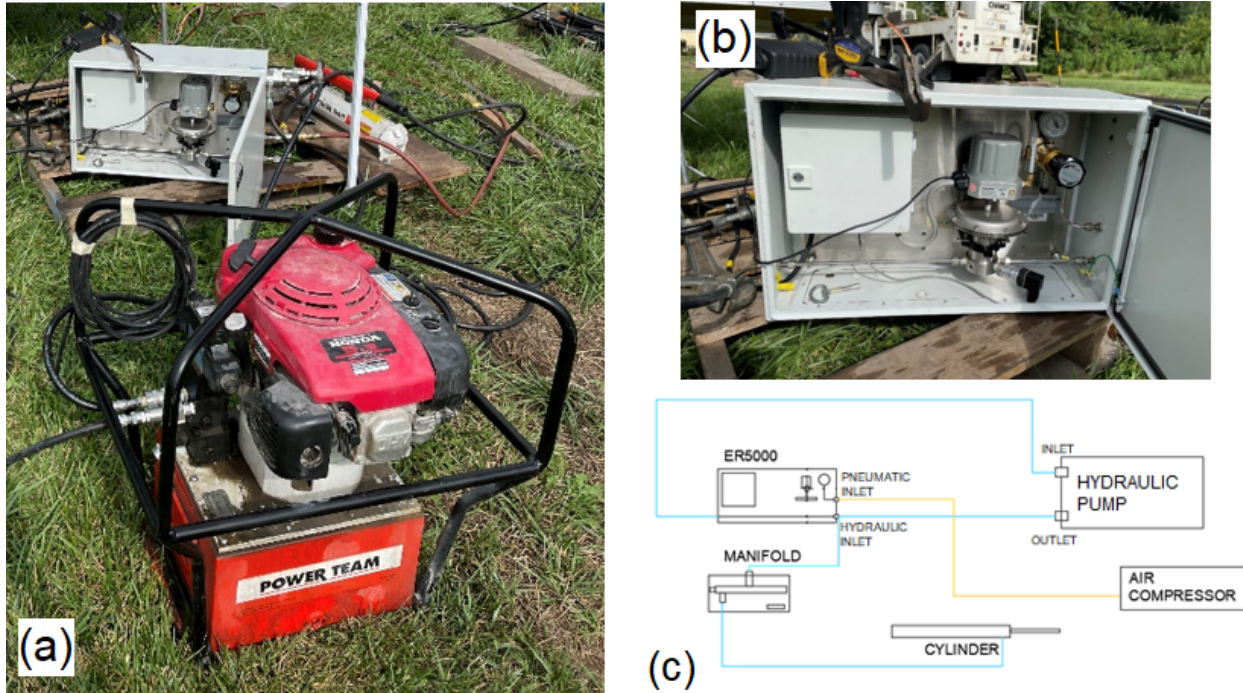
Figure 3.19: (a) PG1204S hydraulic pump; (b) Tescom ER5K hydraulic pressure controller and; (c) flow schematic for the cyclic test.

vent opens, diverting fluid from the flow line to the double-acting cylinders and discharging it through an outlet line back into the hydraulic pump reservoir as shown in Figure 3.19(c). The hydraulic regulator consists of a diaphragm controlled by pneumatic pressure that allows the hydraulic vent valve to open releasing an excess of pressure and fluid back to the hydraulic pump (Keefe, 2020).

The user has the ability to control the pressure over time by employing a profile builder that allows the user to increase, reduce or maintain the load over a period of time, loops, or conditions as shown in Figure 3.20. The software is called ERTune developed by TESCOM. The $y$-axis on the right side shows the pneumatic pressure applied to the diaphragm; the $y$-axis on the left side shows the pressure from the pressure transducer (i.e., feedback) and the objective pressure (i.e., setpoint). The profile window shows the predetermined pressure values and their certain time interval which can be modified using the profile builder shown at the left-bottom. In this particular study, the objective was to apply one thousand load cycles to the pile with a period of eight seconds. Moreover, it is possible to
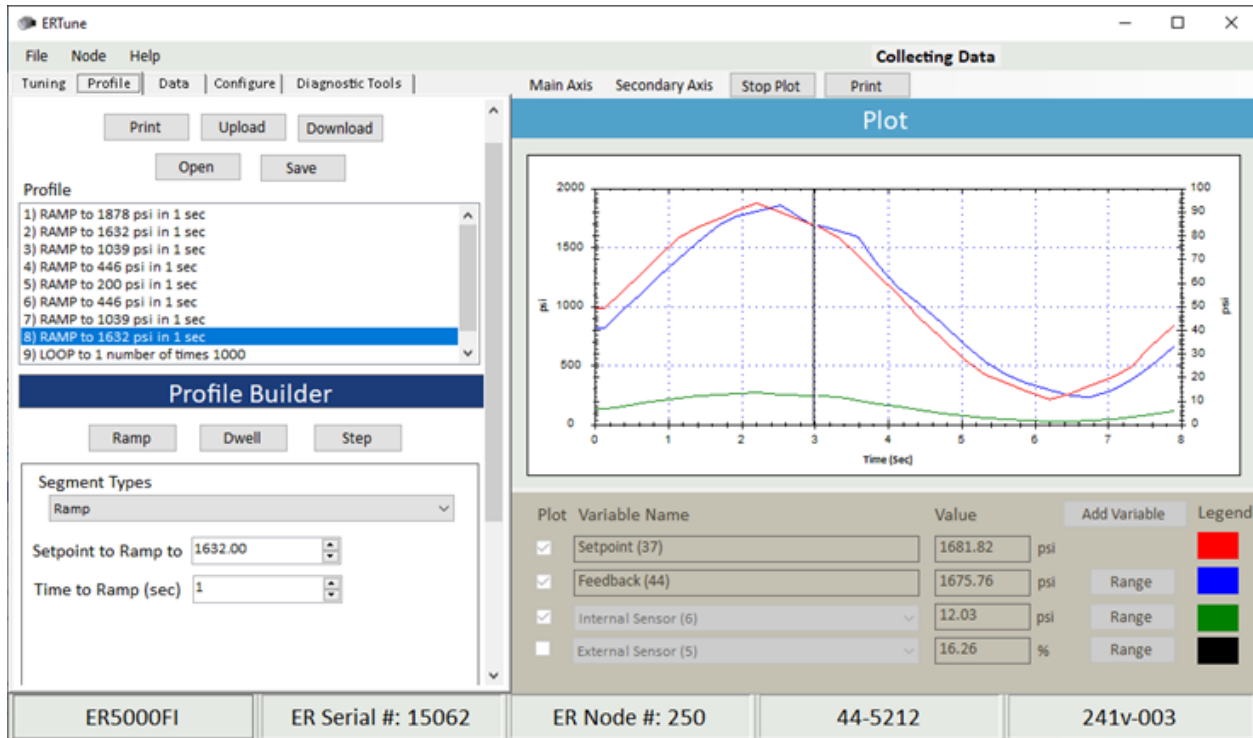
Figure 3.20: ERTune graphical user interface. Profile used for CV2 3-3

modify how quickly the pressure increment would be applied to the controller: in the tuning tab, there is a control system regulator named PID (Proportional-Integral-Derivative) that allows the user to modify the rise time. The user can choose between a steady but relatively slow increment or a ringing but quick pressure increment. In this study, the default values set by the manufacturer were used since they showed a good performance on the regulation response.

To create a profile it is necessary to set the pressure-increment-algorithm on the profile builder. For all the cyclic tests, an eight-second load cyclic that increments and decrements every second was used. To set the setpoints, it was necessary to use a sinusoidal function with the following inputs.

The amplitude, $a$, of the sinusoidal equation is

$$a = \frac{Q - A_c P_{\min}}{2A_c} \tag{3.4}$$

72

with the amplitude of the sinusoidal function known, it is required to shift the $y$-axis to account for the minimum pressure that the controller can operate which is 1379 kPa. The $y$-axis shift is

$$y_{\text{shift}} = a + P_{\text{min}} \tag{3.5}$$

Thus, the sinusoidal equation for cyclic loads is:

$$y(t) = a\sin(t) + y_{\text{shift}} \tag{3.6}$$

$$y(t) = \frac{Q - A_c P_{\text{min}}}{2A_c}\left[1 + \sin(t)\right] + P_{\text{min}} \tag{3.7}$$

where, $Q$, maximum load to apply on the test pile (kN); $A_c$, the effective cylinder's area ($m^2$), and $P_{\text{min}}$, controller's minimum operational pressure (kPa).
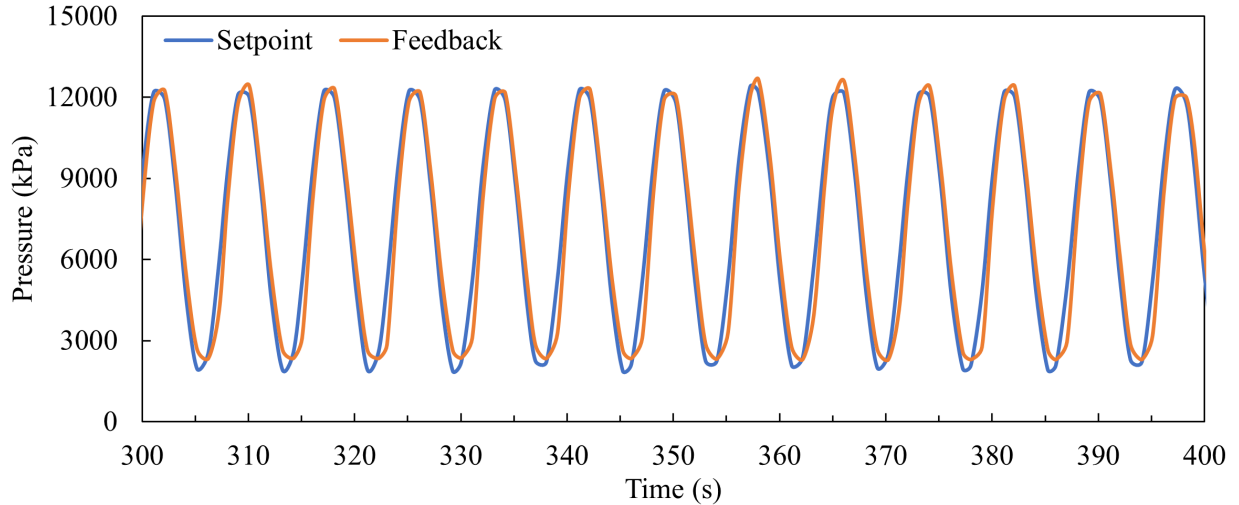


Figure 3.21: Cyclic load using the ER5K system during a test of the CV2 3-2.

Since an eight-second period cycle were applied, increments every $\pi/4$ seconds, that corresponds to one-second intervals, were replaced into Equation (3.7) that can be used to determine the cyclic profile and the pressure setpoints.This method can be tabulated in a spreadsheet to be able to modify it depending on the Collar Vane, load capacity, and type

of test. Figure 3.21 shows the feedback pressure from the pressure transducer and the objective pressures during a test showing that the controller changed the pressure in accordance with the predetermined values.

### 3.3.3  Test Pile and Reaction System

The helical pile tested was manufactured by Hubbell Inc. and consisted of a: (i) a 2.1 m long square shaft (SS175) lead section with 254, 304, and 355 mm diameter helices as shown in Figure 3.22(b); (ii) Two 1.2 m long square shaft (SS175) extensions with a single 355 mm diameter helix added to allow the lead section to be installed to the proper depth as shown in Figure 3.22(c); (iii) round pipe shaft (RS3500.300) with a length of 3.0 m, made of Grade 50 steel (minimum yield strength, $\sigma_y = 350$ MPa); section modulus, $S_x = 34.5$ cm$^3$ with an outer diameter, $O.D. = 88.9$ mm, and wall thickness, $t_w = 7.15$ mm as shown in Figure 3.22(d). Moreover, two tests were performed using a 3.6 m long square shaft (SS175) with the purpose of showing the versatility of the Collar Vane to be adapted to different shaft geometries. The square shaft properties are: $B = 44.45$ mm and $S_x = 14.64$ cm$^3$.
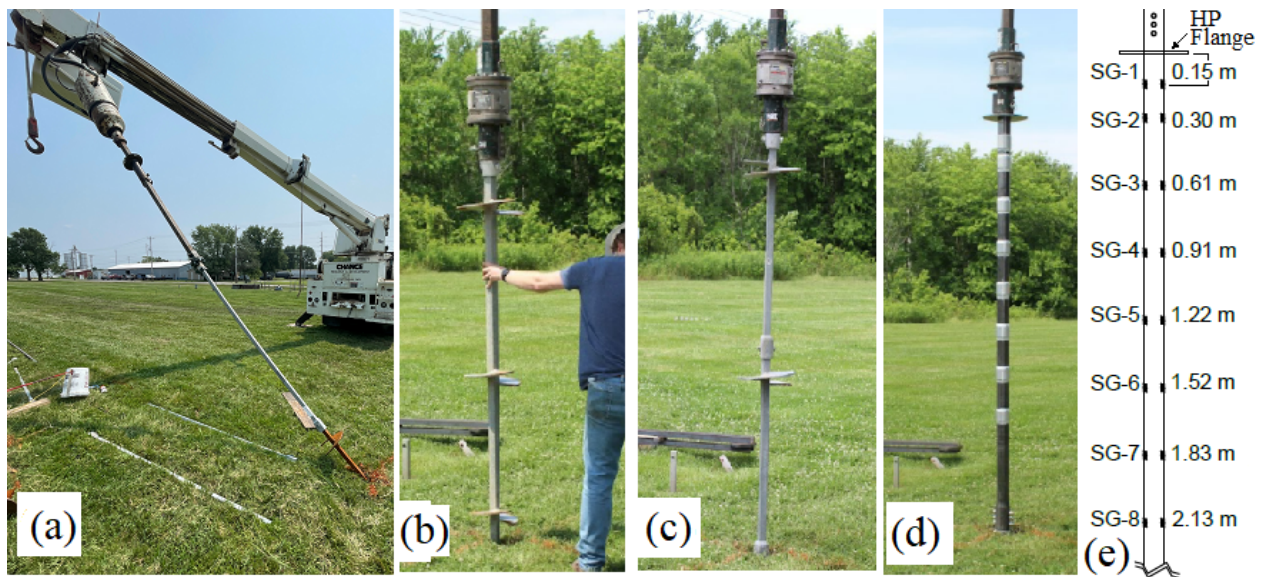


Figure 3.22: (a) Reaction pile installation; (b) helical pile lead section; (c) helical pile extensions; (d) instrumented steel round shaft and; (e) strain gauge locations.

Figure 3.23 presents the layout of the test piles, reaction piles, and soil exploration program for the cohesive soil test site. The testing arrangement in the cohesive soil consisted of reaction piles located 39 m apart. With this configuration, the minimum center-to-center spacing between adjacent piles was 3 m and, 4.5 m between the reaction pile and to test pile to avoid group effects in the radial soil mass in the surroundings. Test pile was installed and uninstalled after each completed test throughout the locations T1-1 to T1-11 (top row), from T2-11 to T2-1 (middle row) and T3-10 to T3-5 (bottom row) in 2021 as shown in Figure 3.23(a). For the second phase in 2022, and using the same configuration as 2021, the test piles were installed throughout locations T4-1 to T4-11, T5-3, and T5-1 in 2022 as shown in Figure 3.23(b). This configuration served with the aim of improving efficiency in data collection and assessment of repeatability.

The reaction piles used for the cohesive site were a 0.9 m long square shaft lead section with 200 and 254 mm diameter helices with a tensile strength of 311 kN. A single 3 m anchor extension was added to allow the lead section to be installed at 45 degrees and reach a suitable depth. Five reaction piles were installed in the top row (locations T1-1 to T1-11): four for the torsion test (R1, R2, R4, R5), and one (R3) for the lateral test. The reaction piles for the torsion test were installed at a distance of 0.75 and 1.5 m from the center line, so depending on the CV size, a force with an arm of 0.75 or 1.5 m can be applied. For the second and third rows, only three reaction piles were installed for each row: one for the lateral test (R7 and R10) and two for the torsional test (R6 and R8; R9 and R11 ) at a distance of 1.5 m from the center line. The test pile and the reaction piles were connected using a combination of 3 m long anchor extensions acting as a tension members. The double-acting hydraulic jack was placed on the line of load application connecting the test pile to the tension members and the load was applied by imposing a pulling force. In the torsion test, string potentiometers were located at the CV blade tips and loading arm ends as shown in Figure 3.28(a) to measure the rotation of these two elements and compare their relative displacement.
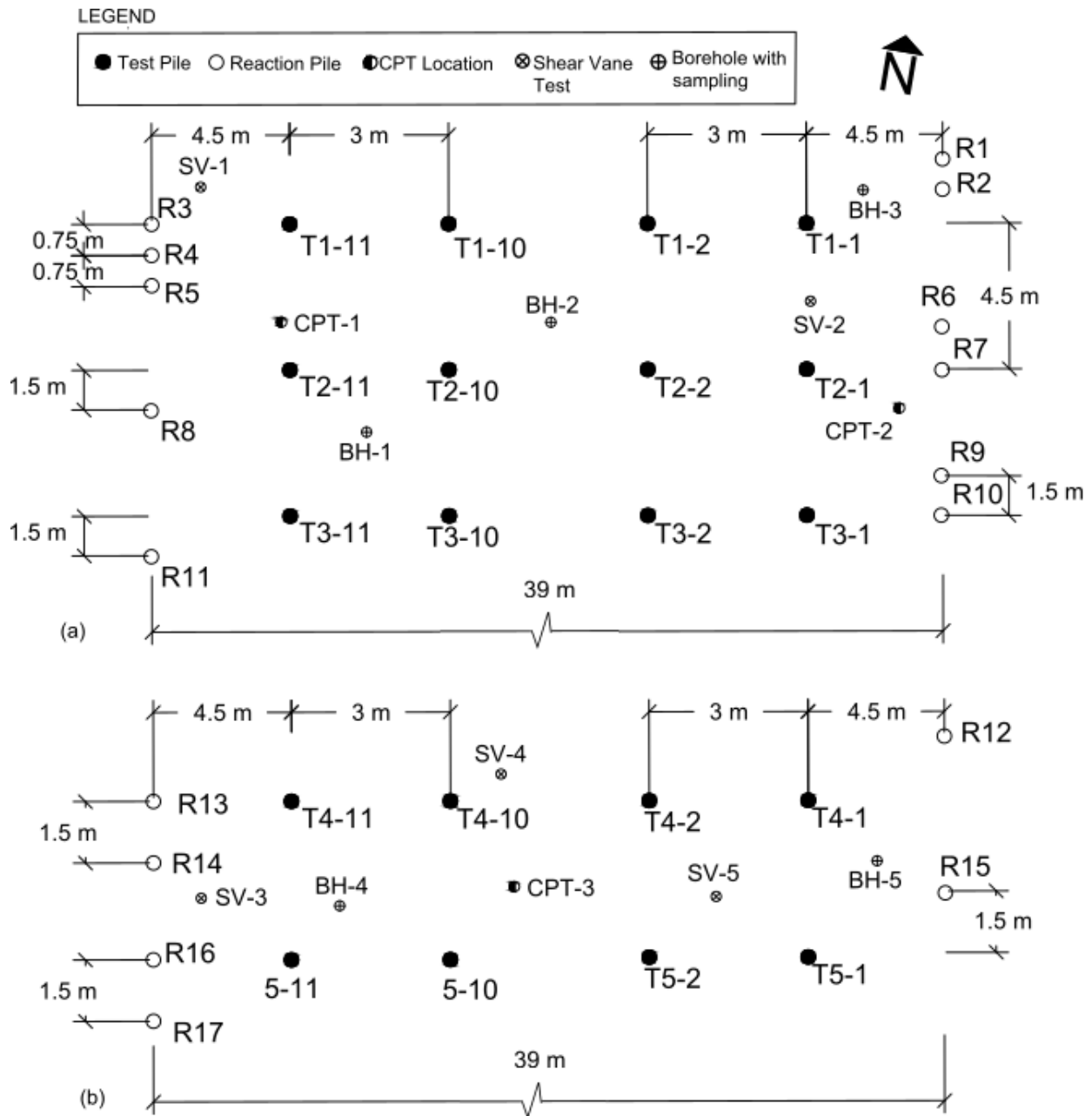
Figure 3.23: Cohesive soil site layout: test piles, reaction piles, and site investigation locations.

The testing arrangement in the granular soil consisted of reaction piles located 15 m apart so the center-to-center spacing between the test pile was 3 and 4.5 m between the test pile reaction pile as shown in Figure 3.24. The test pile was installed and uninstalled after completing the test through the locations TS1-1 to TS3-2. Reaction piles were placed
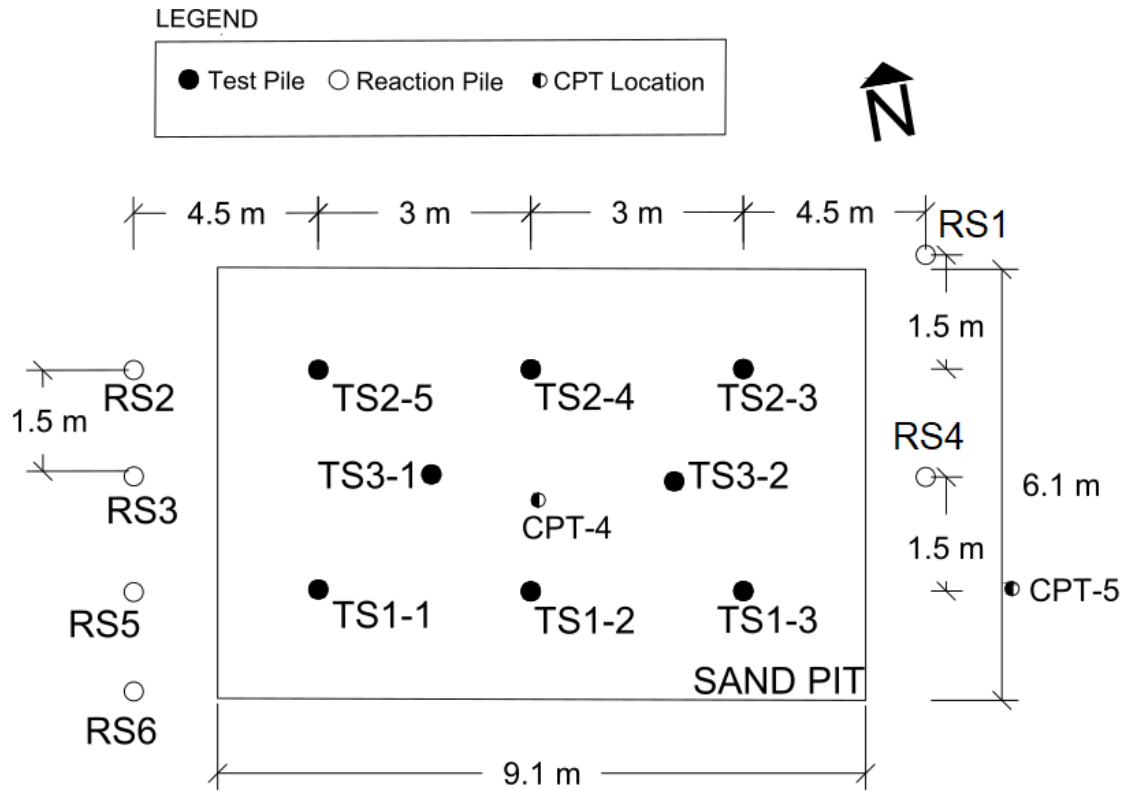
Figure 3.24: Granular soil site layout: test piles, reaction piles, and site investigation locations.

outside the test pit. RS2 and RS5 were used as reaction piles for the lateral test; RS1, RS3, RS4, and RS6, for the torsional test in the top row; and R2S and R6S, for the torsional test in the bottom row. The distance between reaction piles for the torsion test was approximately 3 m to apply a load with an arm of approximately 1.5 m at each end. The reaction piles used for lateral load consisted of a 1.8 m long square shaft lead section with 254 and 304 mm diameter helices with a tensile strength of 667 kN and two 3 m anchor extensions coupled to the lead section to allow the lead section to reach an appropriate depth. Reaction piles for the torsion test consisted of a 0.9 m long square shaft lead section with 200 and 254 mm diameter helices with a tensile strength of 311 kN and a single 3 m anchor extension coupled to the lead section.

Figure 3.25 shows the installation torque for the helical pile without CV and the single-piece CV in both, cohesive and granular soil. For the cohesive soil, it shows that the
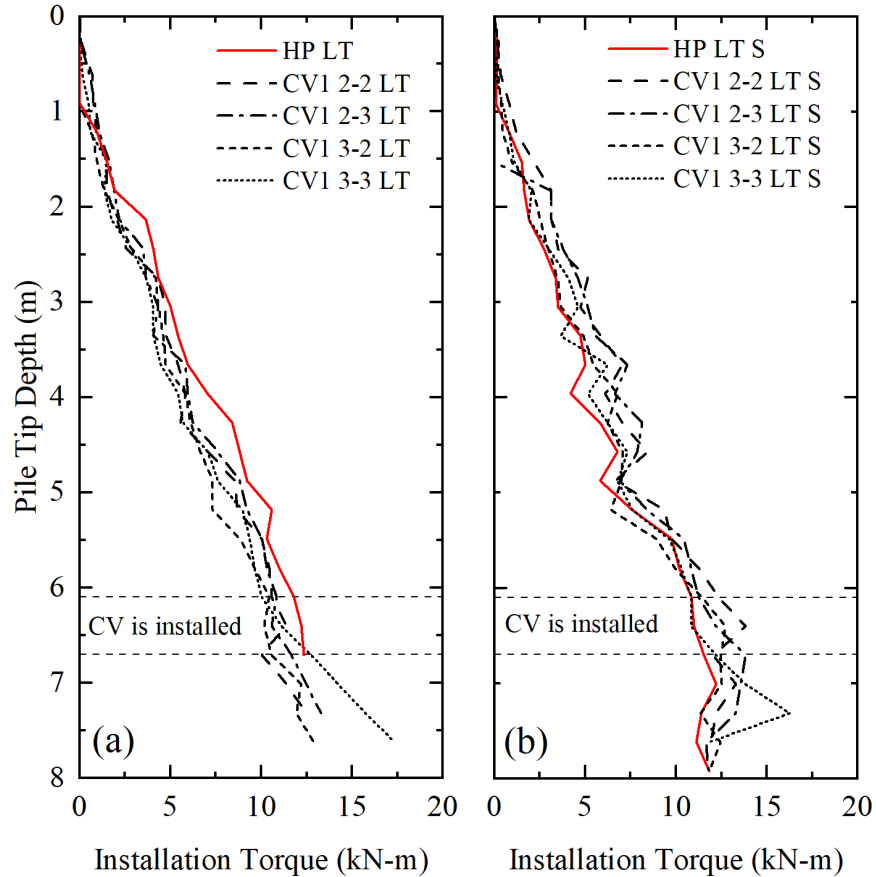
Figure 3.25: Measured installation torque versus helical pile penetration depth: (a) cohesive soil and; (b) granular material.

case without CV (HP LT) presented higher installation forces compared with the cases with the CV. The difference can be attributed to seasonal effects since the HP LT values were measured in the first phase of the testing program in 2021, whereas the CV values were obtained in 2022. Figure 3.25(b) shows the installation values in the granular soil which were obtained in the same year. The CV installation values are slightly higher even when the CV is not being pushed into the ground. In general, it can be deduced that the CV does not increase abruptly the installation torque value necessary to install the CV.

## 3.4   Testing Procedures

This section will show the testing frame arrangement, load procedure, and the load tests performed by CV type, load sequence, and type of soil.

Torsional and lateral load tests were conducted in two different load sequences in the cohesive soil: (i) lateral test was performed within one hour after the helical pile installation and once this test was completed, the 3 m long loading arm was coupled on the helical pile and the torsion test was carried out in the same location. This load sequence will be referenced as $LT$ (lateral-torsional); (ii) after HP installation, the torsion test was performed followed by the lateral test. This load sequence will be referenced as $TL$ (torsional-lateral). In the granular soil, only the $LT$ sequence was applied to the helical pile due to space limitations in the sand test pit. A quick method of loading procedure for each test was chosen to complete the load testing program in a timely manner.

### 3.4.1  Lateral Loading

Figure 3.26 shows the testing frame components used for the lateral test in the cohesive soil. The cylinders were connected to a manifold equipped with a calibrated 69 MPa pressure transducer to record the pressure supplied to the system and, an air hydraulic pump was used to supply pressure to the cylinders. A calibrated S-type load cell with a capacity of 49 kN was used in the lateral test in the cohesive material. The load cell, hydraulic cylinders, and string potentiometers were placed at the same level to minimize eccentric loading. A turnbuckle was used to connect the hydraulic cylinders and loading steel cap which was bolted at the HP pile head. The pile head displacement was measured using a calibrated string potentiometer with a maximum stroke of 254 mm. SP was placed at 2 m from the test pile in an independently supported reference beam. The applied load was generally applied between 8 to 13 cm above the ground surface.

Based on the first phase results, it was necessary to increase the loading capacity of the lateral testing frame for the granular soil site. A different frame was built to adapt the hollow hydraulic cylinder. Figure 3.27 shows the crate where two hollow cylinders were implemented in a series configuration with the purpose to have more piston stroke. Also, a
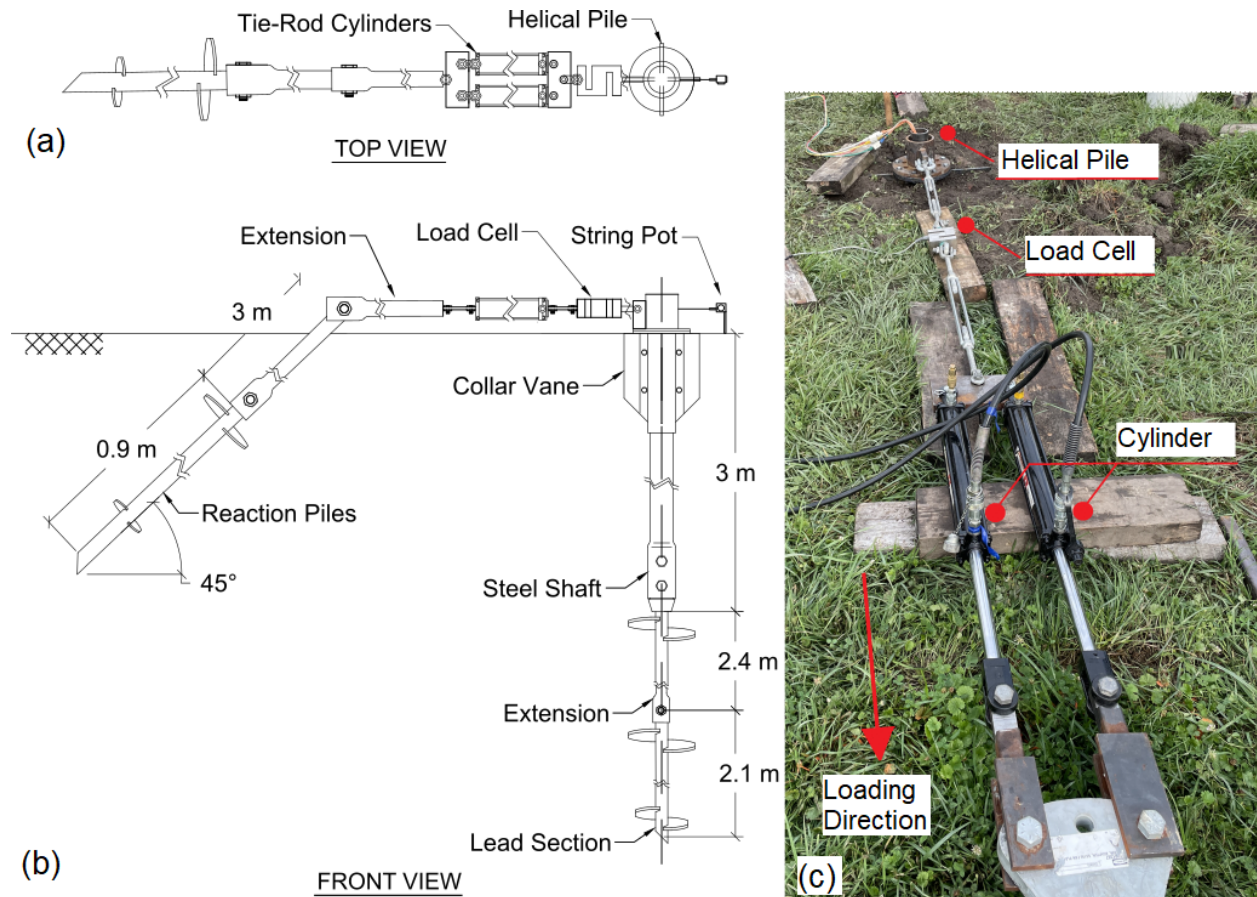
Figure 3.26: Lateral load test setup in cohesive soil: (a) top view; (b) front view; and (c) photo.

178 kN S-type load cell was used in this loading frame to ensure that the new higher applied loads were recorded.

In the monotonic pile load test, the quick maintained load test procedure used in the lateral test consisted of the pile loaded in increments of 20% of the HP bending resistance and maintained for a period of 10 minutes to allow the soil-pile system to reach equilibrium. The pile was unloaded by decreasing the load in four equal decrements while keeping the load constant for a period of 5 minutes. The test duration was similar for all cases, with times ranging between 1 h 20 min and 1 h 40 min.
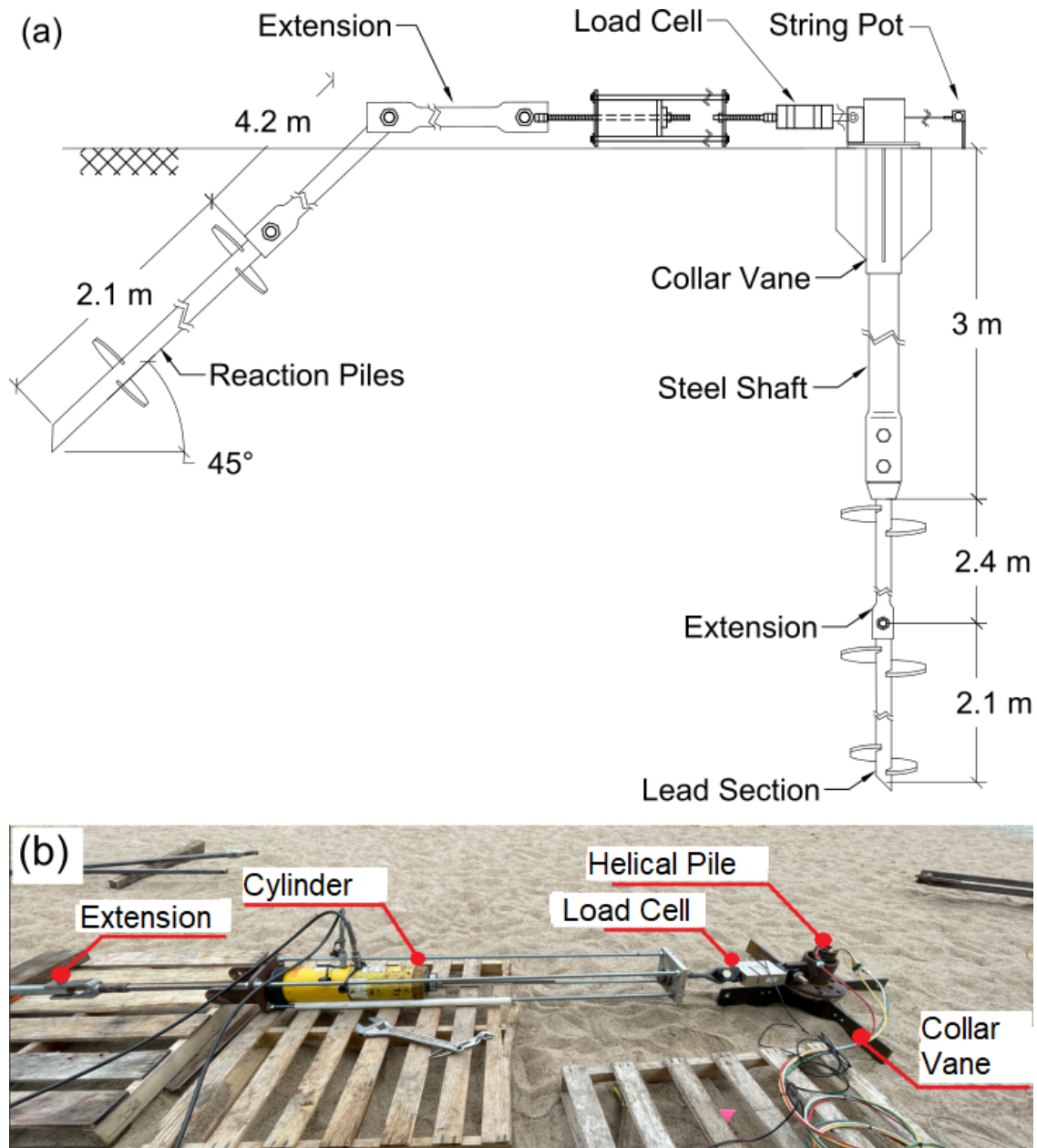
Figure 3.27: Lateral load test setup in granular soil: (a) plan view and (b) photo.

### 3.4.2 Torsional Loading

Figure 3.28(a) shows the schematic of the torsional load setup. Two 29 kN hydraulic cylinders with a stroke of 0.76 m each, were installed at each end of the 3.4 m-long loading arm to apply a pure torsional load. Two sets of 49 kN load cells were used to measure the forces imposed by the hydraulic cylinders. A common manifold, equipped with the pressure transducer, was used to supply pressure to the two tie-rod cylinders. The torque exerted at

the HP was calculated as the product of the loading arm (0.75 or 1.5 m) and the measured force.
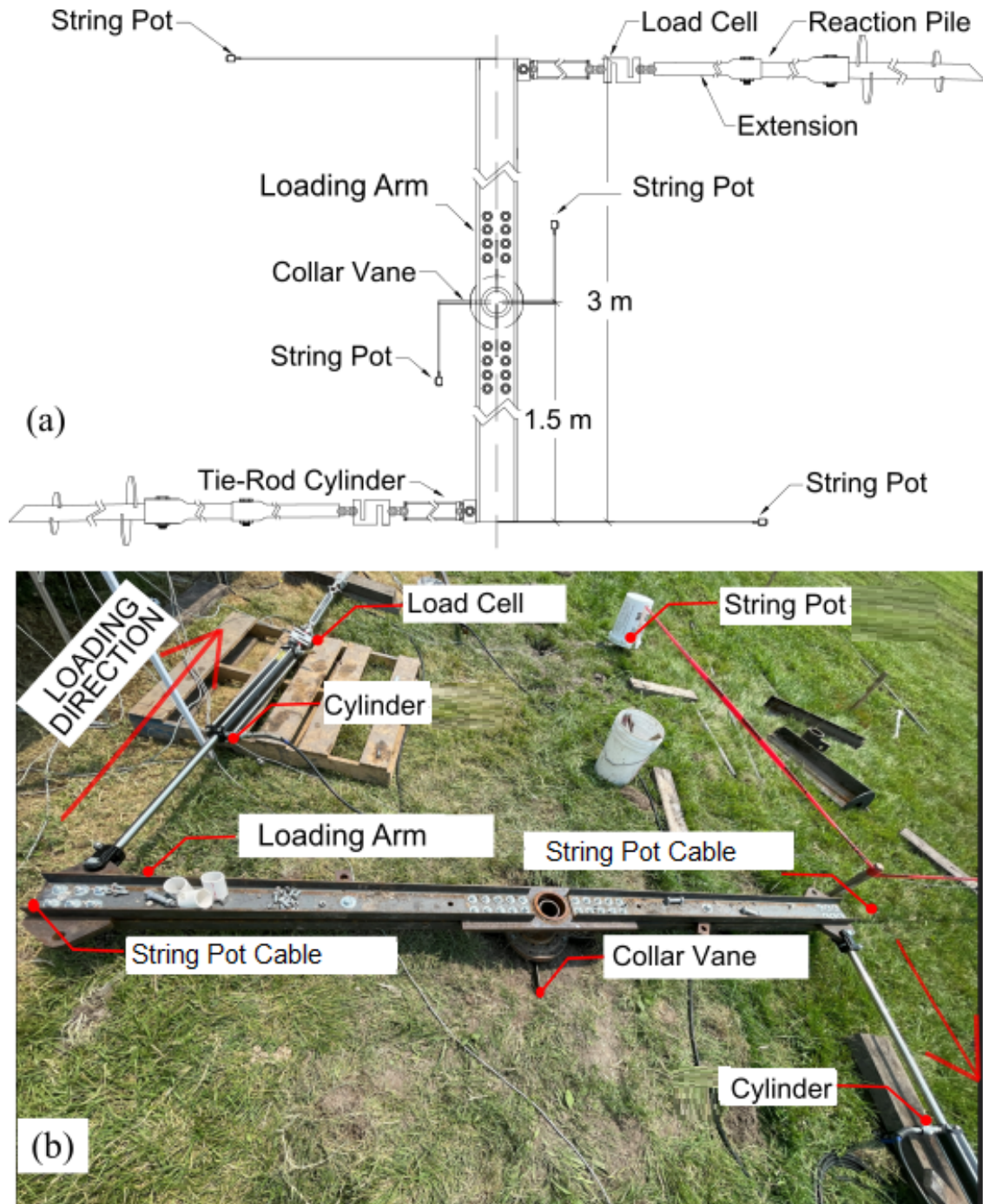


Figure 3.28: Torsion load test setup in cohesive soil: (a) plan view and (b) photo.

The torsional loading test was initiated with low displacement increments to very large target rotations. Thereafter, the CV was unloaded to record the zero-torsion plastic

displacement. The loading protocol included between 16 to 20 loading increments of 0.2, 0.5, and 4°. Each increment was maintained for a period of 5 minutes. Four string potentiometers were used in this test to monitor the displacement and determine the rotation of the loading arm and CV. For redundancy, two string potentiometers were located at each end of the loading arm and two on the CV blades perpendicular to the loading arm as shown in Figure 3.28(a). Torque increments were applied until continuous jacking was required to maintain a constant torque (i.e., $dT/d\theta$ =0) or when the cylinder ran out of stroke. However, the torsion test for the bigger Collar Vanes performed in 2021, was not subjected to high torsional loads and these tests were repeated in 2022.

### 3.4.3  Cyclic Loading

The cyclic loading was to simulate the pile subjected to long-term wind loading. One thousand loads were applied for a period of eight seconds (0.125 Hz) using the hydraulic controller. The cyclic load ratio, $\zeta_b$, implemented were generally 30, 50, and 70% of the pre-defined ultimate capacity. Thereby, cyclic load ratios were estimated based on the ultimate torsional capacity and the interpreted lateral load to displace the pile 12.5 mm. Moreover, after performing the cyclic test, a quick monotonic test was performed to determine the pile lateral capacity after cyclic loading.

A total of approximately one thousand loads were applied for each, lateral and torsional cyclic test, for a single HP in the same installed location. Hence, the torsional response is expected to be affected by the cyclic lateral test. The purpose of this load sequence is to study the effects of both load conditions in the same structure as if the pile was installed and subjected to loads in a real-case scenario.

## 3.5 Summary of Tests Performed

The goal of the project is to study the lateral and torsional response of helical piles augmented with a Collar Vane. To accomplish this, different Collar Vanes sizes were subjected to different types of loads, as presented in Tables 3.3 and 3.4.

Overall, the first phase of the testing plan carried out in 2021, consisted of testing the two-piece Collar Vane in a cohesive soil. The test included monotonic in two different load sequences: lateral-torsional (LT) and torsional-lateral (TL). The cyclic test was performed in only one load sequence order (LT) when using the Collar Vanes plus a cyclic base case was performed for the helical pile without Collar Vane. The second phase in 2022 consisted of performing the torsion test on a certain amount of Collar Vanes that did not fail in phase one. A 'long-term' case is also included using the CV2 3-1 that was installed in September 2021 and tested 10 months later in July. A new single-piece Collar Vane was tested in the cohesive soil and a backfilled sand test pit. Cyclic loads were performed in both soil conditions. Some of the cyclic tests are labeled with an R which stands for a cyclic test performed with a different cyclic load-to-ultimate load ratio, $\zeta_b = P_c/P_u$, for the same CV geometry.

Table 3.3: Tests performed on phase one (2021): cohesive soil test site and two-piece Collar Vane.

| Date | Collar Vane | Location | Load Sequence | Type of Test | Test Name |
|---|---|---|---|---|---|
| 2021-07-12 | Helical Pile no CV | T 1-1 | Lateral | Monotonic in cohesive soil | HP LT |
| 2021-07-13 | Helical Pile no CV | T 1-1 | Torsion | Monotonic in cohesive soil | |
| 2021-07-15 | Helical Pile no CV | T 1-2 | Torsion-Lateral | Monotonic in cohesive soil | HP TL |
| 2021-07-16 | CV2 1-1 | T 1-3 | Lateral-Torsion | Monotonic in cohesive soil | CV2 1-1 LT |
| 2021-07-19 | CV2 2-1 | T 1-4 | Lateral-Torsion | Monotonic in cohesive soil | CV2 2-1 LT |
| 2021-07-20 | CV2 2-1 | T 1-5 | Torsion-Lateral | Monotonic in cohesive soil | CV2 2-1 TL |
| 2021-07-21 | CV2 1-2 | T 1-6 | Lateral-Torsion | Monotonic in cohesive soil | CV2 1-2 LT |
| 2021-07-22 | CV2 1-2 | T 1-7 | Torsion-Lateral | Monotonic in cohesive soil | CV2 1-2 TL |
| 2021-07-23 | CV2 1-1 | T 1-8 | Torsion-Lateral | Monotonic in cohesive soil | CV2 1-1 TL |
| 2021-07-26 | CV2 1-3 | T 1-9 | Lateral-Torsion | Monotonic in cohesive soil | CV2 1-3 LT |
| 2021-07-27 | CV2 1-3 | T 1-10 | Torsion-Lateral | Monotonic in cohesive soil | CV2 1-3 TL |
| 2021-07-28 | CV2 2-2 | T 1-11 | Lateral-Torsion | Monotonic in cohesive soil | CV2 2-2 LT |
| 2021-07-30 | CV2 2-2 | T 2-11 | Torsion-Lateral | Monotonic in cohesive soill | CV2 2-2 TL |
| 2021-08-02 | CV2 2-3 | T 2-10 | Lateral-Torsion | Monotonic in cohesive soil | CV2 2-3 LT |
| 2021-08-10 | CV2 3-1 | T 2-9 | Torsion-Lateral | Monotonic in cohesive soil | CV2 3-1 TL |
| 2021-08-11 | CV2 3-1 | T 2-8 | Lateral-Torsion | Monotonic in cohesive soil | CV2 3-1 LT |
| 2021-08-12 | CV2 3-2 | T 2-7 | Lateral-Torsion | Monotonic in cohesive soil | CV2 3-2 LT |
| 2021-08-13 | CV2 3-3 | T 2-6 | Lateral-Torsion | Monotonic in cohesive soil | CV2 3-3 LT |
| 2021-08-16 | CV2 3-3 | T 2-5 | Torsion-Lateral | Monotonic in cohesive soil | CV2 3-3 TL |
| 2021-08-17 | CV2 3-2 | T 2-4 | Torsion-Lateral | Monotonic in cohesive soil | CV2 3-2 TL |
| 2021-08-18 | CV2 2-3 | T 2-3 | Torsion-Lateral | Monotonic in cohesive soil | CV2 2-3 TL |
| 2021-08-19 | CV2 3-2 | T 2-2 | Lateral-Torsion | Cyclic in cohesive soil | CV2 3-2 LT Cyc |
| 2021-08-20 | CV2 3-3 | T 3-10 | Lateral-Torsion | Cyclic in cohesive soil | CV2 3-3 LT Cyc |
| 2021-08-23 | CV2 3-1 | T 3-9 | Lateral-Torsion | Cyclic in cohesive soil | CV2 3-1 LT Cyc |
| 2021-08-24 | CV2 2-1 | T 3-8 | Lateral-Torsion | Cyclic in cohesive soil | CV2 2-1 LT Cyc |
| 2021-08-25 | CV2 3-3 | T 3-7 | Lateral-Torsion | Cyclic in cohesive soil | CV2 3-3 LT Cyc R |
| 2021-08-26 | CV2 3-2 | T 3-6 | Lateral-Torsion | Cyclic in cohesive soil | CV2 3-2 LT Cyc R |
| 2021-08-27 | Helical Pile no CV | T 3-5 | Lateral | Cyclic in cohesive soil | HP L Cyc |

**Note**: LT, Lateral-Torsion sequence; TL, Torsion-Lateral sequence; Cyc, cyclic loading test; R, repeated test with a different $\zeta_b$; L, only lateral test performed.

Table 3.4: Tests performed on phase two (2022).

| Date | Collar Vane | Location | Load Sequence | Type of Test | Test Name |
|---|---|---|---|---|---|
| 2022-07-22 | CV2 3-1 | T 3-2 | Lateral-Torsion | Long term monotonic test in cohesive soil | CV2 3-1 LT* |
| 2022-07-25/26 | CV2 3-1 | T 3-1 | Torsion | Monotonic in cohesive soil | CV2 3-1 T |
| 2022-07-27 | CV2 3-2 | T 4-1 | Torsion | Monotonic in cohesive soil | CV2 3-2 T |
| 2022-07-28 | CV2 2-2 | T 4-2 | Torsion | Monotonic in cohesive soil | CV2 2-2 T |
|  | CV2 2-3 | T 4-3 | Torsion | Monotonic in cohesive soil | CV2 2-3 T |
| 2022-07-29 | CV2 3-3 | T 4-4 | Torsion | Monotonic in cohesive soil | CV2 3-3 T |
| 2022-08-01 | CV1 2-2 | T 4-5 | Lateral-Torsion | Monotonic in cohesive soil | CV1 2-2 LT |
| 2022-08-02 | CV1 3-2 | T 4-6 | Lateral-Torsion | Monotonic in cohesive soil | CV1 3-2 LT |
| 2022-08-03 | CV1 2-3 | T 4-7 | Lateral-Torsion | Monotonic in cohesive soil | CV1 2-3 LT |
| 2022-08-04 | CV1 3-3 | T 4-8 | Lateral-Torsion | Monotonic in cohesive soil | CV1 3-3 LT |
| 2022-08-08 | Helical Pile no CV | TS 1-1 | Lateral-Torsion | Monotonic in granular soil | HP LT S |
| 2022-08-09 | CV1 2-2 | TS 1-2 | Lateral-Torsion | Monotonic in granular soil | CV1 2-2 LT S |
| 2022-08-10 | CV1 2-3 | TS 1-3 | Lateral-Torsion | Monotonic in granular soil | CV1 2-3 LT S |
| 2022-08-11 | CV1 3-2 | TS 2-3 | Lateral-Torsion | Monotonic in granular soil | CV1 3-2 LT S |
| 2022-08-15 | CV1 3-3 | TS 2-2 | Lateral-Torsion | Monotonic in granular soil | CV1 3-3 LT S |
| 2022-08-17 | CV1 3-2 | TS 2-1 | Lateral | Monotonic in granular soil | CV1 3-2 L S |
| 2022-08-19 | CV1 3-2 | TS 3-2 | Lateral-Torsion | Cyclic in granular soil | CV1 3-2 LT Cyc S |
| 2022-08-22 | CV1 3-2 | TS 3-1 | Lateral-Torsion | Cyclic in granular soil | CV1 3-2 LT Cyc S R |
| 2022-08-23 | CV1 2-2 | T 4-9 | Lateral | Cyclic in cohesive soil | CV1 2-2 L Cyc |
|  | CV1 2-2 | T 4-10 | Torsion | Cyclic in cohesive soil | CV1 2-2 T Cyc |
| 2022-08-24 | CV1 3-2 | T 4-11 | Lateral-Torsion | Cyclic in cohesive soil | CV1 3-2 LT Cyc |
| 2022-08-25 | CV1 2-2 | T 5-1 | Lateral-Torsion | Monotonic in cohesive soil using square shaft | CV1 2-2 LT SS175 |
| 2022-08-26 | CV1 3-2 | T 5-3 | Lateral-Torsion | Monotonic in cohesive soil using square shaft | CV1 3-2 LT SS175 |

**Note**: LT, Lateral-Torsion sequence; TL, Torsion-Lateral sequence; Cyc, cyclic loading test; R, repeated test with different $\zeta_b$; *, Long Term test; S, test performed in granular soil; SS175, square shaft; L, only lateral test performed; T, only torsion test performed

# CHAPTER 4

# MONOTONIC TESTS RESULTS AND ANALYSIS

## 4.1 Introduction

The chapter will summarize the monotonic test results from both, cohesive and granular soil test sites. The first section will present the lateral and torsional results in the cohesive soils plus the deformation analysis using the strain gauges measurements, both Collar Vanes prototypes were tested in this type of soil. The second section will focus on the granular conditions where the CV1 was tested under lateral and torsional loads. Results will be displayed as a series of summarized graphs according to the Collar Vane geometry, load sequence, and soil condition. Only the loading portion is presented. For the complete loading curve (loading-unloading), individual results are shown in the Appendixes C-D and for moment profiles in Appendix E.

## 4.2 Performance in Cohesive Soil

Lateral and torsional responses in the cohesive soil are shown in this section. Tests performed in the first phase in 2021 included the two-piece Collar Vane, and based on the performance of this CV, a one-piece Collar Vane was manufactured and tested in the second phase in 2021 with the intention of improving the Collar Vane torsional resistance.

### 4.2.1 Lateral Loading

The lateral test results were conducted using a quick test protocol initiated with a monotonic loading of up to 25 mm. In some cases, the displacement was lower due to limitations on the cylinder capacity. This limitation was overcome by adding another cylinder to the testing frame so the resulting configuration was two identical cylinders in parallel, mostly used in the cohesive testing site, with a capacity of up to 54 kN. After

applying the loads, the helical piles were unloaded and the plastic deformation was recorded. Complete load-displacement curves are shown in Appendix C.
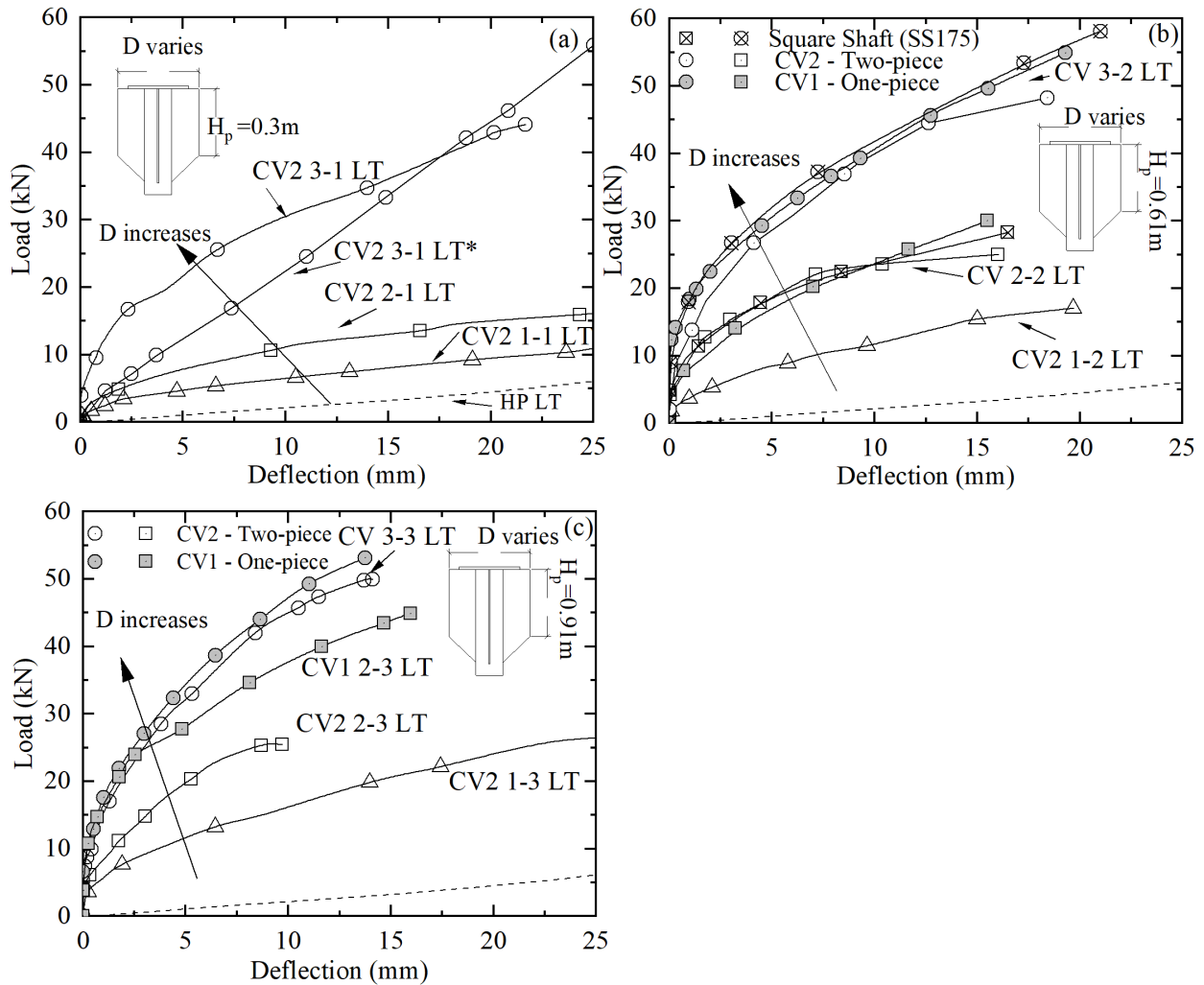


Figure 4.1: Lateral vs Deflection curves for the load sequence LT in cohesive soil.

Figure 4.1 shows the load-displacement curves in the over-consolidated cohesive soil for the Collar Vanes with prismatic heights $H_p$ of 0.30, 0.61 and 0.91 m in order to highlight the influence of the diameter for each fixed height. The base case, HP LT, is also shown to highlight the increase in resistance obtained with the CV. This case shows a fairly linear response that can be attributed to the HP's small diameter and the soil plastic deformation associated with the observed 40 mm gap opening between the HP and upper adjacent soil after installation indicating the impossibility of the HP to fully mobilize lateral resistance.

Furthermore, both CV prototypes (CV1 and CV2) are also included in the plot to compare the performance due to the design effects. Figure 4.1(a) shows the curves for the $H_p= 0.30$ m Collar Vanes. CV 1-1 and 2-1 present and slight increment in the lateral capacity, it takes almost 3-5 times the force to displace the pile 12.5mm compared with the bases case. The CVs 3-1 had the better performance: CV2 3-1 presents a considerable increment compared to the case without CV and the response shows a hyperbolic curve. It takes almost 11 times the force to displace the pile 12.5 without a CV. Finally, CV2 3-1 LT* is the pile tested after approximately nine months of being installed and presents almost a linear response. The response is lower than the CV2 3-1 when the pile head displacement is less than 17 mm. Figure 4.1(b) shows the load-deflection curves for the 0.61 m height Collar Vanes with different diameters. Both, one-piece and two-piece Collar Vane are presented as a closed- and open symbol, respectively. Also, the results are shown for the square shaft with the cross-lines symbol. The performance of both CV prototypes is nearly identical. The force required to displace the pile 12.5 mm is approximately 9 and 17 times for the CVs 2-2 and 3-2 with the round shaft, respectively. Results using the round and square shaft suggest that the capacity is predominantly attributed mobilization of geotechnical resistance in the upper soil profile by the Collar Vane and using the two different CV prototypes did not have an influence on the lateral performance. Figure 4.1(c) shows the results for the 0.91 m height CV. The biggest CV was subjected to a lateral load of 53 kN with a head displacement of 14 mm. This is slightly better than the CV 3-2 (49 kN to displace 14mm) suggesting that the increment in height, from 0.9 to 1.2 m, did not increase the lateral capacity of the HP for these amount of loads. The comparison between the two CV prototypes shows that the lateral response is the same in all the CV sizes except for CV 2-3 where the one-piece CV shows a better performance compared to the two-piece CV. This may be attributed to the variation in soil properties and layering at that particular location since the lateral response of the CV2 2-3 is almost the same as the CV 2-2 and not higher as it would be expected. After test completion, the CVs and HP

were inspected and no signs of structural failure were observed. The plots, in general, show that the lateral load displacements have three characteristic regions: an initial elastic region, a sharply curving transition, and a flattening tendency final region observed. However, the final region was not developed in all curves, and only in some tests, this region was fully mobilized (e.g., CV2 1-2, CV2 1-3, and CV2 2-3). This increase in lateral resistance is then attributed to an increment in the passive resistance due to a larger area (e.g., Collar Vane) forcing the soil to develop its shear resistance from the Collar Vane instead of solely the helical pile.
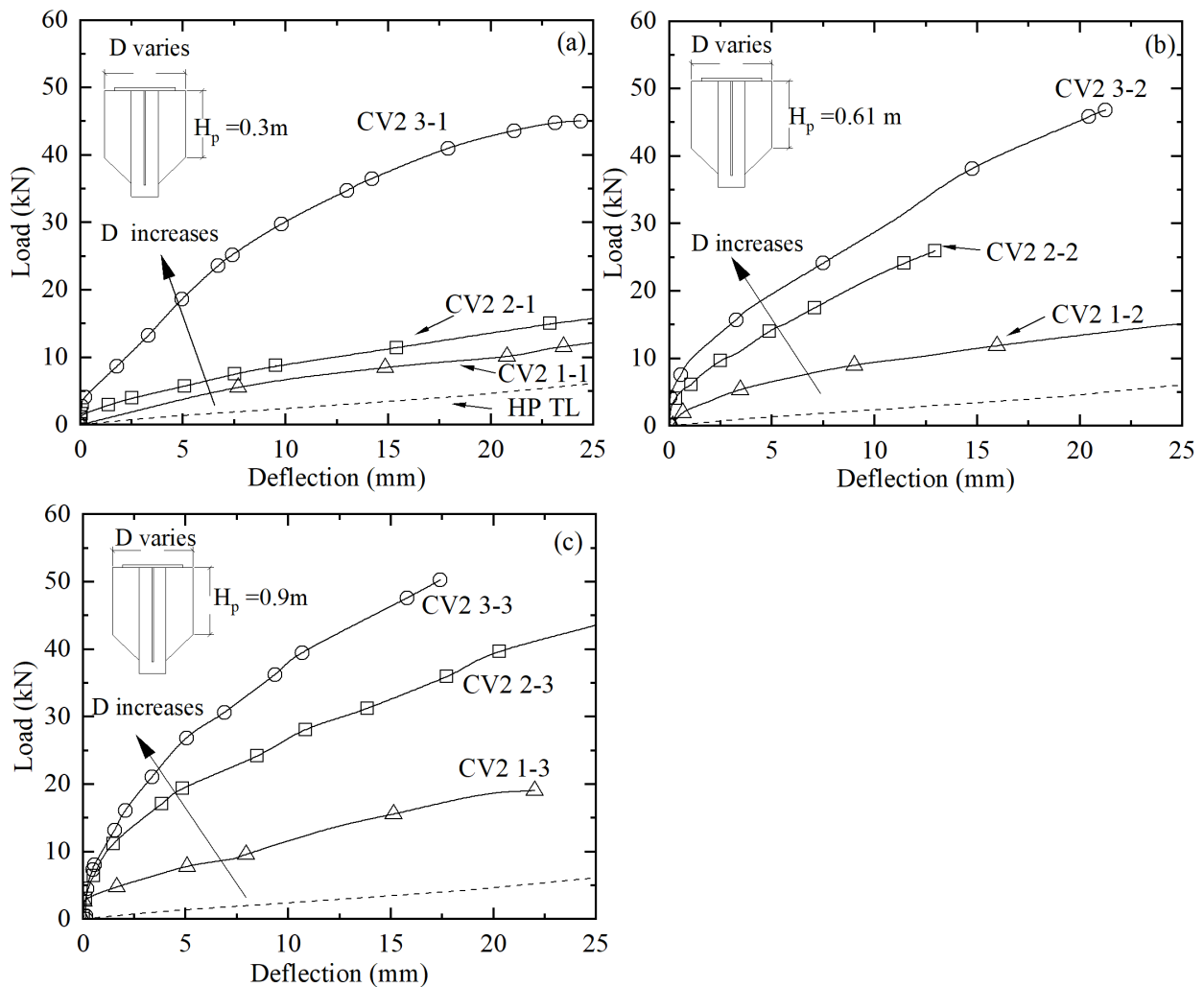


Figure 4.2: Lateral vs Deflection curves for the load sequence TL in cohesive soil.

The results presented are for the load sequence 'Lateral-Torsion' (LT) which means that the lateral test was performed first before performing the torsion test. Thus, the lateral results are not affected by the torsional test. To study the effects of different types of loading, the lateral response influenced by a torsional load is also presented. This load sequence is named 'Torsion-Lateral' (TL) and results are shown in Figure 4.2. Only the two-piece CV was subjected to this load sequence. The torsional loads applied in this sequence vary from 8 to 15 kN-m, for the 0.3 m diameter CV; 12 to 13 kN-m, for the 0.6 m diameter CV; and 22 to 40 kN-m, for the 0.9 m diameter CV. Geotechnical torsional failure was reached in CVs 1-1, 1-2, 1-3, and 2-1. In Appendix D can be found in detail the torsional curves. Figure 4.2(a) shows the curves for the $H_p$= 0.30 m Collar Vanes. The increase in diameter from 0.30 to 0.61 m (CV2 1-1 to CV 2-1, respectively) did not increase substantially the capacity of the CV. This can be attributed to the disturbance of the soil from the torsion test where the maximum torsional capacity of the CV was reached. CV2 3-1 TL has a better performance even when the soil was previously disturbed with the previous torsional test. Figure 4.2(b) shows the lateral response for the 0.61 m height Collar Vanes. Compared with the LT sequence, the curves show a slight decrement in the lateral capacity as expected. Figure 4.2(c) shows the lateral response for the 0.91 m height Collar Vanes. In all the scenarios it is clear that the diameter had an important influence on the lateral capacity of the Collar Vane.

The lateral capacity of most pile foundations is interpreted from load tests utilizing specified displacement criteria as a basic evaluation method for the 'interpreted failure load' using a displacement limiting value (McNulty, 1956; Walker & Cox, 1966) or displacement limit as a function of the shaft diameter (Pyke, 1984; Briaud *et al.*, 1984). Chen & Lee (2010) states that small displacement limits represent a serviceability limit state, whereas large displacement limits represent an ultimate limit state condition. Additionally, when designing foundation-supporting structures that are less sensitive to lateral movements (i.e., power transmission lines), a lateral deflection of 12.5 mm is frequently taken into account.

Table 4.1: Lateral interpretation criteria for cohesive soil

| | Interpreted failure load (kN) | | |
|---|---|---|---|
| Method | McNulty (1956) | Walker & Cox (1966) | City of New York (1981) |
| Definition | 6.25 mm pile head displacement | 12.5 mm pile head displacement | 25 mm pile head displacement |
| HP LT | 1.3 | 2.6 | 6.36 |
| HP TL | 1.5 | 2.8 | 6.2 |
| CV2 1-1 LT | 5 | 7 | 11 |
| CV2 1-1 TL | 5 | 8 | 12 |
| CV2 1-2 LT | 9 | 13 | 18 |
| CV2 1-2 TL | 7 | 10 | 15 |
| CV2 1-3 LT | 13 | 19 | 26 |
| CV2 1-3 TL | 8 | 13 | |
| CV2 2-1 LT | 9 | 12 | 16 |
| CV2 2-1 TL | 6 | 11 | 16 |
| CV2 2-2 LT | 21 | 23 | - |
| CV2 2-2 TL | 15 | 26 | - |
| CV2 2-3 LT | 22 | 27[†] | - |
| CV2 2-3 TL | 21 | 28 | 43 |
| CV2 3-1 LT | 25 | 33 | |
| CV2 3-1 LT* | 15 | 28 | 55 |
| CV2 3-1 TL | 23 | 34 | |
| CV2 3-2 LT | 32 | 45 | |
| CV2 3-2 TL | 18 | 32 | |
| CV2 3-3 LT | 36 | 49 | - |
| CV2 3-3 TL | 28 | 43 | - |
| CV1 2-2 LT | 19 | 27 | - |
| CV1 2-2 LT SS175 | 20 | 25 | - |
| CV1 2-3 LT | 31 | 41 | - |
| CV1 3-2 LT | 33 | 46 | - |
| CV1 3-2 LT SS175 | 35 | 46 | - |
| CV1 3-3 LT | 39 | 52 | - |

**Notes:** [†] value obtained by extrapolating load vs deflection curve.

The interpreted lateral capacities of CVs are listed in Table 4.1. In general, it is shown that the interpreted failure load is lower for the TL cases, the behavior of the square shaft is almost the same as the round shaft, and the CV1 has the same behavior as the CV2.
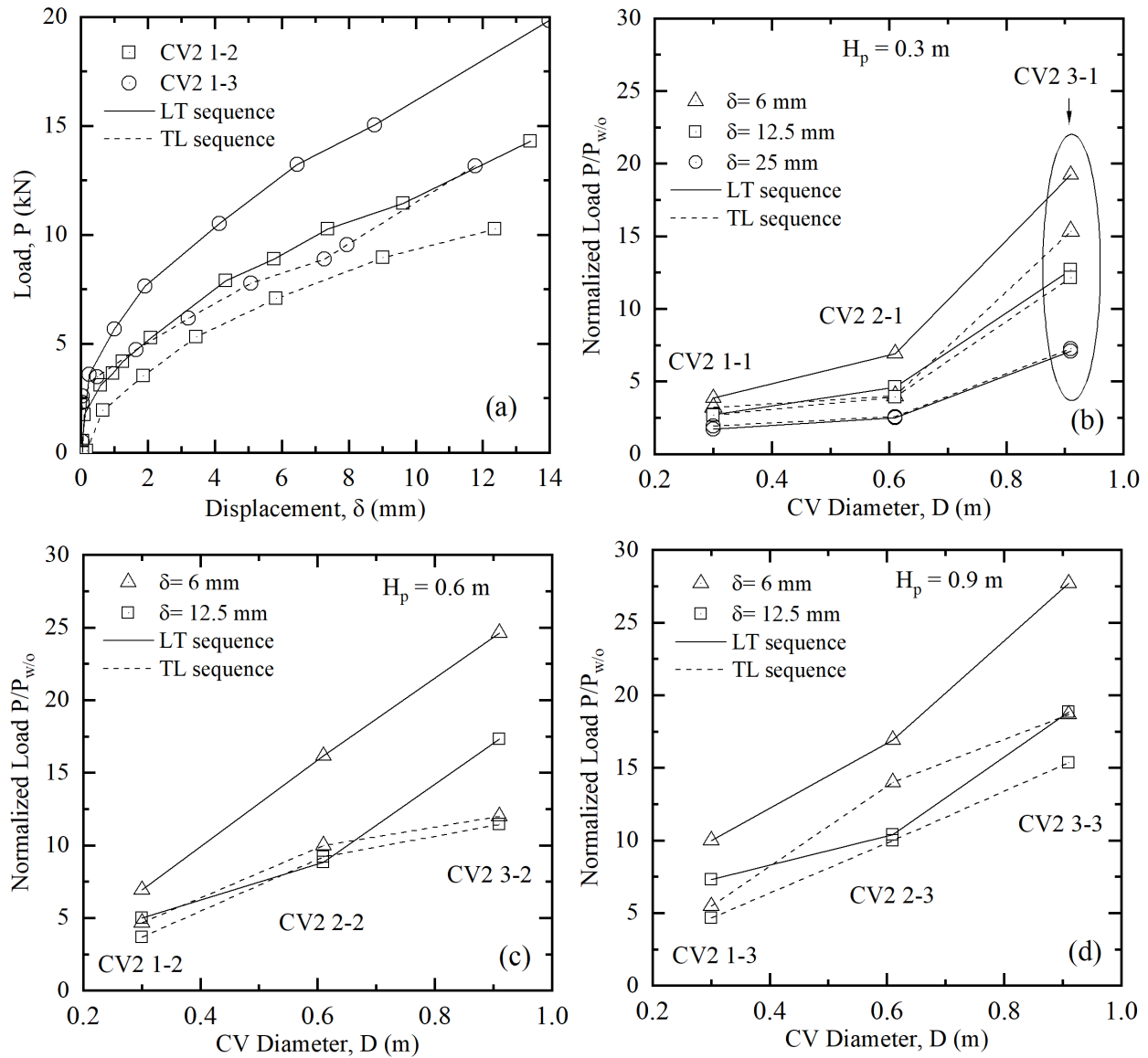


Figure 4.3: Two-piece Collar Vane: (a) comparison between the load sequences and (b-d) normalized load required to move pile head 6, 12.5, and 25 mm for LT and TL sequences.

To show the relative performance of the different CV2 geometries compared to the base case. It is necessary to normalize the load, $P$, required to move the HP head 6, 12.5, and 25 mm with the base case, $P_{wo}$. Then $P/P_{wo}$ is defined as the ratio between the load

applied in the HP with the CV installed over the load applied on the HP with no CV. Also, the load sequence is considered to analyze how this performance is affected by the torsional capacity. As an example, Figure 4.3(a) shows two different Collar Vane geometries tested with the two load sequences in each one. The dashed line is the TL case and it is below the results of the LT sequence. Figure 4.3(b) presents the normalized load $P/P_{wo}$ for the CV with $H_p$=0.3 m in the function of the CV diameter. From this figure, it can be deduced that there is a significant increase in capacity when the diameter changes from 0.6 m to 0.9 m (CV2 2-1 to 3-1, respectively), it required less normalized load to move the pile 6 mm when the pile is subjected to torsional loads first. However, it takes the same amount of normalized load to move the piles 12.5 and 25 mm regardless of the load sequence. Figure 4.3(c) shows the case for $H_p$=0.6 m. The stiffness degradation was more noticeable in CV2 3-2 compared to the cases CV2 1-2 and CV2 2-2. This may be attributed to a higher disturbed area of soil during the torsion due to the increasing diameter reducing the stiffness of the soil once is subjected to lateral loads. This is in agreement with the studies performed by Thiyyakkandi *et al.* (2016); Herrera (2001); Hu *et al.* (2006) where it was found that laterally loaded drilled shafts subject to torque can experience a significant reduction in lateral capacity. The same behavior is observed in Figure 4.3(d) for CVs with $H_p$=0.9 m.

Based on the results, when combining the torsional and lateral loads is shown to have a reduction in the lateral performance after performing the torsional test. Figure 4.4 shows the amount of lateral capacity reduced after the application of torsion for two different displacements. The lateral capacity ratio $P_{TL}/P_{LT}$ is the ratio between the load required to move the pile 12.5 and 25.4 mm in the TL sequence to the LT sequence. In the majority of cases, the lateral capacity was reduced by the previous application of torsion up to a value of 70%. The slender CVs (i.e., CVs with small $D$ and high $H_p$) presented the most reduction in the lateral capacity due to the soil being highly disturbed when the torque was
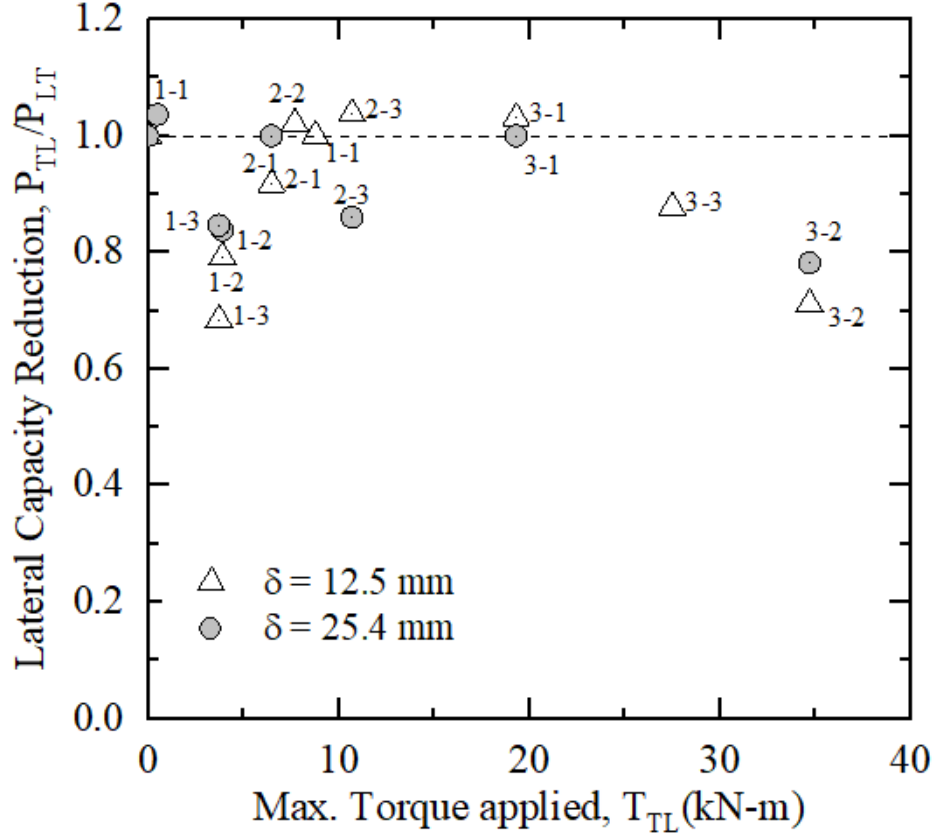
Figure 4.4: Lateral resistance reduction factor due to torsion using CV2.

applied. Moreover, the CVs with a bigger diameter also showed a considerable reduction in the lateral capacity.

### 4.2.2 Strain Gauge Results and Analysis

The bending moment along the HP shaft installed in phase one (2021) was determined from the strain values measured at the strain gauge levels as:

$$M_i = \frac{E_p I_p \varepsilon_i}{R} \tag{4.1}$$

where, $M_i$ = bending moment at depth $z$; $E_p I_p$ = flexural rigidity of pile; $R$ = shaft radius; $\varepsilon_i$ = bending strain at level $i$. To verify the accuracy of the strain gauge responses it is worth noting that the measured bending moment, for the case of the helical pile without the Collar Vane at the top-level strain gauge, is approximately equal to the applied

moment on the pile (i.e., applied load, $P$, multiplied by the distance between where the load is applied to the location of the top-level strain gauge, ($\sim$0.23 m). The top-level strain gauge is located 0.15 m below the HP flange and the load point was applied at 0.08 m above the HP flange. Figure 4.5 shows the comparison of the measured bending moment using the top-level strain gauge and the theoretical bending moment ($M_t = 0.23 \cdot P$). A perfectly linear relationship with a slope of $\sim 1.0$ is obtained for both tests of the helical pile without the Collar Vane meaning that the strain gauge's measurements are accurate.
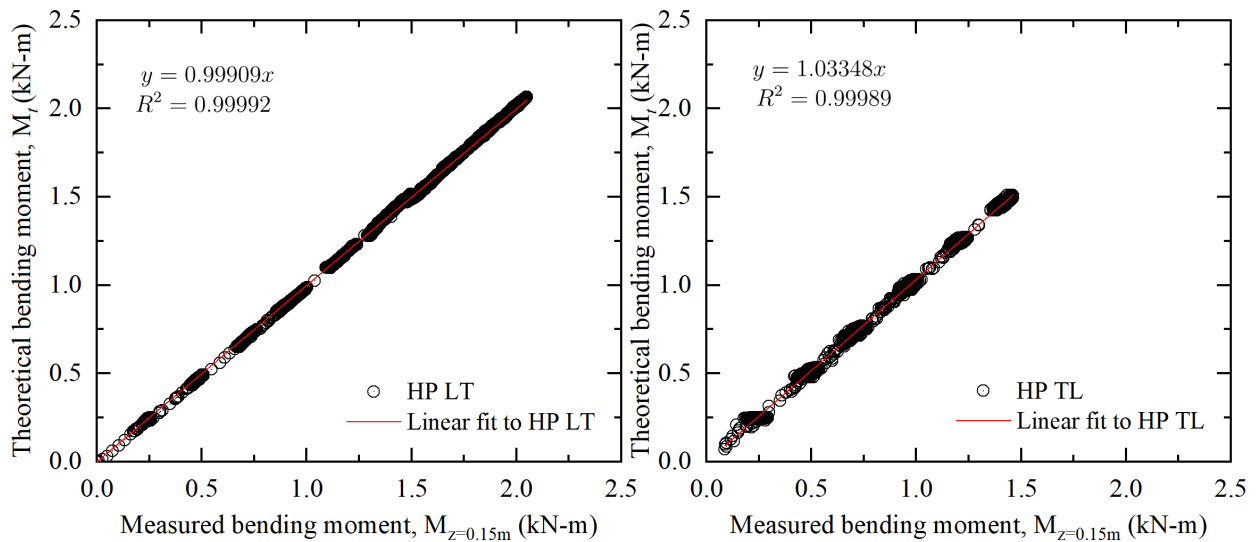


Figure 4.5: Theoretical vs Measured bending moment at the top-level strain gauge for the helical pile without Collar Vane: (a) HP LT and (b) HP TL.

The distributions of bending moment at different displacement values (and loads) are shown in Figure 4.6. The moment profile shows some patterns: i) the maximum bending moment takes place within the CV portion; ii) the bending moment increases almost linearly within the CV prismatic section suggesting that the CV is not interacting with the round shaft and load transfer mechanism occurs at the HP flange in the top; iii) there is a drastic bending moment reduction in the HP shaft due to the CV. The theoretical bending moment values for the case when there is no CV, are shown as closed symbols just for the first strain gauge level. As depth increases, this value will increase exceeding the pile's elastic bending capacity ($\sim$12.5 kN-m). The implementation of the CV reduces the need

for a large-diameter pipe shaft making this small-diameter HP more efficient. Figure 4.7 shows a comparison of the bending moment profiles for different CVs subjected to the same amount of load.
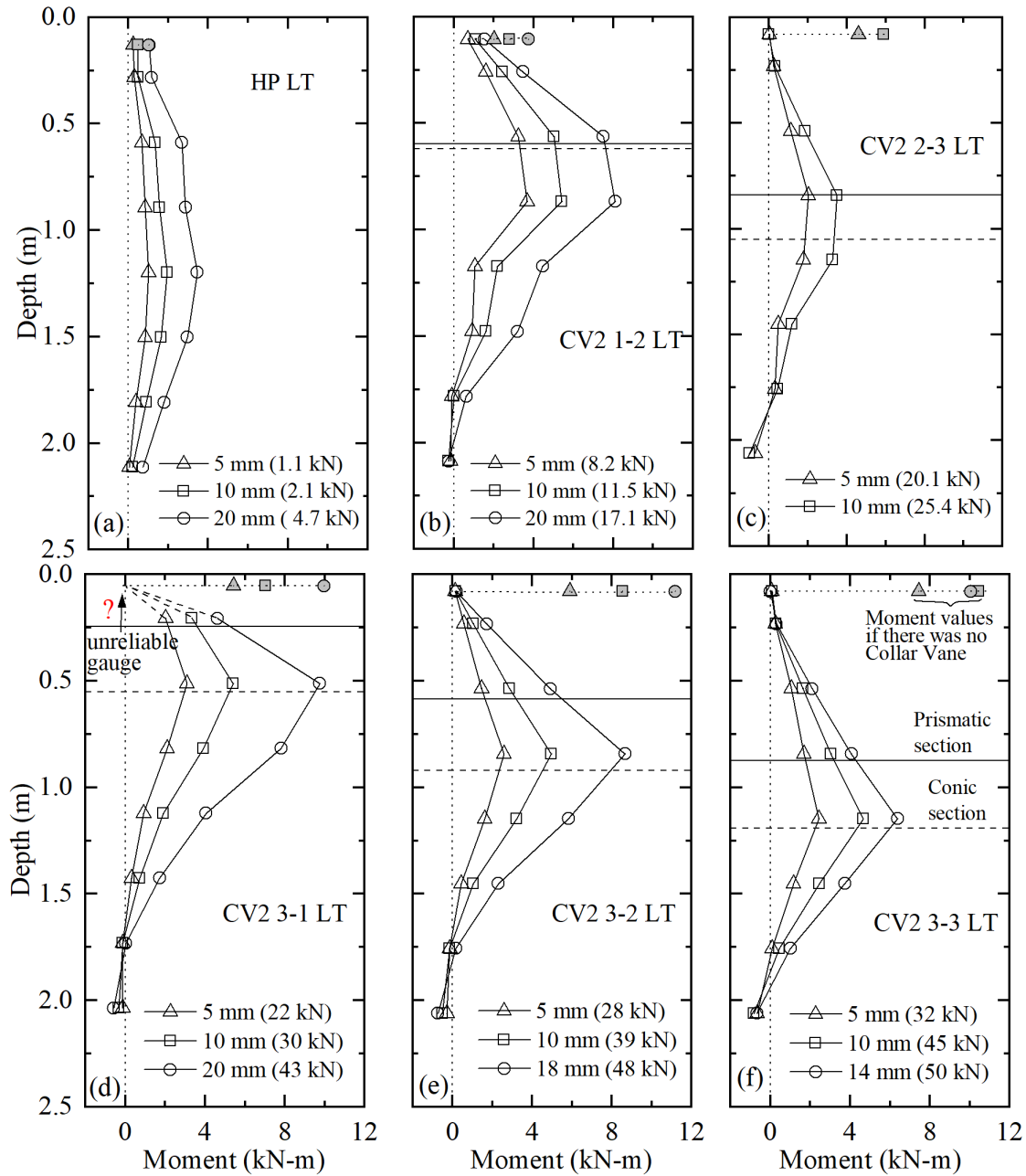


Figure 4.6: Bending moment profiles for load sequence LT: (a) HP without Collar Vane and (b-f) HP with Collar Vane.
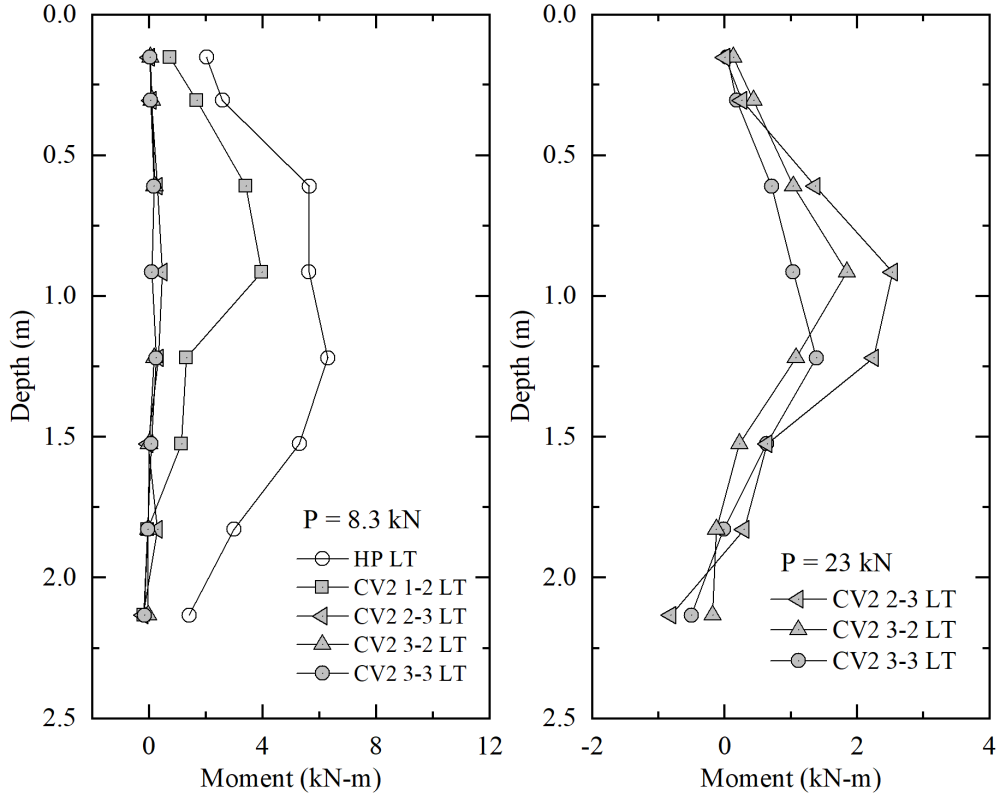
Figure 4.7: Bending moment profiles comparison for different CVs and same applied load in cohesive soil.

To compare the relative CV moment reduction, a ratio between the theoretical bending moment value if there was no CV, $M_t$, with the measured bending moment at the first strain gauge level, $M_{z=0.15\ m}$, is shown in Figure 4.8 in the function of the CV diameter for three different sets of CV heights. $M_{z=0.15\ m}$ is obtained directly using the measurements from the strain gauge located approximately 0.15 m below the HP flange for a pile head displacement of 5 mm, whereas the theoretical $M_t$ value is obtained by multiplying the force required to move the CV times the distance from the strain gauge to the applied load ($M_t = 0.23 \cdot P$). In general, is observed that as the geometry of the CV increases, the reduction factor also increases. For a CV with $D = 0.3$ m, the reduction factor obtained for $H_p = 0.30, 0.61$, and $0.91$ m is 1.1, 2.8, and 4.3, respectively. For a CV with $D = 0.61$ m, the reduction factors are 1.9, 6.4, and 13, respectively. And with a $D = 0.91$ m the reduction factors are 41.6 and 103 for $H_p = 0.61$ and $0.91$ m, respectively. This means that

in the upper portion of the HP with a CV2 3-3, it can effectively reduce the bending moment by almost 100 times for that specific pile head displacement ($\delta$=5 mm). The reduction factor is not calculated for the CV2 3-1 since the strain gauge data is unreliable. The reduction in bending moment is achieved by limiting the displacement of the HP since it is required to apply a large amount of force to mobilize the resistance in the soil.
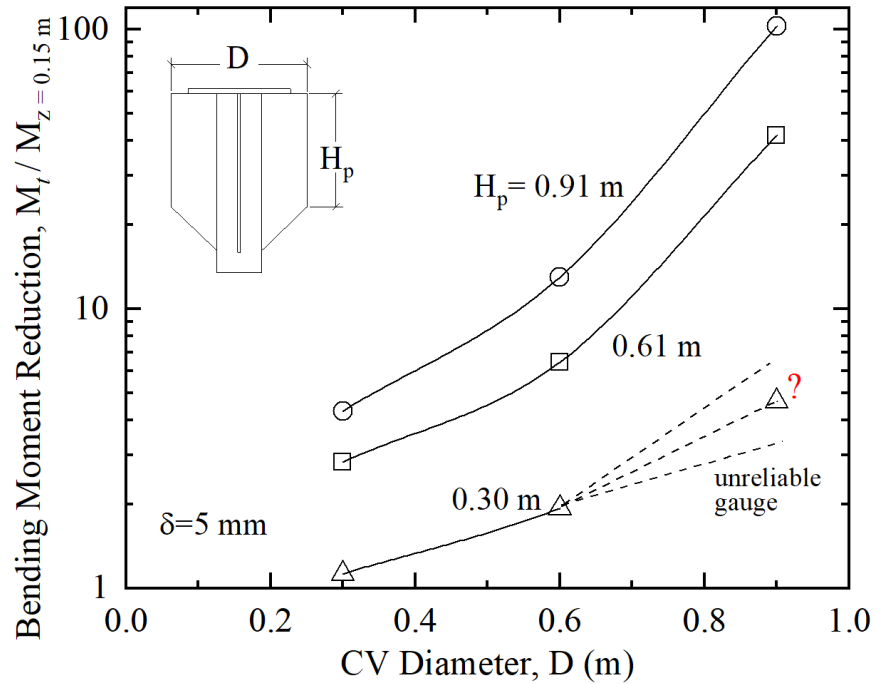


Figure 4.8: Two-piece Collar Vane LT sequence: bending moment reduction for most top strain gauge (z=0.15 m).

The linear increment in moment values within the CV observed in Figure 4.6, suggests that the shear force in the HP may be constant implying that the transfer load mechanism is carried through the HP flanges at the top. The recorded data from the strain gauges are used to quantify this shear force value along different locations of the HP. The shear forces, $V$, can be obtained by differentiating the moment data with respect to depth using the Euler-Bernoulli beam theory relationship (Hetényi, 1946):

$$V(z) = \frac{dM(z)}{dz} \tag{4.2}$$

For discrete moment measurements along the length of the HP shaft and, taking into account the linear increment of the bending moment, it is possible to compute different interpretations of shear forces in the HP shaft at different consecutive locations of strain gauges. Only the strain gauges within the prismatic section will be considered to compute the interpreted shear force using the two-point difference formula:

$$V_{ij} = \frac{M_j - M_i}{z_j - z_i} \qquad (4.3)$$

where, $M_{i,j}$: bending moment obtained using Equation (4.1), and $z_{i,j}$: the distance between two consecutive strain gauges. From the free body diagram shown in Figure 4.9, it is possible to compute the Vane Resistance, $V_R$, as $V_R = P - V_{ij}$. This Vane Resistance parameter is the difference between the applied load, $P$, and the shear force in the pile shaft, $V_{ij}$, which is obtained from the strain gauges. Hence, is possible to show the amount of force that is carried by the Collar Vane in the function of the HP head displacement.

Figures 4.9(a-b) show the Vane Resistance, $V_R$, and the Applied Load, $P$, versus pile head deflection for a different set of Collar Vane sizes. Figure 4.9(a) presents the lateral response for the Collar Vanes with diameter $D$=0.91 m and a different set of $H_p$. Figure 4.9(b) shows the lateral response for the Collar Vane with height $H_p$=0.91 m and a different set of $D$. Depending on the CV height, it is possible to have more than two strain gauges within the CV prismatic portion. For instance, CV2 3-1 only has two strain gauges within the prismatic portion whereas CV2 3-3 has four as shown in Figure 4.6(a) allowing for calculating different interpretations of shear force depending on the CV size. Figure 4.9(a) presents the $V_R$ curves for the CV2 3-2 LT plotted in a shaded region composed with two curves, whereas CV2 3-3 has four strain gauges which makes it possible to obtain three different interpreted shear force values. These different ranges of measurements are shown as a range that is increasing in the function of the displacement. As the applied force increases, the CV is not carrying the load applied uniformly and in some portions, the CV may be in contact with the pile shaft. For instance, in the CV2 3-3 top portion (i.e., where
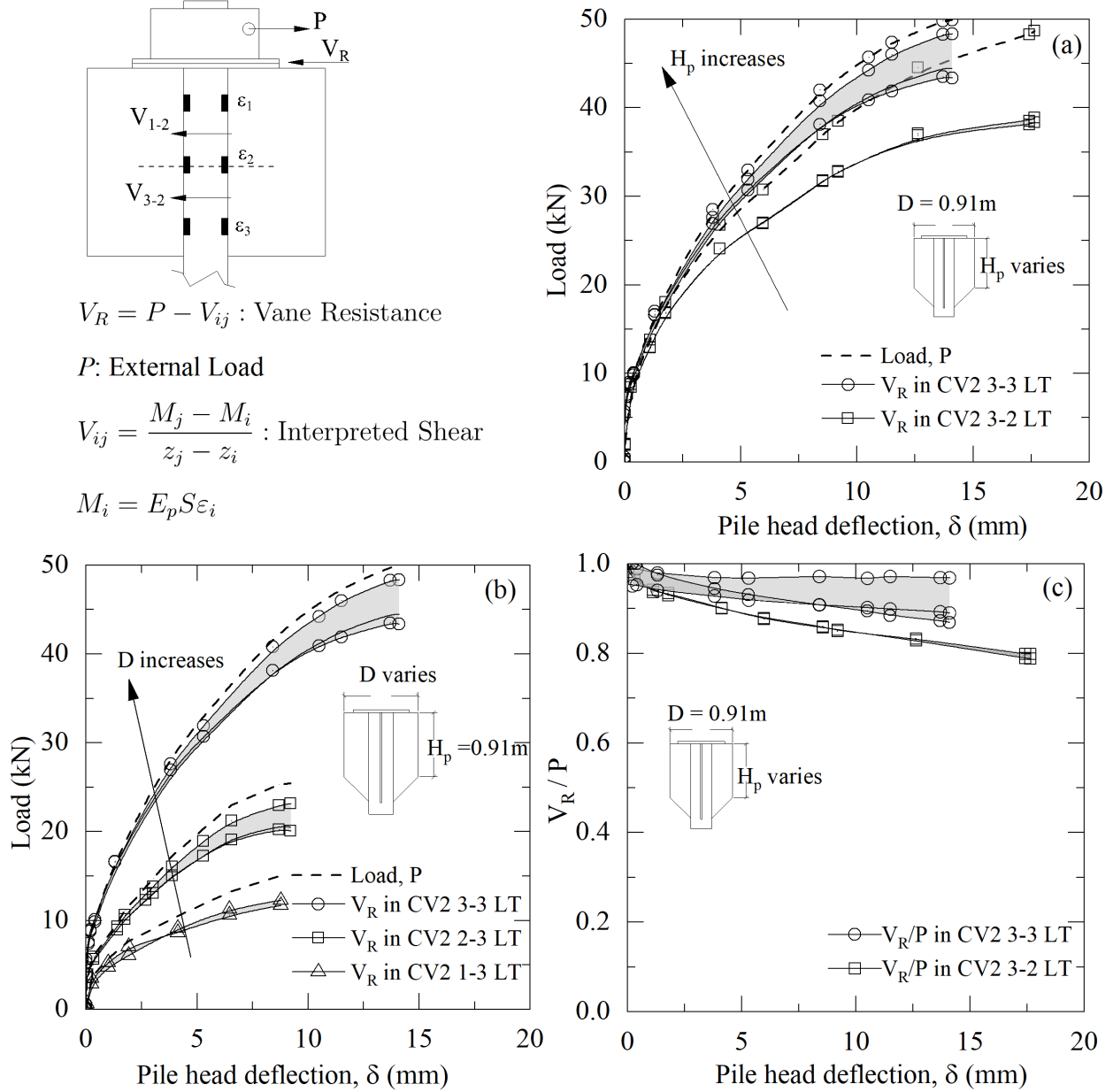
Figure 4.9: Load and Vane Resistance comparison from different interpretations of shear force in the HP shaft. (a) CV with the same diameter $D = 0.91$ m and varying $H_p$; (b) CV with the same height $H_p = 0.91$ m and varying $D$; and (c) Vane resistance to applied load ratio.

$\varepsilon_1$ and $\varepsilon_2$ are located), the $V_R$ is closer to the applied load (i.e., dashed line) and the CV2 3-3 bottom portion (i.e., where $\varepsilon_3$ and $\varepsilon_4$ are located) the continuous line is relatively distant from the applied load. This means that the upper portion of the CV is where more resistance to displacement is occurring compared to the CV bottom portion. Moreover, in
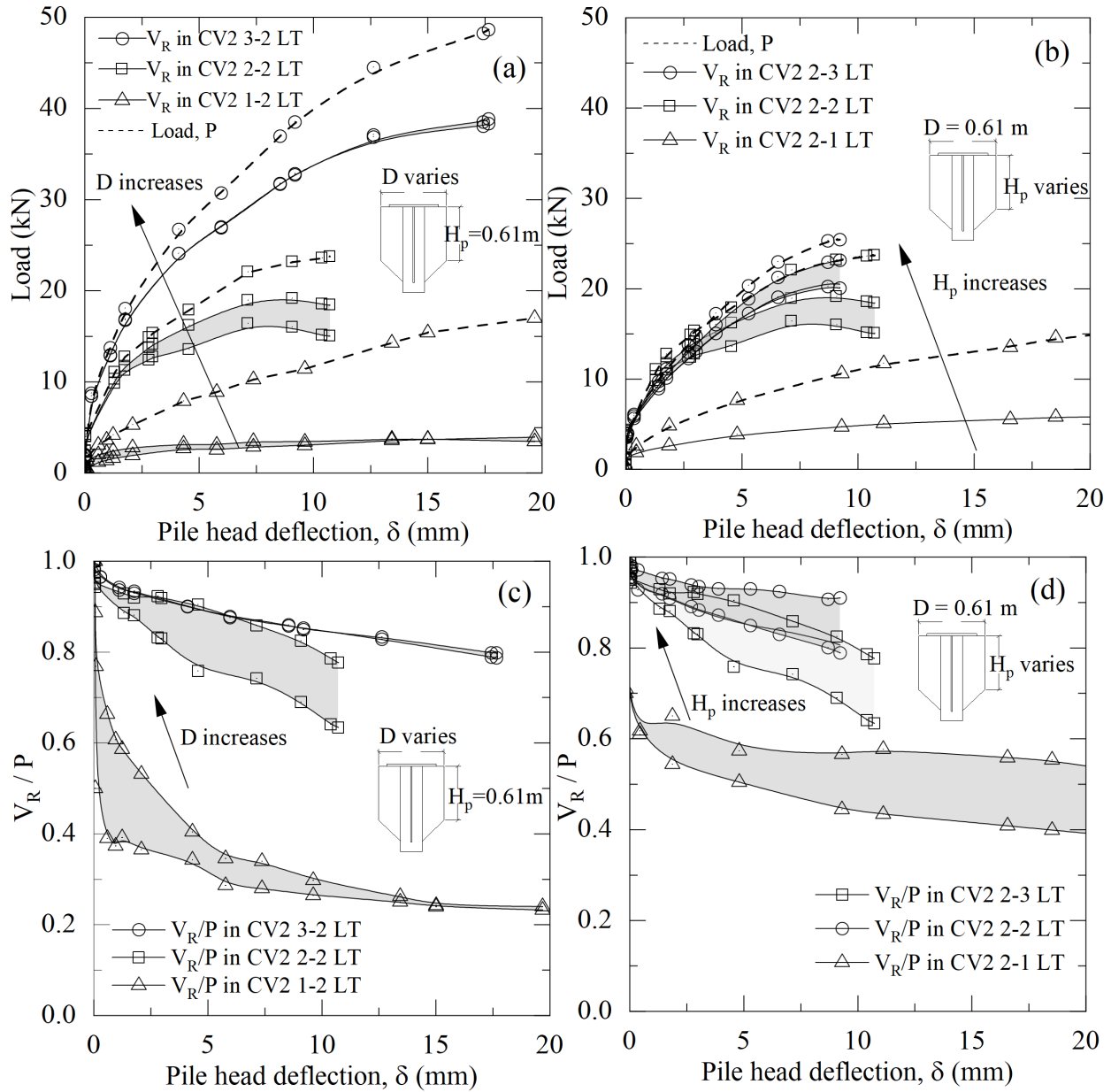
Figure 4.10: Load and Vane Resistance comparison from different interpretations of shear force in the HP shaft. (a) CV with the same height $H_p = 0.61$ m and varying $D$; (b) CV with the same diameter $D = 0.0.6$ m and varying $H_p$; and (c-d) Vane resistance to applied load ratio for above cases.

the case of the CV2 3-2 and 1-3, interpreted values of shear force are similar and the $V_R$ region tends to be a single curve: the CV is not in contact with the pile shaft and the load transfer mechanism occurs solely at the flange where the CV-Pile system is structurally connected using bolts. Furthermore, Figure 4.9(b) shows that when the CV height is

constant, the applied load is relatively close to $V_R$ values unlike Figure 4.9(a), whereas $H_p$ decreases, $V_R$ becomes closer to the shaded region. To highlight the performance of the CV relative to the external loads, Figure 4.9(c) shows the ratio $V_R$ to the applied load, $P$. The ratio for the cases when the diameter is $D = 0.91$ m. The CV2 3-3 range varies between 0.87 and 0.98 suggesting that the CV is carrying almost all the applied load and for the CV2 3-2 LT, this ratio is 0.78 when the displacement is more than 15 mm.

Similarly, this analysis is performed for the CVs with a $H_p$=0.61 varying the diameter, and with a $D$=0.61 varying the $H_p$ as shown Figure 4.10(a-b), respectively. For the CV2 1-2 in Figure 4.10(a), the applied load $P$ is relatively higher than the $V_R$, at 3 mm of displacement the CV was carrying the same amount of load even when $P$ was increasing. The same observation is observed in the CV2 2-1 LT in Figure 4.10(b), $V_R$ was constant after a pile displacement of 10 mm. As a result, the ratio $V_R/P$ is low compared with those shown in Figure 4.9(c), CV2 2-1 is only supporting 0.23 times the applied load at a displacement of 12.5 mm, and CV 2-1 supports between 0.45-0.6 times the applied load as shown in 4.10(c-d), respectively. The CVs that most effectively support the applied load, in this case, are CV2 3-2, CV2 2-3, and CV2 2-2.
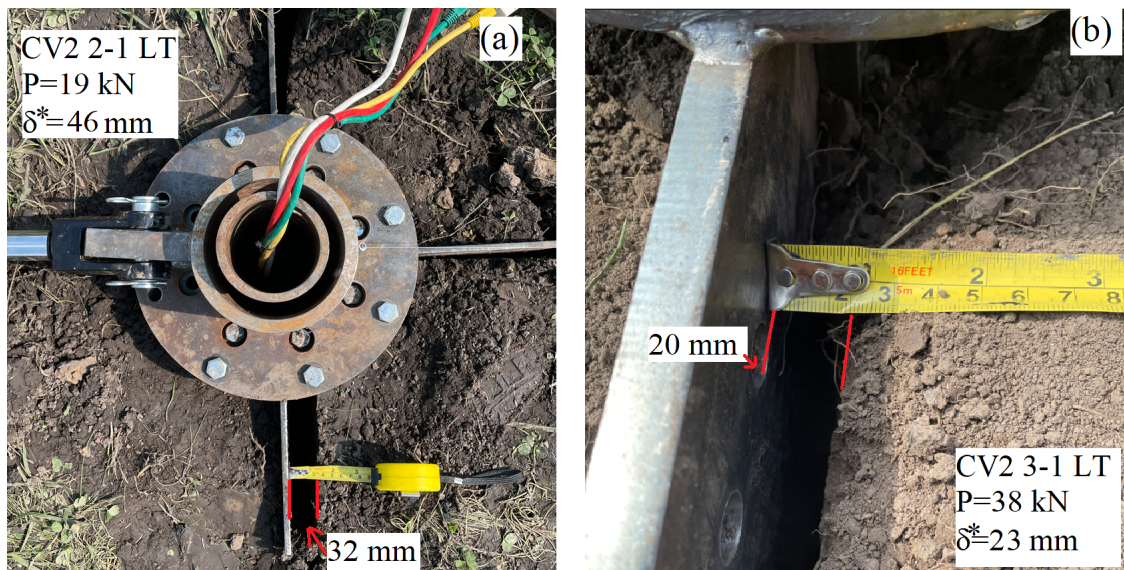


Figure 4.11: Collar Vane displacement during the lateral load test.

During the lateral load test, it was observed a gap between the CV blades and the soil adjacent to them increased with the amount of load applied. Figure 4.11(a) shows the case for the CV2 2-1 LT where a gap between the CV-soil was approximately 32 mm. The photo was taken after reaching the last increment point with a load of 19kN and unloading displacement of $\delta^* = 46$ mm. This displacement is the value obtained when the pile was being unloaded after reaching the maximum loading point as shown in Figure C.5(a). This difference between the gap and the recorded displacement may be attributed to the soil movement due a stress relief as a result of the CV blade displacement. On the other hand, the CV2 3-1 LT was subjected to higher loads and this difference is almost non-existent. The main difference with the previous scenario may be attributed to the soil condition that was relatively in a dry scenario and this relaxation was more notable in the humid condition.

### 4.2.3 Torsional Loading

The torsional loading test commenced with incremental rotation of 0.2° at the loading arms. Once a rotation of 1° was reached, the specified incremental rotation was increased to 0.5° until 5° of total rotation, and finally, the rotation interval was increased to 4° until failure criteria were met. However, for the first series of torsional tests performed in phase one in 2021, the torsional capacity of the two-piece Collar Vane only was subjected to failure in the CVs 1-1, 1-2, 1-3, and 2-1. This is because these CVs have low torsional resistance and failed at low torques. Moreover, the objective of this phase was to study the lateral capacity reduction after applying a torsional load that did not disturb the soil completely. For the second phase in 2022, torsional loads were applied at their maximum capacities for both CV prototypes. The CV2 was retested again under only high torsional loads whereas the CV1 was only tested in the LT sequence. Thus, is expected to have a reduction in the torsional capacity after applying lateral forces to the one-piece Collar Vane.
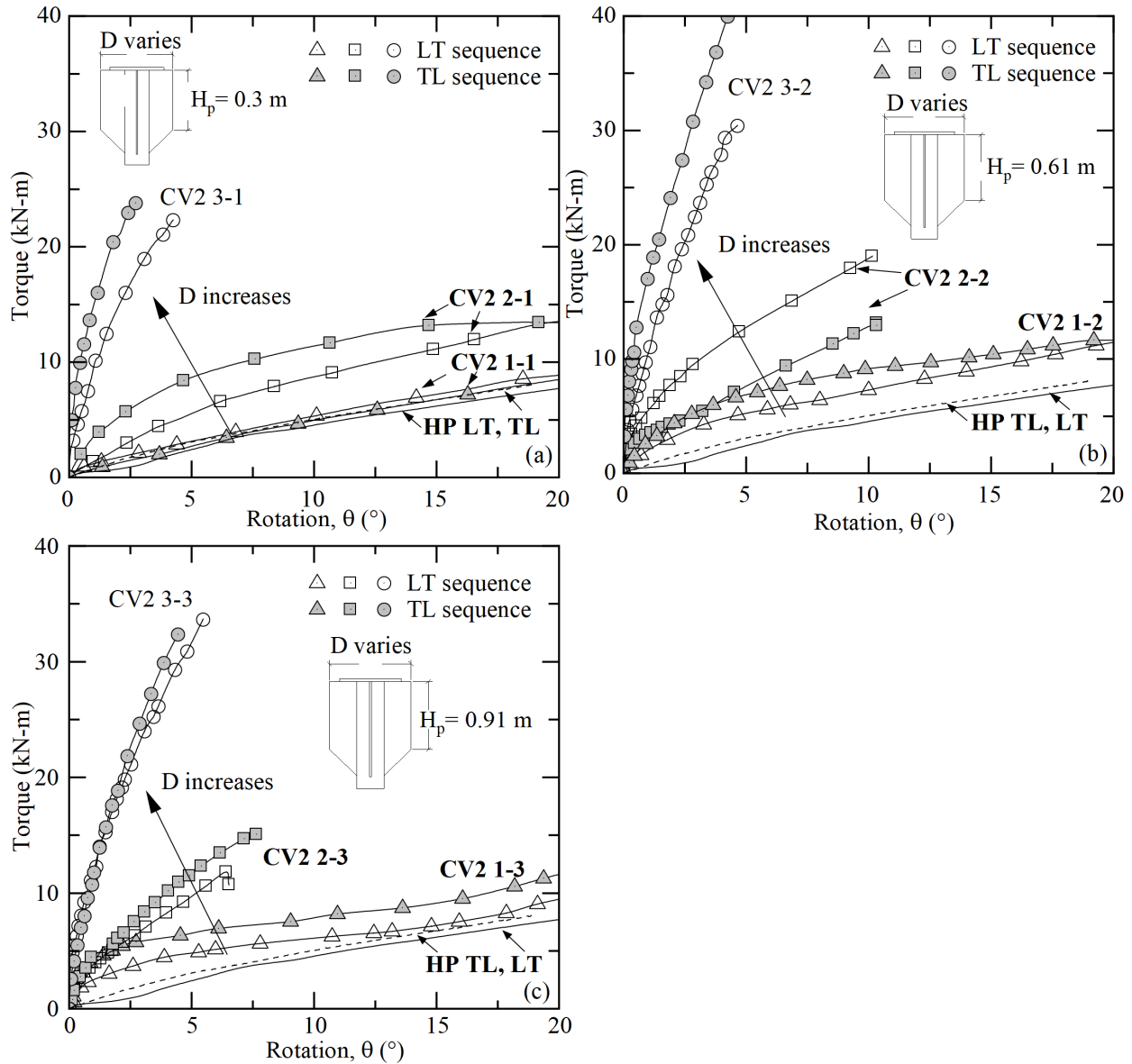
Figure 4.12: Unprocessed Torque vs Rotation curves from phase one (2021) tests: Two-piece Collar Vane, CV2, tested in both load sequences, LT and TL.

Unprocessed (HP's torsional resistance not extracted) phase one results (i.e., CV2 with low torsion loads applied) are shown in Figure 4.12. The CV2 is shown for both load sequences, LT and TL, as well as the case of the helical pile without the Collar Vane shown as a reference. The figure depicts the difference in load sequence showing a decrement in capacity when the CV was subjected to lateral forces before applying torque. The torsional capacity of the CV2 1-1 is exactly the same as the HP without Collar Vane, and CV2 1-2

and 1-3 provide little resistance compared with the base case. The nomenclature shown in bold represents the rotation measured from the string pots located in the loading arm. The rotations shown using CV2 3-1, 3-2, and 3-3 are measured from the Collar Vane blades and these results were taken from the 'three blades side' (Figure 3.2). Measurements from the loading arm might not be a real representation of the CV torsional capacity since it was found that the loading arm and the Collar Vane blades are not rotating uniformly. The slack from these tests is shown in detail in Figure 4.13(a), in the field test; and Figures D.8(c-d), D.10(a-d), D.12(a-d), and D.14(a-f), using the recorded data. The loading arm presents higher rotations than the Collar Vane at the same torque value. Moreover, even the Collar Vane blades are not rotating uniformly. Torsional results for the CV2 are presented in Appendix D showing that the loading arm, one CV blade side, and three CV blade sides are rotating at different rates due to how the CV blades and loading arm are structurally connected. However, the purpose of Figure 4.12 is to show the decrement in torsional capacity after applying a lateral load. This is true in all scenarios except in CV2-2 TL because one of the load cells at the moment arm failed during the torsional test and the torque shown is computed using the working load cell multiplied by two which may not be a real representative value of the torque applied. The torsional degradation due to the lateral load is in agreement with the findings from Tawfiq (2000); Herrera (2001); Hu *et al.* (2006) where it was found that the lateral displacement of in drilled shafts caused by the lateral loading influences the torsional resistance.

Figure 4.14 presents the unprocessed torque vs rotation curves for the test performed in phase two where the CV2 was subjected to high torsional loads (until failure criteria were met) and the CV1 was implemented for the first time. For both CVs, is shown the results from both blades sides highlight the uniform rotation of the CV1 whereas the CV2, in general, shows a slack in rotation between the one-blade (1b) and three-blade (3b) side showing a stiffer response in the one-blade side. This slack was also found in the rotation of the CV blades with respect to the loading arm. This difference in torsional stiffness can be

106
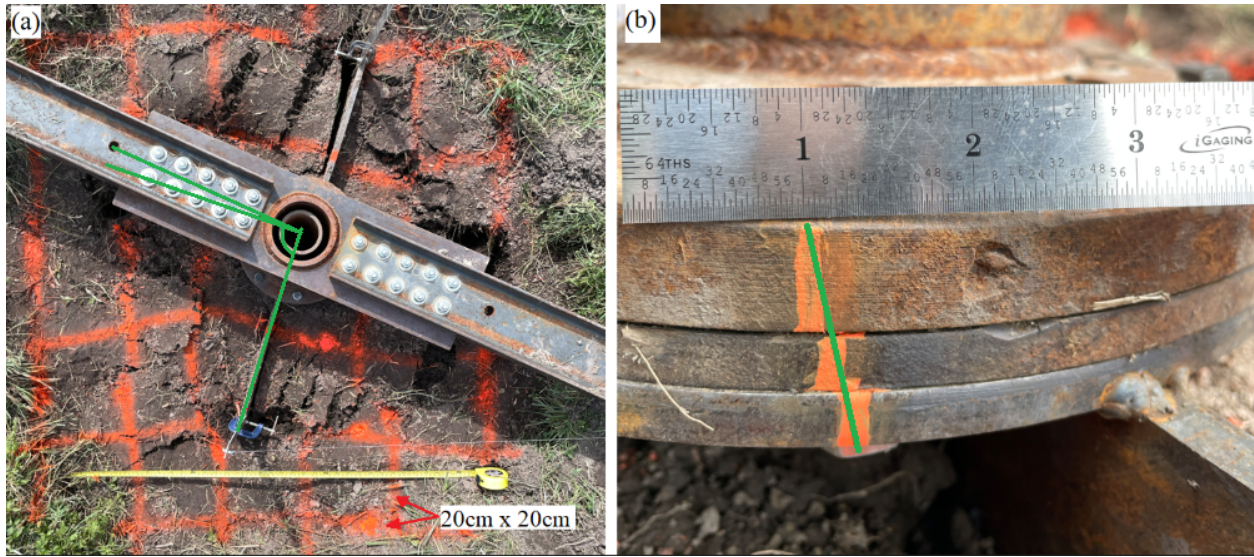
Figure 4.13: CV2 3-2 T: (a) difference in rotation between CV blades and loading arm, and (b) slack in the HP flange contributing to the additional rotation in the loading arm.

attributed to the CV-HP flange-loading arm interface (i.e., drilled holes in the flanges were bigger than the diameter of the bolts) which leads to additional deflections of the loading arm as shown in Figure 4.13(b). Furthermore, the slack between the CV2 blades can be
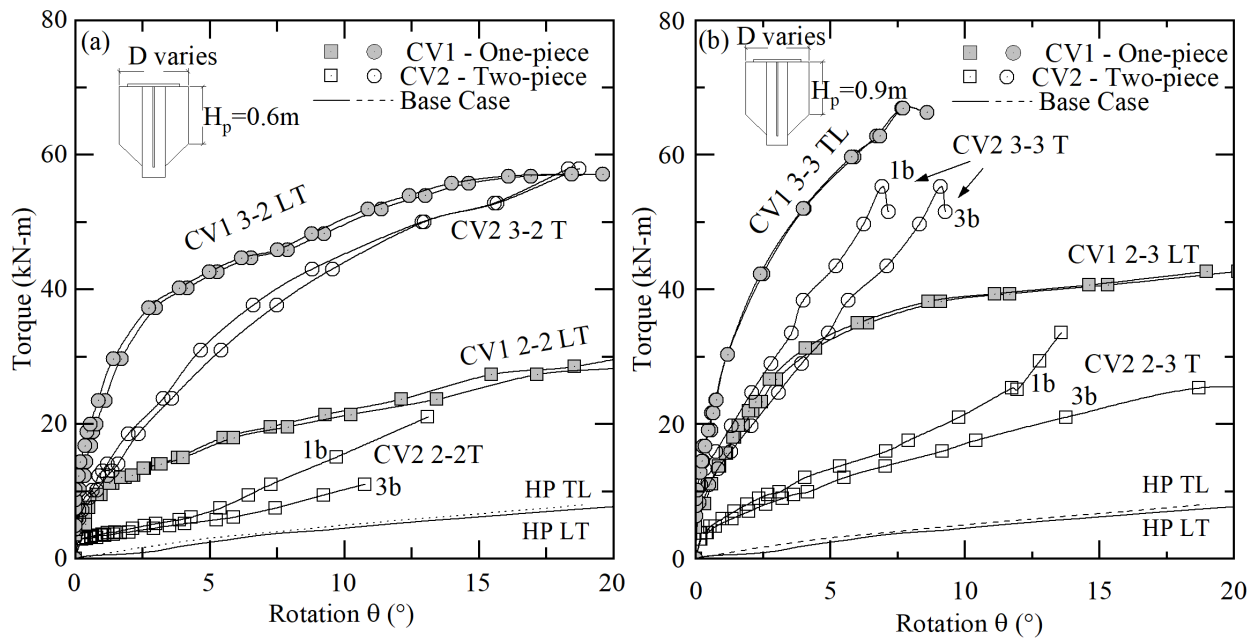


Figure 4.14: Unprocessed Torque vs Rotation curves from phase two (2022) tests: CV2 and CV1.

attributed to the connection in the HP flange: since only the three-blade side of the CV2 was connected directly to it, and the one-blade side was only connected to the three-blade side as shown in Figure 3.2(a). Hence, the rotation of the CV2 sections were not uniform. These differences in rotation between the two sections occurred because the one-blade side was not connected directly where the torque was being applied (HP flange) and the mobilization of the slack of the HP flange and three-blade side system occurred before starting the mobilization of the one-blade side. Thus, three different responses for each element (loading arm, three-blade, and one-blade side) were obtained for the same amount of torque as shown in Figure 4.15(a). To overcome the non-uniformity rotation of the Collar Vane, a single-piece Collar Vane (CV1) was manufactured and tested. It was observed that the slack between the loading arm-CV1 blades was still occurring but the Collar Vane blades were rotating at the same ratio making it possible to measure an accurate representation of the torsional capacity of the Collar Vane. Figure 4.16(b) depicts the CV1 3-2 LT at the last load increment showing the CV blades in a collinear line meaning that the blades rotated at the same ratio and also, the blades are perpendicular to the loading arm, meaning that they had the same rotation. However, the measured data shown in Figure D.13(a) shows that there was an initial slack between the loading arm and the CV1 3-2 blades and just at the last incremental stage these two elements reached equilibrium due do the failed soil.

Since the torsional tests were performed with the HP attached, and it was shown that HP provides a low, but not negligible, torsional resistance, it is necessary to isolate the performance of the CV by subtracting the contribution of the HP in torsion to have a representative torsional capacity of only the Collar Vane. This isolation process consisted in fitting a polynomial curve in function of rotation to the base case and use this function to subtract resistance provided by the HP to the unprocessed curves. The isolated Collar Vane torsional resistance results are shown in Figure 4.17(a-c). Only the measurements from the three-blade side are shown as a representative performance of the CV2 since this

108
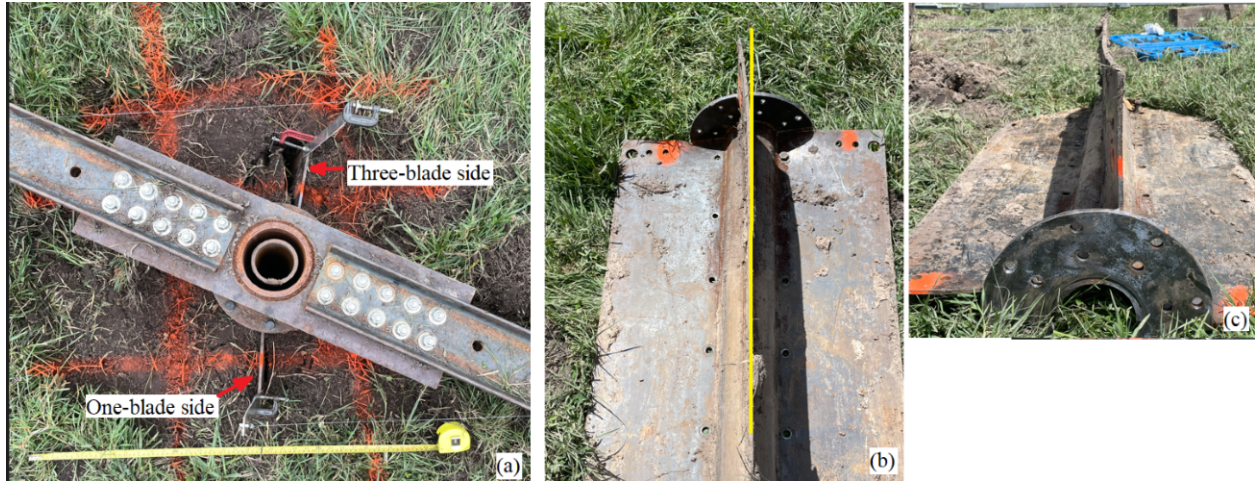
Figure 4.15: CV2 2-3 T: (a) CV blades at maximum torsional load and (b-c) three-blade side yielded blades.
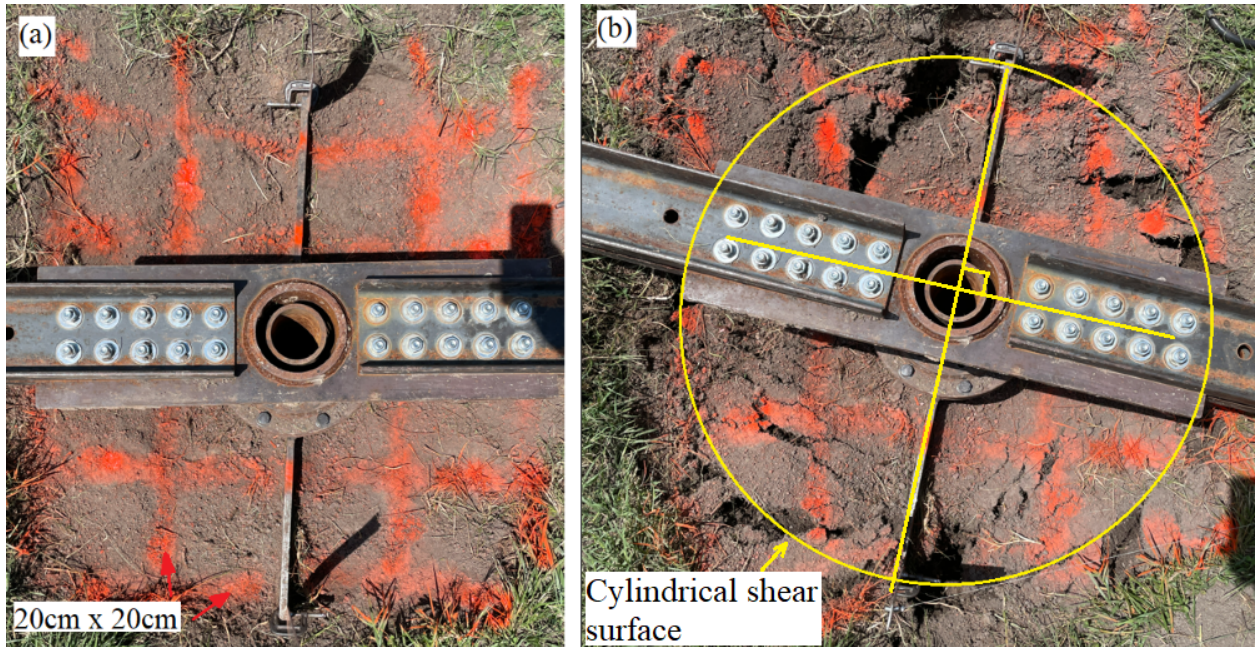


Figure 4.16: CV1 3-2 LT: (a) initial position before starting the test and (b) blades positions at maximum torsional load.

side was connected directly to the loading arm. The general trend in the results is that the CV transitioned from an initial stiff response to a softer response followed by a full mobilization of the ultimate torsional resistance, $T_u$. The increase in $T_u$ is highly influenced by the diameter more than the height. CV1 presents a noticeably stiffer response compared to CV2. Results suggest that the mobilization of the torsional resistance in the single-piece

CV requires more torque since the four blades behave as a single element that is connected directly to the HP top flange. However, the mobilization of the shear strength with respect to depth might not be uniform if the blades do not behave as a rigid element. In some cases, the CV with small thickness and high $H_p$ (i.e., CV2 2-2 and 2-3) was observed that the shallow portion of the blades was bent with respect to the bottom as shown in Figure 4.15, suggesting that the mobilization of shear strength was not developed at its maximum values in some portions of the CV. Furthermore, it is important to mention that the results presented for the CV1, although were not subjected to a "clean" torsion test, may be used as the representative torsional maximum capacity of the CV1.

The torsional response of the Collar Vanes CV2 1-2 and 1-3 (i.e., two-piece Collar Vanes with diameter $D = 0.30$ and $H = 0.61$ m; $D = 0.30$ and $H = 0.91$ m, respectively) plotted in Figures 4.17(b-c) shows that transitions from stiff to softer response occur between rotations 0.2-0.5° with an ultimate resistance, $T_u$, equal to approximately 4 kN-m. Results for the CV2 with a $D = 0.6$ m is observed that torsional capacity for the CV2 2-2 is $T_u$=9 kN-m and; for the CV2 2-3 is $T_u$=19.7 kN-m. For the same set of CVs with just one-piece CV, the $T_u$ were 22 and 35 kN-m, respectively. The increment of $T_u$ by just making the CV a single piece is almost twice. However, that increment of $T_u$ due to CV design was not observed in CVs 3-2: both CVs were reaching almost the same torsional resistance value. During the test, it was observed that the rotation of both sections of CV2 3-2 were moving at the same ratio meaning that there was no rotational slack in this particular CV. This could be attributed to the soil conditions when the CV2 3-2 was tested: a significant amount of precipitation was observed before starting the test which may have influenced the soil strength allowing the two-piece CV to shear the soil uniformly. $T_u$ for both CVs 3-2 prototypes was approximately equal to 50 kN-m. The last CV tested in the cohesive soil was CV 3-3, results in Figure 4.17(c) show that in both cases there is a sudden drop in Torsion caused by breakout failure in the bolts at the HP flange in shear caused by the torsional loading. In all scenarios described so far, the bolts used to connect
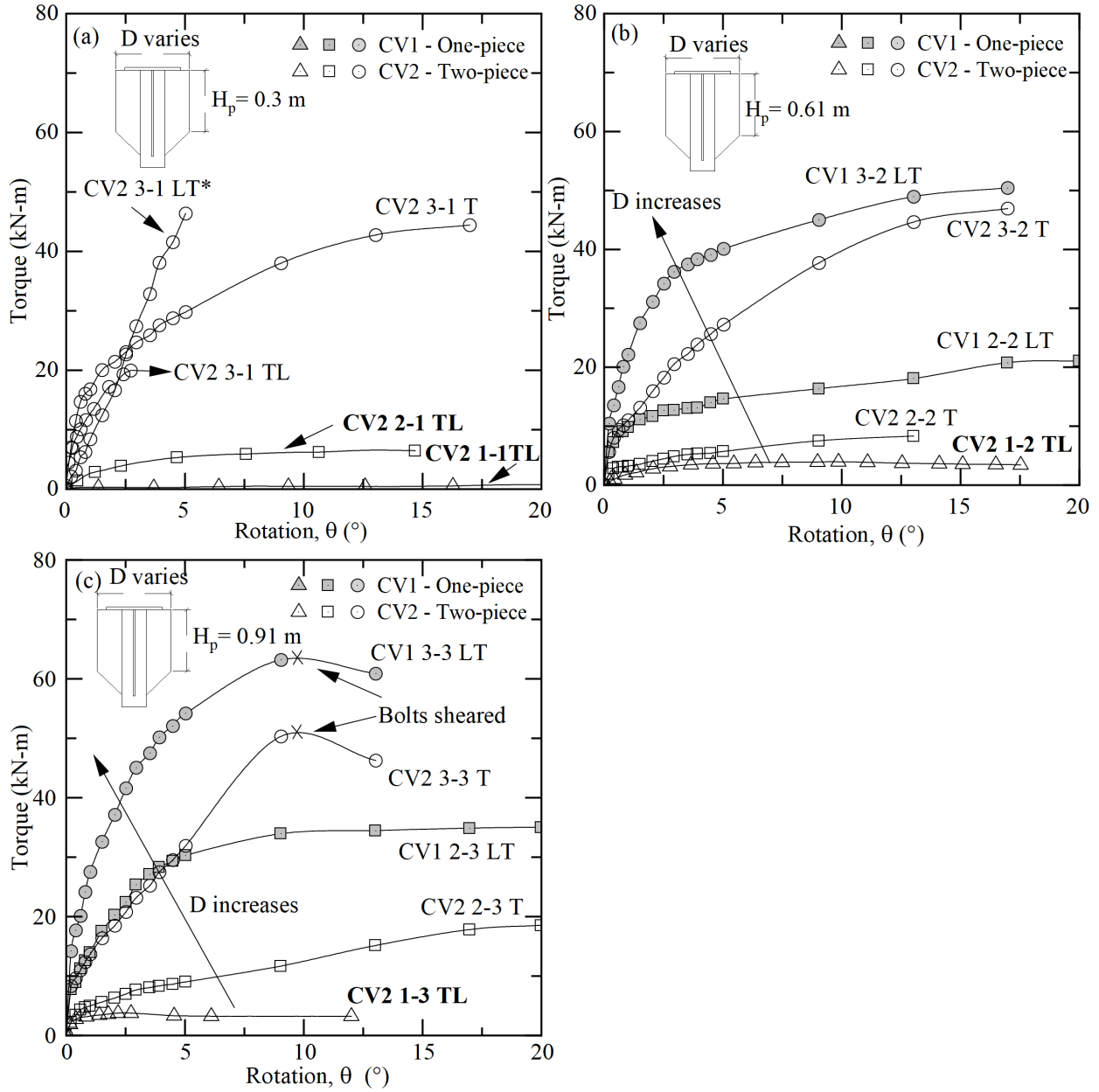
Figure 4.17: Processed Torque vs Rotation curves for CV1 and CV2 in cohesive soil.

the CV to HP and the loading arm were a set of Grade-5 1/2-13X1-1/2 bolts. The mobilized torsional resistance reached in the CV2 3-3 was approximately equal to $T = 50$ kN-m. Furthermore, to test the CV1 3-3, a better set of Grade-8 1/2-13X2-1/2 bolts was used and the mobilized torsional resistance reached was approximately equal to $T = 63$ kN-m before shearing the bolts through the Loading arm-HP Flange-CV system.

Consequently, a need for a better pin connection through the system to support the torsional loads is required to fully mobilize the torsional resistance for this particular CV.

Failure in the torsion test can be defined based on load or displacement-based criteria. For instance, it can be defined that failure has occurred when the rate of shear stress increase is zero with additional rotation. (i.e., $dT/d\theta = 0$). However, this may correspond to large rotation angles which could be difficult to achieve in load tests. Li *et al.* (2017) used a hyperbolic curve fit technique to extrapolate the torque-rotation behavior beyond the measurements and to estimate the torsional resistance. Furthermore, based on serviceability criteria, FDOT recommends a 15° twist angle as a failure criterion for traffic sign supports (Hu *et al.*, 2006; Aguilar, 2018). Moreover, none of the load tests that were examined achieved a 15° twist angle. For this study, an angle of 4° will be used for the cyclic torsional analysis.

## 4.3 Performance in Sand

Lateral and torsional responses in the granular conditions are shown in this section. The tests were performed in the second phase in 2022 using the one-piece Collar Vane. Only the Lateral-Torsional sequence was considered for this scenario. Thus, the torsional capacity may be affected by the lateral loads applied previously.

### 4.3.1 Lateral Loading

The load vs deflection curves in the granular soil are plotted in Figure 4.18. Just like the base case in the cohesive soil, the HP with no CV presented almost a linear behavior attributed to the slenderness of the HP and the gap between the pile and soil observed after the installation. The CV1 2-3 LT S was only loaded with 48 kN due to the maximum capacity of the tie-rods cylinders being reached. Thus, it was necessary to implement the hollow plunger cylinders to test the remaining CVs. The response of the HPs with CV presents a nonlinear behavior. HPs were loaded to a maximum of 70 kN, which
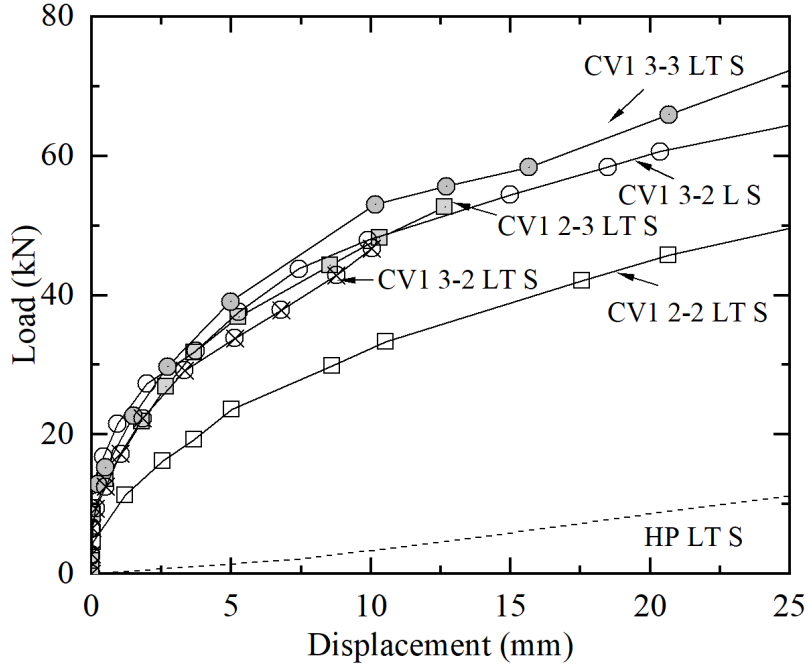
Figure 4.18: Lateral vs Deflection curves for CV1 in granular soil.

corresponded to maximum deflections of about 25 mm. Unlike the CV1 2-2 LT S, the other CVs had a similar response with only the CV1 3-3 LT S showing a slightly better performance. The response of CV1 2-3 and 3-2 in both were almost identical.

Table 4.2: Lateral interpretation criteria for granular soil.

| Method | Interpreted failure load (kN) | |
|---|---|---|
| | McNulty (1956) | Walker & Cox (1966) |
| Definition | 6.25 mm pile head displacement | 12.5 mm pile head displacement |
| HP LT S | 1.7 | 4.5 |
| CV1 2-2 LT S | 26 | 36 |
| CV1 2-3 LT S | 38 | 53 |
| CV1 3-2 LT S | 35 | - |
| CV1 3-2 L S | 38 | 50 |
| CV1 3-3 LT S | 42 | 55 |

113

The interpreted failure load is presented in Table 4.2 for the Collar Vane in the granular soil. The results presented for CV1 3-2 are shown twice since it was not possible to reach a 12.5 mm displacement on the first try using the tie-rod cylinders and the hollow cylinder had to be used for the following tests.
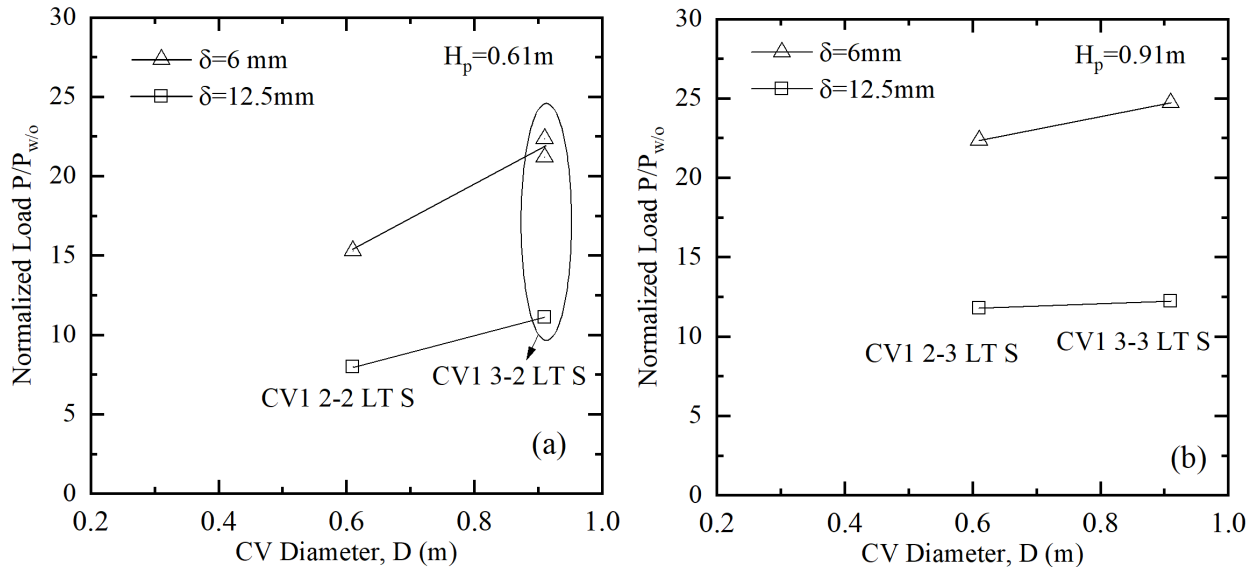


Figure 4.19: Normalized force required to move pile head 6 and 12.5 mm in granular soil. (a) CV with $H_p = 0.61$ m and (b) CV with $H_p = 0.91$.

The normalized force required to move the HP in the granular soil is shown in Figure 4.19. As depicted in the Load vs Deflection curves, increasing the diameter did not change the capacity of the Collar Vane with $H_p$= 0.91 m for the deflection $\delta = 12.5$ mm. The normalized load for these two CVs is approximately $P/P_{w/o}$ =11 which is almost the same as the CV1 3-2 LT S case.

The strain gauge analysis for the second phase was only performed in the CV1 tests in the granular soil. Figure 4.20 shows a comparison of the bending moment profiles for different CVs and the base case subjected to the same amount of load. Just as observed in the cohesive soil, the Collar Vane reduces the amount of bending moment in the helical pile shaft.
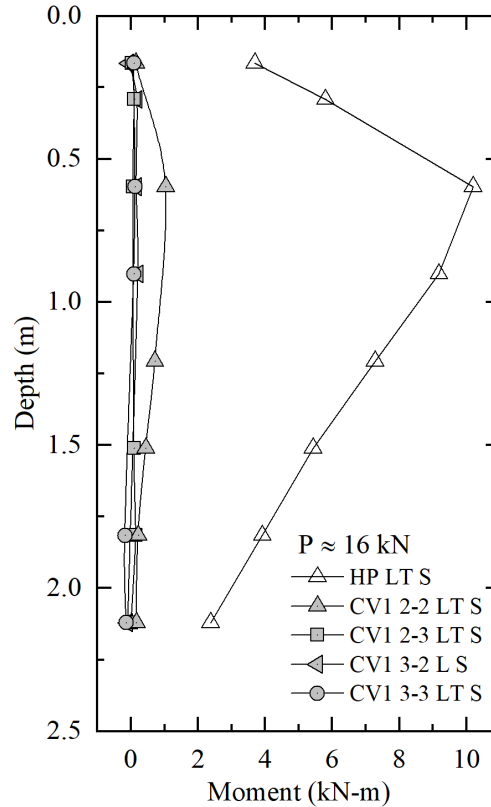
Figure 4.20: Bending moment profiles comparison for different CVs and same applied load in cohesionless soil.

### 4.3.2 Torsional Loading

The processed torsional response of the one-piece Collar Vane in the granular soil is presented in Figure 4.21. The four tests were measured from the Collar Vane blades and both sides showed the same rotation ratio (Figures D.7(d), D.9(d), D.13(d), D.15(d)) and the slack between the CV blades and the loading arm was not as noticeable as observed in the cohesive soil.

The CVs show a transition from stiff to softer response taking place between rotations 0.2-0.5°. The softening curve depends on the CV size and varies between 0.5 to 4° for the CV 2-2; 0.5-10° for the CV 2-3 and CV 3-2; and between 0.5-12° for the CV 3-3. In all scenarios it was possible to mobilize the maximum torsional resistance at 18 kN-m for the CV 2-2; 38 kN-m, for the CV 2-3; 48 kN-m, for the CV 3-2; and 69 kN-m, for the CV 3-3. It was observed that after reaching the peak torsional value, the CVs had a softening

115
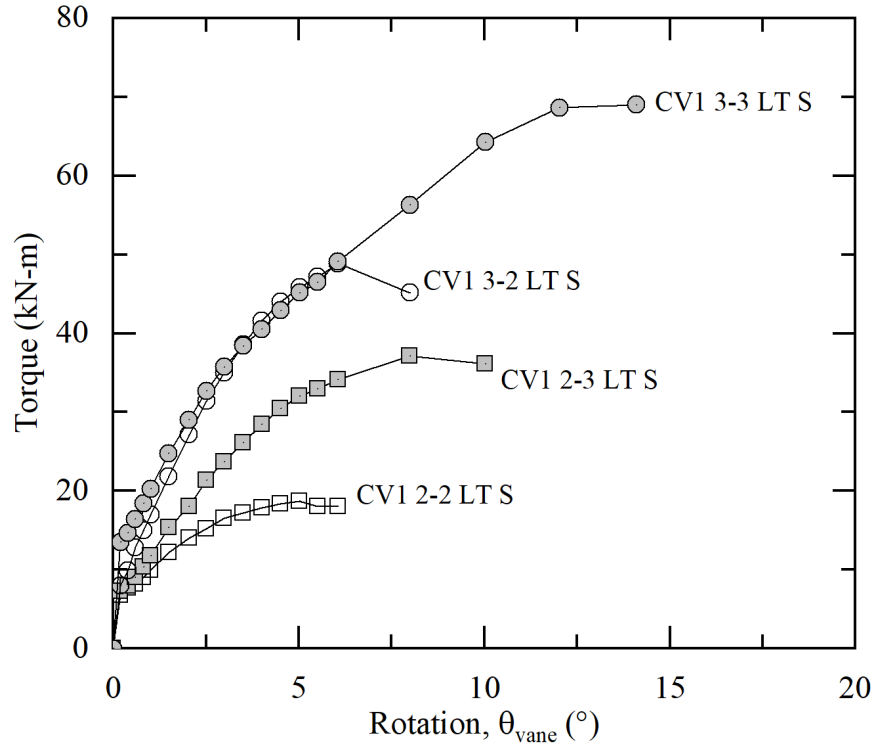
Figure 4.21: Processed Torque vs Rotation curves for CV1 in granular soil.

transition when the rotation was increasing but in the CV1 3-3 it was observed a secondary-hardening curve as shown in Figure D.15(c). The Collar Vanes generated a circumscribed cylindrical surface through the CVs blades surface after reaching failure shown in Figure 4.22(b). This idealized cylindrical surface will be used to estimate the torsional capacity of the Collar Vane in both site conditions in the following section.

## 4.4   Design Analyses and Considerations

### 4.4.1   Lateral Loading

AASHTO specifications for highway signs, luminaires, and traffic signals are based on the Allowable Stress Design (ASD) philosophy (AASHTO, 2009), whereas AASHTO (2012) uses a Load and Resistance Factors Design (LRFD) philosophy. In both documents is established that the embedment length for a foundation should be sufficient to provide vertical and lateral load capacities within a limited displacement. In AASHTO (2012) is

Figure 4.22: CV1 3-2 LT S under torsional loads in the sand.

suggested that to determine the lateral resistance a $p - y$ analysis should be performed. However, Broms' procedures (Broms, 1964b,a) can be also used for the estimation of the lateral capacity. Broms suggested an under-capacity factor of 0.7 and an overload factor of 2 to 3, which corresponds to a factor of safety between 2.86 and 4.29, respectively.

Colorado DOT Bridge Manual Colorado DOT (2020) presents a drilled shaft foundation design process for a cantilever sign structure that supports a sign panel attached to the horizontal support. It is important to note that this example focuses solely on the shaft foundation design and does not address the design of cover members or attachment methods. The design follows the LRFD Specifications for Structural Supports for Highway Signs, Luminaires, and Traffic Signals (AASHTO, 2015). The lateral resistance is calculated using a $p - y$ approach using LPile using as input the factored loads and moments at the top of the shaft due to wind loads and geotechnical parameters. In section 6.5 a brief example of a standard foundation element being subjected to lateral loads is shown using LPile along with an estimation of the torsional and axial capacity in two different soils.

### 4.4.2 Assessment of Torsional Resistance

Thiyyakkandi *et al.* (2016); Coriat & Frydman (2023); Nusairat *et al.* (2004) provide a summary of design methodologies for the torsional resistance of drilled shafts for different soil conditions. Although the side and tip resistance from a drilled shaft contributes to the torsional resistance, the major contribution is from the side (skin friction). The assumptions assumed to compute the torsional resistance in drilled shafts can be also applied to the Collar Vane since the assumption of a torsional contribution around a cylindrical failure surface can be applied in both cases. The expression commonly used to estimate torsional resistance due to skin friction for a constant diameter is

$$T_p = \frac{\pi}{2} D^2 H_p f_s \tag{4.4a}$$

For the Collar Vane conic portion, the torsional contribution is

$$T_c = \frac{\pi}{6} D^2 H_c f_s \tag{4.4b}$$

Thus, the nominal torsional capacity is given by

$$T_n = T_p + T_c \tag{4.5}$$

where, $f_s$ is the unit skin friction; $D$ is the CV diameter; $H_p$ and $H_c$ are the prismatic and conic CV height, respectively. Several authors have reported numerous design methods to estimate skin friction. The methods considered in this study are listed in Tables 2.3, 2.5, and 2.9. The unit skin friction can be estimated using variants of Tomlinson (1957) $\alpha$-method, for cohesive soils; $\beta$-method, for granular materials; or CPT-based methods for both soil conditions.

To evaluate the accuracy of the methodologies to estimate the torsional capacity of the Collar Vane, the capacity ratio, defined as the predicted capacity divided by the measured capacity is calculated and plotted with the mean, mean plus one standard deviation, and mean minus one standard deviation is presented in Figures 4.23 and 4.24.

Table 4.3: Comparison of measured and predicted torsional resistance in cohesive material. $\alpha$- and CPT methods.

| Method for torsional resistance | Torsional Capacity Collar Vanes (kN-m) | | | | | |
|---|---|---|---|---|---|---|
| | CV 1-2 | CV 1-3 | CV 2-2 | CV 2-3 | CV 3-2 | CV 3-3 |
| Measured using CV2 | 4 | 4 | 9 | 19 | 48 | 51[†] |
| Measured using CV1 | NA | NA | 22 | 35 | 50 | 63[†] |
| $s_u$ (FVST) | 13 | 20 | 59 | 86 | 201 | 59 |
| $s_u$ (CPT) | 15 | 22 | 68 | 98 | 163 | 230 |
| $s_{ur}$ (FVST) | 7 | 10 | 30 | 43 | 72 | 102 |
| $s_{ur}$ (CPT) | 7 | 11 | 32 | 46 | 66 | 107 |
| O'Neil *et al.* (1999) | 8 | 12 | 36 | 52 | 87 | 122 |
| Coleman & Arcement (2002) | 5 | 7 | 20 | 30 | 49 | 69 |
| Salgado (2010) | 2 | 3 | 9 | 14 | 23 | 32 |
| Loehr *et al.* (2011) | 6 | 9 | 27 | 39 | 65 | 91 |
| LCPC method (Bustamante & Gianeselli, 1982) | 3 | 5 | 14 | 20 | 33 | 47 |
| Aoki & Velloso (1975) | 4 | 6 | 17 | 24 | 41 | 57 |
| UIUC method (Alsamman, 1995) | 5 | 8 | 23 | 33 | 54 | 77 |
| Doan & Lehane (2021) | 4 | 6 | 18 | 26 | 43 | 61 |

**Note:** [†] torsional capacity not fully mobilized; $s_{ur}$ (CPT) is the sleeve friction from CPT.

Figure 4.23 presents the capacity ratio for Collar Vane in the cohesive material. The predicted torsion using the peak and residual undrained shear strength is also computed replacing the values into Equation (3.2). The average $s_u$ using the field vane shear test (FVST) and CPT are 150 and 172 kPa, respectively. The average remolded undrained strength, $s_{ur}$, using the FSVT and CPT is 76 and 80 kPa, respectively. When replacing the $s_u$ values into Equation (4.4a) the torsional capacity is overpredicted significantly since the CV blades are not rotating as a rigid body and therefore the mobilization of shear strength is not uniform. To account for this non-uniform mobilization, the remolded undrained strength is used. The $s_u$ from CPT was used in the $\alpha$-methods, the predictions show

Table 4.4: Comparison of measured and predicted torsional resistance in granular material. $\beta$- and CPT methods.

| Method for torsional resistance | Torsional Capacity Collar Vanes (kN-m) | | | |
|---|---|---|---|---|
| | CV 2-2 | CV 2-3 | CV 3-2 | CV 3-3 |
| Measured using CV1 | 18 | 36 | 50 | 69 |
| Touma & Reese (1974) | 1.5 | 3.3 | 4.2 | 8.2 |
| O'Neil *et al.* (1999) | 2.7 | 6 | 7.7 | 15.1 |
| Zelada & Stephenson (2000) | 3 | 4.8 | 6.2 | 12.1 |
| Coleman & Arcement (2002) | 5.6 | 12.6 | 16 | 31.5 |
| Stuedlein *et al.* (2014) | 3.4 | 7.6 | 9.6 | 18.9 |
| FHWA (2018) | 7.3 | 16.2 | 20.6 | 40.5 |
| LCPC method (Bustamante & Gianeselli, 1982) | 12.4 | 18 | 29.9 | 42.1 |
| Aoki & Velloso (1975) | 10 | 14.4 | 23.9 | 42.1 |
| UIUC method (Alsamman, 1995) | 29.5 | 42.6 | 70.8 | 99.9 |
| Doan & Lehane (2021) | 17.8 | 25.8 | 42.8 | 60.5 |

different trends: O'Neil *et al.* (1999) overpredicts for both CVs designs; Coleman & Arcement (2002) and Loehr *et al.* (2011) overpredicts for the CV2 but predicts good capacity ratio for the CV1, and Salgado (2010) underpredicts the capacity ratio for both CVs. Using CPT-based methods for cohesive soils, it shows that the LCPC method, Aoki & Velloso (1975) and Doan & Lehane (2021) presents in average good estimations of the torsional capacity whereas the UIUC method overpredicts for the CV2 and shows a reasonable good prediction for the CV1. In general, the majority of the methods present good predictions for the single-piece Collar Vane. Most of the scattered data correspond to the two-piece Collar Vane due to the impossibility of fully mobilizing the torsional resistance as shown in Figure 4.23 where for the same CV size always the CV1 had better predictions.

Figure 4.24 shows the capacity ratio for Collar Vane in the granular material. $\beta$ methods underpredict significantly the torsional capacity. The skin friction in granular soils
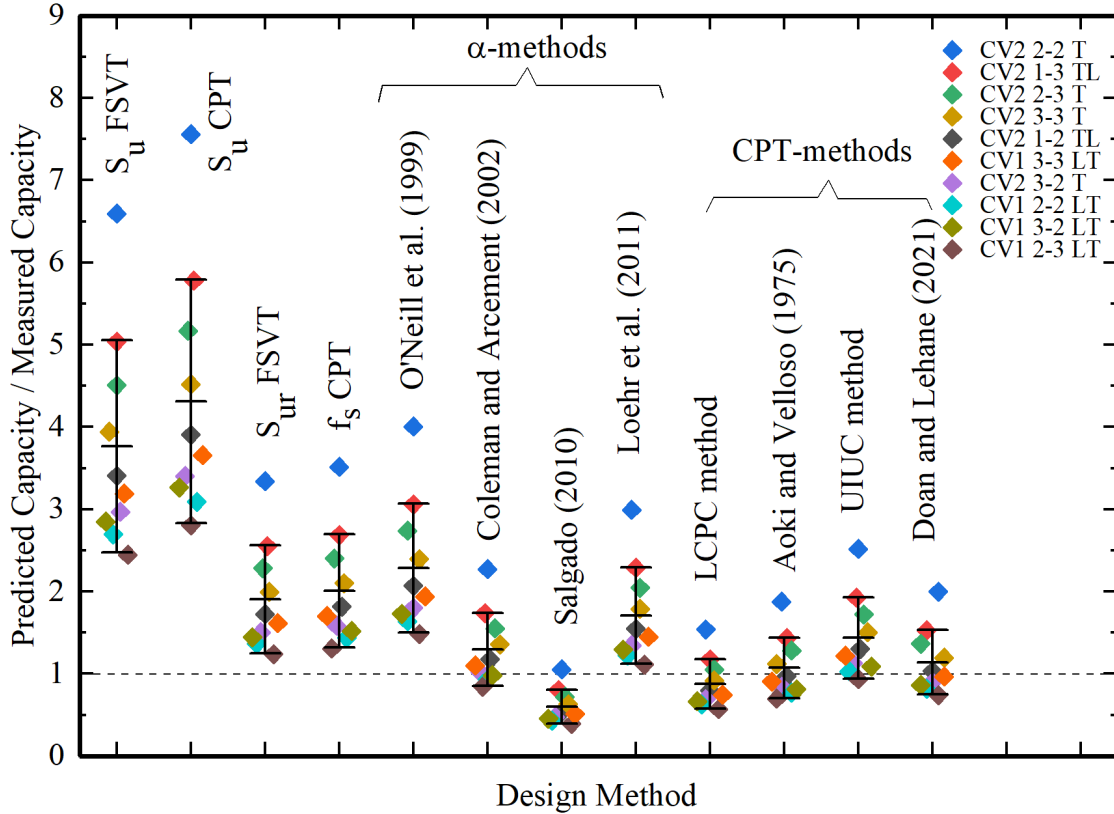
Figure 4.23: Mean ± standard deviation of the capacity ratios for cohesive soil.

is dependent on the factor $\beta$ and the effective vertical stress, $\sigma'_v$, at the midpoint of the element. Since the Collar Vane is relatively a short element, the effective vertical stresses values are low, making the $\beta$ values shown in Table 4.4 inappropriate for this type of element considering that the shown $\beta$-coefficient are suitable for longer elements (i.e., drilled shafts). CPT-based methods LCPC method and Aoki & Velloso (1975) also underpredict the torsional capacity by a 50% as well as Doan & Lehane (2021) method that slightly underpredicts with a mean value of 0.8. However, The UIUC method overpredicts the capacity with a mean value of 1.5. These observations indicate that UIUC and Doan's procedure offers significant advantages over the other methodologies for granular soil.

Rollins *et al.* (2005) performed uplift static loading tests in granular soils to calculate the $\beta$-coefficients at ultimate resistance and showed that the $\beta$-coefficient tends to be high when the embedment length is low and vice versa. For instance, $\beta$ for a 1 m long pile is
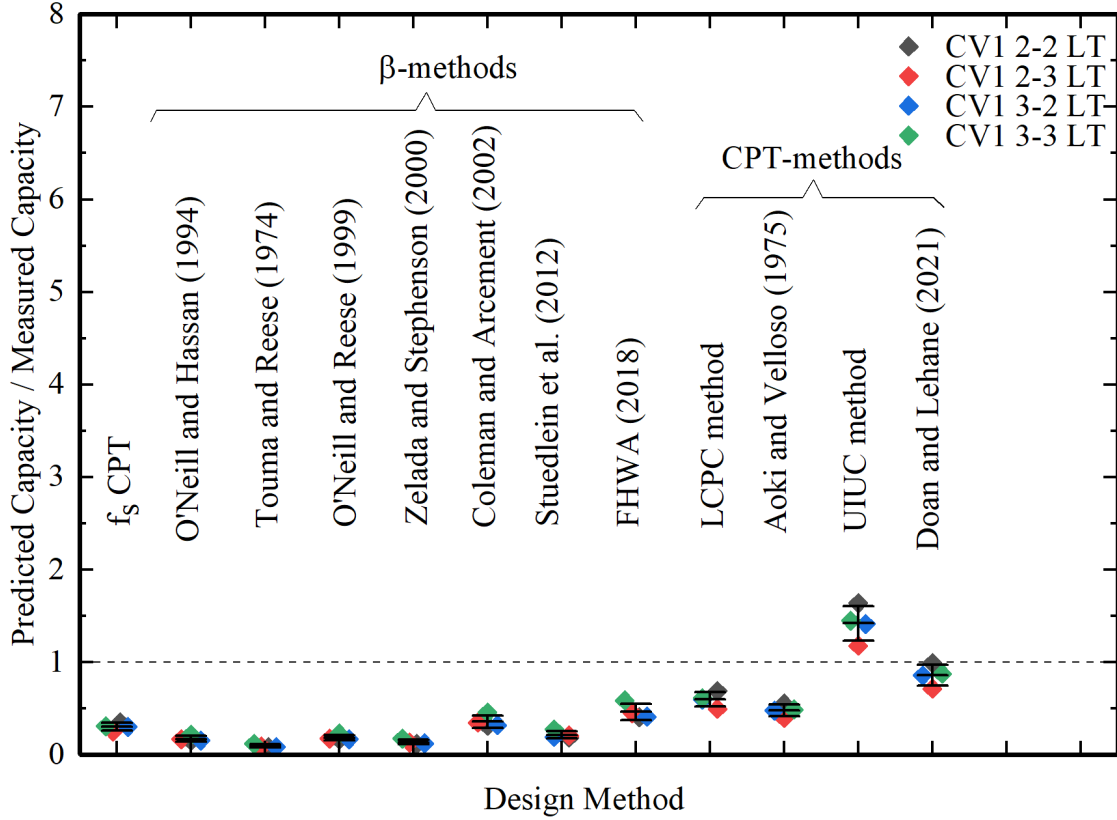
Figure 4.24: Mean ± standard deviation of the capacity ratios for granular soil.

between 4-5 based on the back-calculated data from the measured skin friction values (Fellenius, 2017) this can be verified in Figure 2.13 where it depicts the trend of the $\beta$ value in function of the pile length.

Table 4.5: Back-calculated $\alpha$ values for two-piece and one-piece CV; and $\beta$ for one-piece CV.

|  | CV 1-2 | CV 1-3 | CV 2-2 | CV 2-3 | CV 3-2 | CV 3-3 |
|---|---|---|---|---|---|---|
| $\alpha$ value CV2 | 0.26 | 0.17 | 0.13 | 0.19 | 0.29 | 0.22 |
| $\alpha$ value CV1 | - | - | 0.32 | 0.36 | 0.31 | 0.27 |
| $\beta$ value CV1 | - | - | 8.1 | 7.3 | 7.2 | 5.5 |

For the Collar Vane in a granular material, an appropriate $\beta$-coefficient would range between 5.5-8.1 as shown in Table 4.5, up to four times the $\beta$-coefficient proposed in Table 4.4, this may be attributed to different factors: the sand test pit consisted of compacted sand where at low confining stresses, dilation will yield higher friction angles (Giampa &

Bradshaw, 2018). Moreover, the compaction of the sand and the insertion of the CV increases the initial lateral stress. Finally, under constant normal stiffness conditions, when dense sand experiences shear, the shear band will undergo significant dilation, particularly at low confining pressures. This leads to an additional increase in lateral stress (Lehane *et al.*, 2005). The back-calculated $\beta$-coefficients from the Collar Vane test are shown in Figure 4.25 along with other cases of study.
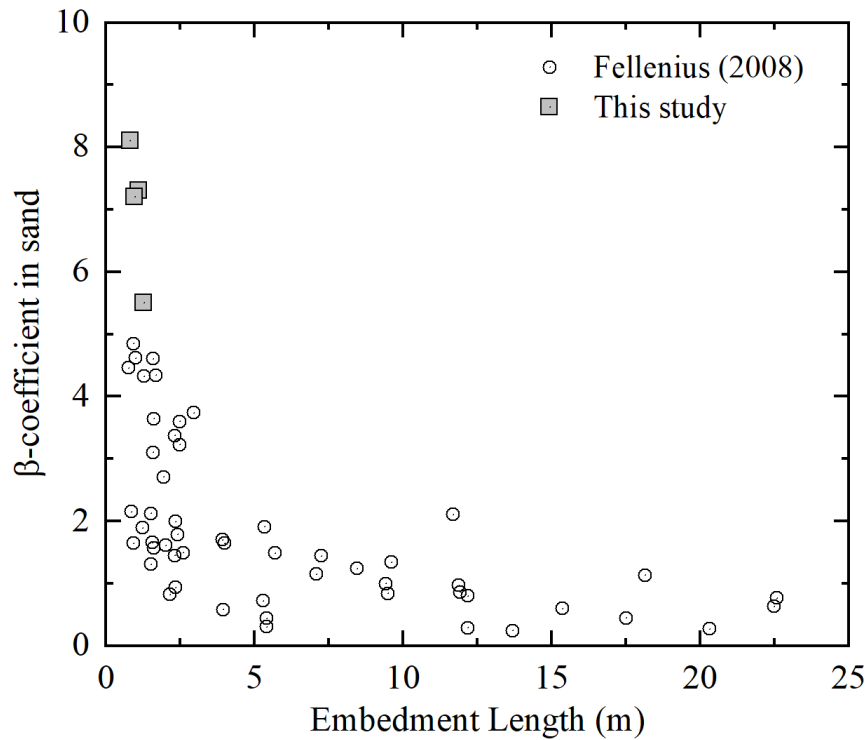


Figure 4.25: $\beta$ values comparison with other studies Fellenius (2008).

The nominal torsional capacity of the Collar Vanes for different CV geometries in the function of the undrained shear strength and $\beta$-coefficient is shown in Figure 4.26. The values covered in the study correspond to the remolded undrained shear strength since it was found that these values are a more accurate representation of the failure mechanism across the rupture surface shown in Figure 4.27. For the $\beta$-coefficient, a dry unit weight of $\gamma_d = 17$ kN/m$^3$ was considered to estimate the torsional capacity in a cohesionless material.

The estimation of the torsional capacity using the $\alpha$- and $\beta$- coefficients was carried out based on the assumption of a unit skin friction associated with a perfectly cylindrical
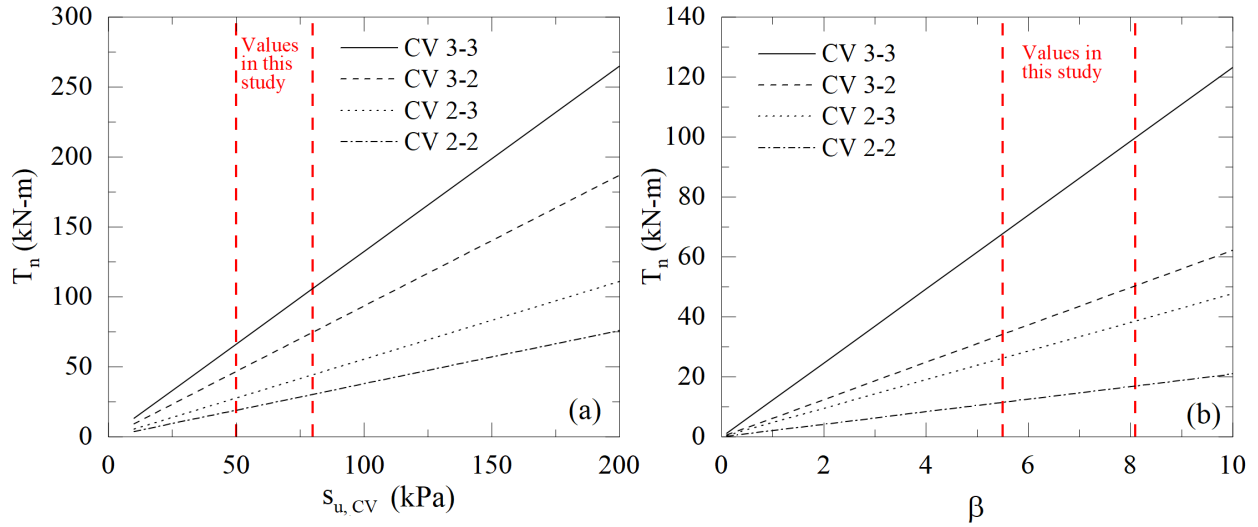
Figure 4.26: Nominal torsional resistance for the Collar Vanes in function of: (a) effective shear strength for the Collar Vane $s_{u,CV}$ and (b) $\beta$-values.
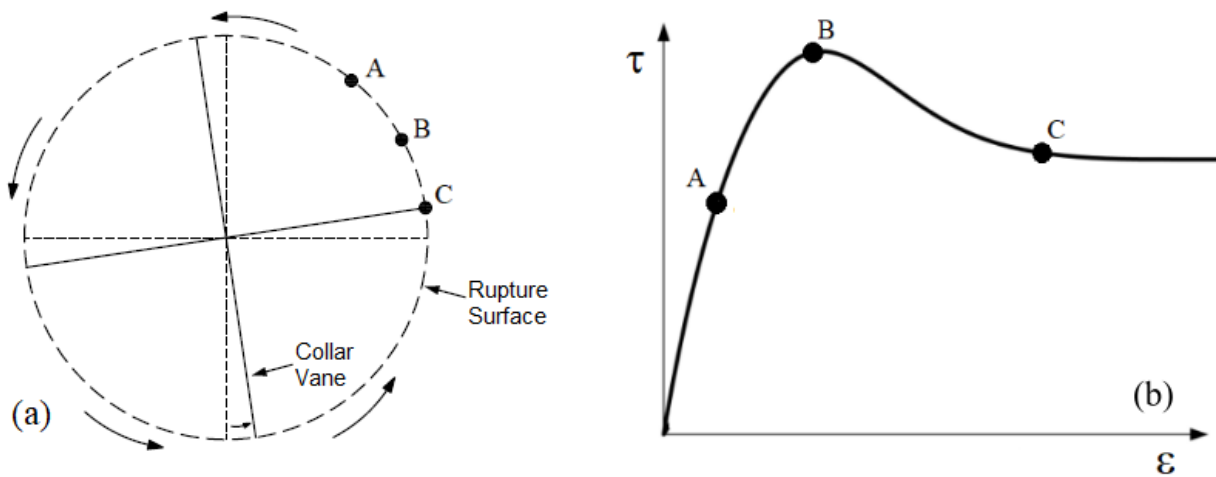


Figure 4.27: Shear resistance mobilization along rupture surface plane.

interface between the pile and the soil. However, this may not be the same case for Collar Vane where the blade surfaces are in contact with the soil. A more detailed mechanism is depicted in Figure 4.27 where, as the load increases, different points along the rupture surface are subjected to different stress conditions. At a certain amount of load, the soil element in point 'A' is in the pre-failure stage, and the shear stress acting in the soil element is below the peak shear strength of the soil. At point 'B' the shear stress is higher, and the soil passes from linear elastic to nonlinear plastic stress-strain behavior until the

shear stress eventually reaches the peak shear strength. At point 'C', the soil mass is in the post-failure stage where a decrease in stress after failure takes place until a level of constant stress is reached at large strains, which is the residual strength $s_{ur}$.
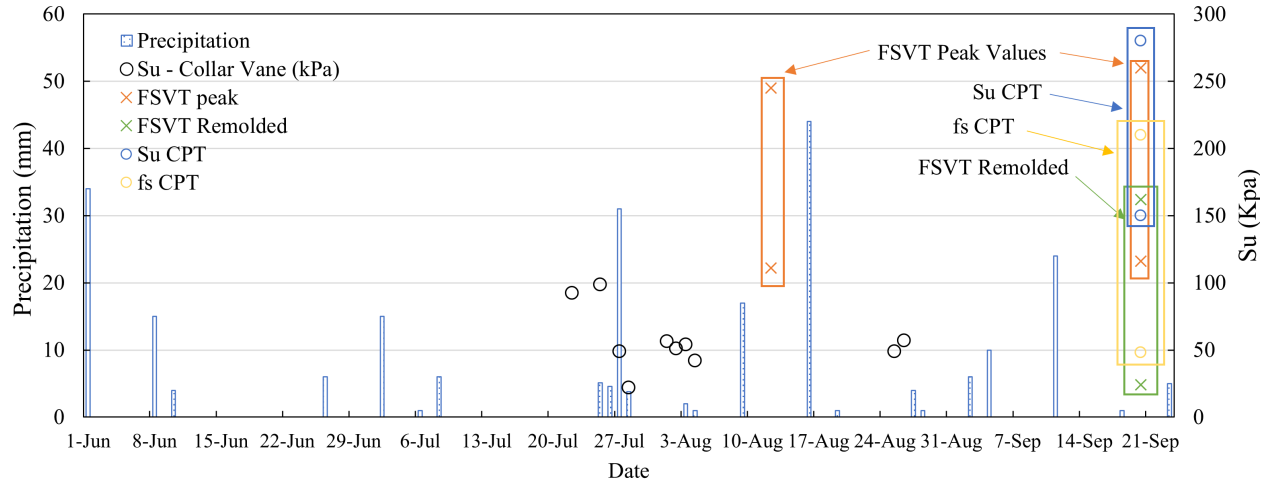


Figure 4.28: Influence of precipitation on the back-calculated $s_u$.

Moreover, the performance of the Collar Vanes was observed to be influenced by the amount of precipitation, in particular in the case of the CV2 3-2 T where it had almost the same torsional resistance as the CV1 3-2 TL. Since the geometry of the Collar Vanes and the failure torque are known, the back-calculated undrained shear strength is plotted and compared with the amount of precipitation in Figure 4.28. On the day of July 27th, the same day that the CV2 3-2 was tested, a considerable amount of precipitation was recorded and it shows a decrease in the undrained shear strength.

## 4.5   Summary and Conclusions

Helical piles are deep foundation elements that are commonly installed to support only axial loads. They can be installed relatively quickly and are considered a low-cost alternative to support structures. However, a limitation is an inability to support torsional and lateral loads. This study investigated the lateral and torsional performance of a full-scale helical pile augmented with a novel Collar Vane installed in cohesive and granular soil. Two Collar Vanes prototypes were manufactured, installed, and tested: a two-piece

Collar Vane (CV2) tested in a cohesive soil, and a one-piece Collar Vane (CV1) tested in a cohesive and granular soil. The following conclusions are drawn:

1. Collar Vane is a relatively easy-to-install element that is installed near the head of helical piles with conventional equipment such as a drive head or torque motor. Two CVs prototypes were manufactured and tested: a two-piece Collar Vane (CV2), in nine different size geometries; and a single-piece Collar Vane (CV1), in four different size geometries.

2. Lateral capacity of the HP using the Collar Vane was increased. An interpreted failure load is presented using different criteria methods based on the pile head displacements that can be suitable to represent the serviceability limit state or ultimate limit state condition.

3. Two load sequences (Lateral-Torsional and Torsional-Lateral) were considered to study the effects of different types of loading conditions on the HP performance. A reduction in lateral capacity was found after performing the torsion test and viceversa.

4. Collar Vane effectively increases the lateral resistance due to an increase in effective diameter associated with the mobilization of shear resistance. The increase in the lateral resistance was up to 52 times for a displacement of 12.5 mm. Lateral responses between CV1 and CV2 were in general the same and no difference between the round and square shaft responses was observed.

5. Reduction in bending moment values due to Collar Vane was observed by limiting the pile displacement and thus, eliminating the need for shafts with bigger diameters making possible a more efficient pile design.

6. When the helical pile is subjected to lateral loads the load-transfer mechanism is carried out at the HP top flange and it was found the Collar Vane carries up to 90%

of the applied load. Supporting the idea that a large diameter shaft would not be needed.

7. Torsional capacity is substantially increased when the Collar Vane is coupled to the helical pile. It was found that the one-piece Collar Vane mobilizes more torsional strength than the two-piece Collar Vane due to the connection system and load transfer mechanism carried out at the HP head.

8. A comparison of the predicted torsional capacity with the measured capacity using different methodologies was undertaken and its accuracy was quantified. For the cohesive material, $\alpha$ methods tend to overestimate the capacity ratio, whereas the CPT-based methods show the best average capacity ratio. However, for the granular soil, $\beta$ methods underpredicted the capacity significantly. This is attributed to the underestimation of the $\beta$-coefficient for that particular soil condition. The CV2 exhibited the largest scatter of the capacity ratio, while CV1 predictions were consistent.

# CHAPTER 5

# CYCLIC TEST RESULTS AND ANALYSIS

## 5.1  Introduction

This chapter will present the cyclic results from both soil conditions using different Collar Vane geometries and prototypes. The test piles were subjected to different magnitudes and amplitudes of cyclic loads with a frequency of 0.125 Hz. The intended number of cycles applied was approximately 1000 cycles. The raw load and displacement data is attached in Appendix F.

The load sequence considered for this study was Lateral-Torsional: the helical pile was installed and subjected to one thousand lateral loads followed by one thousand torsional loads in the same location. Loads were applied implementing the hydraulic pressure controller into the testing frame and cyclic profiles were established using the controller profile builder ERTune software. Maximum applied loads were chosen based on the monotonic test results using displacement/rotation-based criteria.

## 5.2  Cyclic Lateral Loading

According to LeBlanc *et al.* (2010), parameters $\zeta_b$ and $\zeta_c$ can be used to describe the characteristic of the cyclic loading. The term $\zeta_b$, describes the ratio between the maximum cyclic and maximum static load capacity $P_{c,max}/P_u$; The term $\zeta_c$, describes the ratio between minimum and maximum cyclic loads $P_{c,min}/P_{c,max}$. $\zeta_c$ characterizes the load symmetry ($\zeta_c$=0 for one-way loading, $\zeta_c$=-1 for symmetric two-way loading, and $\zeta_c$=1 for constant loading). Parameters $\zeta_b$ and $\zeta_c$ together describe the load amplitude relative to an arbitrary reference load $P_u$, where $P_u$ is defined at a reference pile displacement value $\delta = 12.5$ mm at the load application point. Table 5.1 summarizes the characteristic of the one-way lateral cyclic loading used in this study. It was not possible to have a $\zeta_c$=0 in the tests since the hydraulic controller requires a minimum amount of flowing pressure.

Table 5.1: Summary of lateral forces applied in the cyclic tests.

| Collar Vane | $P_u$ (kN) | $P_{c,max}$ (kN) | $\Delta P$ (kN) | $\zeta_b$ | $\zeta_c$ | $N$ |
|---|---|---|---|---|---|---|
| | | | Cohesive Soil | | | |
| HP L Cyc | 2.6 | 8 | 4 | 3.1 | 0.50 | 1000 |
| CV2 2-1 LT Cyc | 12 | 13 | 8 | 1.0 | 0.38 | 1000 |
| CV1 2-2 L Cyc | 27 | 15 | 12 | 0.5 | 0.17 | 850 |
| CV2 3-1 LT Cyc | 34 | 31 | 24 | 0.9 | 0.23 | 1000 |
| CV2 3-2 LT Cyc | 45 | 18 | 11 | 0.4 | 0.39 | 1100 |
| CV2 3-2 LT Cyc R | 45 | 31 | 26 | 0.7 | 0.16 | 1000 |
| CV1 3-2 LT Cyc | 46 | 32 | 27 | 0.7 | 0.16 | 1000 |
| CV2 3-3 LT Cyc | 49 | 31 | 21 | 0.6 | 0.32 | 850 |
| CV2 3-3 LT Cyc R | 49 | 34 | 29 | 0.7 | 0.15 | 1000 |
| | | | Cohesionless Soil | | | |
| CV1 3-2 LT Cyc S | 50 | 49 | 40 | 1.0 | 0.18 | 700 |
| CV1 3-2 LT Cyc S R | 50 | 25 | 19 | 0.5 | 0.24 | 1000 |

**Note:** R stands for 'repeated' test for the same CV with a different $\zeta_b$ or $\zeta_c$.

Typical lateral load and displacement curves are presented in Figures 5.1-5.2, for the HP installed in the cohesive soil; and Figure 5.3, for the granular soil. It is observed that the first cycle generates a bigger displacement than the following ones.

Figure 5.1(a) presents the results for the Helical Pile without Collar Vane. The $\zeta_b$ parameter was set to 3 due to the low capacity of the HP itself and the minimum load that the controller is able to supply. Moreover, the HP subjected to lateral loads presents an accumulated displacement due to the high amount of load applied. Figure 5.1(b) shows the case for the CV2 2-1, an increment in the accumulated displacement is observed after each cycle. The color change in the load-displacement curves occurs approximately every 100 cycles. Thus, the color distribution shows a larger displacement at the early stages of the cyclic load. Figure 5.1(c) presents the results for the CV1 2-2. A sudden jump in load was recorded at cycle 100 (Figure F.3) making the displacement change abruptly. After this, it is not observed a change in the accumulated displacement.
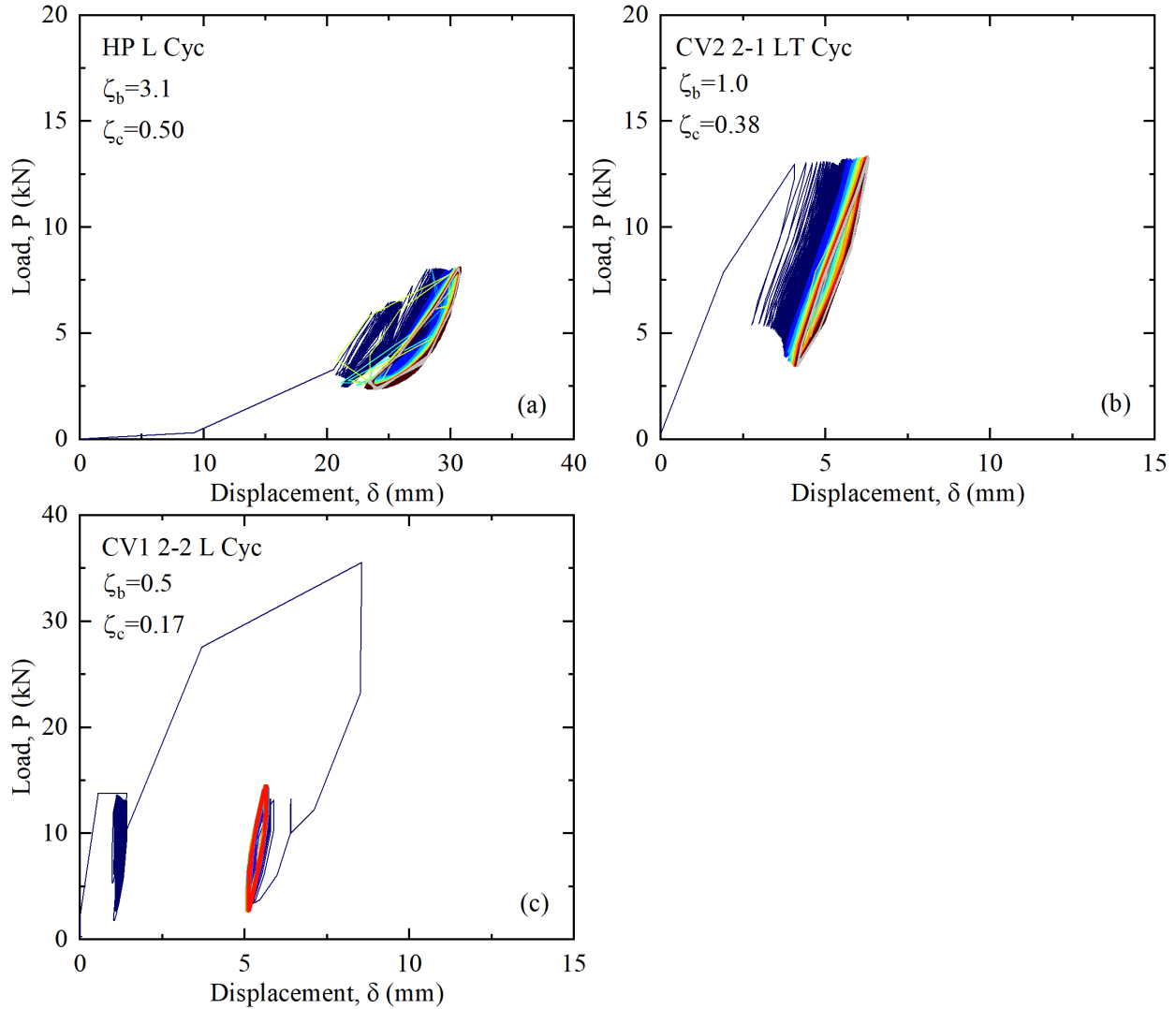
Figure 5.1: Variation of pile head lateral load with displacement in cohesive soil: (a) HP without CV; (b) CV2 2-1 and; (c) CV1 2-2.

Cyclic loads in the CVs with diameter $D = 0.91$ m are presented in Figure 5.1. CV2 3-1 presents a large displacement accumulation with a $\zeta_b = 1$ whereas CV 3-2 with a $\zeta_b = 0.4$ does not present an accumulation in the displacement and shows a hysterical behavior. Figure 5.1(c-d) have the same CV geometry and were subjected to the same cyclic loads. However, they differ in the prototype: the two-piece CV was tested in 2021, and the one-piece in 2022. Although having the same geometry and were subjected to the same cyclical loads, their response was different: the CV1 did not have a ratcheting displacement behavior and it was measured as a hysterical response. The reason for the difference may
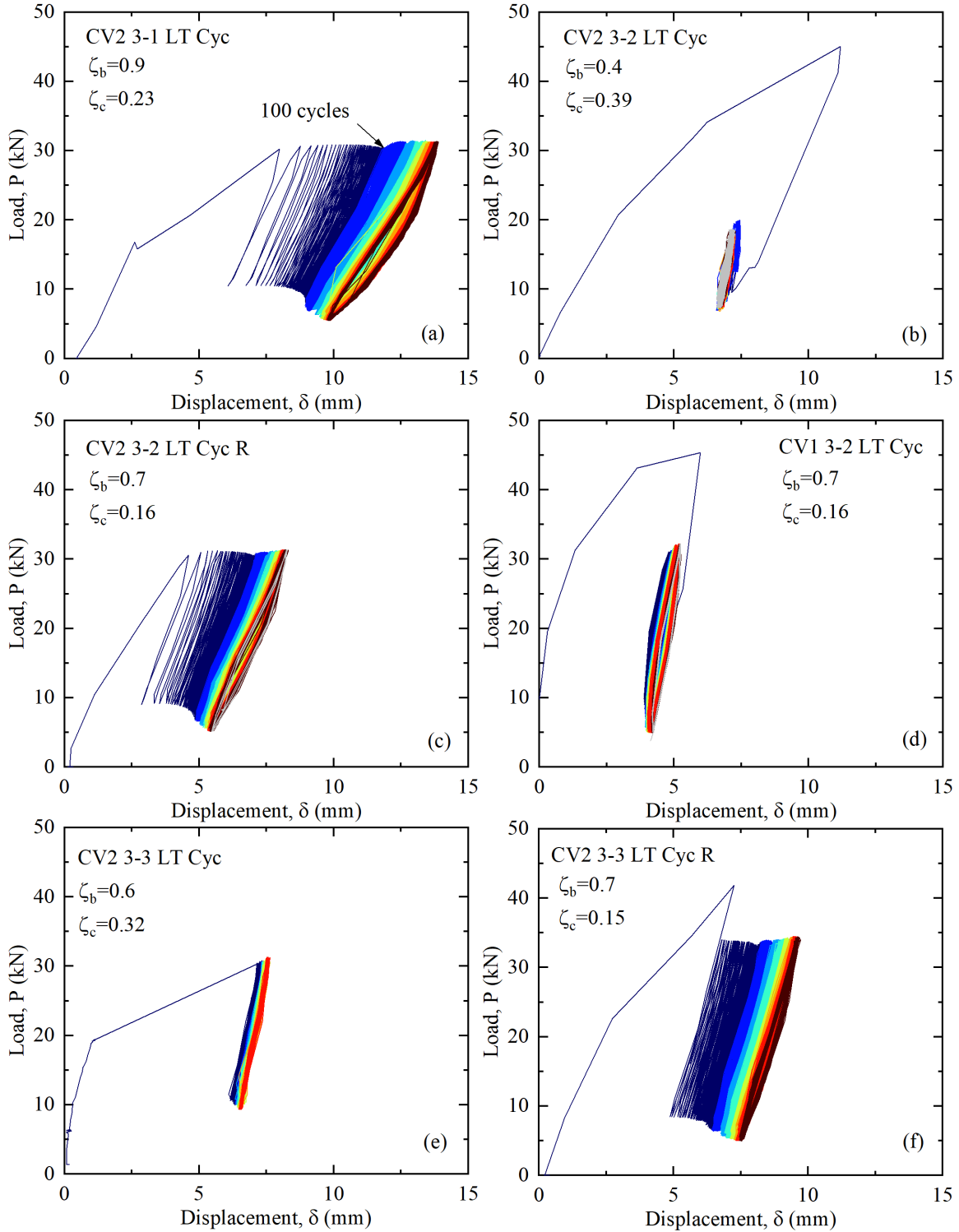
Figure 5.2: Variation of pile head lateral load with displacement: (a) CV2 3-1; (b) CV2 3-2; (c) CV2 3-2 with a different $\zeta_b$; (d) CV1 3-2; (e) CV2 3-3 and; (f) CV2 3-3 with a different $\zeta_b$.

be attributed to the fact that the local densities immediately adjacent to the pile were different since both tests were performed in different years.
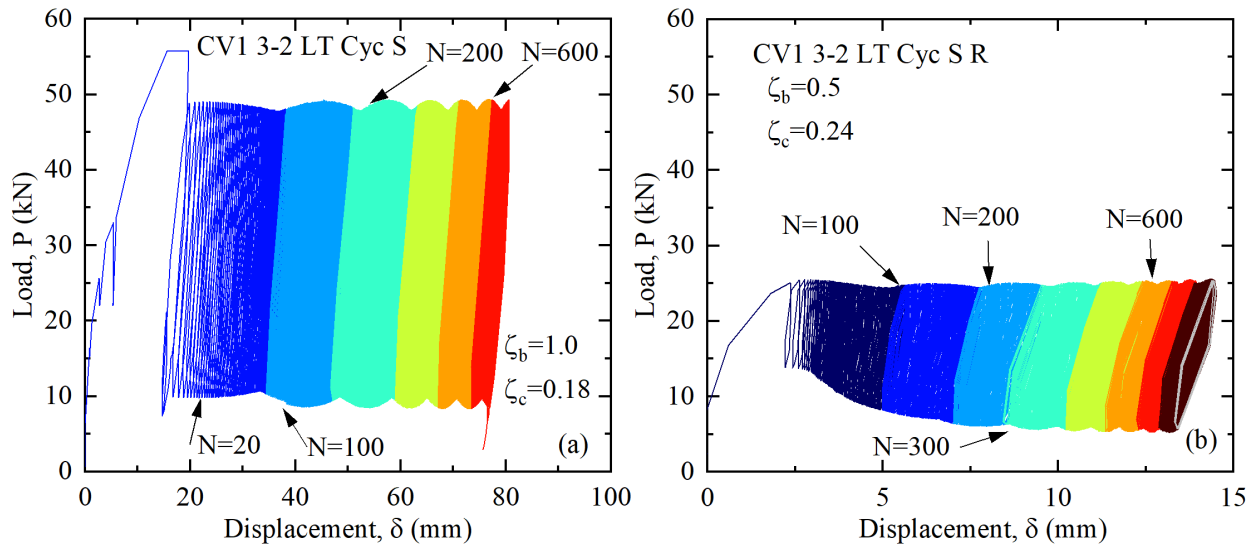


Figure 5.3: Variation of pile head lateral load with displacement in granular soil using the CV1 3-2 with different $\zeta_b$.
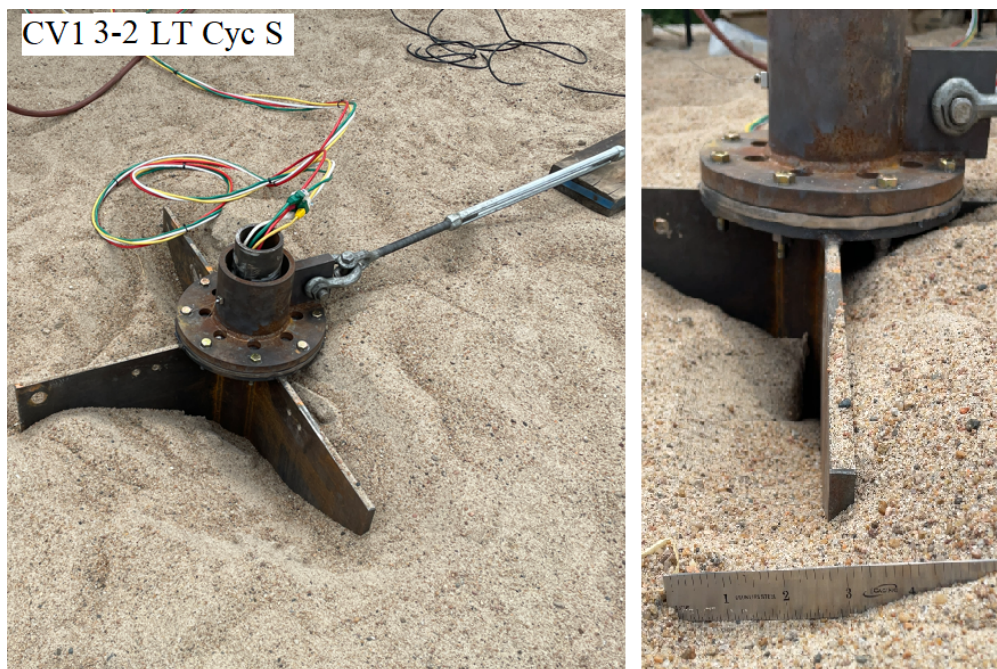


Figure 5.4: Soil subsidence around the laterally loaded Collar Vane CV1 3-2 in sand.

For the piles that presented a ratcheting displacement, it was generally observed that the piles moved significantly during the initial 100 cycles. However, the displacement

increment rate decreased afterward. The same behavior was observed in the cyclic test performed in the sand. Figure 5.3 presents accumulated lateral displacement for the CV1 3-2 with two different $\zeta_b$. Figure 5.3(a) was subjected to only 800 cycles and the final displacement was 80mm. This type of cyclic response is categorized as unstable cyclic loading. Also, Figure 5.4 depicts the observed soil subsidence adjacent to the CV due to the imposed load causing yielding of the soil. Under cyclic loading, the continuous structure movement would lead to particle migration and bed subsidence of the surrounding soil (Lu & Zhang, 2019; Nanda $et\ al.$, 2017; Li $et\ al.$, 2021). The same effects were reported by Cheang & Matlock (1983); Brown $et\ al.$ (1988). Cuéllar $et\ al.$ (2009) explained that if sand is dense enough, the rearrangement phase starts immediately after the first cycle, which causes the visible subsidence of soil.
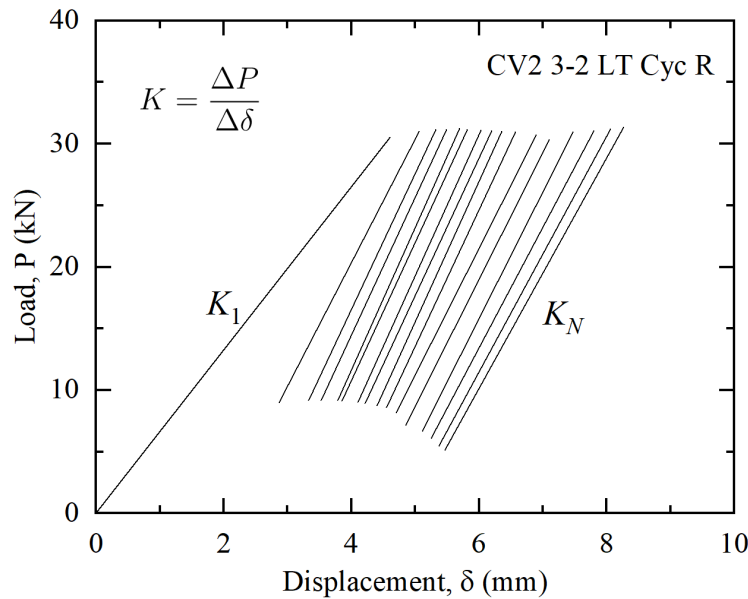


Figure 5.5: Method of determination of the soil-pile secant stiffness.

To examine the degradation effect of cyclic loading on the helical pile stiffness, two types of stiffness are defined. The equivalent stiffness is defined as the slope from the origin to the peak load point at each cycle. This type of stiffness is used to analyze the cumulative displacement. The second stiffness is the secant stiffness which is defined as the stiffness of the HP head at the $N^{\text{th}}$ cycle divided by the stiffness of the pile head at the

first cycle as shown in Equation (5.1). Which is the secant slope from the beginning point to the peak point (Chiou *et al.*, 2018).

$$K = \frac{P_{max} - P_{min}}{y_{max} - y_{min}} \tag{5.1}$$

where $K$ = helical pile head stiffness; $P_{max}$ and $P_{min}$ = maximum and minimum applied loads in each load cycle; and $y_{max}$ and $y_{min}$ = corresponding pile head deflections. Figure 5.5 depicts the head stiffness at different cycles for the CV2 3-2. The initial slope $K_1$ is less steep than the following slopes $K_N$. Through many cycles of movement, the cumulative increase in total strain and the consequent remolding of the local soil leads to a reduction in the lateral resistance (Zhang *et al.*, 2011).
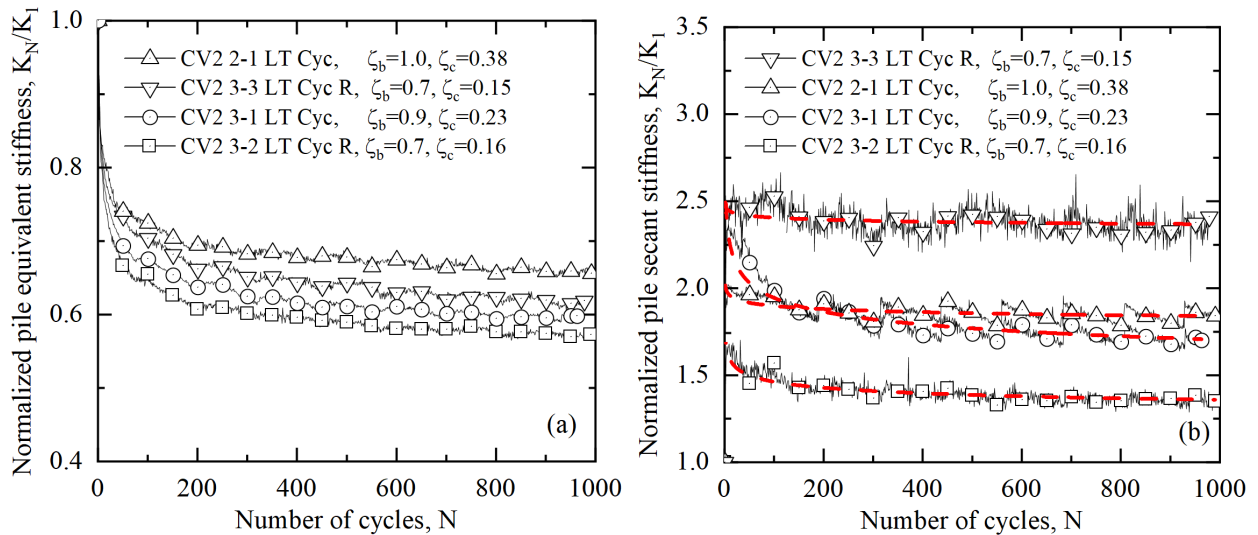


Figure 5.6: (a) Pile head equivalent stiffness and (b) pile head secant stiffness.

Figure 5.6(a-b) depicts the variations of equivalent and secant stiffness in the function of the number of cycles, respectively. The decrease in the equivalent stiffness is related to the accumulation of displacement. Moreover, the secant stiffness had an increment after the first cycle and decreased as the number of load cycles increased. The same tendency was reported by Abd Elaziz & El Naggar (2015); Mondal & Disfani (2022). The effect of the first cycle is significant on the pile-soil stiffness, which reduces with an increasing number of cycles (Long & Vanneste, 1994) as shown in the load-deflection slopes in Figure

5.5. These changes in soil and pile stiffness are influenced by the magnitude of load, the character of load ($\zeta_b$ and $\zeta_c$), and the initial stiffness of the pile and soil.

The design of cyclic laterally loaded pile design is calculated using a global analysis, where the initial pile displacements and rotations are computed using static analysis and then modified to take into account the cyclic effects Garnier (2013). A current methodology to predict the lateral cyclic response is using a logarithmic function (Equation 5.2) or a power function (Equation 5.3).

$$\frac{y_N}{y_1} = (1 + b\ln(N)) \tag{5.2}$$

$$\frac{y_N}{y_1} = N^\alpha \tag{5.3}$$

where $b$ and $\alpha$ are degradation parameters.
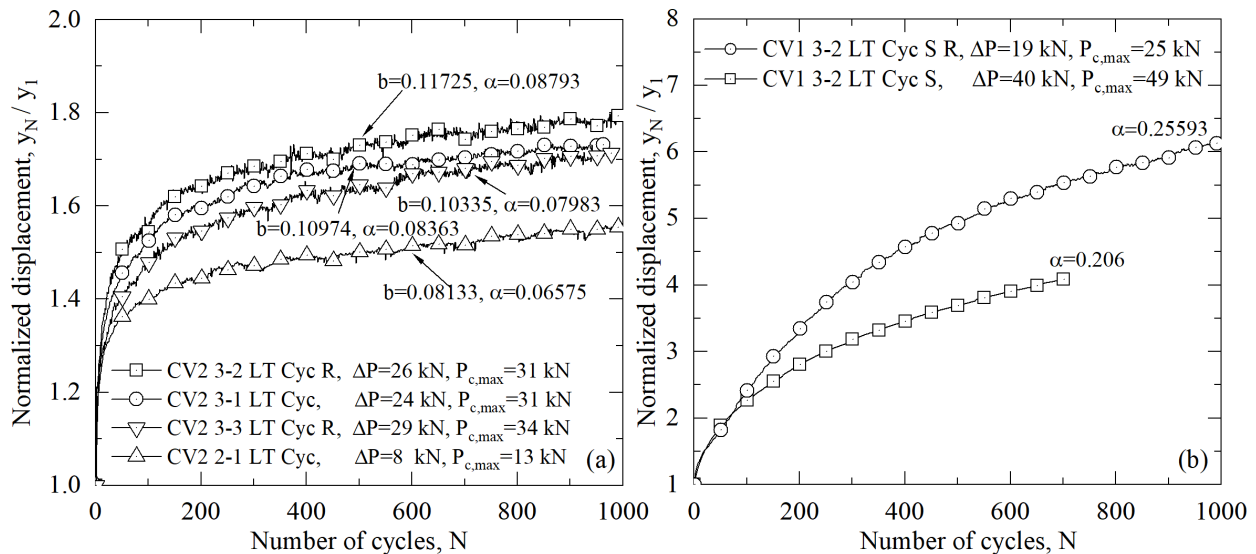


Figure 5.7: Relative pile head displacement for different CVs versus the number of cycles N: (a) cohesive soil and (b) granular soil.

Figure 5.7 presents the evolution of the pile head relative displacement in the function of the number of cycles. It is noted that for higher $\zeta_c$ the higher $\frac{y_N}{y_1}$ is. The plots are well represented by a logarithmic function and a power function. The fitting values shown in

135
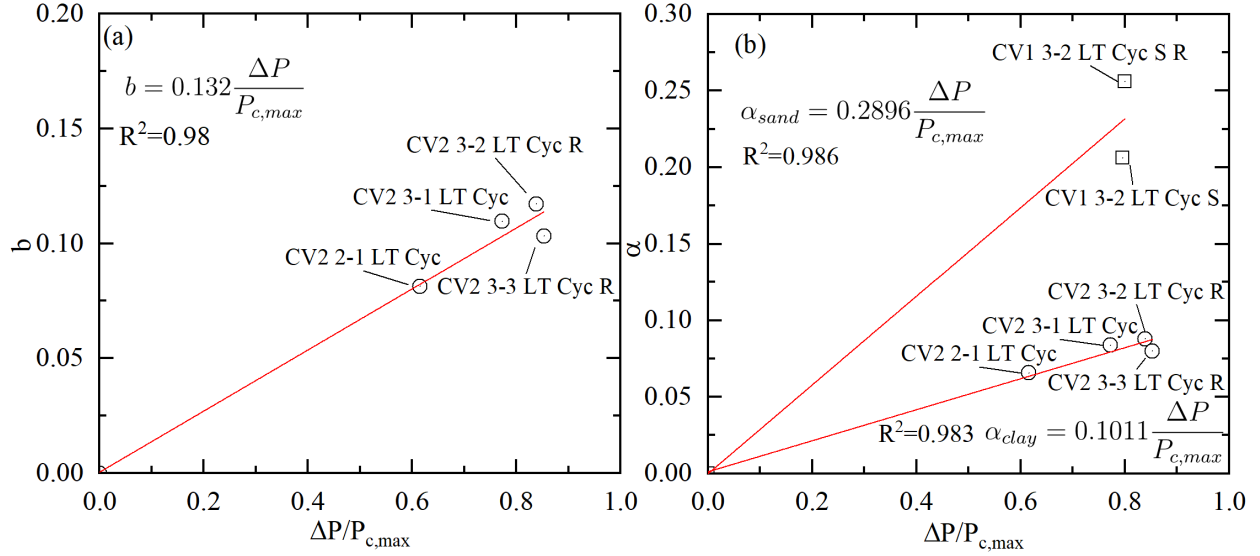
Figure 5.8: (a) $b$ coefficient for cohesive soil and (b) $\alpha$-coefficients for cohesive and granular soil. Coefficients are plotted versus cyclic load ratio $\Delta P/P_{c,max}$.

Figure 5.7 are plotted in Figure 5.8 versus cycle amplitude ratio. Linear relationships are obtained with a good correlation coefficient.

From the test results, the pile head horizontal displacement under $P_{c,max}$ can be represented by the following equations:

In cohesive soil:

$$y_N = y_1 \left[ 1 + 0.132 \frac{\Delta P}{P_{c,max}} \ln N \right] \tag{5.4a}$$

or

$$y_N = y_1 N^{0.1011 \frac{\Delta P}{P_{c,max}}} \tag{5.4b}$$

in granular soil:

$$y_N = y_1 N^{0.2896 \frac{\Delta P}{P_{c,max}}} \tag{5.4c}$$

where, $\Delta P$ is the cycle amplitude and $N$ the number of cycles. This relationship may be used to determine the accumulated displacement since $y_1$ can be easily obtained using $p - y$ curves used in pile design or in this case, from the monotonic test results. However, these coefficients may depend on the CV size, soil properties ($s_u$ or $D_r$), and also on the $\zeta_c$

136

value. Only it was possible to obtain these relationships when the CV was subjected to a $\zeta_c \geq 0.7$ and presented accumulated displacement. Moreover, more data points at low amplitude are required to verify the accuracy at low $\Delta P/P_{c,max}$.
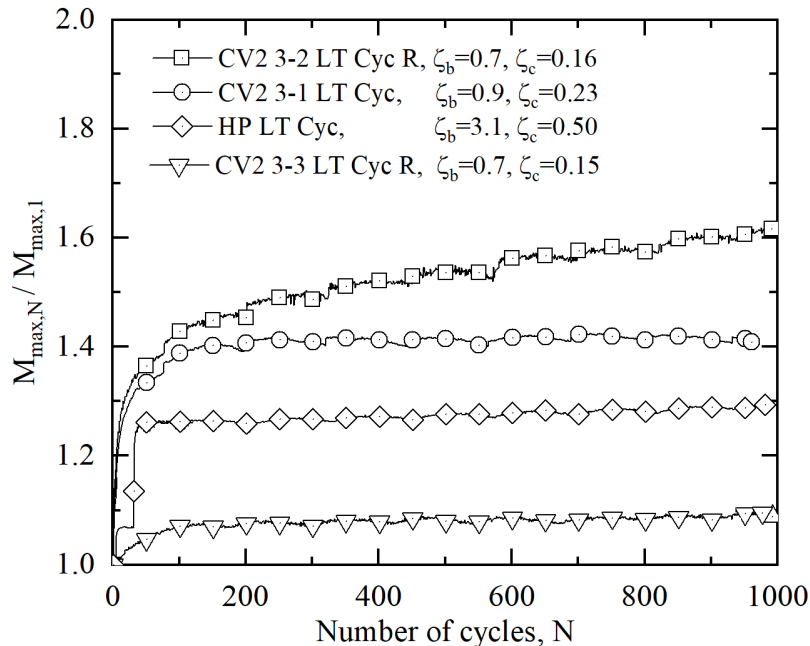


Figure 5.9: Normalized maximum moment vs loading cycles.

The maximum bending moment, in most cases, is considered the key parameter in laterally loaded pile design. Figure 5.10 shows the pile moment profiles with depth for different CVs geometries. It could be seen that with increasing loading cycles, the maximum bending moment increases with the number of cycles; and for the initial 100 cycles the moment distribution changed significantly. This increase may be attributed to the decrease in the lateral resistance at shallow depths of soil.

The effect of the load cycles in the bending moment can be determined by studying the ratio $M_{max,N}/M_{max,1}$, where $M_{max,N}$ and $M_{max,1}$ are the maximum bending moment in at cycle $N$ peak load and the max moment in the first cycle, respectively. Figure 5.9 shows the normalized maximum bending moment and it is observed that, in general, all the responses had a cumulative relative bending moment but this increment was less significant than the displacement. This was also reported by Garnier (2013).
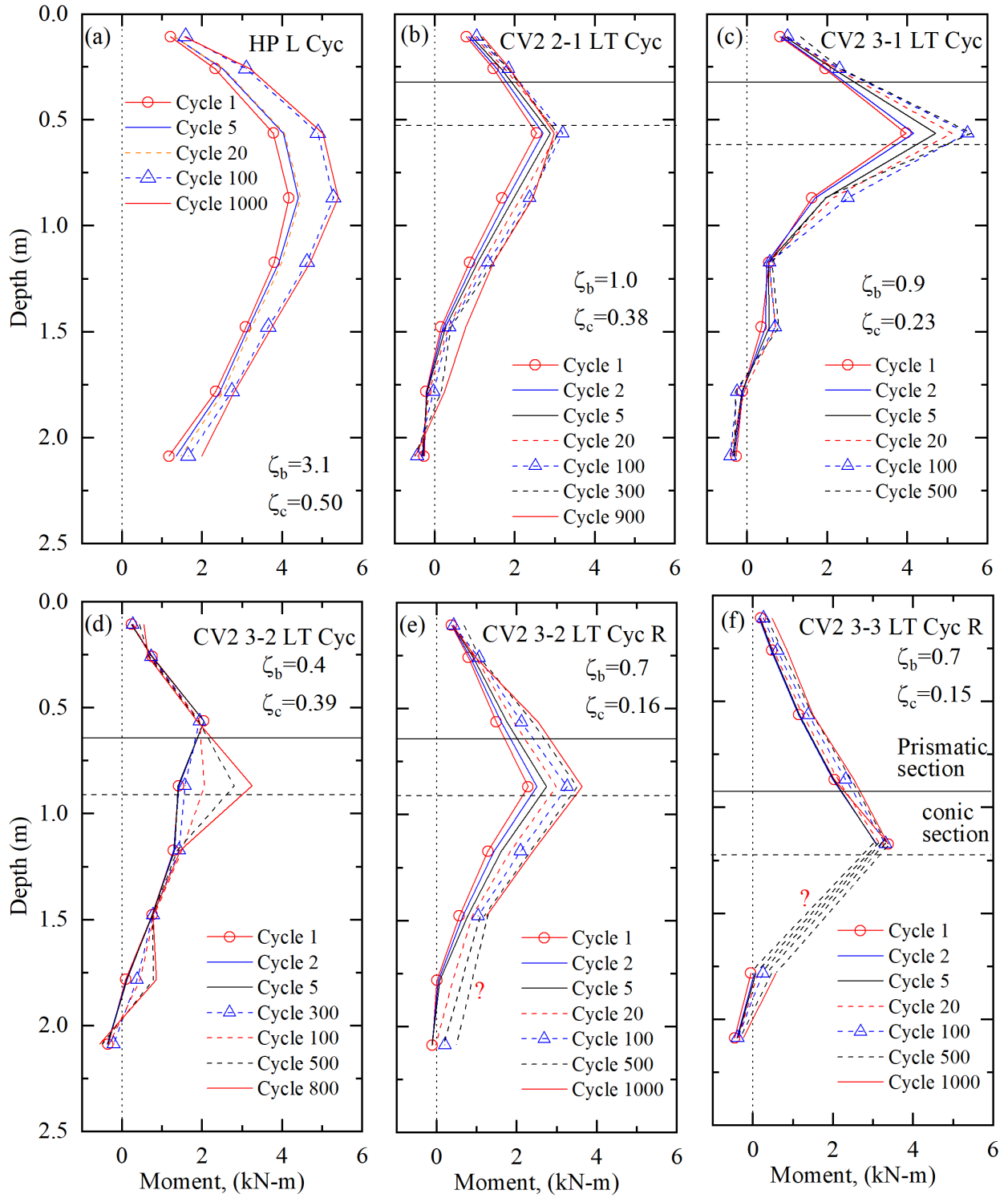
Figure 5.10: Cyclic bending moment profiles: (a) HP without Collar Vane and (b-f) HP with Collar Vane

## 5.3 Cyclic Torsional Loading

The cyclic torsional response of the pile foundations is of particular interest in pile design since wind gusts frequently act on traffic signs and signal structures. Table 5.2 summarizes the Collar Vanes tested at different cyclical load combinations. The relationship between the torque and rotation is shown in Figures 5.11-5.12 in the cohesive soil, and Figure 5.13, for the granular soil. The figures include the HP's torsion resistance contribution due to the impossibility to isolate it in this case. Also, all the torsional tests were performed after applying the lateral cyclic load. As a result, the cyclic torsional behavior presented here is influenced by the cyclic lateral loads,

Table 5.2: Summary of torque applied in the cyclic tests.

| Collar Vane | $T_{\theta=4^\circ}$ (kN-m) | $T_{c,max}$ (kN-m) | $\Delta T$ (kN-m) | $\zeta_b$ | $\zeta_c$ | N |
|---|---|---|---|---|---|---|
| | | Cohesive Soil | | | | |
| CV2 2-1 LT Cyc | 7.8 | 13.7 | 7.3 | 1.8 | 0.47 | 950 |
| CV1 2-2 T Cyc | 15 | 26 | 18 | 1.7 | 0.31 | 1000 |
| CV2 3-1 LT Cyc | 23 | 24 | 15 | 1.0 | 0.38 | 1000 |
| CV2 3-2 LT Cyc | 24 | 18 | 8 | 0.8 | 0.56 | 1000 |
| CV2 3-2 LT Cyc R | 24 | 18 | 12 | 0.8 | 0.33 | 1000 |
| CV1 3-2 LT Cyc | 41 | 43 | 33 | 1.0 | 0.23 | 1000 |
| CV2 3-3 LT Cyc | 24 | 23 | 14 | 1.0 | 0.39 | 850 |
| CV2 3-3 LT Cyc R | 24 | 26 | 16 | 1.1 | 0.38 | 930 |
| | | Granular Soil | | | | |
| CV1 3-2 LT Cyc S | 45 | 44 | 34 | 1.0 | 0.22 | 85 |
| CV1 3-2 LT Cyc S R | 45 | 32 | 24 | 0.7 | 0.25 | 800 |

**Note:** R stands for 'repeated' test with a different $\zeta_b$ or $\zeta_c$.

The characteristic cycling loads are defined as $\zeta_b = T_{c,max}/T_{\theta=4^\circ}$ and $\zeta_c = T_{c,min}/T_{c,max}$, where $T_{\theta=4^\circ}$ is the reference point taken as the torque required to rotate the Collar Vane 4°. FDOT failure criterion for rotation is 15 ° for traffic sign supports based on serviceability requirements (Hu *et al.*, 2006). However, the value chosen in this study is based on the

monotonic results where the CVs used in the cyclic test had a linear T-$\theta$ response for the bigger CVs. The torque and rotation curves for the CVs with D=0.61 m are shown in Figure 5.11. The two-piece CV had a different accumulated rotation in each blade whereas the one-blade side had less accumulated rotation as observed in the monotonic results. The one-piece CV blades presented a very uniform response on both sides.
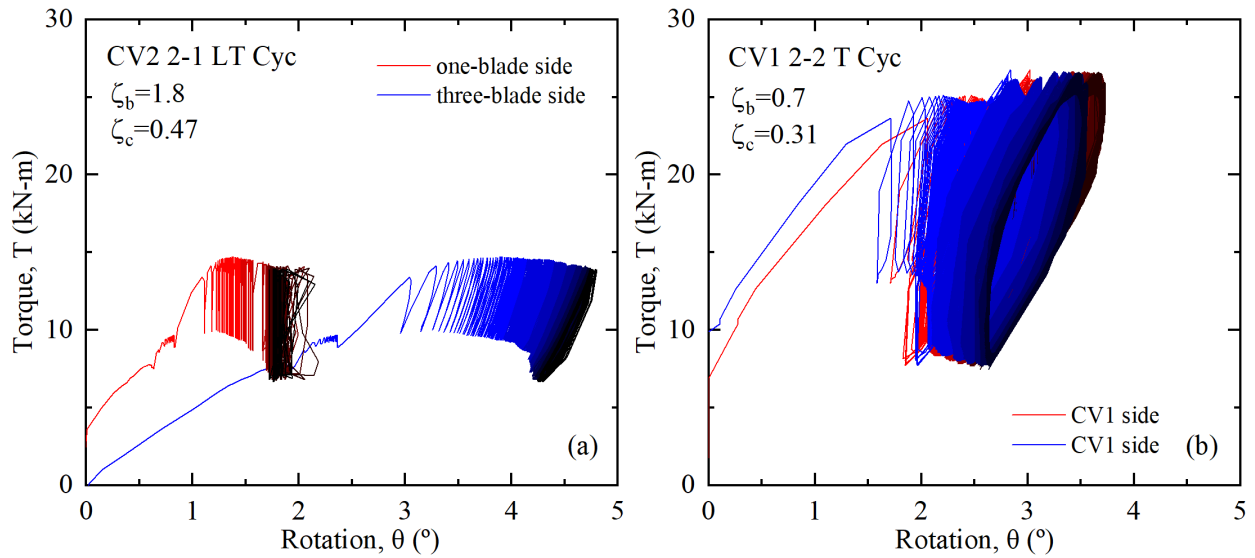


Figure 5.11: Variation of torque with rotation: (a) CV2 2-1 and (b) CV1 2-2

Figure 5.12 presents the results for the CVs with $D = 0.91$ m. In general, a high and constant $\zeta_b$ was chosen throughout all the tests. Three tests were performed using CV 3-2: the two-piece CV shows different accumulated rotations for each blade side whereas the one-piece shows a uniform ratcheting displacement. Moreover, CVs 3-3 present a different response although the characteristic cycling load is the same. This can be attributed to the cyclic lateral loads performed earlier. In the cyclic lateral test, the CV2 3-3 LT did not have accumulated displacement (Figure 5.2e) whereas the CV2 3-3 LT R (Figure 5.2f) presented this ratcheting displacement. The soil was subjected to a cumulative increase in total strain during the lateral test leading to the reduction in the torsional resistance making it have an accumulated rotation.
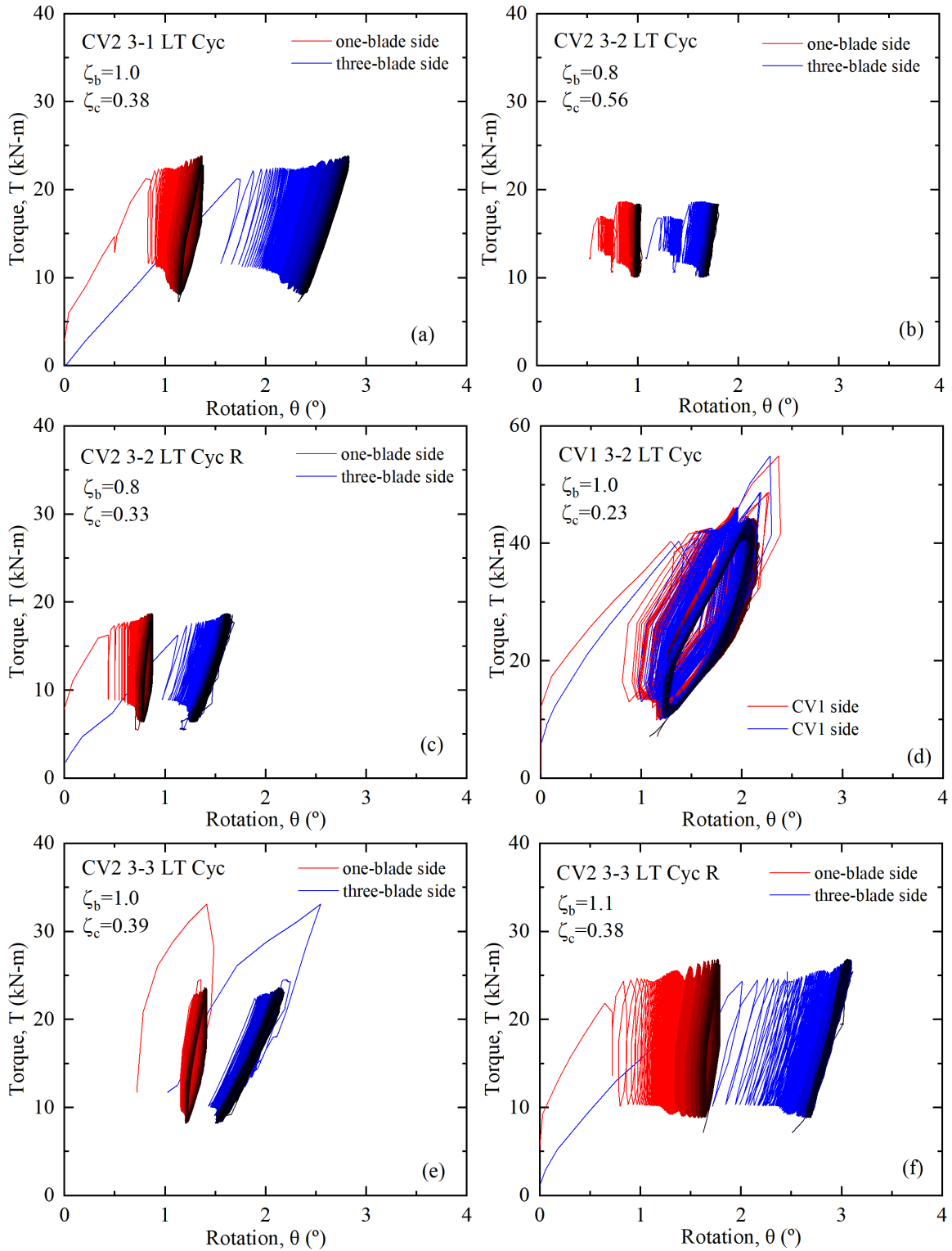
Figure 5.12: Variation of torque with rotation: (a) CV2 3-1; (b) CV2 3-2; (c) CV2 3-2 with a different $\zeta_c$; (d) CV1 3-2 and; (e-f) CV2 3-3.
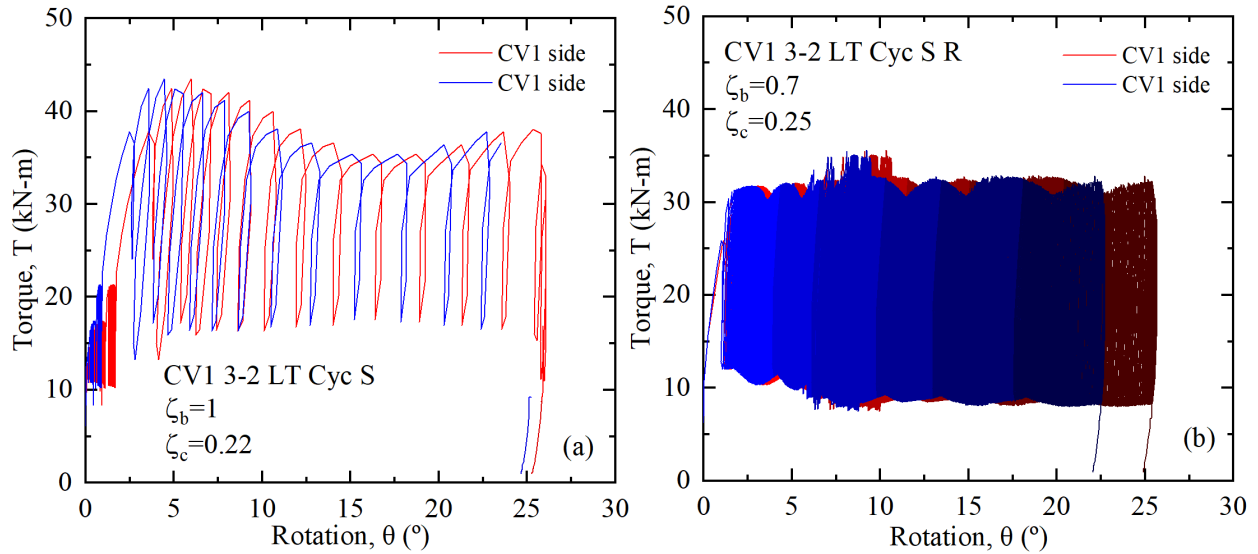
Figure 5.13: Variation of torque with rotation in granular soil: (a) CV1 3-2 ($N$=90) and (b) CV2 3-2 with different $\zeta_b$.
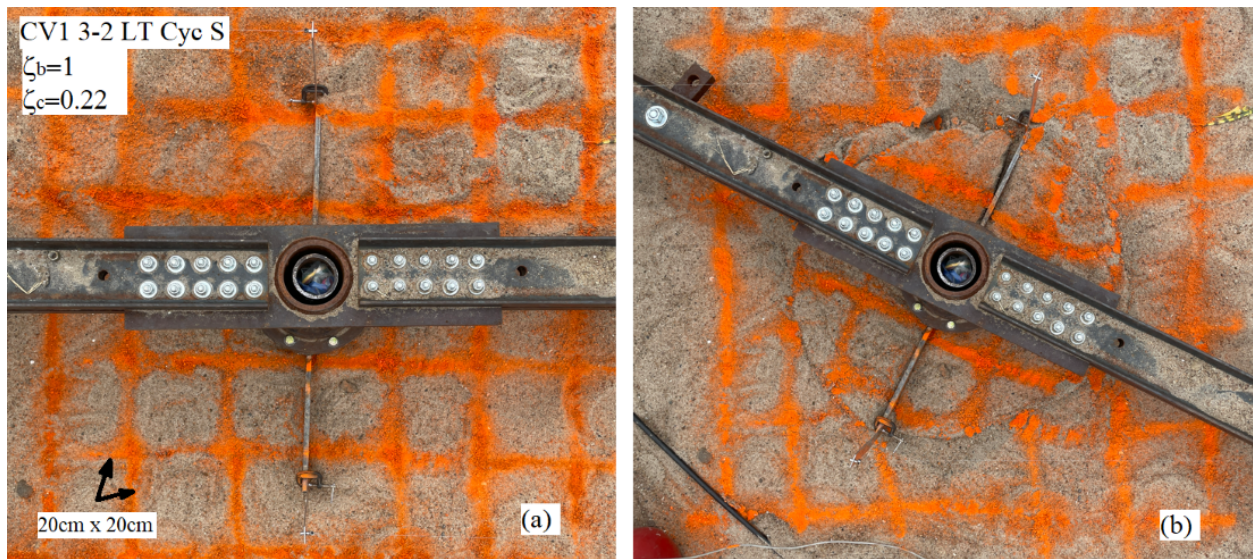


Figure 5.14: Cylindrical failure surface around CV1 3-2 in sand.

Figure 5.13 presents the cyclic torsional results in the sand. The same CV was used for both tests with a different $\zeta_b$. The first test of the CV1 3-2 only was able to 85 before reaching the ultimate torque capacity. This may be attributed to the cyclical lateral load effects: CV1 3-2 was subjected to a large accumulated displacement, as shown in Figure 5.3(a), and high cumulative strain developing soil subsidence around the CV, as shown in Figure 5.4.

142

Figure 5.15: Soil subsidence around the CV1 3-2 after $N$ cycles in the sand.

Figures 5.14 and 5.15 show the field photos of the torsional cyclic test performed in the sand. The test shown in Figures 5.14 was subjected to high cyclic lateral loads ($\zeta_b = 1$) making it fail in torsion in only 85 cycles. The figure depicts a clear cylindrical shear failure surface around the Collar Vane blades. Moreover, the test shown in 5.15 was subjected to lower cyclic lateral loads ($\zeta_b = 0.7$) and it was possible to apply approximately 800 torsional cycles where soil subsidence due to torsion was observed around the CV surroundings. Figures depict the increment of this subsidence over the number of cycles applied and also the rearrangement of soil particles.
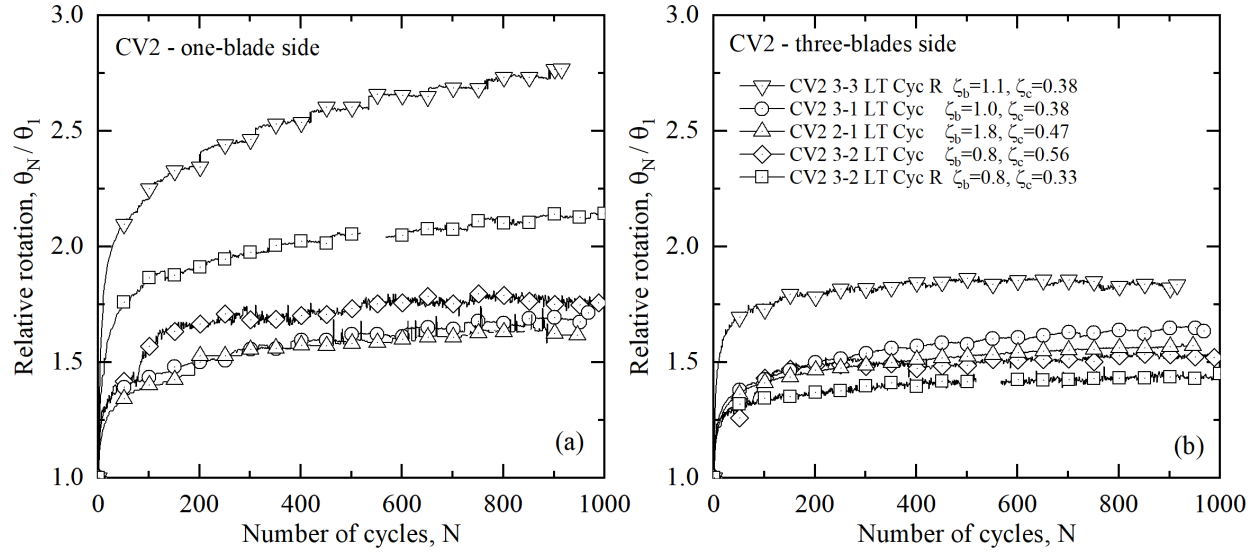
Figure 5.16: Normalized cumulative rotation vs number of cycles using CV2 in cohesive soil.

Figure 5.16 presents the evolution of the accumulated rotation in the function of the number of cycles for each of the CVs sides (one- and three-blade sides). In general, the graph depicts that the one-blade side has a higher accumulated rotation that can be attributed to the non-uniform resistance mobilization: the one-blade side had a small initial rotation $\theta_1$ and eventually the rotation $\theta_N$ increases after the three-blade side has mobilized torsional resistance in that side. Nevertheless, it is important to note that these results are influenced by the cyclic lateral loads.

## 5.4   Summary and Conclusions

This chapter studies the conducted one-way lateral and torsional cyclic load test on the helical pile with the Collar Vanes in cohesive and granular soils. The cyclic and load-level effects on the pile-head displacement and rotation, maximum moment, and pile-head stiffness were investigated. The number of cycles was approximately 1000 with a loading rate of 1 cycle per eight seconds (0.125 Hz). According to the field results, the following conclusions can be drawn.

1. For the lateral and torsional loads, the cyclic effect was significant within the first 100 cycles. The lateral cyclic load increased the ratcheting displacement and bending moment.

2. In general, the soil-pile lateral stiffness decreased with the number of cycles. This is associated with the soil yielding and degradation effects.

3. The effects of the cyclic load were more significant in the granular soil where soil subsidence was observed due to strain accumulation leading to a particle migration in the Collar Vane surroundings.

4. Equivalent stiffness and secant stiffness were plotted for lateral loads. The equivalent stiffness is used to compute the change in lateral displacement after cycling load, whereas the secant stiffness is used to analyze the soil-pile stiffness at each cycle. This stiffness appeared to increase in the first 20 cycles and started to decrease due to soil yielding and degradation effects.

5. A simple approach has been proposed to link the cumulative lateral pile movement to the number of cycles using a logarithmic and power function. The fitting parameters were found to be correlated with the cyclic amplitude and maximum cyclic load applied. However, more tests with a lower cyclic amplitude must be performed to extensively investigate the influencing factors due to cycling loading.

6. Lateral cyclic load ratios $\zeta_b$ of less than 0.6 were determined to generate small pile head displacement rates and provide stable responses, whereas piles above a ratio of 0.7 were generally unstable.

7. Cyclic bending profiles for different Collar Vanes are presented and it was found that the maximum moment increases with the number of cycles when $\zeta_b > 0.6$.

8. Cyclic torsional tests were influenced by the cyclic lateral test performed. Two torsional tests with the same cyclic characteristic loads showed different responses after different cyclic lateral load conditions.

However, all the above results on cyclic load effects have been obtained for particular conditions. More testing should be considered using different load combinations.

# CHAPTER 6

# NUMERICAL ANALYSIS OF HELICAL PILE WITH THE COLLAR VANE AND DESIGN EXAMPLE

## 6.1 Introduction

The main purpose of this chapter is to study the behavior of helical piles with a Collar Vane under torsional loads using a 3D finite element analysis and to show a comparison of the lateral and torsional performance of a standard foundation structure with the Collar Vane using a finite difference approach. The objectives of this chapter are:

- Validate PLAXIS 3D volume pile under torsional loads with currently published results with the objective of showing the FEM accuracy when predicting Torque and Rotation values.

- Model and validate a simplified Collar Vane model with results obtained from the cohesive test site using a Mohr-Coulumb constitutive soil model.

- Investigate the Collar Vane blade deformation under different torque levels and the interaction between the mobilized torsional resistance generated by the Collar Vane blades.

- Investigate the influence of soil strength and soil stiffness on the Collar Vane torsional capacity by performing a sensitivity analysis varying the soil parameters. Collar Vanes CV 2-2 and CV 3-3 will be implemented in the analysis.

- Compare the performance of the Collar Vane to standard foundation structures used for transportation structures using a finite difference method. Both cohesive and granular soil conditions are considered in this analysis.

- Show a road sign structure design example to highlight the applicability of the Collar Vane for lightweight transportation structures.

The Mohr-Coulomb constitutive soil model is widely used in geotechnical engineering to model the behavior of soils under various loading conditions. Mohr-Coulomb uses a 'linear-elastic-perfectly-plastic' constitutive model, where the stress-strain relationship develops linearly up to a point of yielding, and perfectly plastic beyond it, which is not always the case in reality. However, will serve as a first-order approximation to simulate the Collar Vane response under torsional load due to its simplicity and low computational cost.

This chapter will present the model assumptions, input parameters, and results of the models. Also, a summary will be presented, and recommendations for future numerical analysis work.

## 6.2 Validation of PLAXIS 3D Under Torsional Loads with Cases of Study
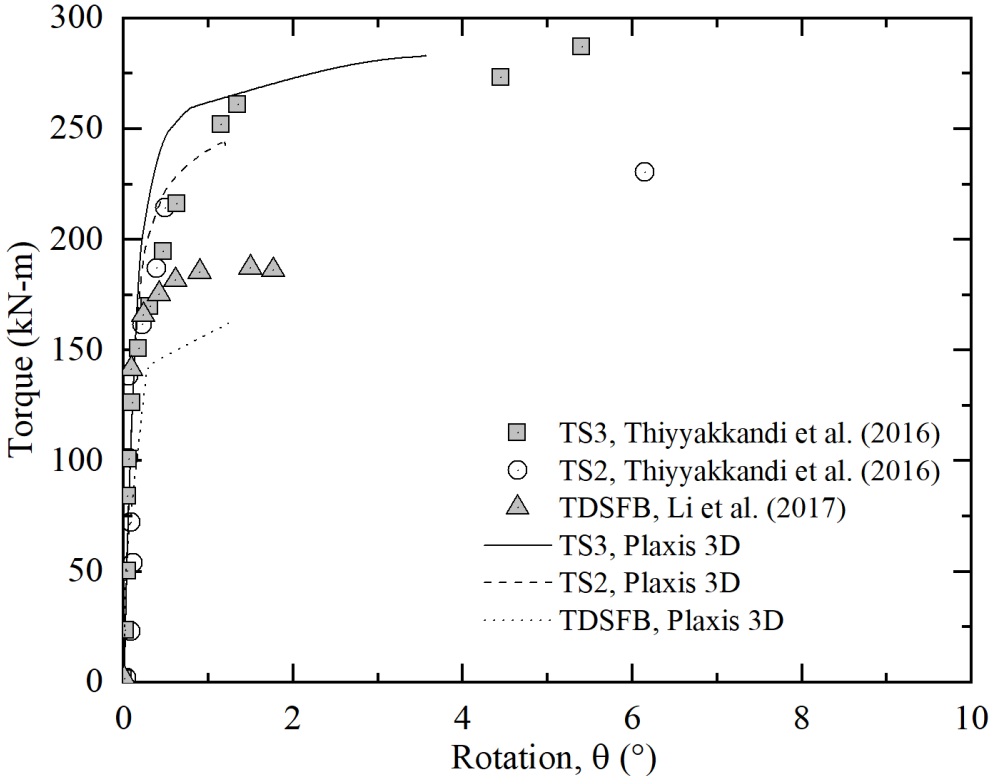


Figure 6.1: Validation of PLAXIS 3D with cases of study for torsional loading.

Two cases of study of drilled shafts subjected to torsion were modeled in PLAXIS 3D in order to validate the volume pile element by comparing it with the measured data. The

first example is drawn from Thiyyakkandi *et al.* (2016) study where two test drilled shafts were considered in his study: two 1.22 m diameter × 5.49 m deep (TS2 and TS3) installed in a mixed soil profile composed of granular and cohesive materials with different thickness. In PLAXIS, the pile was modeled using a volume pile, and soil layers using a Mohr-Coulumb constitutive soil model. Moreover, another example was drawn from Li *et al.* (2017), a 0.9 m diameter × 5.50 m deep drilled shaft installed in a medium-stiff clay. The soil profiles were obtained from their subsurface exploration results. The soil profile for both studies was modeled using Mohr-Coulomb constitutive soil model choosing: drained, for the granular soils; and undrained B type, for the cohesive material.

The validation model results are shown in Figure 6.1. It can be seen the good approximation between the volume pile and the real pile. In general, it can be concluded that the volume pile shows a good performance in terms of being subjected to torsional loads and simulating the pile-soil interaction.

## 6.3   Collar Vane Modeling Using PLAXIS 3D for Torsional Loading

The design of the model in PLAXIS 3D begins with the soil model. The soil model helps in defining the soil stratigraphy by drilling boreholes and including the soil properties. This analysis employs undrained B-type drainage, which allows effective stress analysis with undrained strength parameters. Soil parameters are shown in Table 6.1. A Mohr-Coulomb (MC) constitutive soil model was used for the numerical analysis due to its simplicity, and reduced computational cost. A strength reduction factor $R_{\text{inter}}$ was used to reduce the friction between the structural element and the soil (Brinkgreve *et al.*, 2013). A value of 0.5 is recommended for interaction between clay/steel as reported from Brinkgreeve & Shen (2011).

This model can be used for first approximation since the MC model overestimates soil stiffness due to its inability to capture stiffness degradation imposed by mobilization of shear strength (Govindasamy *et al.*, 2020). Thus, torsional capacities are dependent on the

Table 6.1: Properties of the soil in PLAXIS 3D

| Parameter | Name | Value | Unit |
|---|---|---|---|
| Material Model | Type | MC | - |
| Drainage Type | Type | Undrained B | - |
| Unit weight | $\gamma_{\text{unsat}}$ | 17 | kN/m$^3$ |
|  | $\gamma_{\text{sat}}$ | 18 | kN/m$^3$ |
| Elastic modulus | $E$ | $20 \times 10^3$ | kN/m$^2$ |
| Poisson's ratio | $\nu$ | 0.31 | - |
| Undrained shear strength | $s_u$ | 80 | kN/m$^2$ |
| Interface reduction factor | $R_{\text{inter}}$ | 0.5 | - |

stiffness parameters. Moreover, soil disturbance associated with installation effects is not considered. Bagheri & El Naggar (2015) states that the helical pile shaft causes significant disturbance to adjacent soil and the mobilized undrained shear strength would be completely remolded. Therefore, assuming a residual undrained shear strength would account for installation effects.

Table 6.2: Properties of the volume pile.

| Parameter | Name | Value | Unit |
|---|---|---|---|
| Material Model | - | Linear Elastic | - |
| Drainage Type | - | Non-porous | - |
| Unit weight | $\gamma$ | 78 | kN/m$^3$ |
| Elastic modulus | $E$ | $2 \times 10^8$ | kN/m$^2$ |
| Poisson's ratio | $\nu$ | 0.3 | - |

The properties of the volume pile and the Collar Vane plates are summarized in Tables 6.2 and 6.3. In order to avoid the influence of size effect on the calculation results, the total height of the model is three times the embedded length of the volume pile, and the whole width and length of the model are ten times the wider Collar Vane diameter (0.9 m) as shown in Figure 6.2 where a triangular shaped mesh is generated with a medium size. The volume pile was modeled as a non-porous linear elastic material with an O.D. equal to

Table 6.3: Properties of the Collar Vane plates.

| Parameter | Name | Value | Unit |
|-----------|------|-------|------|
| Material Type | - | Elastic | - |
| Unit weight | $\gamma$ | 78 | kN/m$^3$ |
| Elastic modulus | $E$ | $2 \times 10^8$ | kN/m$^2$ |
| Poisson's ratio | $\nu$ | 0.35 | - |
| Thickness | $d$ | $0.0095^\ddagger$ or $0.0127^\dagger$ | m |

**Note**: $^\ddagger$ CV 2-2, $^\dagger$ CV 3-3.
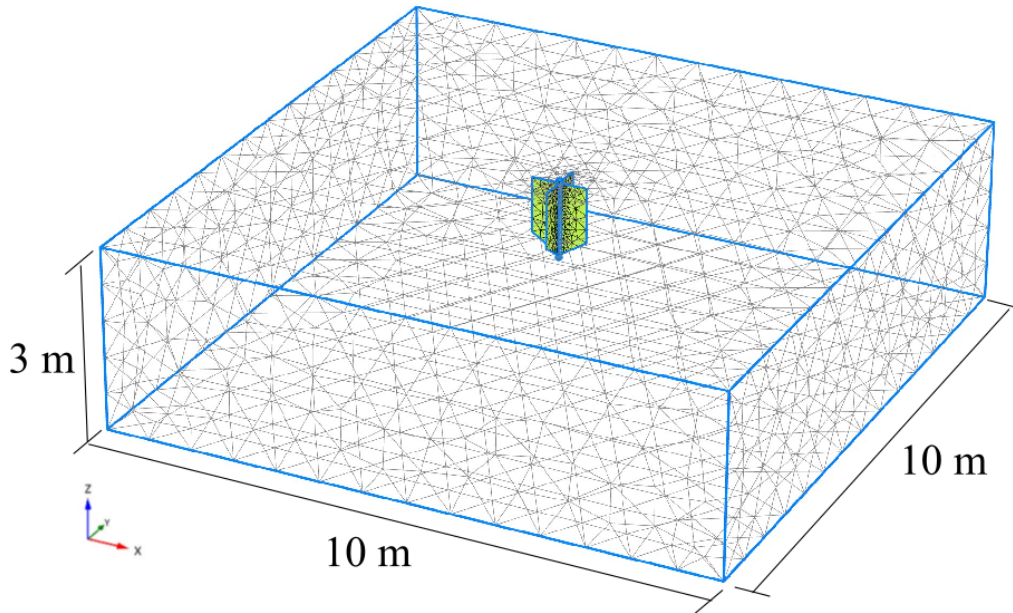


Figure 6.2: PLAXIS 3D finite element model.

0.0889 m and a length equal to the total height of the Collar Vane with the objective of plotting the torsional resistance provided by the Collar Vane without the helical pile contribution. The Collar Vane plates were modeled as a plate element that crosses the volume pile shaft simulating a modular Collar Vane element. The loads were applied to a loading arm modeled with the same properties as the Collar Vane plates but with a

151

thickness equal to $d = 0.10$ m and placed at the top of the volume pile. Two point loads on the loading arm were located at a distance of -0.5 and 0.5 m from the center line to apply a pure torsion load on the loading arm. The interfaces were created in the Collar Vane plates and around the volume pile to simulate the soil-structure interaction.
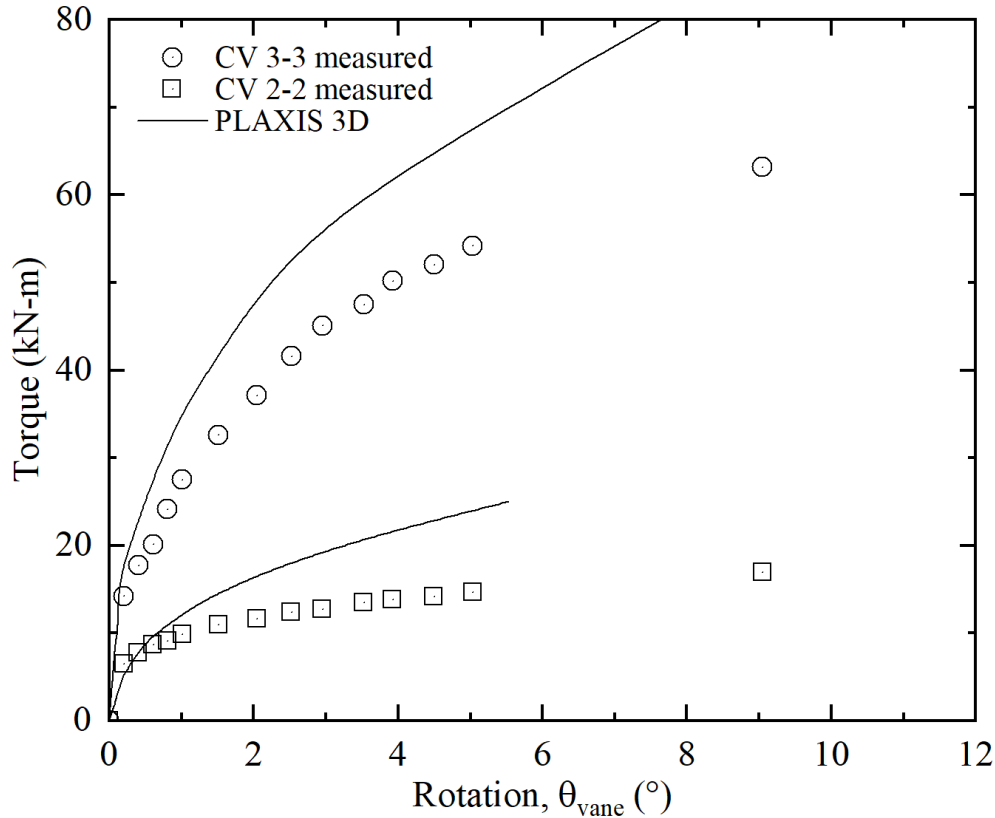


Figure 6.3: Measured and predicted torsional results in cohesive soil.

Figure 6.3 illustrates the torque-rotation behavior. In general, PLAXIS 3D presents good agreement with the measured values at low rotation values. However, the model fails to capture the stiffness degradation associated with the mobilization of shear resistance at relatively high load levels. Furthermore, the plate deformation is shown in Figure 6.4. It can be seen that the higher displacements are taking place in the upper portion of the plate in the tip section as observed in field results depicted in Figure 4.15(c). This non-uniformity displacement is associated with the impossibility of the Collar Vane rotating as a rigid element. The torsional load applied at the top is not being transferred
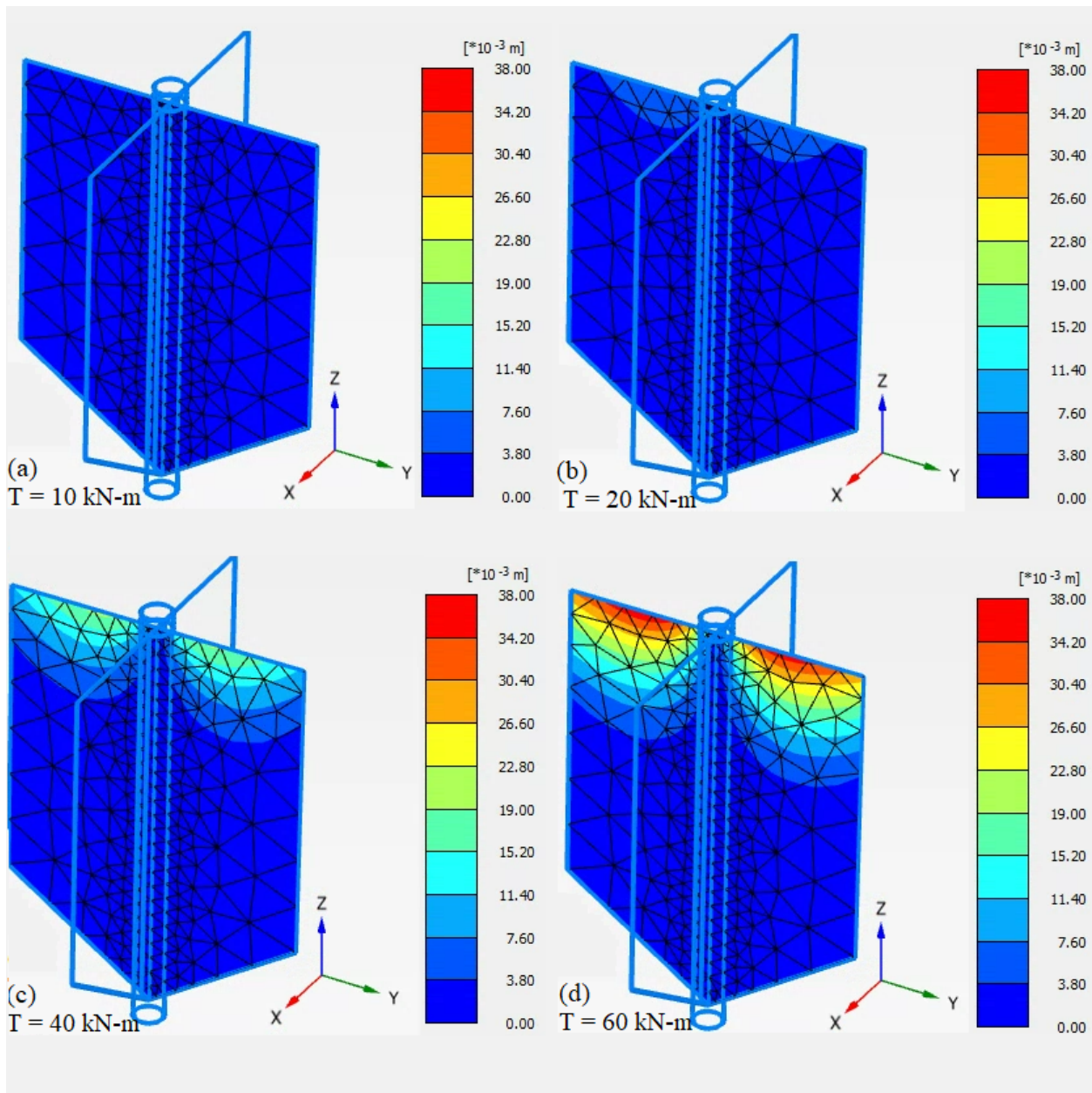
Figure 6.4: Collar Vane CV 3-3 plate displacements for different torsion values.

to the adjacent soil uniformly, developing a non-uniform shear strength mobilization as depicted in Figure 6.5. The mobilization of shear strength starts near the top, where the displacements are the greatest, whereas at the bottom it did not develop any shear resistance with torque values up to 60 kN-m. Moreover, this shear mobilization was observed during the torsional field test depicted in Figure 6.6(a). The Figure shows the
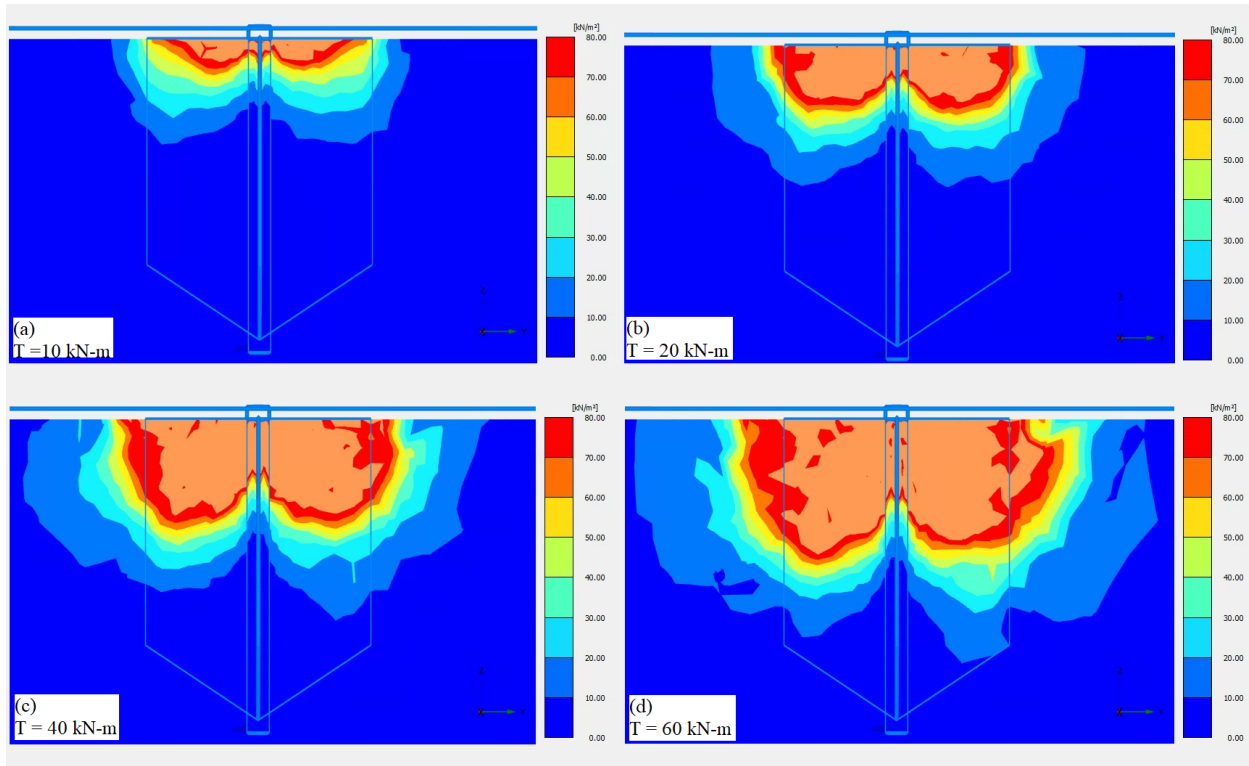
Figure 6.5: Collar Vane CV 3-3 mobilized shear strength during torsional loading.
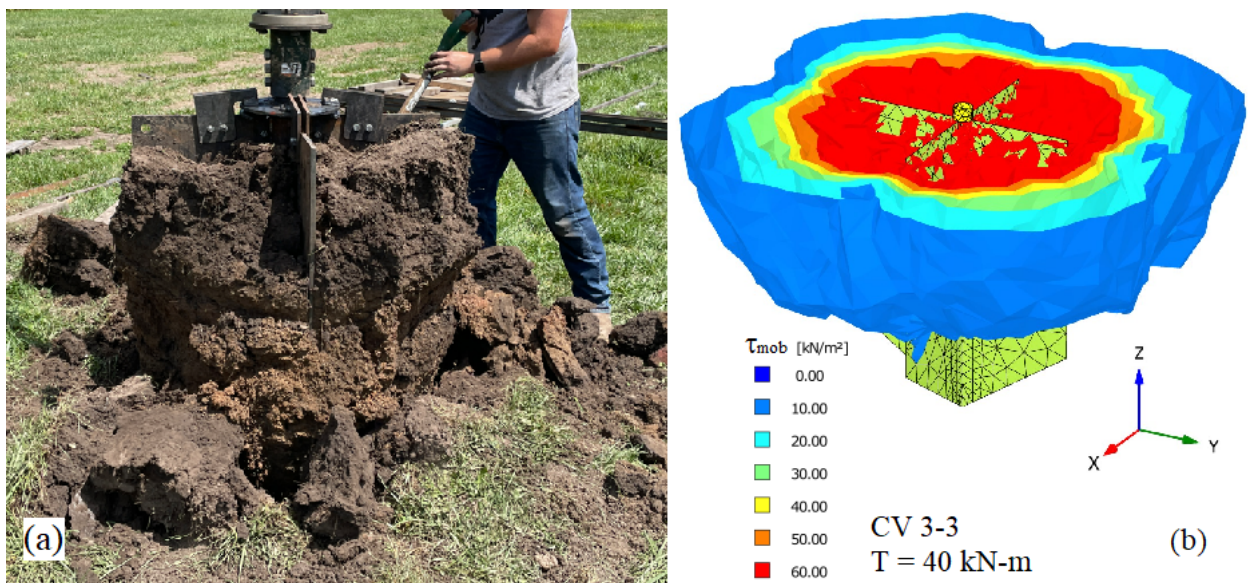


Figure 6.6: Mobilized shear resistance: (a) CV2 3-3 being removed after test and (b) 3D FEM model.

mobilized undrained shear strength observed in the field and the 3D view of the cylindrical shear failure around the Collar Vane plates.

## 6.4 Parametric Study of the Collar Vane Under Torsional Loads
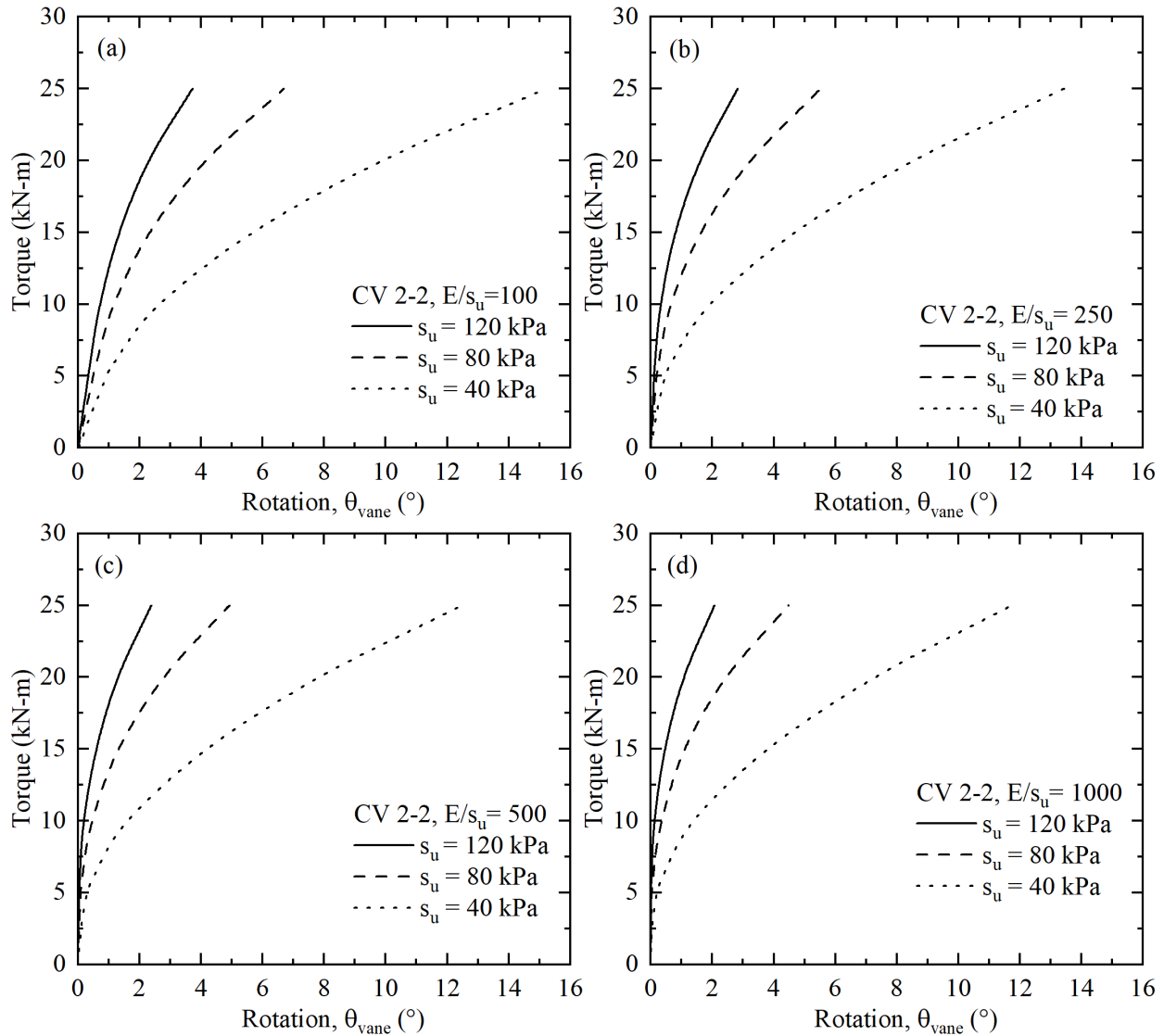


Figure 6.7: CV 2-2 torsional response. Changing $s_u$ for a different set of $E/s_u$.

A parametric study of soil sensitivity is performed using PLAXIS 3D with the objective of the study of how the variations in the soil parameters influence the Collar Vanes CV 2-2 and CV 3-3 response under torsional loading. Two different parameters were considered to evaluate the performance of the Collar Vanes: the undrained shear resistance, $s_u$, and the soil's elastic modulus, $E$.
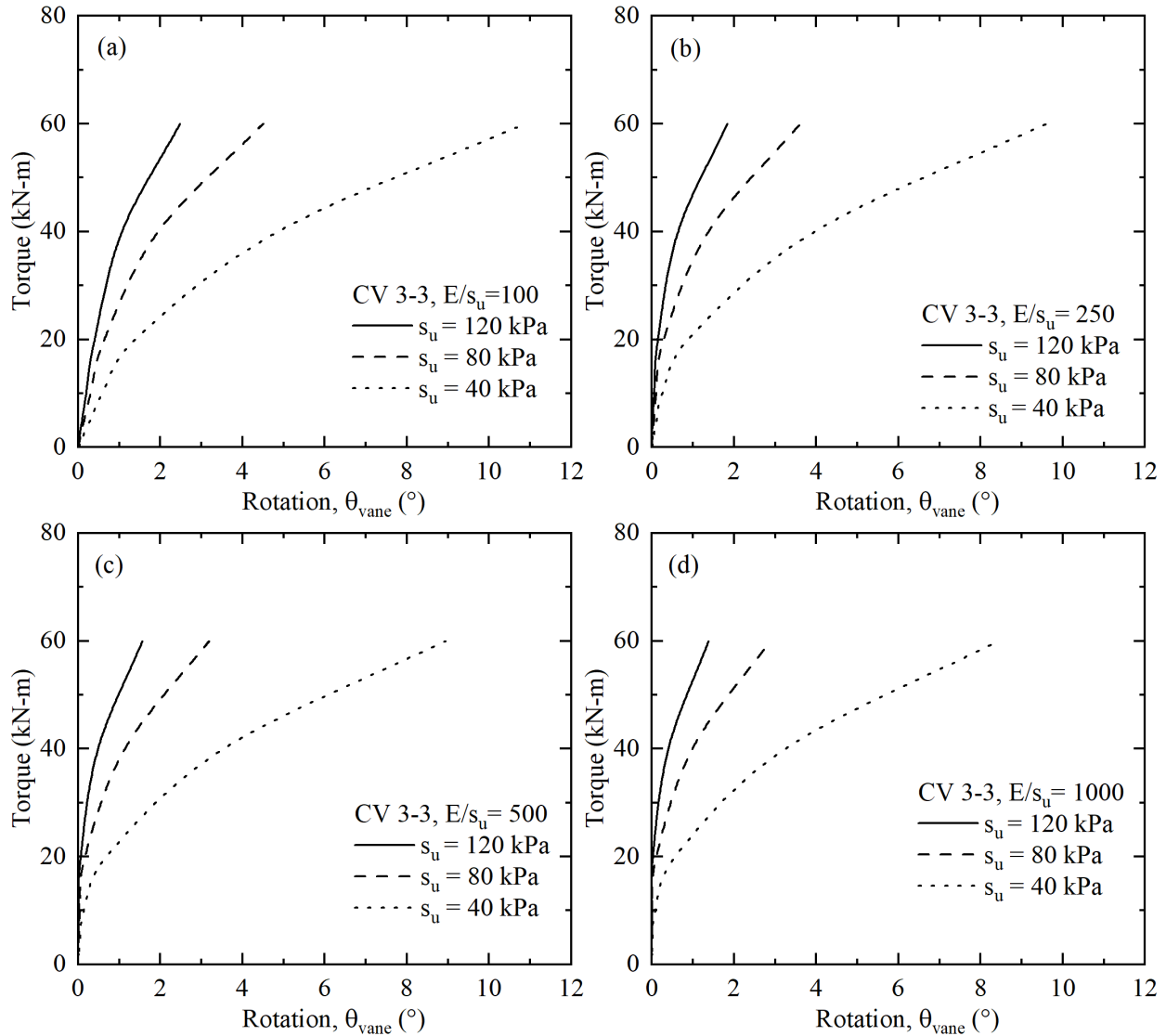
Figure 6.8: CV 3-3 torsional response. Changing $s_u$ for a different set of $E/s_u$

Figure 6.7 shows the influence of $s_u$ on the torsional response for a different set of $E/s_u$ using the Collar Vane CV 2-2. The plots highlight the influence of the undrained shear resistance on the torsional capacity where high values of rotation were present in the soil with low $s_u$ even when the stiffness ratio, $E/s_u$, is high. The torsional response for high $s_u$ is not increased significantly when $E/s_u$ is high. Moreover, Figure 6.8 is shown the same study for CV 3-3 where the same behavior was observed. Figure 6.9 highlights the influence of the stiffness ratio $E/s_u$ with varying undrained shear strength. It can be drawn that the
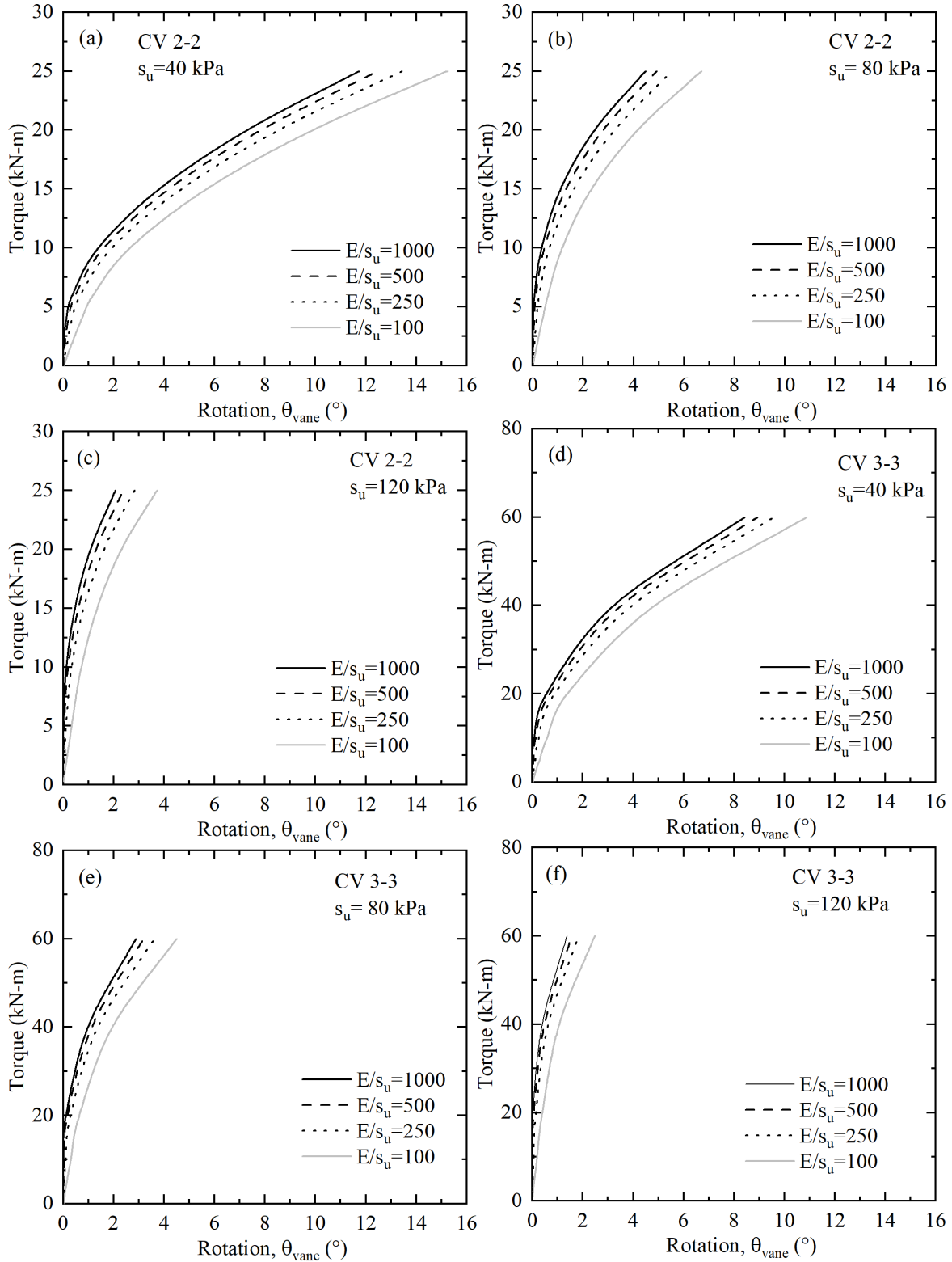
Figure 6.9: Torsional response variation changing $E/s_u$ for a different set of $s_u$. (a-c) CV 2-2 and (d-f) CV 3-3.

increment in torsional capacity is not as noticeable when the stiffness ratio increases and the undrained shear resistance has a major influence on the torsional capacity.

## 6.5 Comparison of the Collar Vane with a Standard Foundation Structure

The objective of this project is to present a cost-effective and more efficient foundation alternative for lightweight transportation structures. It was shown that the Collar Vane effectively increases the lateral and the torsional resistance of helical piles. However, is necessary to compare the performance of the Collar Vane with long-established foundations structures. This section will study the performance of the Collar Vane compared to traditional foundation elements used for sign structures using a finite difference program and well-known methodologies used in industry.

A standard foundation structure for a traffic signal, highway signing, and lighting is presented in Maine DOT (2020) handbook (Item No. 626.411). The structure consists of a drilled shaft foundation with the parameters listed in Table 6.4. The shafts use six longitudinal reinforcement bars with a US Std. #6 size with a concrete-to-cover distance of 51 mm, and for the transversal reinforcement, a US Std. #3 size spaced every 305 mm as depicted in Figure 6.10. LPile is used to model the drilled shaft since is possible to input all these reinforcement properties.

Table 6.4: Drilled shaft geometry and reinforcement properties.

| Parameter | Value | Unit |
|---|---|---|
| Shaft Diameter, $D_{\mathrm{shaft}}$ | 0.46 | m |
| Shaft Length, $L_{\mathrm{shaft}}$ | 1.67 | m |
| Concrete Compressive Strength, $f'_c$ | 28 | MPa |
| Reinforcement Yield Strength, $f_y$ | 420 | MPa |
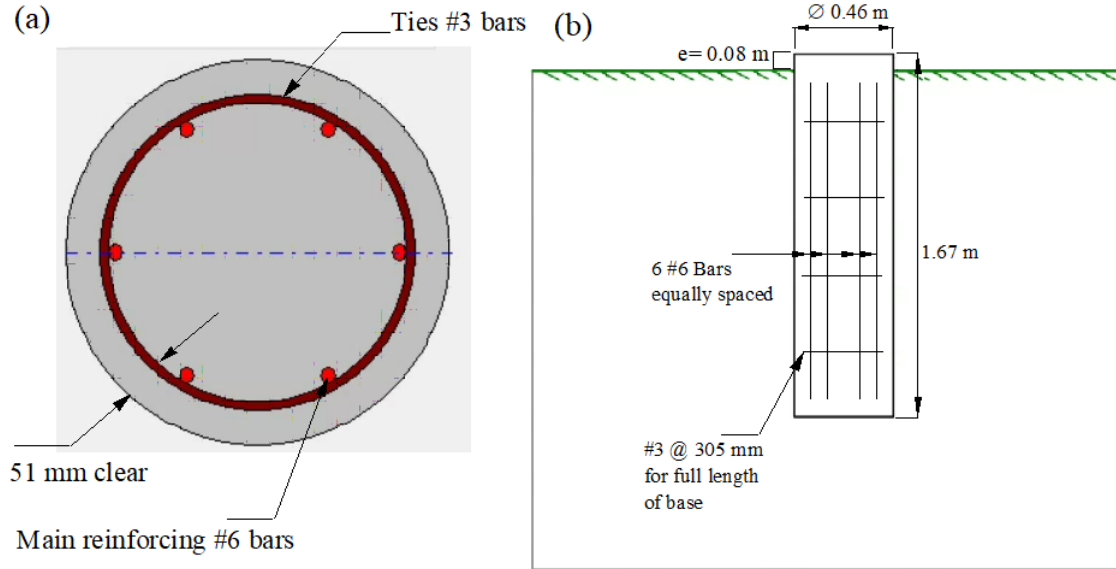
Figure 6.10: Drilled shaft properties: (a) reinforcement cross-section, (b) side view.

### 6.5.1 Lateral Load Comparison

The modeling of the pile using LPile for lateral analysis starts by defining the soil profiles. Two different soil types: a homogeneous cohesive soil, and a granular soil are considered for the analysis. The soil consists of a homogeneous 4 m thick layer with the properties listed in Table 6.5. The $p - y$ models chosen were 'stiff clay without free water' (Reese *et al.*, 1975), for the cohesive soil; and 'Sand' (Reese *et al.*, 1974), for the granular material. The applied load has an eccentricity of 0.08 m above the mud line, the same used with the Collar Vane lateral test.

Table 6.5: Soil parameters used in LPile for lateral analysis.

| Parameter | Cohesive Soil | Granular Soil | Unit |
|---|---|---|---|
| Unit Weight, $\gamma$ | 18 | 17 | kN/m$^3$ |
| Undrained Shear Resistance, $s_u$ | 120 | - | kN/m$^2$ |
| Friction Angle, $\phi$ | - | 45 | $^\circ$ |
| Soil Modulus, $k$ | - | 60 | MN/m$^3$ |
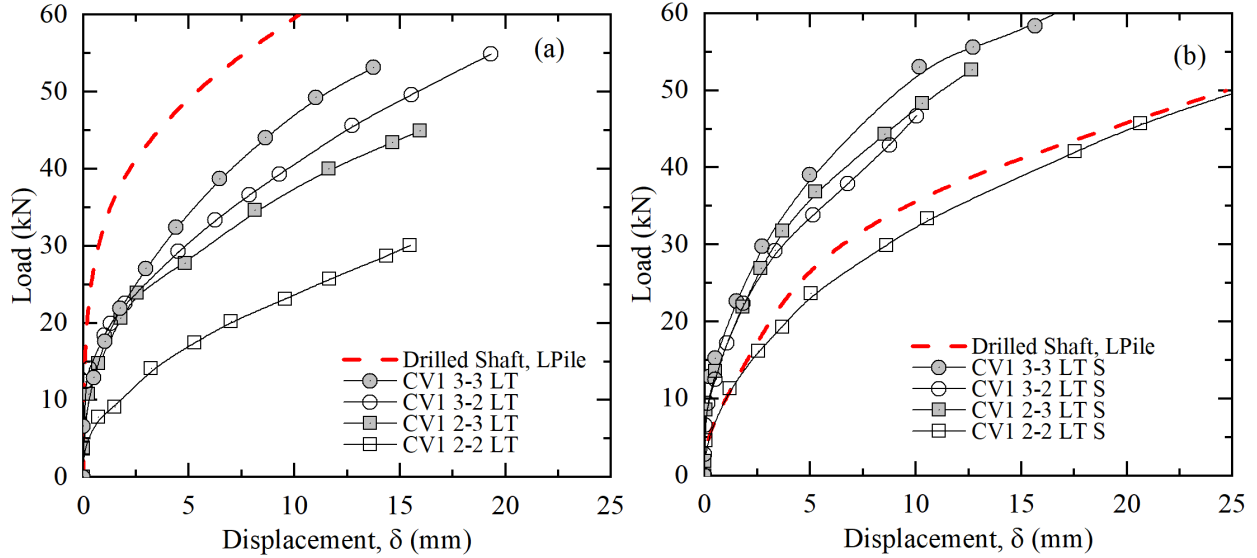
Figure 6.11: Drilled shaft and Collar Vane lateral response: (a) cohesive soil and (b) granular soil.

The comparison of the Collar Vane lateral response to the drilled shaft for the medium-stiff homogeneous clay and the medium-dense homogeneous sand are shown in Figure 6.11(a) and Figure 6.11(b), respectively. In the cohesive soil, the Collar Vane CV 2-2 presents the same response as the drilled shaft up to a load of 5 kN; CVs 2-3, 3-2, and 3-3, present the same lateral response as the drilled shaft up to a load of 11 kN as shown in Figure 6.11(a). Nevertheless, the Collar Vane has a better performance than the drilled shaft in the sand site. The drilled shaft starts to have a displacement at low load levels whereas the Collar Vane starts deflection at a load of 10 kN as depicted in Figure 6.11(b). In general, wind loads that act on signal panels transmit a relatively low shear force at the foundation base. The Collar Vane has the potential to sustain this type of load but some limitations arise when considering the eccentric load that will induce a turning moment at the base foundation. The section 6.6 shows a road sign design example that will quantify the amount of force that acts on the top of a foundation element due to wind loads.

160

## 6.5.2 Torsional Capacity Comparison

Usually, the shaft length is controlled by the soil torsion capacity. The torsional capacity of the drilled shaft can be addressed using the Equations (2.15) and (2.16) using Coleman & Arcement (2002) method for the cohesive soil where it is assumed an $\alpha = 0.43$ for an $s_u = 120$ kPa. For the granular material, The effective overburden stress is computed at the midpoint of the shaft length and the value of $\beta$ is estimated using the back-calculated value from the Collar Vanes results in the sand which has a minimum value of 5.5.

Table 6.6: Drilled shaft torsional capacity in cohesive soil.

| | | | |
|---|---|---|---|
| Undrained Shear Resistance | $s_u=$ | 120 | kPa |
| Adhesion Factor | $\alpha=$ | 0.43 | - |
| Drilled Shaft side Resistance | $T_s = \frac{1}{2}\pi D^2 L \alpha s_u =$ | 28.64 | kN-m |
| Drilled shaft Toe Resistance | $T_t = \frac{1}{12}\pi D^3 \alpha s_u =$ | 1.31 | kN-m |
| Nominal Total Torsion Resistance | $T_n = T_s + T_t =$ | 29.95 | kN-m |

Table 6.7: Drilled shaft torsional capacity in granular soil.

| | | | |
|---|---|---|---|
| $\beta$-coefficient | $\beta=$ | 5.5 | - |
| Effective Overburden Stress | $\sigma'_v=$ | 14 | kN/m$^2$ |
| Drilled Shaft Side Resistance | $T_s = \frac{1}{2}\pi D^2 L \beta \sigma'_v =$ | 42.74 | kN-m |
| Drilled Shaft Toe Resistance | $T_t = \frac{1}{12}\pi D^3 \beta \sigma'_v =$ | 1.96 | kN-m |
| Nominal Total Torsional Resistance | $T_n = T_s + T_t =$ | 44.7 | kN-m |

Tables 6.6 and 6.7 summarizes the nominal torsional capacity calculation process for the standard foundation element in the cohesive and cohesionless test sites, respectively. Figure 6.12 shows the comparison of the isolated Collar Vane torsional response to the drilled shaft capacity. The Collar Vanes 3-2 and 3-3 have better performance in the sand compared to the drilled shaft. However, in the cohesive tests site, it is shown that only the CV1 2-2 had under-performance than the drilled shaft. The section 6.6 will put in contrast how much
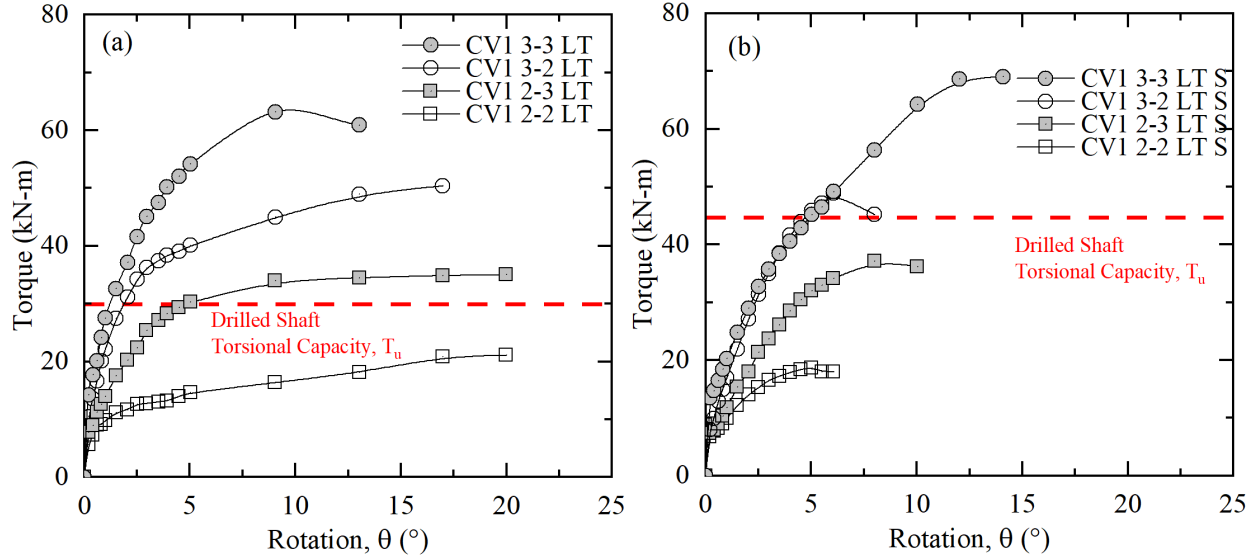
Figure 6.12: Drilled shaft and Collar Vane torsional capacity: (a) cohesive soil and (b) granular soil.

torque is required to support a roadside sign structure and verify the applicability of the Collar Vane to lightweight transportation structures under torsional loads.

### 6.5.3 Axial Capacity Comparison

The axial capacity of the drilled shaft is computed using the CPT-based LCPC method (Bustamante & Gianeselli, 1982) which uses the CPT tip resistance to estimate the tip and side resistance.

Table 6.8: Drilled shaft axial capacity in cohesive and granular soil.

| Parameter | | Cohesive | Granular | Unit |
|---|---|---|---|---|
| Shaft End Bearing Area | $A_{\text{shaft}}$ | 1.17 | | $\text{m}^2$ |
| Shaft Perimeter | $P_{\text{shaft}} =$ | 1.45 | | m |
| Unit End Bearing Resistance | $q_p =$ | 435 | 2400 | kPa |
| Unit Side Resistance | $q_s =$ | 35 | 80 | kPa |
| End Bearing Resistance | $R_p = q_p A_{\text{shaft}} =$ | 72.29 | 398.86 | kN |
| Side Shear Resistance | $R_s = q_s L P_{\text{shaft}} =$ | 58.45 | 133.60 | kN |
| Ultimate Axial Resistance | $T_u = R_p + R_s$ | 130.74 | 532.46 | kN |

162

Table 6.8 summarizes the calculation steps to estimate the drilled shaft ultimate axial capacity in both test sites using conventional and widely-used methods. The unit resistances are obtained from the average tip resistance $q_c$ in the soil profile shown in Figure 3.10.

Table 6.9: Helical pile axial capacity in cohesive and granular soil.

| Parameter | | Cohesive | Granular | Unit |
|---|---|---|---|---|
| Helical Pile Correlation Factor | $K_t =$ | 23 | | $m^{-1}$ |
| Installation Torque | $T_m=$ | 11.83 | 11.63 | kN-m |
| Ultimate Axial Resistance, Eq. (2.7) | $T_u=$ | 272.09 | 267.49 | kN |

Helical pile axial capacity is shown in Table 6.9 and it is computed as $T_u = K_t T_m$. Where $T_m$ is the installation torque measured for the last meter from Figure 3.25; and $K_t$, is the correlation factor for an 89 mm diameter cylindrical shaft (Livneh & El Naggar, 2008; Hoyt & Clemence, 1989). It is demonstrated that the helical pile outperforms the drilled shaft axial nominal capacity in the cohesive site. However, the drilled shaft has better performance in the sand site but is important to note that for lightweight structures the axial capacity provided by HP will be enough to resist the loads.

## 6.6   Roadside Sign Structure Design Example

A road sign structure foundation design example is presented in Colorado DOT (2020) for a cantilever structure in a drilled shaft. Most of their assumptions will be drawn in the example proposed in this section to show a brief design example for a roadside sign on a single support as shown in Figure 6.13 following AASTHO specifications. The sign structure used is a *3 digit gore exit (E5-1a-90)* with standard dimensions 2.3 m x 1.5 m (FHWA, 2009). Table 6.10 summarizes the sign structure properties and dimensions used to estimate the loads.
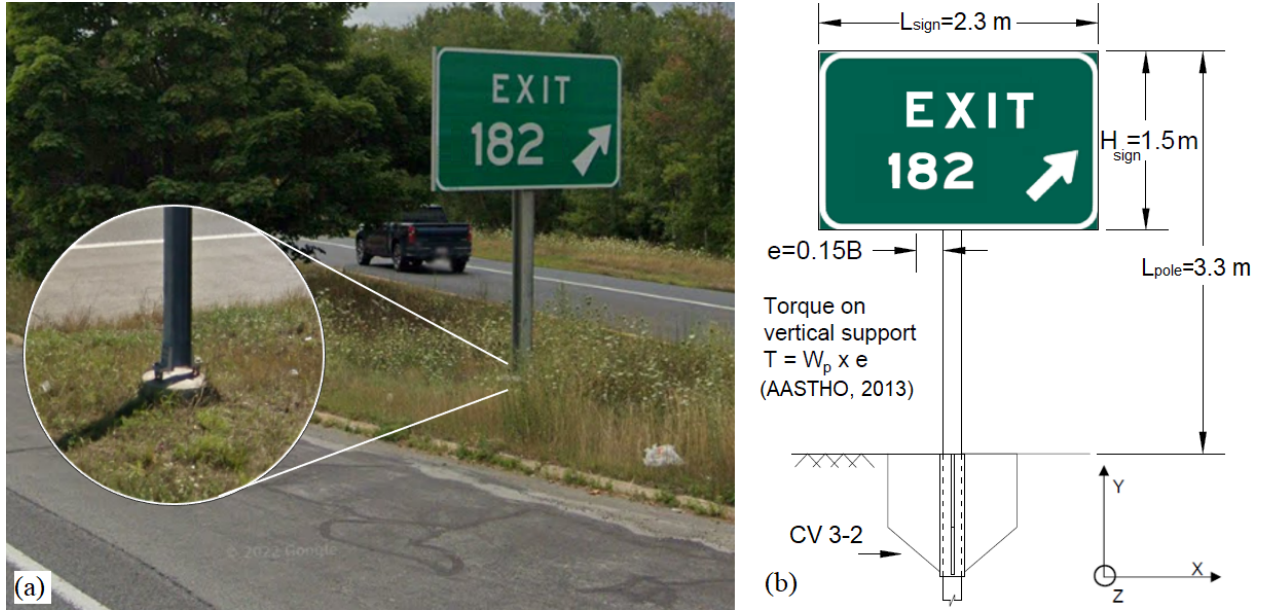
Figure 6.13: (a) Roadside sign used for design example (Google Street View, 2023) and (b) roadside sign dimensions.

Table 6.10: Sign structure properties and dimensions.

| Parameter | | Value | Unit |
|---|---|---|---|
| Steel Unit Weight | $\gamma_{\text{steel}}=$ | 76.9 | kN/m$^3$ |
| Aluminum Unit Weight | $\gamma_{\text{aluminum}}=$ | 27.5 | kN/m$^3$ |
| Pole Length | $L_{\text{pole}}=$ | 3.3 | m |
| Pole Diameter (O.D.) | $D_{\text{pole}}=$ | 0.09 | m |
| Pole Wall Thickness | $t_{\text{pole}}=$ | 7.6 | mm |
| Sign Panel Length | $L_{\text{sign}}=$ | 2.3 | m |
| Sign Panel Height | $H_{\text{sign}}=$ | 1.5 | m |
| Sign Panel Area | $A_{\text{sign}}=$ | 3.5 | m$^2$ |

The wind loads are calculated according to AASHTO (2015) specifications corresponding to a 10-yr mean recurrence interval basic wind speed for a roadside sign structure using Equation (6.1)

$$P_z = 0.613 K_z K_d G V^2 C_d \ \ (\text{Pa}) \qquad (6.1)$$

164

The parameters necessary to estimate the wind loads are listed in Table 6.11. The basic wind speed, $V$, is the nominal 3-s gust wind speed at 10 m above the ground; $K_z$ depends on the height of the structure, if the structure is less than 5 m, then $K_z = 0.84$; the directionality factor, $K_d$, for a sign support is 0.85; Gust Effect Factor is taken as a minimum value of 1.14; and the Wind Drag Coefficient for a roadside panel sign with $L_{\text{sign}}/H_{\text{sign}} < 2.0$ is $C_{\text{d-sign}} = 1.19$, and for the member is $C_{\text{d-pole}} = 0.45$ (AASHTO, 2013, 2009).

Table 6.11: Wind load parameters for roadside sign example.

| Parameter | Value | Section-Reference |
|---|---|---|
| Basic Wind Speed, $V$ (m/s) | 34 | 3.8.2 (AASHTO, 2015) |
| Height and Exposure Factor, $K_z$ | 0.84 | 3.8.4 (AASHTO, 2015) |
| Directionality Factor, $K_d$ | 0.85 | 3.8.5 (AASHTO, 2015) |
| Gust Effect Factor, $G$ | 1.14 | 3.8.6 (AASHTO, 2015) |
| Drag Coefficient on Member, $C_{\text{d-member}}$ | 0.45 | 3.8.7 (AASHTO, 2015) |
| Drag Coefficient on Sign Panel, $C_{\text{d-sp}}$ | 1.19 | 3.8.7 (AASHTO, 2015) |

Replacing values listed in Table 6.11 into Equation (6.1), the wind pressure for the pole member and the sign panel is

$$P_{\text{z-member}} = 0.613 \cdot 0.84 \cdot 0.85 \cdot 1.14 \cdot 34^2 \cdot 0.45 = 260 \text{ Pa} \tag{6.2a}$$

$$P_{\text{z-sp}} = 0.613 \cdot 0.84 \cdot 0.85 \cdot 1.14 \cdot 34^2 \cdot 1.19 = 687 \text{ Pa} \tag{6.2b}$$

Table 6.12 shows the load calculations on the roadside sign structure. The dead loads of the pole member are estimated using the specifications of the helical pile shaft used in the test program. Ice loads are computed using a load of 145 Pa around the pole surfaces and one side of the sign panel. The wind load in the sign is $\text{WS}_{\text{z-sign}} = 2.50$ kN. Moreover, the wind acting on the sign pole must be also considered, assuming a rectangular pole with a

Table 6.12: Load calculations.

| Dead Loads of structural components (DC) | | | |
|---|---|---|---|
| Pole Weight | $DC_1 =$ | 0.49 | kN |
| Sign Weight[†] | $DC_2=$ | 0.53 | kN |
| Misc. Weight[‡] (Anchors and Sign Support) | $DC_3 =$ | 0.26 | kN |
| **Ice Load (IC)** | | | |
| Ice Loads (Sign Panel and Pole) | $IC =$ | 0.67 | kN |
| **Wind Load on Structure (WS)** | | | |
| Wind Pressure on Pole, Eq. (6.2a) | $P_{\text{z-pole}} =$ | 0.26 | kPa |
| Wind Pressure on Sign Panels, Eq. (6.2b) | $P_{\text{z-sp}} =$ | 0.69 | kPa |
| Pole Surface Area (along $x$-axis) | $A_{1x}=$ | 0.30 | m$^2$ |
| Sign Panels Surface Area (along $x$-axis) | $A_{2x}=$ | 3.45 | m$^2$ |
| Wind Load on Pole ($x, z$-direction) | $WS_{x,z-\text{pole}} =$ | 0.09 | kN |
| Wind Load on Sign Panel ($z$-direction) | $WS_{z-\text{sign}}=$ | 2.50 | kN |

**Notes:** [†] Assumed 5 mm Sign Thickness; [‡] 50% of Sign Weight.

width equal to 0.1 m, the wind load on the pole in the $x$- and $z$-direction are $WS_{\text{x,z-pole}} = 0.08$ kN.

Table 6.13 presents a summary of the unfactored at the top of the helical pile. The torsion load or moment around the $y$-axis in a roadside sign structure on a single support element (Figure 6.13b) is calculated using the formulation shown in AASHTO (2013) where $e$ is the load eccentricity that will induce a turning moment around the $y$-axis on the foundation base.

$$M_y = WS_{\text{z-sign}}(0.15B) = 0.88 \text{ kN-m} \tag{6.3}$$

The total factored force effects should be taken as

$$Q = \sum \gamma_i Q_i = \gamma_{\text{DC}}DC + \gamma_{\text{LL}}LL + \gamma_{\text{WS}}WS \tag{6.4}$$

where, $\gamma_{DC}$, $\gamma_{LL}$, and $\gamma_{WS}$ are the load factors for dead loads, ice loads, and wind loads, respectively. The factored loads for different load combinations are presented in Table 6.14. 'Strength I' is used to estimate the basic load combination related to the normal use of the structure without wind; for the load combination 'Extreme', the wind loads are already factored using Equation (6.1), and 'Service I' is for the normal operation of the structure (AASHTO, 2015).

Table 6.13: Unfactored loads at the top of the helical pile.

| Load | Description | Load Direction $(x, y, z)$ | Load (kN) | Moment Arm (m) | Moment Direction $(x, y, z)$ | Moment at the top of the HP (kN-m) |
|------|-------------|----------------------------|-----------|----------------|------------------------------|------------------------------------|
| $DC_1$ | Pole Weight | $y$ | 0.49 | - | - | - |
| $DC_2$ | Sign Weight | $y$ | 0.53 | - | - | - |
| $DC_3$ | Misc. Weight | $y$ | 0.26 | - | - | - |
| IC | Ice Loads | $y$ | 0.67 | - | - | - |
| $WS_{x\text{-pole}}$ | Wind on Pole | $x$ | 0.09 | 1.65 | $z$ | 0.15 |
| $WS_{z\text{-pole}}$ | Wind on Pole | $z$ | 0.09 | 1.65 | $x$ | 0.15 |
| $WS_{z\text{-sign}}$ | Wind on Signs | $z$ | 2.50 | 2.55 | $x$ | 6.40 |
| $WS_{z\text{-sign}}$ | Wind on Signs | $z$ | 2.50 | 0.35 | $y$ | 0.88 |

Table 6.14: Load combinations (AASHTO, 2013).

| Load Combination | $\gamma_{DC}$ | $\gamma_{LL}$ | $\gamma_{WS}$ | Description |
|------------------|---------------|---------------|---------------|-------------|
| Strength I | 1.25 | 1.6 | - | Gravity |
| Extreme Ia | 1.1 | - | 1.0 | Wind Max |
| Extreme Ib | 0.9 | - | 1.0 | Wind Min |
| Service I | 1.0 | - | 1.0 | Translation |

Table 6.15 shows the factored loads and moments at the top of the helical pile. The Collar Vane will support the axial force and torsion loads (Figure 6.11). However, to study the shear and moment loads acting simultaneously on the HP head, it will be necessary to perform a $p - y$ analysis. For reference, the helical pile shaft nominal moment capacity is

Table 6.15: Summary of factored loads and moments at the top of the helical pile.

| Load Combination | Axial (kN) | Moment about $x$-axis (kN-m) | Moment about $y$-axis[†] (kN-m) | Moment about $z$-axis (kN-m) | Shear in the $x$-axis (kN) | Shear in the $z$-axis (kN) |
|---|---|---|---|---|---|---|
| Strength I | 2.84 | - | - | - | - | - |
| Extreme Ia | 1.48 | 6.40 | 0.88 | 0.15 | 0.09 | 2.50 |
| Extreme Ib | 1.09 | 6.40 | 0.88 | 0.15 | 0.09 | 2.50 |
| Service I | 1.28 | 6.40 | 0.88 | 0.15 | 0.09 | 2.50 |

**Notes:** [†] $M_y$ to be used for torsion calculation

$M_n = 17.4$ kN-m. When multiplying the nominal capacity by the resistance factor one can obtain $\varphi M_n = 13.05$ kN-m. It was shown that the Collar Vane will reduce the amount of bending moment applied in the shaft as shown in Figures 4.6 and 4.7. Nevertheless, field testing and numerical analysis will be required to study the Collar Vane performance under a considerable amount of applied moment at the pile head.

Figure 6.14 presents a wind-load parametric analysis for a 1.5W:1H roadside sign subjected to a different set of loading conditions considering the basic wind speed for the State of Maine. Figure 6.14(a) presents the torsion load of a single supported sign at the base foundation in the function of the sign area for a different set of heights. It is important to note that the load acting on the sign panel depends on the sign's height according to Equation (6.1) as observed in Figure 6.14(b) where at $z = 6.1$ there is a change in the slope. Figure 6.14(c) presents the torsion loads (for a sign with a height $z < 9.1$ m) of a cantilever sign at the base foundation in function of the eccentricity. Figure 6.14(d) presents the shear forces at the base foundation for a different set of heights in function of the sign area.

## 6.7 Summary and Conclusions

A three-dimensional numerical analysis was performed using PLAXIS 3D software to study the torsional capacity of the Collar Vane installed in cohesive soil. Validation of the
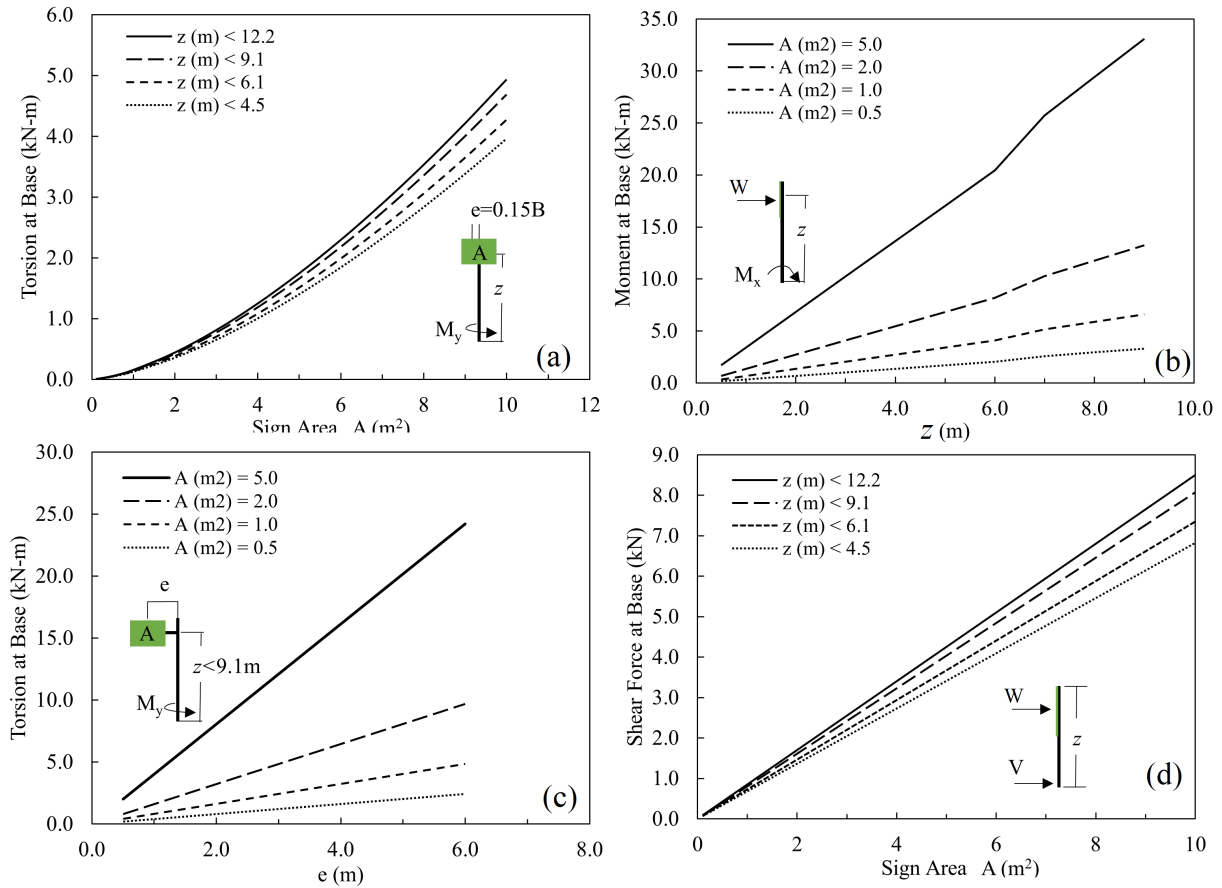
Figure 6.14: Loads at the foundation base: (a) Torsion single supported sign; (b) bending moment single sign; (c) torsion cantilever sign and; (d) shear single supported sign.

torsional field results, effects of variation in Collar Vane dimensions, soil elastic modulus, and undrained shear strength on the torsional capacity were also considered in this study. Moreover, a comparison of the Collar Vane to a conventional drilled foundation was carried out using the finite difference commercial software LPile. Also, a design example of a roadside sign structure was presented to demonstrate the applicability of the Collar Vane to support this type of structure. The following conclusions are drawn:

1. It is concluded that PLAXIS 3D can be used to perform a first-order approximation of the Collar Vane torsional response in cohesive soil. The model showed good agreement at low displacements levels. However, the model fails to capture the

stiffness degradation associated with the mobilization of shear resistance at relatively high load levels.

2. The model shows that the Collar Vane when subjected to torsion loads, the mobilization of shear resistance is not uniform around the Collar Vane plates. The plates start deforming at the top and eventually to the bottom as the load increases. This behavior has effects on the mobilization of shear resistance.

3. The parametric study varying $E$ and $s_u$, shows that the increase in the undrained shear resistance increases the torsional capacity more than increasing the stiffness ratio $E/s_u$.

4. The comparison of the Collar Vane to the drilled shaft demonstrated that the Collar Vane has resistance advantages over this type of foundation in a particular soil condition analyzed. The Collar Vane presents better lateral and torsion resistance in cohesionless soil. However, in the cohesive soil of the Collar Vane, the lateral response is the same as the drilled shaft up to a certain amount of load (10 kN), and the torsional capacity of the CV1 2-3, 3-2, and 3-3 were equal or higher than the drilled shaft. However, the comparison was performed only for two particular soil conditions which were the same where the Collar Vanes were tested.

5. An example design of a roadside sign structure with dimensions 2.3 x 1.5 m was used to demonstrate the applicability of the Collar Vane for this type of structures. The helical pile and the Collar Vane can support the imposed axial and torsional loads. However, to estimate shear and moment loads geotechnical resistance, it will be necessary to perform more field testing and numerical analysis.

# CHAPTER 7
## SUMMARY AND CONCLUSIONS

Helical piles are lightweight deep foundation elements that are screwed into the ground and efficiently generate geotechnical compressive and uplift resistance by mobilizing the shear strength of soil adjacent to helical plates that are welded to an extendable shaft. Helical piles are quick and simple to install, utilizing non-specialized equipment that is ubiquitous in the United States construction industry, eliminating the need for a specialty contractor. The helical pile is installed by rotating it into the soil by a torque motor and a crowd. As the helix is screwed into the soil, it generates resistance that allows the pile to support axial loads. The depth of the pile can vary depending on the load requirements and the soil conditions.

Helical piles are commonly used as an alternative to traditional deep foundations, such as driven piles or drilled shafts, or in situations where the soil conditions are not suitable for these types of foundations. They can be installed quickly, with minimal disturbance to the site, and they are suitable for a wide range of soil conditions. However, helical piles are precluded from many applications due to their inability to resist substantial lateral and torsional loads. To overcome this limitation, a novel easy-to-install Collar Vane, which increases the effective diameter attributed to the mobilization of geotechnical resistance in the upper soil profile, was incorporated to enhance the lateral and torsional capacity of helical piles. The Collar Vane consists of four steel fins welded to a hollow steel collar that wraps around, but does not interact with, the helical pile shaft. The Collar Vane is structurally coupled to the helical pile via flanges near the pile head to transfer lateral and torsional loads through the vane to the soil.

## 7.1 Summary of Objectives and Methods

The goals of the investigation were to detail the implementation of the Collar Vane into a helical pile to increase the lateral and torsional resistance. A different set of Collar Vane geometries and prototypes were tested in different soil conditions under static and cyclic loads. Furthermore, Collar Vanes were loaded to different load sequences to study the reduction in capacity when subjected to different loading combinations. Also, stiffness degradation, displacement accumulation, and increment in bending moment due to cyclic loading were addressed since is envisioned to implement the Collar Vane to support lightweight transportation structures. The methods implemented are:

1. Instrumenting a full-scale helical pile with: strain gauges along the shaft to measure deformation; calibrated string potentiometers to measure displacement; calibrated load cells to measure applied loads, and a calibrated pressure transducer to measure the pressure in the system. A DAQ system was implemented to collect the results automatically.

2. Helical piles were installed in two different soil conditions. The local test site consisted of a uniform medium-stiff cohesive soil. Furthermore, a sand pit was built to analyze the performance of the Collar Vane in a granular environment.

3. An exploratory geotechnical borings investigation was carried out at the test site locations with the objective of investigating the site's subsurface conditions. Cone penetration test soundings; standard penetration test, with sample recovering for index parameters; and field shear vane tests were used to characterize the testing site.

4. A lateral and torsional monotonic loading protocol was designed specifically to test the Collar Vanes in a timely manner. The loading protocol consisted of small load increments for a short period of time. Torsional loads were applied until the Collar Vane shared the soil or the hydraulic jack ran out of stroke.

5. Cyclic loading was implemented using a hydraulic controller to apply approximately 1000 lateral and torsional loads at a frequency of 0.125 Hz. Different cyclic load ratios were performed to study the CV strain accumulation.

6. Compare the Collar Vane response to the standard foundation elements to highlight the helical pile effectiveness with the Collar Vane.

## 7.2 Summary and Conclusions

This study presents the field results of a full-scale helical pile tested with different Collar Vanes configurations subjected to monotonic lateral, monotonic torsional, cyclic lateral, and cyclic torsional loads installed in cohesive and granular soils. Field results demonstrated that:

1. Heavily instrumented full-scale lateral and torsional load tests demonstrate the substantial increase in lateral and torsional geotechnical resistance of helical piles incorporating an easy-to-install Collar Vane at the pile head.

2. The helical pile lateral capacity was increased using different Collar Vanes prototypes (i.e., CV1 and CV2). Results suggest that the lateral response of CV1 and CV2; using a round shaft or square shaft is practically the same based on the tests performed in the cohesive soil site.

3. The Collar Vane transfers external lateral and torsional loads to the adjacent soil through the Collar Vane flanges. It was demonstrated that the Collar Vane carries up to 90% of the lateral loads applied. Moreover, a substantial reduction in bending moments in the helical pile shaft was observed. Meaning that the required section modulus can be reduced making possible a more efficient pile design, which is an added benefit of the Collar Vane.

4. Torsional capacity based on field results is substantially increased when the Collar Vane is installed. The one-piece Collar Vane has better performance carrying

173

torsional loads than the two-piece Collar Vane. The one-piece Collar Vane presents more torsional resistance due to a more uniform mobilization of shear resistance. The CV1 was manufactured as a modular section where the four fins are welded to the collar whereas the CV2 consists of two sections that are connected by bolts in the collar shaft.

5. Torsional capacity was evaluated using simple tractable models. For the cohesive material, $\alpha$ methods tend to overestimate the capacity ratio, whereas the CPT-based methods show the best average capacity ratio. However, for the granular soil, conventional $\beta$ methods underpredicted the capacity significantly due to an underestimation of the $\beta$-coefficient; only UIUC and Doan & Lehane (2021) show the best capacity ratios. Two-piece Collar Vane exhibited the largest scatter of the capacity ratio, while one-piece Collar Vane predictions were consistent.

6. In the cyclic test, the Collar Vane had a significant increase in the accumulated displacement within the first 100 cycles. The same was observed in the accumulated bending moment and rotation. Results suggest that when the cyclic ratio $\zeta_b > 0.6$ a ratcheting displacement will take place and a cumulative displacement will be observed.

7. A simple approach to determine the cumulative lateral displacement of the Collar Vane is proposed. The expression correlates characteristics of the cyclic load, the initial displacement, and the number of cycles to the lateral accumulated displacement.

8. A comparison of the Collar Vane performance to a standard foundation structure is presented with some insights: Some Collar Vanes may have more capacity than the drilled shaft under those particular soil conditions. Moreover, the results from the medium-stiff clay suggest that Collar Vane has the same lateral response as the

174

drilled shaft up to a certain amount of load. Moreover, CV1 3-2 and CV 3-3 had better torsional capacity.

9. A roadside sign structure design example was presented to illustrate the applicability of the Collar Vane. The example shows the amount of loads transmitted at the base of the foundation and it was demonstrated that the Collar Vane can support the required loads. However, more information is needed when the structure is subjected to considerable amounts of moments due to wind forces.

## 7.3  Recommendations for Future Work

Additional research is recommended to confirm some explanations based on the observations in this study, The recommendations include additional field testing and numerical modeling.

1. The Collar Vane installation torque is shown and the value recorded is within the helical pile's torque ratio. However, addressing the amount of crowd applied during the installation process is also of common interest to contractors and construction companies since knowing the axial load would make it possible to know if the Collar Vane can be installed with relatively light equipment (i.e., skid-steer loaders or mini-excavators).

2. Single support structures may be controlled by the bending moment resistance. The Collar Vane subjected to bending moments at the pile head must be addressed to analyze the bending reduction capabilities of the Collar Vane.

3. Numerical analysis is the most effective way to understand the Collar Vane behavior for any soil conditions and any load combinations. It is necessary to develop a model that accounts for different load combinations.

4. Figure 7.1 presents the Collar Vane structural model. The CV can be represented with a transversal, $S_1$, and a rotational spring, $\rho_1$, at the top of the pile and the

non-linear soil springs are considered outside the CV section. The numerical method proposed in Low *et al.* (2001) can be adapted to implement the proposed structural model.
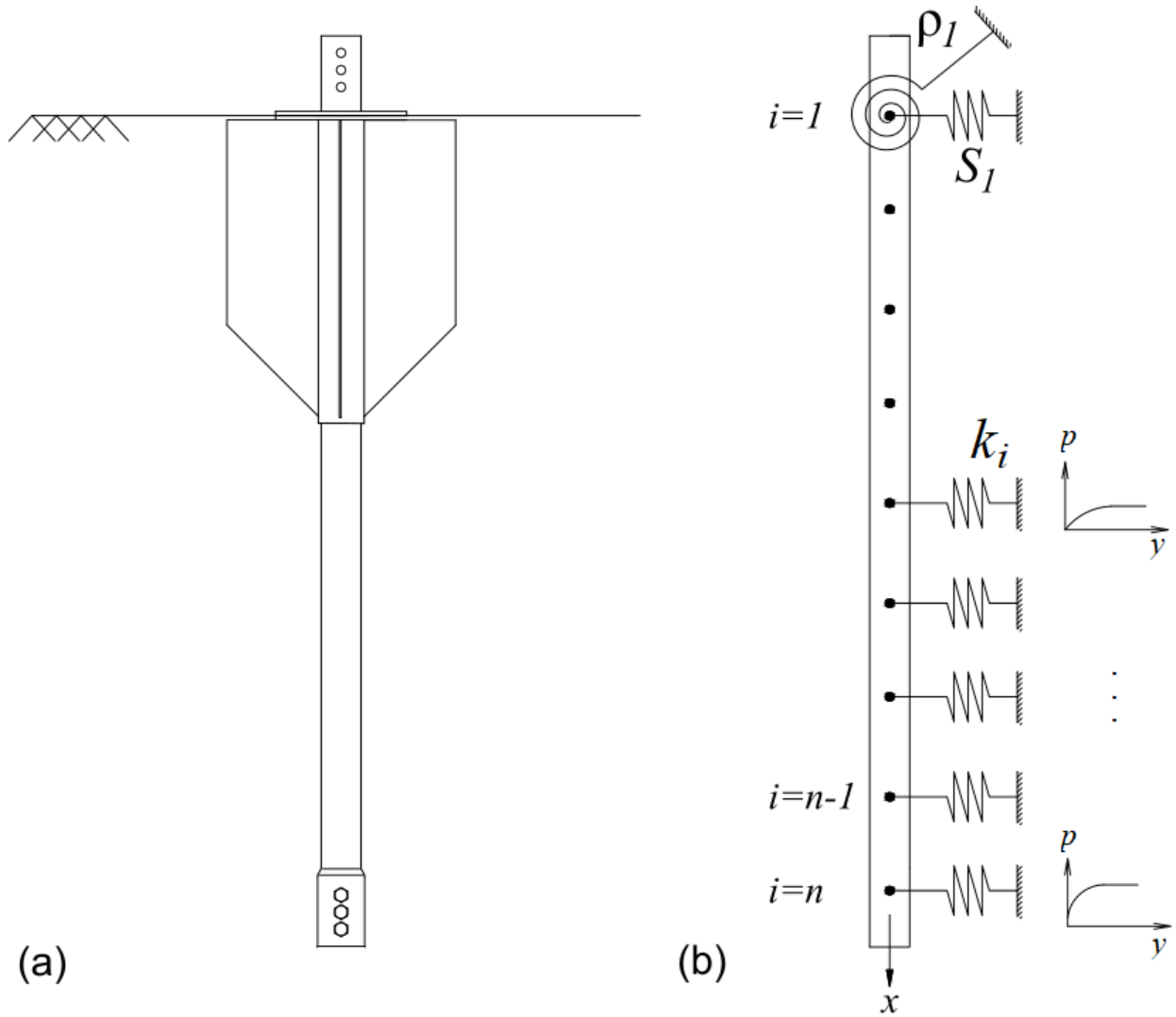


Figure 7.1: Collar Vane proposed structural model.

# REFERENCES

AASHTO (2009). Standard specifications for structural supports for highway signs, luminaires and traffic signals. *American Association of State Highway and Transportation Officials* .

AASHTO (2012). LRFD bridge design specifications. *American Association of State Highway and Transportation Officials* .

AASHTO (2013). Standard specifications for structural supports for highway signs, luminaires, and traffic signals. *American Association of State Highway and Transportation Officials* .

AASHTO (2015). LRFD specifications for structural supports for highway signs, luminaires, and traffic signals. *American Association of State Highway and Transportation Officials* .

Abd Elaziz, A. Y. & El Naggar, M. H. (2015). Performance of hollow bar micropiles under monotonic and cyclic lateral loads. *Journal of Geotechnical and Geoenvironmental Engineering* **141**, No. 5, 04015010.

Adams, J. & Klym, T. (1972). A study of anchorages for transmission tower foundations. *Canadian Geotechnical Journal* **9**, No. 1, 89–104.

Aguilar, V. (2018). Torsional resistance of drilled shaft foundations. *Master's thesis. Auburn University, AL, USA* .

Alpha Anchor & Pile Ltd (2014). Installers of helical and anchors. URL `http://www.alpha-maritime.ca/helical-anchor-and-pile.php`.

Alsamman, O. M. (1995). *The use of cpt for calculating axial capacity of drilled shafts*. University of Illinois at Urbana-Champaign.

Aoki, N. & Velloso, D. d. A. (1975). An approximate method to estimate the bearing capacity of piles. In *Proc., 5th Pan-American Conf. of Soil Mechanics and Foundation Engineering*, vol. 1, International Society of Soil Mechanics and Geotechnical Engineering Buenos . . . , pp. 367–376.

API, R. (2000). 2a-wsd. *Recommended practice for planning, designing and constructing fixed offshore platforms-working stress design* **21**.

Ashcroft (2021). 1305D & 1305DH Dead Weight Tester - Ashcroft. URL `https://www.instrumart.com/products/34602/ashcroft-1305d-deadweight-tester`.

Ashour, M. & Norris, G. (2000). Modeling lateral soil-pile response based on soil-pile interaction. *Journal of Geotechnical and Geoenvironmental Engineering* **126**, No. 5, 420–428.

Bagheri, F. & El Naggar, M. (2015). Effects of installation disturbance on behavior of multi-helix piles in structured clays. *DFI Journal-The Journal of the Deep Foundations Institute* **9**, No. 2, 80–91.

Bienen, B., Dührkop, J., Grabe, J., Randolph, M. F. & White, D. J. (2012). Response of piles with wings to monotonic and cyclic lateral loading in sand. *Journal of Geotechnical and Geoenvironmental Engineering* **138**, No. 3, 364–375.

Bierschwale, M. W., Coyle, H. M. & Bartoskewitz, R. E. (1981). Field tests and new design procedure for laterally loaded drilled shafts in clay. *Technical report*, Texas Transportation Institute.

Bouafia, A. (1995). Experimental study of repetitive cyclic lateral loading on sand piles using a centrifuge. In *International Journal of Rock Mechanics and Mining Sciences and Geomechanics Abstracts*, vol. 6, p. 282A.

Bradshaw, A. S., Cullen, L. & Miller, Z. (2022). Field study of group effects on the pullout capacity of "deep" helical piles in sand. *Canadian Geotechnical Journal* **59**, No. 4, 538–545.

Briaud, J. (1984). Panel discussion, laterally loaded deep foundation. *Philadelphia: American Society for Testing and Materials (ASTM)* .

Briaud, J.-L., Smith, T. & Meyer, B. (1984). Laterally loaded piles and the pressuremeter: comparison of existing methods. In *Laterally loaded deep foundations: Analysis and performance*, ASTM International.

Brinkgreeve, R. & Shen, R. (2011). Structural elements & modelling excavations in plaxis .

Brinkgreve, R., Engin, E. & Swolfs, W. (2013). PLAXIS 3D 2013 user manual .

Broms, B. B. (1964a). Lateral resistance of piles in cohesionless soils. *Journal of the Soil Mechanics and Foundations Division* **90**, No. 3, 123–156.

Broms, B. B. (1964b). Lateral resistance of piles in cohesive soils. *Journal of the soil mechanics and foundations division* **90**, No. 2, 27–63.

Brown, D. A., Morrison, C. & Reese, L. C. (1988). Lateral load behavior of pile group in sand. *Journal of Geotechnical Engineering* **114**, No. 11, 1261–1276.

Bustamante, M. & Gianeselli, L. (1982). Pile bearing capacity prediction by means of static penetrometer cpt. In *Proceedings of the 2nd European symposium on penetration testing*, vol. 2, Balkema, Amsterdam, the Netherlands, pp. 493–500.

Byrne, B. & Houlsby, G. (2015). Helical piles: an innovative foundation design option for offshore wind turbines. *Philosophical Transactions of the Royal Society A: Mathematical, Physical and Engineering Sciences* **373**, No. 2035, 20140081.

Cerato, A. B. & Victor, R. (2008). Effects of helical anchor geometry on long-term performance of small wind tower foundations subject to dynamic loads. *DFI Journal-the Journal of the Deep Foundations Institute* **2**, No. 1, 30–41.

Cheang, L. & Matlock, H. (1983). Static and cyclic lateral load tests on instrumented piles in sand. *The Earth Technology Corporation, Long Beach, California* .

Chen, Y.-J. & Lee, Y.-H. (2010). Evaluation of lateral interpretation criteria for drilled shaft capacity. *Journal of geotechnical and geoenvironmental engineering* **136**, No. 8, 1124–1136.

Chiou, J.-S., Xu, Z.-W., Tsai, C.-C. & Hwang, J.-H. (2018). Lateral cyclic response of an aluminum model pile in sand. *Marine Georesources & Geotechnology* **36**, No. 5, 554–563.

City of New York (1981). Building Code of the City of New York.

Coleman, D. M. & Arcement, B. J. (2002). Evaluation of design methods for auger cast piles in mixed soil conditions. In *Deep Foundations 2002: An International Perspective on Theory, Design, Construction, and Performance*, pp. 1404–1420.

Colorado DOT (2020). Bridge Design Manual .

Coriat, Y. & Frydman, S. (2023). Estimation of shaft and base resistances of cast-in-place piles in israel from analysis of pile loading tests. *Journal of Geotechnical and Geoenvironmental Engineering* **149**, No. 4, 04023009.

Cortes-Garcia, L. D., Landon, M. E., Gallant, A. P. & Huguenard, K. D. (2019). Assessment of helical anchor capacity in marine clays for aquaculture applications. In *Geo-Congress 2019: Foundations*, American Society of Civil Engineers Reston, VA, pp. 299–307.

Cuéllar, P., Baeßler, M. & Rücker, W. (2009). Ratcheting convective cells of sand grains around offshore piles under cyclic lateral loads. *Granular Matter* **11**, 379–390.

Davidson, H. (1982). Laterally loaded drilled pier research. volume 2: research documentation. final report.[analysis of pier foundation movement using padll computer code]. *Technical report*, GAI Consultants, Inc., Monroeville, PA (USA).

Doan, L. & Lehane, B. (2021). Cpt-based design method for axial capacities of drilled shafts and auger cast-in-place piles. *Journal of Geotechnical and Geoenvironmental Engineering* **147**, No. 8, 04021077.

Dutt, R. & O'Neill, M. (1983). Torsional behavior of model piles in sand. In *Geotechnical practice in offshore engineering*, ASCE, pp. 315–334.

Elkasabgy, M. & El Naggar, M. H. (2015). Axial compressive response of large-capacity helical and driven steel piles in cohesive soil. *Canadian Geotechnical Journal* **52**, No. 2, 224–243.

Elkasabgy, M. & El Naggar, M. H. (2019). Lateral performance and p-y curves for large-capacity helical piles installed in clayey glacial deposit. *Journal of Geotechnical and Geoenvironmental Engineering* **145**, No. 10, 04019078.

Fellenius, B. (2017). *Basics of foundation design.*

Fellenius, B. H. (2008). Effective stress analysis and set-up for shaft capacity of piles in clay. In *From research to practice in geotechnical engineering*, pp. 384–406.

FHWA (2009). Manual on uniform traffic control devices. *Federal Highway Administration* .

FHWA (2018). Drilled shafts: Construction procedures and design methods. *US Department of Transportation, Federal Highway Administration* .

Frank, R. (2017). Some aspects of research and practice for pile design in france. *Innovative Infrastructure Solutions* **2**, 1–15.

Garnier, J. (2013). Advances in lateral cyclic pile design: contribution of the solcyp project. In *Puech A: Proc TC 209 Workshop 18th ICSMGE-Design for cyclic loading: piles and other foundations. Paris*, pp. 59–68.

Ghaly, A. M. & Clemence, S. P. (1998). Pullout performance of inclined helical screw anchors in sand. *Journal of geotechnical and geoenvironmental engineering* **124**, No. 7, 617–627.

Ghazavi, M., Ghomi, Y., Heidari, P. & Jelogir, B. M. (2022). Effects of helix shapes and locations on compression capacity of helical piles for offshore foundations. *Marine Georesources & Geotechnology* , 1–14.

Giampa, J. R. & Bradshaw, A. S. (2018). A simple method for assessing the peak friction angle of sand at very low confining pressures. *Geotechnical Testing Journal* **41**, No. 4, 639–647.

Govindasamy, D., Ismail, M. A. M. & Zaki, M. F. M. (2020). Influence of twin tunnel depth in numerical ground movement prediction using mohr coulomb and hardening soil model. In *Proceedings of AICCE'19: Transforming the Nation for a Sustainable Tomorrow 4*, Springer, pp. 647–661.

Gui, F., Kong, J., Feng, D., Qu, X., Zhu, F. & You, Y. (2021). Uplift resistance capacity of anchor piles used in marine aquaculture. *Scientific Reports* **11**, No. 1, 20321.

Hadjadji, T. (1993). *Analyse du comportement experimental de pieux sous chargements horizontaux*. Ph.D. thesis, Marne-la-vallée, ENPC.

Hansen, M., Wolf, T. K., Rasmussen, K. L., Roesen, H. R. & Ibsen, L. B. (2013). Physical modelling of cyclic laterally loaded pile in cohesionless soil .

Herrera, R. (2001). *Determine optimum depths of drilled shafts subjected to combined torsion and lateral loads using the centrifuge*. Ph.D. thesis, University of Florida.

Hetényi, M. (1946). *Beams on elastic foundation: theory with applications in the fields of civil and mechanical engineering*, vol. 16. University of Michigan press Ann Arbor, MI.

Hettler, A. (1981). Verschiebungen starrer und elastischer gründungskörper in sand bei monotoner und zyklischer belastung .

Hirany, A. & Kulhawy, F. (1988). Conduct and interpretation of load tests on drilled shaft foundations: volume 1, detailed guidelines. *Technical report*, Electric Power Research Inst., Palo Alto, CA (USA); Cornell Univ., Ithaca . . . .

Hoyt, R. (2007). Engineering manual: Ram jack helix screw anchors, ram jack steel piers. *Ada, OK: Ram Jack Systems Distribution, LLC* .

Hoyt, R. & Clemence, S. (1989). Uplift capacity of helical anchors in soil. proc.

Hu, Z., McVay, M., Bloomquist, D., Herrera, R. & Lai, P. (2006). Influence of torque on lateral capacity of drilled shafts in sands. *Journal of Geotechnical and Geoenvironmental Engineering* **132**, No. 4, 456–464.

Ivey, D. L. & Dunlap, W. A. (1969). Design procedure compared to full scale tests of drilled shaft footings .

Jamiolkowski, M., Lo Presti, D. & Manassero, M. (2003). Evaluation of relative density and shear strength of sands from cpt and dmt. In *Soil behavior and soft ground construction*, pp. 201–238.

Keefe, T. (2020). *Field study of pile axial cyclic degradation and aging.* Ph.D. thesis, University of Rhode Island.

Khazaei, J. & Eslami, A. (2017). Postgrouted helical piles behavior through physical modeling by fcv. *Marine Georesources & Geotechnology* **35**, No. 4, 528–537.

Klinkvort, R. T. & Hededal, O. (2013). Lateral response of monopile supporting an offshore wind turbine. *Proceedings of the Institution of Civil Engineers-Geotechnical Engineering* **166**, No. 2, 147–158.

Klym, T., Radhakrishna, H. & Howard, J. (1986). Helical plate anchors for tower foundations. In *of the 25th Canadian Geotechnical Conference*, vol. 1, pp. 141–159.

Kong, J., Zhang, T., Gui, F., Qu, X. & Feng, D. (2022). Dynamic response analysis of anchor piles for marine aquaculture under cyclic loading. *Journal of Marine Science and Engineering* **10**, No. 6, 785.

Kulhawy, F. H. & Mayne, P. W. (1990). Manual on estimating soil properties for foundation design. *Technical report*, Electric Power Research Inst., Palo Alto, CA (USA); Cornell Univ., Ithaca . . . .

LCM Systems (2021). STA-4 S-Type Tension and Compression Load Cell. URL https://www.lcmsystems.com/STA-4.

LeBlanc, C., Houlsby, G. & Byrne, B. (2010). Response of stiff piles in sand to long-term cyclic lateral loading. *Géotechnique* **60**, No. 2, 79–90.

Lehane, B., Gaudin, C. & Schneider, J. (2005). Scale effects on tension capacity for rough piles buried in dense sand. *Géotechnique* **55**, No. 10, 709–719.

Li, L., Liu, H., Wu, W., Wen, M., El Naggar, M. H. & Yang, Y. (2021). Investigation on the behavior of hybrid pile foundation and its surrounding soil during cyclic lateral loading. *Ocean Engineering* **240**, 110006.

Li, Q., Stuedlein, A. W. & Barbosa, A. R. (2017). Torsional load transfer of drilled shaft foundations. *Journal of Geotechnical and Geoenvironmental Engineering* **143**, No. 8, 04017036.

Li, Q. & Yang, Z. (2017). P–y approach for laterally loaded piles in frozen silt. *Journal of geotechnical and geoenvironmental engineering* **143**, No. 5, 04017001.

Li, W., Gavin, K., Igoe, D. & Doherty, P. (2014). Review of design models for lateral cyclic loading of monopiles in sand. In *Proceedings of the 8th International Conference on Physical Modelling in Geotechnics, Perth, Australia*, Balkema Rortterdam, the Netherlands, pp. 819–825.

Li, W., Igoe, D. & Gavin, K. (2015). Field tests to investigate the cyclic response of monopiles in sand. *Proceedings of the Institution of Civil Engineers-Geotechnical Engineering* **168**, No. 5, 407–421.

Li, Z., Haigh, S. & Bolton, M. (2010). Centrifuge modelling of mono-pile under cyclic lateral loads. *Physical Modelling in Geotechnics* **2**, 965–970.

Liao, W., Zhang, J., Wu, J. & Yan, K. (2018). Response of flexible monopile in marine clay under cyclic lateral load. *Ocean Engineering* **147**, 89–106.

Lin, S.-S. & Liao, J.-C. (1999). Permanent strains of piles in sand due to cyclic lateral loads. *Journal of geotechnical and geoenvironmental engineering* **125**, No. 9, 798–802.

Lin, Y., Xiao, J., Le, C., Zhang, P., Chen, Q. & Ding, H. (2022). Bearing characteristics of helical pile foundations for offshore wind turbines in sandy soil. *Journal of Marine Science and Engineering* **10**, No. 7, 889.

Little, R. L. & Briaud, J.-L. (1988). Full scale cyclic lateral load tests on six single piles in sand. *Technical report*, Texas A and M Univ College Station Dept of Civil Engineering.

Livneh, B. & El Naggar, M. H. (2008). Axial testing and numerical modeling of square shaft helical piles under compressive and tensile loading. *Canadian Geotechnical Journal* **45**, No. 8, 1142–1155.

Loehr, J. E., Bowders, J. J., Ge, Y.-N. L., Likos, W. J., Luna, R., Maerz, N. H. & Stephenson, R. W. (2011). Engineering policy guidelines for design of drilled shafts .

Long, J. & Vanneste, G. (1994). Effects of cyclic lateral loads on piles in sand. *Journal of Geotechnical Engineering* **120**, No. 1, 225–244.

Low, B., Teh, C. & Tang, W. H. (2001). Stochastic nonlinear p-y analysis of laterally loaded piles. *Structural Safety and Reliability: ICOSSAR'01* , 2001.

Lu, W. & Zhang, G. (2019). Long-term cyclic loading tests for offshore pile foundations based on hydraulic gradient modeling. *Ocean Eng* **44**.

Lutenegger, A. J. (2009). Cylindrical shear or plate bearing?—uplift behavior of multi-helix screw anchors in clay. In *Contemporary topics in deep foundations*, American Society of Civil Engineers (ASCE), pp. 456–463.

Lutenegger, A. J. (2011a). Behavior of multi-helix screw anchors in sand. In *Proceedings of the 14th Pan-American Conference on Soil Mechanics and Geotechnical Engineering, Toronto, Ont.[CD ROM]*.

Lutenegger, A. J. (2011b). Historical development of iron screw-pile foundations: 1836–1900. *The International Journal for the History of Engineering & Technology* **81**, No. 1, 108–128.

Maine DOT (2020). Maine DOT Standard Specifications .

Manoliu, I., Dimitriu, D., Radulescu, N. & Dobrescu, G. (1985). Load-deformation characteristics of drilled piers. In *International conference on soil mechanics and foundation engineering. 11*, pp. 1553–1558.

Matlock, H. (1970). Correlation for design of laterally loaded piles in soft clay. In *Offshore technology conference*, OnePetro.

McNulty, J. (1956). Thrust loading on piles. In *Proc. ASCE*, vol. 82, pp. 940–1.

Menzies, B. & Merrifield, C. (1980). Measurements of shear stress distribution on the edges of a shear vane blade. *Geotechnique* **30**, No. 3, 314–318.

Meyerhof, G. (1951). The ultimate bearing capacity of foudations. *Geotechnique* **2**, No. 4, 301–332.

Micro-Measurements (2021). 250BF series Strain Gauge. URL `https://micro-measurements.com/pca/detail/250bf`.

Mitsch, M. P. & Clemence, S. P. (1985). Uplift capacity of helix anchors in sand. American Society of Civil Engineers (ASCE), pp. 26–47.

Mondal, S. & Disfani, M. M. (2022). Battered minipile response to low-frequency cyclic lateral loading in very dense sand. *Acta Geotechnica* **17**, No. 9, 4033–4050.

Mooney, J. S., Adamczak, S. & Clemence, S. P. (1985). Uplift capacity of helical anchors in clay and silt. In *Unknown Host Publication Title*, American Society of Civil Engineers (ASCE), pp. 48–72.

Morgan, H. D. (1944). The design of wharves on soft ground. *Journal of the Institution of Civil Engineers* **22**, No. 5, 5–25.

Nadim, F., Lacasse, S., Liu, Z. & Lehane, B. (2020). Improving the reliability of the calculated axial capacity of piles in sand. In *Proceedings of 4th International Symposium on Frontiers in Offshore Geotechnics (ISFOG 21)*, pp. 8–11.

Nanda, S., Arthur, I., Sivakumar, V., Donohue, S., Bradshaw, A., Keltai, R., Gavin, K., Mackinnon, P., Rankin, B. & Glynn, D. (2017). Monopiles subjected to uni-and multi-lateral cyclic loading. *Proceedings of the Institution of Civil Engineers-Geotechnical Engineering* **170**, No. 3, 246–258.

Narasimha, R. S., Prasad, Y. & Veeresh, C. (1993). Behavior of embedded model screw anchors in soft clays. *Geotechnique* **43**, No. 4, 605–614.

Narasimha Rao, S., Prasad, Y., Shetty, M. & Joshi, V. (1989). Uplift capacity of screw pile anchors .

Nusairat, J., Liang, R. Y., Engel, R., Hanneman, D., Abu-Hejleh, N. & Yang, K. (2004). Drilled shaft design for sound barrier walls, signs, and signals. *Rep. No. CDOT-DTD-R-2004* **8**.

Omega Engineering Inc. (2021). General Purpose, Stainless Steel Pressure Transducers. URL https://www.omega.com/en-us/pressure-measurement/pressure-transducers/px309/p/PX359-5KG5V.

O'Neil, M. W., Reese, L. C. *et al.* (1999). Drilled shafts: Construction procedures and design methods. *Technical report*, United States. Federal Highway Administration. Office of Infrastructure.

Peralta, P. (2010). *Investigations on the behavior of large diameter piles under long-term lateral cyclic loading in cohesionless soil*. na.

Perko, H. (2003). Lateral capacity and buckling resistance of helix pier foundations. In *Foundations Technology Seminar-Helical Foundations and Tiebacks, Deep Foundation Institute, Helical Pile Committee, University of Cincinnati, Cincinnati, OH*.

Perko, H. A. (2009). *Helical piles: a practical guide to design and installation*. John Wiley & Sons.

Phoon, K.-K. & Retief, J. V. (2016). *Reliability of geotechnical structures in iso2394*. CRC Press.

Prasad, Y. V. & Rao, S. N. (1996). Lateral capacity of helical piles in clays. *Journal of geotechnical engineering* **122**, No. 11, 938–941.

Puri, V. K., Stephenson, R., Dziedzic, E. & Goen, L. (1984). Helical anchor piles under lateral loading. In *Laterally loaded deep foundations: Analysis and performance*, ASTM International.

Pyke, R. (1984). Panel discussion, laterally loaded deep foundation (stp 835). *ASTM, Philadelphia* , 239–243.

Randolph, M. F. & Murphy, B. (1985). Shaft capacity of driven piles in clay. In *Offshore technology conference*, OnePetro.

Rao, S. N. & Prasad, Y. (1993). Estimation of uplift capacity of helical anchors in clays. *Journal of Geotechnical Engineering* **119**, No. 2, 352–357.

Rao, S. N., Prasad, Y. & Shetty, M. D. (1991). The behaviour of model screw piles in cohesive soils. *Soils and Foundations* **31**, No. 2, 35–50.

Reese, L. & Matlock, H. (1956). Non-dimensional solutions for laterally loaded piles with soil modulus.

Reese, L. C. (1986). Behavior of piles and pile groups under lateral load. *Report FHWA/RD-85/106 to Federal Highway Administration* .

Reese, L. C. (1997). Analysis of laterally loaded piles in weak rock. *Journal of Geotechnical and Geoenvironmental engineering* **123**, No. 11, 1010–1017.

Reese, L. C., Cox, W. R. & Koop, F. D. (1974). Analysis of laterally loaded piles in sand. In *Offshore Technology Conference*, OnePetro.

Reese, L. C., Cox, W. R. & Koop, F. D. (1975). Field testing and analysis of laterally loaded piles om stiff clay. In *Offshore technology conference*, OnePetro.

Reese, L. C., Isenhower, W. M. & Wang, S.-T. (2005). *Analysis and design of shallow and deep foundations*, vol. 10. John Wiley & Sons.

Reese, L. C. & Welch, R. C. (1975). Lateral loading of deep foundations in stiff clay. *Journal of the Geotechnical engineering division* **101**, No. 7, 633–649.

Robertson, P. K. (2009). Interpretation of cone penetration tests—a unified approach. *Canadian geotechnical journal* **46**, No. 11, 1337–1355.

Robertson, P. K. & Cabal, K. (2010). Estimating soil unit weight from cpt. In *2nd International symposium on cone penetration testing*, pp. 2–40.

Rollins, K. M., Clayton, R. J., Mikesell, R. C. & Blaise, B. C. (2005). Drilled shaft side friction in gravelly soils. *Journal of Geotechnical and Geoenvironmental Engineering* **131**, No. 8, 987–1003.

Rosquoet, F., Thorel, L., Garnier, J. & Canepa, Y. (2007). Lateral cyclic loading of sand-installed piles. *Soils and foundations* **47**, No. 5, 821–832.

Rosquoët, F., Thorel, L., Garnier, J. & Puech, A. (2013). Pile in sand under lateral loading: Development of degradation laws for describing cyclic load effects. *Design for cyclic loading: Piles and other foundations, Proceeding of TC* **209**, 89–93.

Sakr, M. (2009). Performance of helical piles in oil sand. *Canadian Geotechnical Journal* **46**, No. 9, 1046–1061.

Salgado, R. (2010). The axial resistance of nondisplacement piles. In *Art of foundation engineering practice*, pp. 584–604.

Schneider, J. A., Xu, X. & Lehane, B. M. (2008). Database assessment of cpt-based design methods for axial capacity of driven piles in siliceous sands. *Journal of geotechnical and geoenvironmental engineering* **134**, No. 9, 1227–1244.

Semple, R. M. & Rigden, W. J. (1984). Shaft capacity of driven pipe piles in clay. In *Analysis and design of pile foundations*, ASCE, pp. 59–79.

Skempton, A. (1951). The bearing capacity of clays. *Selected papers on soil mechanics* , 50–59.

Slack, D. & Walker, J. (1970). Deflection of pier foundations subjected to horizontal loads of long duration. In *Agricultural Engineering*, vol. 51, AMER SOC AGRICULTURAL ENGINEERS 2950 NILES RD, ST JOSEPH, MI 49085-9659, p. 293.

Spagnoli, G. (2017). A cpt-based model to predict the installation torque of helical piles in sand. *Marine georesources & geotechnology* **35**, No. 4, 578–585.

Spagnoli, G., de Hollanda Cavalcanti Tsuha, C., Oreste, P. & Mendez Solarte, C. M. (2018). A sensitivity analysis on the parameters affecting large diameter helical pile installation torque, depth and installation power for offshore applications. *DFI Journal-The Journal of the Deep Foundations Institute* **12**, No. 3, 171–185.

Spagnoli, G. & Gavin, K. (2015). Helical piles as a novel foundation system for offshore piled facilities. In *Abu Dhabi International Petroleum Exhibition and Conference*, OnePetro.

Stuedlein, A., Reddy, S. & Evans, T. (2014). Interpretation of augered cast in place pile capacity using static loading tests. *DFI Journal-The Journal of the Deep Foundations Institute* **8**, No. 1, 39–47.

Tawfiq, K. (2000). Drilled shaft under torsional loading conditions. *Technical report*.

Terzaghi, K. (1943). *Theoretical soil mechanics*. John Wiley & Sons.

Thiyyakkandi, S., McVay, M., Lai, P. & Herrera, R. (2016). Full-scale coupled torsion and lateral response of mast arm drilled shaft foundations. *Canadian Geotechnical Journal* **53**, No. 12, 1928–1938.

Tomlinson, M. (1957). The adhesion of piles driven in clay soils. In *Proceedings of the 4th international conference on soil mechanics and foundation engineering*, vol. 2, pp. 66–71.

Touma, F. T. & Reese, L. C. (1974). Behavior of bored piles in sand. *Journal of the Geotechnical Engineering Division* **100**, No. 7, 749–761.

Trombly, B. (2006). The international building code (ibc). *CMGT 564-Term Paper* .

Vega-Posada, C. A., Gallant, A. P. & Areiza-Hurtado, M. (2020). Simple approach for analysis of beam-column elements on homogeneous and non-homogeneous elastic soil. *Engineering Structures* **221**, 111110.

Verdure, L., Garnier, J. & Levacher, D. (2003). Lateral cyclic loading of single piles in sand. *International journal of physical modelling in geotechnics* **3**, No. 3, 17–28.

Vito, D. & Cook, T. (2011). Case histories on the use of helical piles for retrofitting and new construction. In *Pan-Am CGS Geotechnical Conference.*

Walker, J. & Cox, E. (1966). Design of pier foundations for lateral loads. *Transactions of the ASAE* **9**, No. 3, 417–0420.

Wilson, G. (1950). The bearing capacity of screw piles and screwcrete cylinders. *Journal of the Institution of Civil Engineers* **34**, No. 5, 4–73.

Zelada, G. A. & Stephenson, R. W. (2000). Design methods for auger cip piles in compression. In *New technological and design developments in deep foundations*, pp. 418–432.

Zhang, C., White, D. & Randolph, M. (2011). Centrifuge modeling of the cyclic lateral response of a rigid pile in soft clay. *Journal of Geotechnical and Geoenvironmental Engineering* **137**, No. 7, 717–729.

Zhang, D. J. Y. (1999). Predicting capacity of helical screw piles in alberta soils .

Zhang, L. & Kong, L. (2006). Centrifuge modeling of torsional response of piles in sand. *Canadian Geotechnical Journal* **43**, No. 5, 500–515.

# APPENDIX A

# EQUIPMENT CALIBRATION

## A.1 Pressure Transducer

Pressure transducer calibration was performed using an Ashcroft 1305D dead-weight tester shown in Figure A.1. This unit provides precise means for generating pressure based on the physical principle of pressure = force/area with high accuracy that can be used as a primary calibration standard. This dead-weight tester has an operating pressure between 103 and 68,947 kPa (15 and 10,000 psi) and an accuracy of $\pm 0.1\%$ of produced pressure. Ashcroft (2021)
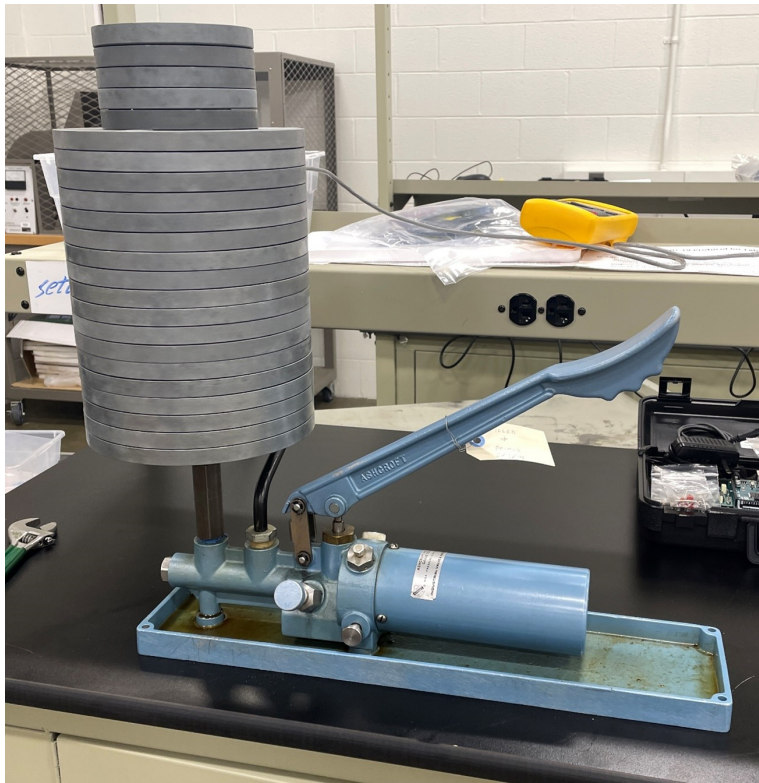


Figure A.1: Ashcroft 1305D Deadweight Tester.

The calibration equation of this pressure transducer, in pounds square inch versus output volts is:

$$y = 1,001.4904x - 1.6478$$

with an R-squared value of $R^2 = 1.0$ the calibration proved enough accuracy and was implemented in the load test. Figure A.2 shows a plot of this calibration in U.S imperial units.
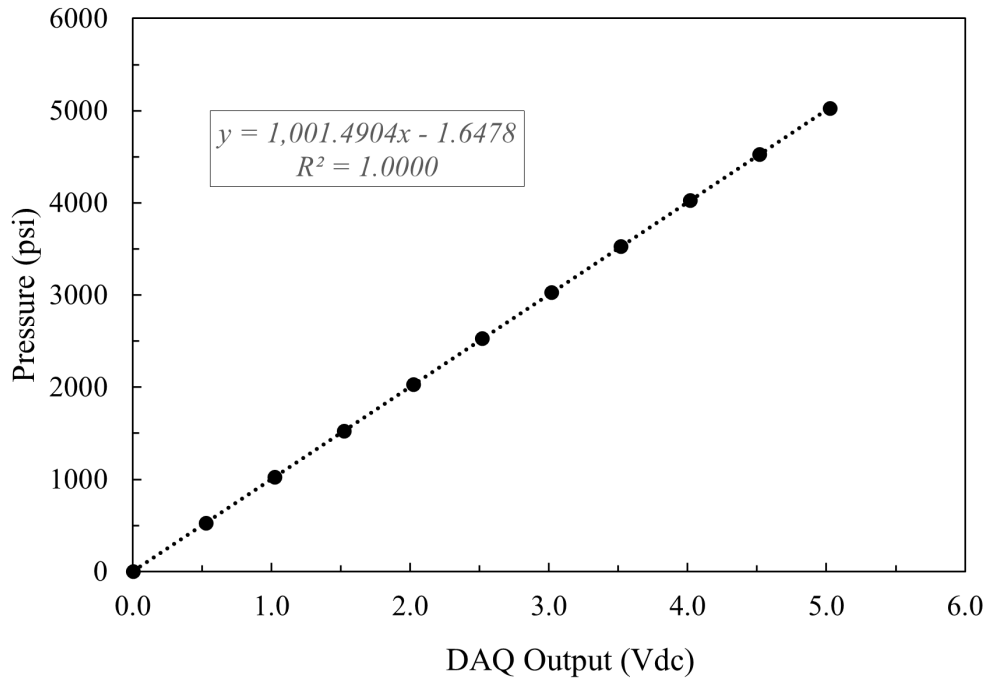


Figure A.2: Omega PX359-5KG5V pressure sensor calibration.

## A.2 Load Cell

Load Cell calibration is performed using a tensile test machine as shown in Figure A.3. During calibration, a known load is applied to the load cell incrementally, and output readings are taken at each step. A maximum load of 38 kN (8500 lb) was placed on each S-Type load cell.

The following equation is developed for the Load Cell with S/N: 17662038 in U.S. Imperial pounds to millivolts:

Figure A.3: STA-4 S-Type Load Cell Calibration in test frame.

$$y = 5,522,947.613x + 5.2013$$

This calibration has an $R^2$ value of 0.9994 as shown in Figure A.4.

The following equation is developed for the Load Cell with S/N: 17649090 in U.S. Imperial pounds to millivolts:
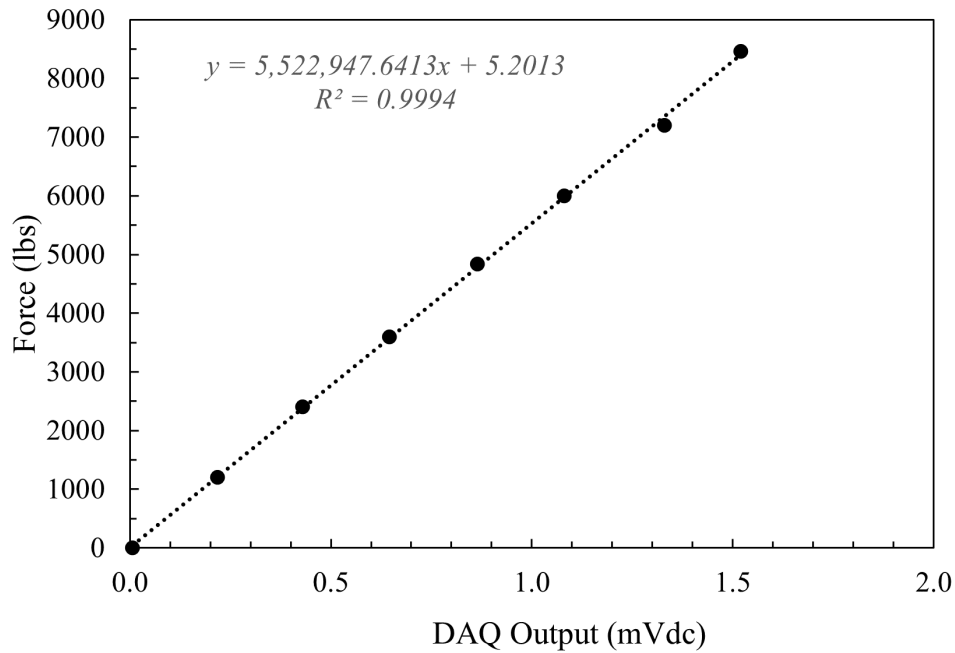
Figure A.4: STA-4 S-Type Load Cell with S/N: LC17662038 calibration outcome.

$$y = 5,544,451.6316x - 20.1756$$

This calibration has an $R^2$ value of 1.0000 as shown in Figure A.5.

A higher load capacity load cell was also calibrated using the same tensile testing machine. The calibration for the 178 kN RAS1-40KS-S load cell is shown in Figure A.6. with an $R^2$ value of 1.00

The equation developed for the RAS1-40KS-S load cell in U.S. Imperial pounds to millivolts is:

$$y = 13,038,029.31x - 63.99$$
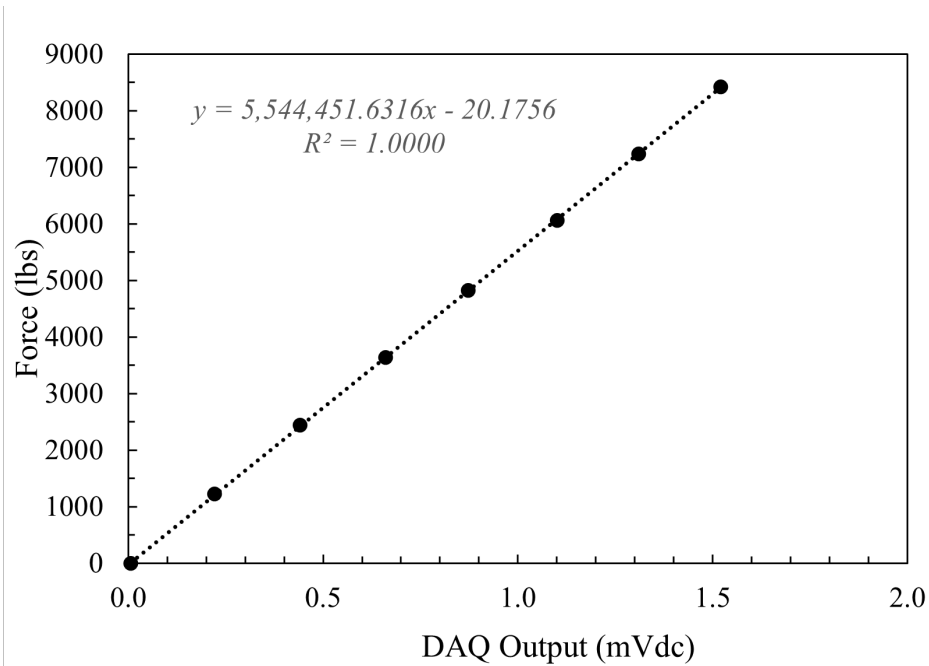
Figure A.5: STA-4 S-Type Load Cell with S/N: LC17649090 calibration outcome.
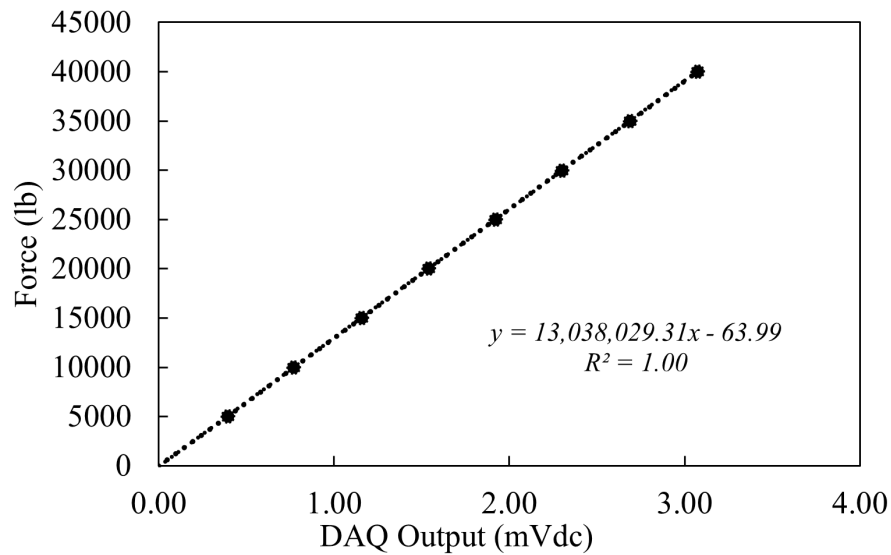


Figure A.6: Load Cell RAS1-40KS-S calibration outcome.

## A.3  String Potentiometers

The string pot calibration was performed using a frame with the string pot in a fixed position on one end and by pulling the cable using a caliper the change in voltage output was measured at least eight times as shown in Figure. A.7.
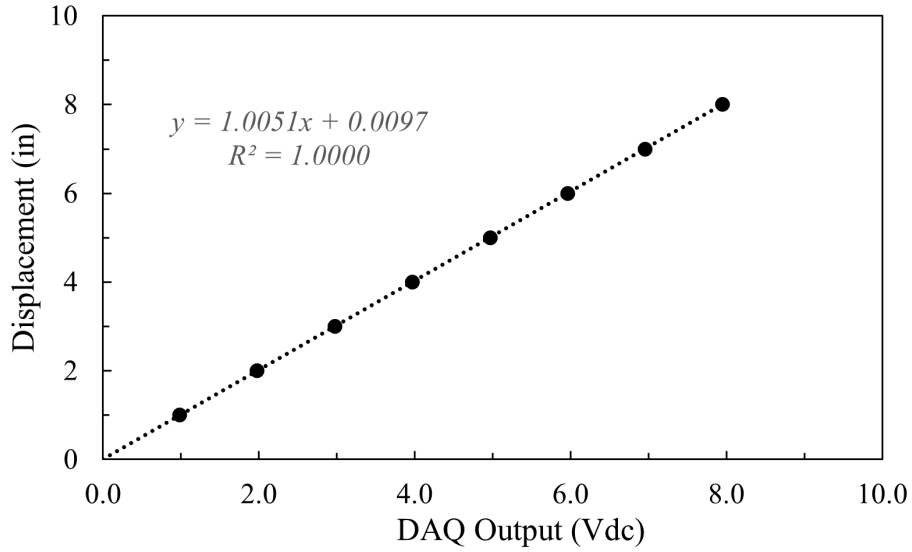
Figure A.7: String potentiometer ET PT1DC 10" S/N: J1406292A calibration.

The PT1DC calibration is shown in Figure A.7 in imperial inches versus volts with a $R^2 = 1.00$. A total of eight string pots were used in field testing Table A.1 shows the slope and $R^2$ values for all string pots.

Table A.1: String potentiometers calibration.

| String Pot | Slope Loading | $R^2$ | Range mm (in) |
|---|---|---|---|
| PT1DC-10 J1406295A | 0.99621 | 0.99999 | 25.4 (10) |
| PT1DC-10 J1406292A | 1.00508 | 1 | 25.4 (10) |
| PT1DC-10 J1406291A | 0.99643 | 1 | 25.4 (10) |
| PT1DC-10 J1406290A | 0.99783 | 1 | 25.4 (10) |
| SP2-25 AS2757 | 1.78223 | 1 | 635 (25) |
| SP2-25 AS2819 | 1.78275 | 0.99999 | 635 (25) |
| SGD-80 1814 | 8.31748 | 1 | 2032 (80) |
| SGD-80 2315 | 5.72541 | 0.99999 | 1727 (68) |

# APPENDIX B

## SUBSURFACE INVESTIGATION REPORT

Attached report starts in next page.

## B.1 Boring Logs

| Project No.: **22-1064** | **Boring Log** | Rig: **CME 55 (B-55)** |
| Project: **Hubbell 2022 Centralia MO Site** | | Location: **Centralia, MO** |
| Client: **University of Maine** | | Driller: **AJK** |
| Boring No.: **SB-1** | | |

**SUBSURFACE PROFILE** / **SAMPLE**

| Depth (ft.) | Symbol | Description | Qp, t.s.f. | Dry Density, P.C.F. | Depth/Elev. | Number | Type | Blows/ft. | Qu, T.S.F. | Standard Penetration Test blows/ft. | Water Content % Wp • Wl |
|---|---|---|---|---|---|---|---|---|---|---|---|
| 0 | | Ground Surface | | | 0.0 | | | | | | |
| | | Topsoil (±8") | | | -0.7 | | | | | | |
| | | Fat Clay (CH), Light Brown mottled Yellow Brown, Stiff, Moist | 2.75 | | 0.7 | 1 | SS | 8 | | 8 | 28.1 |
| | | (CH), Light Gray mottled Yellow Brown, Stiff, Moist | 2.75 | | | 2 | SS | 11 | | 11 | 24.9 |
| 5 | | Lean Clay (CL), Light Gray mottled Yellow Brown, Silty, Medium, Moist | 0.25 | | -5.0 / 5.0 | 3 | SS | 6 | | 6 | 30.5 |
| | | Fat Clay (CH), Light Gray mottled Yellow Brown, Silty, Medium, Moist | 0.50 | | -7.0 / 7.0 | 4 | SS | 7 | | 7 | 24.1 |
| | | End of Boring @ 8½ Ft. | | | -8.5 / 8.5 | | | | | | |
| 10 | | | | | | | | | | | |
| 15 | | | | | | | | | | | |
| 20 | | | | | | | | | | | |
| 25 | | | | | | | | | | | |
| 30 | | | | | | | | | | | |

| Drill Method: **3 1/4" HSA with AW Rod** | Groundwater Elev. During Drilling: ▽ |
| Boring Started: **8/11/2022** | **GEOTECHNICS** | Groundwater Elev. @ Comp.: ▽ |
| Boring Completed: **8/11/2022** | Soil & Material Testing | Groundwater Elev. @ **Hrs.:** ▽ |
| Tested By: **BRH/DAW/DJS/NPP** | | Boring Location: **See Location Sketch** |
| Logging By: **BRH** | | Sheet 1 of 1 |

| Project No.: **22-1064** | **Boring Log** | Rig: **CME 55 (B-55)** |
|---|---|---|
| Project: **Hubbell 2022 Centralia MO Site** | | Location: **Centralia, MO** |
| | | Driller: **AJK** |
| Client: **University of Maine** | | |
| Boring No.: **SB-2** | | |

| Depth (ft.) | Symbol | Description | Qp, t.s.f. | Dry Density, P.C.F. | Depth/Elev. | Number | Type | Blows/ft. | Qu, T.S.F. | Standard Penetration Test blows/ft. | Water Content % |
|---|---|---|---|---|---|---|---|---|---|---|---|
| | | | | | | | | | | 10 20 30 40 | Wp ●─ WI  10 20 30 40 |
| 0 | | Ground Surface | | | 0.0 | | | | | | |
| | | Topsoil (±8") | | | -0.7 | | | | | | |
| | | Fat Clay (CH), Light Brown mottled Yellow Brown, Medium, Moist | 1.75 | | 0.7 | 1 | SS | 7 | | 7 | 33.7  93 |
| | | (CH), Light Gray mottled Yellow Brown, Stiff, Moist | 1.50 | | | 2 | SS | 9 | | 9 | 26.7  62 |
| 5 | | Lean Clay (CL), Light Gray mottled Yellow Brown, Silty, Medium, Moist | 0.75 | | -5.0 / 5.0 | 3 | SS | 6 | | 6 | 24.4 |
| | | Fat Clay (CH), Light Gray mottled Yellow Brown/ Reddish Brown, Stiff, Moist | 1.00 | | -7.0 / 7.0 | 4 | SS | 8 | | 8 | 24.4  64 |
| | | End of Boring @ 8½ Ft. | | | -8.5 / 8.5 | | | | | | |
| 10 | | | | | | | | | | | |
| 15 | | | | | | | | | | | |
| 20 | | | | | | | | | | | |
| 25 | | | | | | | | | | | |
| 30 | | | | | | | | | | | |

Drill Method: **3 1/4" HSA with AW Rod**
Boring Started: **8/11/2022**
Boring Completed: **8/11/2022**
Tested By: **BRH/DAW/DJS/NPP**
Logging By: **BRH**

**GEOTECHNICS**
**Soil & Material Testing**

Groundwater Elev. During Drilling: ☒
Groundwater Elev. @ Comp.: ☒
Groundwater Elev. @     Hrs.: ☒
Boring Location: **See Location Sketch**
Sheet 1 of 1

| Project No.: **22-1064** | **Boring Log** | Rig: **CME 55 (B-55)** |
|---|---|---|
| Project: **Hubbell 2022 Centralia MO Site** | | Location: **Centralia, MO** |
| Client: **University of Maine** | | Driller: **AJK** |
| Boring No.: **SB-3** | | |

| Depth (ft.) | Symbol | SUBSURFACE PROFILE — Description | Qp, t.s.f. | Dry Density, P.C.F. | Depth/Elev. | SAMPLE Number | Type | Blows/ft. | Qu, T.S.F. | Standard Penetration Test blows/ft. 10 20 30 40 | Water Content % Wp — Wl 10 20 30 40 |
|---|---|---|---|---|---|---|---|---|---|---|---|
| 0 | | Ground Surface | | | 0.0 | | | | | | |
| | | Topsoil (±8") | | | -0.7 | | | | | | |
| | | | | | 0.7 | | | | | | |
| | | Fat Clay (CH), Light Brown mottled Reddish Brown, Silty, Medium, Moist | 3.00 | | | 1 | SS | 7 | | 7 | 23.5 |
| | | (CH), Light Gray mottled Yellow Brown, Silty, Stiff, Moist | 0.50 | | | 2 | SS | 9 | | 9 | 26.2 |
| | | | | | -5.0 | | | | | | |
| 5 | | Lean Clay (CL), Light Gray mottled Yellow Brown, Silty, Medium, Moist | 0.75 | | 5.0 / -6.0 / 6.0 | 3 | SS | 5 | | 5 | 24.6 |
| | | Fat Clay (CH), Light Brown/Yellow Brown mottled Light Gray, Medium, Moist | 1.00 | | -8.5 / 8.5 | 4 | SS | 7 | | 7 | 25.2 |
| | | End of Boring @ 8½ Ft. | | | | | | | | | |
| 10 | | | | | | | | | | | |
| 15 | | | | | | | | | | | |
| 20 | | | | | | | | | | | |
| 25 | | | | | | | | | | | |
| 30 | | | | | | | | | | | |

**Drill Method: 3 1/4" HSA with AW Rod**
**Boring Started: 8/11/2022**
**Boring Completed: 8/11/2022**
**Tested By: BRH/DAW/DJS/NPP**
**Logging By: BRH**

**GEOTECHNICS**
Soil & Material Testing

**Groundwater Elev. During Drilling:**
**Groundwater Elev. @ Comp.:**
**Groundwater Elev. @** **Hrs.:**
**Boring Location: See Location Sketch**
**Sheet 1 of 1**

| Project No.: **22-1064** | | Rig: **CME 55 (B-55)** |
|---|---|---|
| Project: **Hubbell 2022 Centralia MO Site** | | Location: **Centralia, MO** |
| | | Driller: **AJK** |
| Client: **University of Maine** | | |
| Boring No.: **SB-4** | | |

### SUBSURFACE PROFILE / SAMPLE

| Depth (ft.) | Symbol | Description | Qp, t.s.f. | Dry Density, P.C.F. | Depth/Elev. | Number | Type | Blows/ft. | Qu, T.S.F. | Standard Penetration Test blows/ft. | Water Content % |
|---|---|---|---|---|---|---|---|---|---|---|---|
| 0 | | Ground Surface | | | 0.0 | | | | | | |
| | | Topsoil (±8") | | | -0.7 | | | | | | |
| | | Fat Clay (CH), Light Brown mottled Yellow Brown, Stiff, Moist | 3.00 | | 0.7 | 1 | SS | 9 | | 9 | 30.6 |
| | | (CH), Light Gray mottled Yellow Brown, Silty, Medium, Moist | 1.00 | | | 2 | SS | 7 | | 7 | 27.8 |
| 5 | | Lean Clay (CL), Light Gray mottled Yellow Brown, Silty, Medium, Moist | 0.50 | | -5.0 / 5.0 / -6.0 | 3 | SS | 7 | | 7 | 23.9 |
| | | Fat Clay (CL), Light Gray mottled Reddish Brown, Stiff, Moist | 1.00 | | 6.0 / -8.5 | 4 | SS | 8 | | 8 | 23.6 |
| | | End of Boring @ 8½ Ft. | | | 8.5 | | | | | | |
| 10 | | | | | | | | | | | |
| 15 | | | | | | | | | | | |
| 20 | | | | | | | | | | | |
| 25 | | | | | | | | | | | |
| 30 | | | | | | | | | | | |

SPT scale: 10 20 30 40
Water Content scale: Wp |——•——| Wl   10 20 30 40

| | |
|---|---|
| Drill Method: **3 1/4" HSA with AW Rod** | Groundwater Elev. During Drilling: |
| Boring Started: **8/11/2022** | Groundwater Elev. @ Comp.: |
| Boring Completed: **8/11/2022** | Groundwater Elev. @      Hrs.: |
| Tested By: **BRH/DAW/DJS/NPP** | Boring Location: **See Location Sketch** |
| Logging By: **BRH** | Sheet 1 of 1 |

**GEOTECHNICS**
Soil & Material Testing

| | Boring Log | |
|---|---|---|
| **Project No.: 22-1064** | | **Rig: CME 55 (B-55)** |
| **Project: Hubbell 2022 Centralia MO Site** | | **Location: Centralia, MO** |
| | | **Driller: AJK** |
| **Client: University of Maine** | | |
| **Boring No.: SB-5** | | |

## SUBSURFACE PROFILE / SAMPLE

| Depth (ft.) | Symbol | Description | Qp, t.s.f. | Dry Density, P.C.F. | Depth/Elev. | Number | Type | Blows/ft. | Qu, T.S.F. | Standard Penetration Test blows/ft. | Water Content % (Wp ● Wl) |
|---|---|---|---|---|---|---|---|---|---|---|---|
| 0 | | Ground Surface | | | 0.0 | | | | | | |
| | | Topsoil (±8") | | | -0.7 | | | | | | |
| | | Fat Clay (CH), Light Brown mottled Yellow Brown, Medium, Moist | 2.25 | | 0.7 | 1 | SS | 5 | | 5 | 21.6 / 78 |
| | | (CH), Light Gray mottled Yellow Brown, Stiff, Moist | 2.25 | | | 2 | SS | 10 | | 10 | 25.0 / 60 |
| 5 | | Lean Clay (CL), Light Gray mottled Yellow Brown, Medium, Moist | 0.25 | | -5.0 / 5.0 | 3 | SS | 5 | | 5 | 25.3 |
| | | Fat (CH), Light Gray mottled Yellow Brown, Moist | 1.50 | | -7.0 / 7.0 | 4 | ST | | | | 24.9 / 61 |
| | | | | | -9.0 / 9.0 | | | | | | |
| 10 | | End of Boring @ 9 Ft. | | | | | | | | | |
| 15 | | | | | | | | | | | |
| 20 | | | | | | | | | | | |
| 25 | | | | | | | | | | | |
| 30 | | | | | | | | | | | |

Standard Penetration Test scale: 10 20 30 40
Water Content % scale: 10 20 30 40

**Drill Method: 3 1/4" HSA with AW Rod**
**Boring Started: 8/11/2022**
**Boring Completed: 8/11/2022**
**Tested By: BRH/DAW/DJS/NPP**
**Logging By: BRH**

**GEOTECHNICS**
Soil & Material Testing

**Groundwater Elev. During Drilling:** ▽
**Groundwater Elev. @ Comp.:** ▽
**Groundwater Elev. @** **Hrs.:** ▽
**Boring Location: See Location Sketch**
**Sheet 1 of 1**

## B.2  Field Shear Vane Test

| | |
|---|---|
| **Project No.: 22-1064** | **Rig: CME 55 (B-55)** |
| **Project: Hubbell 2022 Centralia MO Site** | **Location: Centralia, MO** |
| **Client: University of Maine** | **Driller: AJK** |
| **Boring No.: VS-1** | |

**Boring Log**

### SUBSURFACE PROFILE / SAMPLE

| Depth (ft.) | Symbol | Description | Qp, t.s.f. | Dry Density, P.C.F. | Depth/Elev. | Number | Type | Blows/ft. | Qu, T.S.F. | Standard Penetration Test blows/ft. | Water Content % Wp ● Wl |
|---|---|---|---|---|---|---|---|---|---|---|---|
| 0 | | Ground Surface | | | 0.0 | | | | | | |
| | | Topsoil (±8") | | | -0.7 | | | | | | |
| | | Small Vane Shear Reading @ 1 ft. = 9.2 (1.84 T.S.F.) | | | 0.7 | 1 | VS | | | | |
| | | Small Vane Shear Reading @ 3 ft. = 11.6 (2.32 T.S.F.) | | | | 2 | VS | | | | |
| 5 | | Small Vane Shear Reading @ 5 ft. = 7.2 (1.44 T.S.F.) | | | -5.0 / 5.0 | 3 | VS | | | | |
| | | Small Vane Shear Reading @ 7 ft. = 8.0 (1.60 T.S.F.) | | | -7.0 / 7.0 | 4 | VS | | | | |
| 10 | | Small Vane Shear Reading @ 10 ft. = 7.9 (1.58 T.S.F.) | | | | 5 | VS | | | | |
| | | Small Vane Shear Reading @ 12 ft. = 9.3 (1.86 T.S.F.) | | | -12.0 / 12.0 | 6 | VS | | | | |
| | | End of Boring @ 12 Ft. | | | | | | | | | |
| 15 | | | | | | | | | | | |
| 20 | | | | | | | | | | | |
| 25 | | | | | | | | | | | |
| 30 | | | | | | | | | | | |

Standard Penetration Test scale: 10 20 30 40
Water Content % scale: 10 20 30 40

| | |
|---|---|
| **Drill Method: 3 1/4" HSA with AW Rod** | **Groundwater Elev. During Drilling:** |
| **Boring Started: 8/11/2022** | **Groundwater Elev. @ Comp.:** |
| **Boring Completed: 8/11/2022** | **Groundwater Elev. @      Hrs.:** |
| **Tested By: BRH** | **Boring Location: See Location Sketch** |
| **Logging By: BRH** | **Sheet 1 of 1** |

**GEOTECHNICS**
**Soil & Material Testing**

| Project No.: **22-1064** | **Boring Log** | Rig: |
| --- | --- | --- |
| Project: **Hubbell 2022 Centralia MO Site** | | Location: **Centralia, MO** |
| | | Driller: **MAS** |
| Client: **University of Maine** | | |
| Boring No.: **VS-1A** | | |

### SUBSURFACE PROFILE / SAMPLE

| Depth (ft.) | Symbol | Description | Qp, t.s.f. | Dry Density, P.C.F. | Depth/Elev. | Number | Type | Blows/ft. | Qu, T.S.F. | Standard Penetration Test blows/ft. 10 20 30 40 | Water Content % Wp ●—— Wl 10 20 30 40 |
| --- | --- | --- | --- | --- | --- | --- | --- | --- | --- | --- | --- |
| 0 | | Ground Surface | | | 0.0 | | | | | | |
| | | Topsoil (±8") | | | -0.7 | | | | | | |
| | | | | | 0.7 | | | | | | |
| | | Small Vane Shear Reading @ 1 ft. = 15.0 (3.14 T.S.F.) Remolded=4.3 (0.9 T.S.F.) | | | | 1 | VS | | | | |
| 2.5 | | | | | | | | | | | |
| | | Small Vane Shear Reading @ 3 ft. = 17.2 (3.59 T.S.F.) Remolded=4.7 (0.98 T.S.F.) | | | | 2 | VS | | | | |
| 5 | | | | | -5.0 | 3 | VS | | | | |
| | | Small Vane Shear Reading @ 5 ft. = 8.7 (1.82 T.S.F.) Remolded=4.6 (0.96 T.S.F.) | | | 5.0 | | | | | | |
| | | | | | -7.0 | | | | | | |
| | | Small Vane Shear Reading @ 7 ft. = 10.3 (2.15 T.S.F.) Remolded=5.2 (1.09 T.S.F.) | | | 7.0 | 4 | VS | | | | |
| 7.5 | | | | | | | | | | | |
| 10 | | | | | | | | | | | |
| 12.5 | | | | | | | | | | | |
| 15 | | | | | | | | | | | |

| | | |
| --- | --- | --- |
| Drill Method: **Probe rod** | | Groundwater Elev. During Drilling: ▽ |
| Boring Started: **9/20/2022** | **GEOTECHNICS** | Groundwater Elev. @ Comp.: ▽ |
| Boring Completed: **9/20/2022** | **Soil & Material Testing** | Groundwater Elev. @ ____ Hrs.: ▽ |
| Tested By: **MAS** | | Boring Location: **39.21477, -92.1421** |
| Logging By: **MAS** | | Sheet 1 of 1 |

| Depth (ft.) | Symbol | SUBSURFACE PROFILE Description | Qp, t.s.f. | Dry Density, P.C.F. | Depth/Elev. | SAMPLE Number | Type | Blows/ft. | Qu, T.S.F. | Standard Penetration Test blows/ft. 10 20 30 40 | Water Content % Wp ●—— Wl 10 20 30 40 |
|---|---|---|---|---|---|---|---|---|---|---|---|
| 0 | | Ground Surface | | | 0.0 | | | | | | |
| | | Topsoil (±8") | | | -0.7 | | | | | | |
| | | Small Vane Shear Reading @ 1 ft. = 8.0 (1.60 T.S.F.) | | | 0.7 | 1 | VS | | | | |
| | | Small Vane Shear Reading @ 3 ft. = 10.0 (2.0 T.S.F.) | | | | 2 | VS | | | | |
| 5 | | Small Vane Shear Reading @ 5 ft. = 7.2 (1.44 T.S.F.) | | | -5.0 / 5.0 | 3 | VS | | | | |
| | | Small Vane Shear Reading @ 7 ft. = 9.6 (1.92 T.S.F.) | | | -7.0 / 7.0 | 4 | VS | | | | |
| 10 | | Small Vane Shear Reading @ 10 ft. = 7.6 (1.52 T.S.F.) | | | -10.0 / 10.0 | 5 | VS | | | | |
| | | End of Boring @ 10 Ft. | | | | | | | | | |
| 15 | | | | | | | | | | | |
| 20 | | | | | | | | | | | |
| 25 | | | | | | | | | | | |
| 30 | | | | | | | | | | | |

Drill Method: **3 1/4" HSA with AW Rod**
Boring Started: **8/11/2022**
Boring Completed: **8/11/2022**
Tested By: **BRH**
Logging By: **BRH**

**GEOTECHNICS**
Soil & Material Testing

Groundwater Elev. During Drilling: ▽
Groundwater Elev. @ Comp.: ▽
Groundwater Elev. @    Hrs.: ▽
Boring Location: **See Location Sketch**

Sheet 1 of 1

**Project No.: 22-1064**

**Project: Hubbell 2022 Centralia MO Site**

**Client: University of Maine**

**Boring No.: VS-2A**

**Rig:**

**Location: Centralia, MO**

**Driller: MAS**

| Depth (ft.) | Symbol | SUBSURFACE PROFILE Description | Qp, t.s.f. | Dry Density, P.C.F. | Depth/Elev. | SAMPLE Number | SAMPLE Type | SAMPLE Blows/ft. | Qu, T.S.F. | Standard Penetration Test blows/ft. | Water Content % |
|---|---|---|---|---|---|---|---|---|---|---|---|
| 0 | | Ground Surface | | | 0.0 | | | | | 10 20 30 40 | Wp ●—— Wl  10 20 30 40 |
| | | Topsoil (±8") | | | -0.7 | | | | | | |
| | | | | | 0.7 | | | | | | |
| | | Small Vane Shear Reading @ 1 ft. = 9.4 (1.97 T.S.F.) Remolded=2.9 (0.61 T.S.F.) | | | | 1 | VS | | | | |
| 2.5 | | | | | | | | | | | |
| | | Small Vane Shear Reading @ 3 ft. = 14.7 (3.07 T.S.F.) Remolded=6.5 (1.36 T.S.F.) | | | | 2 | VS | | | | |
| | | | | | -5.0 | | | | | | |
| 5 | | Small Vane Shear Reading @ 5 ft. = 5.8 (1.21 T.S.F.) Remolded=2.8 (0.59 T.S.F.) | | | 5.0 | 3 | VS | | | | |
| | | | | | -7.0 | | | | | | |
| | | Small Vane Shear Reading @ 7 ft. = 6.8 (1.42 T.S.F.) Remolded=3.0 (0.63 T.S.F.) | | | 7.0 | 4 | VS | | | | |
| 7.5 | | | | | | | | | | | |
| 10 | | | | | | | | | | | |
| 12.5 | | | | | | | | | | | |
| 15 | | | | | | | | | | | |

**Drill Method: Probe rod**

**Boring Started: 9/20/2022**

**Boring Completed: 9/20/2022**

**Tested By: MAS**

**Logging By: MAS**

**GEOTECHNICS**
**Soil & Material Testing**

**Groundwater Elev. During Drilling:** ▽

**Groundwater Elev. @ Comp.:** ▽

**Groundwater Elev. @        Hrs.:** ▽

**Boring Location: 39.21471, -92.142**

**Sheet 1 of 1**

| Project No.: **22-1064** | **Boring Log** | Rig: **CME 55 (B-55)** |
|---|---|---|
| Project: **Hubbell 2022 Centralia MO Site** | | Location: **Centralia, MO** |
| | | Driller: **AJK** |
| Client: **University of Maine** | | |
| Boring No.: **VS-3** | | |

### SUBSURFACE PROFILE / SAMPLE

| Depth (ft.) | Symbol | Description | Qp, t.s.f. | Dry Density, P.C.F. | Depth/Elev. | Number | Type | Blows/ft. | Qu, T.S.F. | Standard Penetration Test blows/ft. | Water Content % |
|---|---|---|---|---|---|---|---|---|---|---|---|
| 0 | | Ground Surface | | | 0.0 | | | | | | |
| | | Topsoil (±8") | | | -0.7 | | | | | | |
| | | Standard Vane Shear Reading @ 1 ft. = 12.6 (1.26 T.S.F.) | | | 0.7 | 1 | VS | | | | |
| | | Small Vane Shear Reading @ 3 ft. = 11.8 (2.36 T.S.F.) | | | | 2 | VS | | | | |
| | | | | | -5.0 | | | | | | |
| 5 | | Standard Vane Shear Reading @ 5 ft. = 12.0 (1.20 T.S.F.) | | | 5.0 | 3 | SS | 6 | | ▲ | |
| | | | | | -7.0 | | | | | | |
| | | Small Vane Shear Reading @ 7 ft. = 9.2 (1.84 T.S.F.) | | | 7.0 | 4 | VS | | | | |
| | | End of Boring @ 7 Ft. | | | | | | | | | |
| 10 | | | | | | | | | | | |
| 15 | | | | | | | | | | | |
| 20 | | | | | | | | | | | |
| 25 | | | | | | | | | | | |
| 30 | | | | | | | | | | | |

Water Content % scale: Wp ├——●——┤ WI  (10 20 30 40)
Standard Penetration Test scale: 10 20 30 40

| | |
|---|---|
| Drill Method: **3 1/4" HSA with AW Rod** | Groundwater Elev. During Drilling: ☿ |
| Boring Started: **8/11/2022** | Groundwater Elev. @ Comp.: ☿ |
| Boring Completed: **8/11/2022** | Groundwater Elev. @      Hrs.: ☿ |
| Tested By: **BRH** | Boring Location: **See Location Sketch** |
| Logging By: **BRH** | Sheet 1 of 1 |

**GEOTECHNICS**
Soil & Material Testing

| Project No.: **22-1064** | **Boring Log** | Rig: |
|---|---|---|
| Project: **Hubbell 2022 Centralia MO Site** | | Location: **Centralia, MO** |
| | | Driller: **MAS** |
| Client: **University of Maine** | | |
| Boring No.: **VS-3A** | | |

| Depth (ft.) | Symbol | SUBSURFACE PROFILE Description | Qp, t.s.f. | Dry Density, P.C.F. | Depth/Elev. | SAMPLE Number | Type | Blows/ft. | Qu, T.S.F. | Standard Penetration Test blows/ft. 10 20 30 40 | Water Content % Wp ●— WI 10 20 30 40 |
|---|---|---|---|---|---|---|---|---|---|---|---|
| 0 | | Ground Surface | | | 0.0 | | | | | | |
| | | Topsoil (±8") | | | -0.7 | | | | | | |
| | | | | | 0.7 | | | | | | |
| | | Small Vane Shear Reading @ 1 ft. = 18.1 (3.78 T.S.F.) Remolded=8.1 (1.69 T.S.F.) | | | | 1 | VS | | | | |
| 2.5 | | | | | | | | | | | |
| | | Small Vane Shear Reading @ 3 ft. = 12.0 (2.51 T.S.F.) Remolded=6.5 (1.36 T.S.F.) | | | | 2 | VS | | | | |
| 5 | | Small Vane Shear Reading @ 5 ft. = 9.6 (2.01 T.S.F.) Remolded=4.9 (1.02 T.S.F.) | | | -5.0 5.0 | 3 | VS | | | | |
| | | | | | -7.0 7.0 | | | | | | |
| 7.5 | | Small Vane Shear Reading @ 7 ft. = 9.2 (1.92 T.S.F.) Remolded=4.4 (0.92 T.S.F.) | | | | 4 | VS | | | | |
| 10 | | | | | | | | | | | |
| 12.5 | | | | | | | | | | | |
| 15 | | | | | | | | | | | |

| | **GEOTECHNICS** Soil & Material Testing | |
|---|---|---|
| Drill Method: **Probe rod** | | Groundwater Elev. During Drilling: ▽ |
| Boring Started: **9/20/2022** | | Groundwater Elev. @ Comp.: ▽ |
| Boring Completed: **9/20/2022** | | Groundwater Elev. @     Hrs.: ▽ |
| Tested By: **MAS** | | Boring Location: **39.21466,-92.1418** |
| Logging By: **MAS** | | Sheet 1 of 1 |

| Project No.: **22-1064** | **Boring Log** | Rig: **CME 55 (B-55)** |
|---|---|---|
| Project: **Hubbell 2022 Centralia MO Site** | | Location: **Centralia, MO** |
| | | Driller: **AJK** |
| Client: **University of Maine** | | |
| Boring No.: **VS-4** | | |

| Depth (ft.) | Symbol | Description | Qp, t.s.f. | Dry Density, P.C.F. | Depth/Elev. | Number | Type | Blows/ft. | Qu, T.S.F. | Standard Penetration Test blows/ft. 10 20 30 40 | Water Content % Wp •———• Wl 10 20 30 40 |
|---|---|---|---|---|---|---|---|---|---|---|---|
| 0 | | Ground Surface | | | 0.0 | | | | | | |
| | | Topsoil (±8") | | | -0.7 | | | | | | |
| | | | | | 0.7 | | | | | | |
| | | Small Vane Shear Reading @ 1 ft. = 6.2 (1.24 T.S.F.) | | | | 1 | VS | | | | |
| | | Small Vane Shear Reading @ 3 ft. = 13.0 (2.60 T.S.F.) | | | | 2 | VS | | | | |
| 5 | | | | | -5.0 5.0 | | | | | | |
| | | Small Vane Shear Reading @ 5 ft. = 6.6 (1.32 T.S.F.) | | | | 3 | VS | | | | |
| | | | | | -7.0 7.0 | | | | | | |
| | | Small Vane Shear Reading @ 7 ft. = 8.6 (1.72 T.S.F.) | | | | 4 | VS | | | | |
| 10 | | | | | -10.0 10.0 | | | | | | |
| | | Small Vane Shear Reading @ 10 ft. = 10.8 (2.16 T.S.F.) | | | | 5 | VS | | | | |
| | | End of Boring @ 10 Ft. | | | | | | | | | |
| 15 | | | | | | | | | | | |
| 20 | | | | | | | | | | | |
| 25 | | | | | | | | | | | |
| 30 | | | | | | | | | | | |

Drill Method: **3 1/4" HSA with AW Rod**
Boring Started: **8/11/2022**
Boring Completed: **8/11/2022**
Tested By: **BRH**
Logging By: **BRH**

**GEOTECHNICS**
**Soil & Material Testing**

Groundwater Elev. During Drilling: ▽
Groundwater Elev. @ Comp.: ▽
Groundwater Elev. @    Hrs.: ▽
Boring Location: **See Location Sketch**
Sheet 1 of 1

| | | | | | | | | | | |
|---|---|---|---|---|---|---|---|---|---|---|

**Project No.: 22-1064**

**Project: Hubbell 2022 Centralia MO Site**

**Client: University of Maine**

**Boring No.: VS-4A**

# Boring Log

**Rig:**

**Location: Centralia, MO**

**Driller: MAS**

| SUBSURFACE PROFILE | | | | | | SAMPLE | | | | Standard Penetration Test blows/ft. | Water Content % |
|---|---|---|---|---|---|---|---|---|---|---|---|
| Depth (ft.) | Symbol | Description | Qp, t.s.f. | Dry Density, P.C.F. | Depth/Elev. | Number | Type | Blows/ft. | Qu, T.S.F. | 10 20 30 40 | Wp ●─── Wl  10 20 30 40 |
| 0 | | Ground Surface | | | 0.0 | | | | | | |
| | | Topsoil (±8") | | | -0.7 | | | | | | |
| | | | | | 0.7 | | | | | | |
| | | Small Vane Shear Reading @ 1 ft. = 8.7 (1.81 T.S.F.)  Remolded=2.5 (0.52 T.S.F.) | | | | 1 | VS | | | | |
| 2.5 | | | | | | | | | | | |
| | | Small Vane Shear Reading @ 3 ft. = 9.8 (2.05 T.S.F.)  Remolded=3.8 (0.79 T.S.F.) | | | | 2 | VS | | | | |
| 5 | | | | | -5.0 | | | | | | |
| | | Small Vane Shear Reading @ 5 ft. = 10.4 (2.17 T.S.F.)  Remolded=5.0(1.05 T.S.F.) | | | 5.0 | 3 | VS | | | | |
| | | | | | -7.0 | | | | | | |
| 7.5 | | Small Vane Shear Reading @ 7 ft. = 7.7 (1.61 T.S.F.)  Remolded=3.0 (0.63 T.S.F.) | | | 7.0 | 4 | VS | | | | |
| 10 | | | | | | | | | | | |
| 12.5 | | | | | | | | | | | |
| 15 | | | | | | | | | | | |

**Drill Method: Probe rod**
**Boring Started: 9/28/2022**
**Boring Completed: 9/28/2022**
**Tested By: MAS**
**Logging By: MAS**

**GEOTECHNICS**
**Soil & Material Testing**

**Groundwater Elev. During Drilling:** ▽
**Groundwater Elev. @ Comp.:** ▽
**Groundwater Elev. @      Hrs.:** ▽
**Boring Location: 39.2147,-92.1415**

**Sheet 1 of 1**

| Project No.: **22-1064** | **Boring Log** | Rig: **CME 55 (B-55)** |
|---|---|---|
| Project: **Hubbell 2022 Centralia MO Site** | | Location: **Centralia, MO** |
| | | Driller: **AJK** |
| Client: **University of Maine** | | |
| Boring No.: **VS-5** | | |

| Depth (ft.) | Symbol | SUBSURFACE PROFILE Description | Qp, t.s.f. | Dry Density, P.C.F. | Depth/Elev. | SAMPLE Number | Type | Blows/ft. | Qu, T.S.F. | Standard Penetration Test blows/ft. 10 20 30 40 | Water Content % Wp ●—— Wl 10 20 30 40 |
|---|---|---|---|---|---|---|---|---|---|---|---|
| 0 | | Ground Surface | | | 0.0 | | | | | | |
| | | Topsoil (±8") | | | -0.7 | | | | | | |
| | | Small Vane Shear Reading @ 1 ft. = 10.2 (2.04 T.S.F.) | | | 0.7 | 1 | VS | | | | |
| | | Small Vane Shear Reading @ 3 ft. = 10.6 (2.12 T.S.F.) | | | | 2 | VS | | | | |
| 5 | | Small Vane Shear Reading @ 5 ft. = 5.8 (1.16 T.S.F.) | | | -5.0 / 5.0 | 3 | VS | | | | |
| | | Small Vane Shear Reading @ 7 ft. = 10.8 (2.16 T.S.F.) | | | -7.0 / 7.0 | 4 | VS | | | | |
| 10 | | Small Vane Shear Reading @ 10 ft. = 12.8 (2.56 T.S.F.) | | | -10.0 / 10.0 | 5 | VS | | | | |
| | | End of Boring @ 10 Ft. | | | | | | | | | |
| 15 | | | | | | | | | | | |
| 20 | | | | | | | | | | | |
| 25 | | | | | | | | | | | |
| 30 | | | | | | | | | | | |

Drill Method: **3 1/4" HSA with AW Rod**
Boring Started: **8/11/2022**
Boring Completed: **8/11/2022**
Tested By: **BRH**
Logging By: **BRH**

**GEOTECHNICS**
**Soil & Material Testing**

Groundwater Elev. During Drilling: ▽
Groundwater Elev. @ Comp.: ▽
Groundwater Elev. @   Hrs.: ▽
Boring Location: **See Location Sketch**
Sheet 1 of 1

| Project No.: **22-1064** | **Boring Log** | Rig: |
|---|---|---|
| Project: **Hubbell 2022 Centralia MO Site** | | Location: **Centralia, MO** |
| | | Driller: **MAS** |
| Client: **University of Maine** | | |
| Boring No.: **VS-5a** | | |

### SUBSURFACE PROFILE / SAMPLE

| Depth (ft.) | Symbol | Description | Qp, t.s.f. | Dry Density, P.C.F. | Depth/Elev. | Number | Type | Blows/ft. | Qu, T.S.F. | Standard Penetration Test blows/ft. 10 20 30 40 | Water Content % Wp Wl 10 20 30 40 |
|---|---|---|---|---|---|---|---|---|---|---|---|
| 0 | | Ground Surface | | | 0.0 | | | | | | |
| | | Topsoil (±8") | | | -0.7 | | | | | | |
| | | | | | 0.7 | | | | | | |
| | | Small Vane Shear Reading @ 1 ft. = 10.2 (2.13 T.S.F.) Remolded=1.2 (0.25 T.S.F.) | | | | 1 | VS | | | | |
| 2.5 | | | | | | | | | | | |
| | | Small Vane Shear Reading @ 3 ft. = 8.4 (1.76 T.S.F.) Remolded=4.3 (0.90 T.S.F.) | | | | 2 | VS | | | | |
| 5 | | | | | -5.0 | | | | | | |
| | | Small Vane Shear Reading @ 5 ft. = 6.7 (1.40 T.S.F.) Remolded=3.5 (0.73 T.S.F.) | | | 5.0 | 3 | VS | | | | |
| | | | | | -7.0 | | | | | | |
| | | Small Vane Shear Reading @ 7 ft. = 9.4 (1.96 T.S.F.) Remolded=3.8 (0.79 T.S.F.) | | | 7.0 | 4 | VS | | | | |
| 7.5 | | | | | | | | | | | |
| 10 | | | | | | | | | | | |
| 12.5 | | | | | | | | | | | |
| 15 | | | | | | | | | | | |

| Drill Method: **Probe rod** | Groundwater Elev. During Drilling: ⛢ |
|---|---|
| Boring Started: **9/28/2022** | Groundwater Elev. @ Comp.: ⛢ |
| Boring Completed: **9/28/2022** | Groundwater Elev. @    Hrs.: ⛢ |
| Tested By: **MAS** | Boring Location: **39.21457,-92.1414** |
| Logging By: **MAS** | Sheet 1 of 1 |

**GEOTECHNICS**
Soil & Material Testing

| | | | | | | | | | |
|---|---|---|---|---|---|---|---|---|---|
| **Project No.: 22-1064** | | | **Boring Log** | | | | **Rig: CME 55 (B-55)** | | |
| **Project: Hubbell 2022 Centralia MO Site** | | | | | | | **Location: Centralia, MO** | | |
| **Client: University of Maine** | | | | | | | **Driller: AJK** | | |
| **Boring No.: VS-6** | | | | | | | | | |

| SUBSURFACE PROFILE | | | | | | | SAMPLE | | | | | |
|---|---|---|---|---|---|---|---|---|---|---|---|---|
| Depth (ft.) | Symbol | Description | Qp, t.s.f. | Dry Density, P.C.F. | Depth/Elev. | Number | Type | Blows/ft. | Qu, T.S.F. | Standard Penetration Test blows/ft. | Water Content % |
| 0 | | Ground Surface | | | 0.0 | | | | | 10 20 30 40 | Wp ●──── Wl  10 20 30 40 |
| | | Sand | | | -1.0 | | | | | | |
| 1.0 | | Small Vane Shear Reading @ 1 ft. = 5.2 (1.04 T.S.F.) | | | 1.0 | 1 | VS | | | | |
| | | Small Vane Shear Reading @ 3 ft. = 9.9 (1.98 T.S.F.) | | | | 2 | VS | | | | |
| 5 | | Small Vane Shear Reading @ 5 ft. = 8.4 (1.68 T.S.F.) | | | -5.0  5.0 | 3 | VS | | | | |
| | | Small Vane Shear Reading @ 7 ft. = 7.4 (1.48 T.S.F.) | | | -7.0  7.0 | 4 | VS | | | | |
| 10 | | Small Vane Shear Reading @ 10 ft. = 8.4 (1.68 T.S.F.) | | | -10.0  10.0 | 5 | VS | | | | |
| | | End of Boring @ 10 Ft. | | | | | | | | | |
| 15 | | | | | | | | | | | |
| 20 | | | | | | | | | | | |
| 25 | | | | | | | | | | | |
| 30 | | | | | | | | | | | |

**Drill Method: 3 1/4" HSA with AW Rod**
**Boring Started: 8/11/2022**
**Boring Completed: 8/11/2022**
**Tested By: BRH**
**Logging By: BRH**

**GEOTECHNICS**
**Soil & Material Testing**

**Groundwater Elev. During Drilling:** ☱
**Groundwater Elev. @ Comp.:** ☱
**Groundwater Elev. @        Hrs.:** ☱
**Boring Location: See Location Sketch**
**Sheet 1 of 1**

| Project No.: **22-1064** | **Boring Log** | Rig: |
|---|---|---|
| Project: **Hubbell 2022 Centralia MO Site** | | Location: **Centralia, MO** |
| | | Driller: **MAS** |
| Client: **University of Maine** | | |
| Boring No.: **VS-6a** | | |

| | | SUBSURFACE PROFILE | | | | | SAMPLE | | | | Standard Penetration Test blows/ft. | Water Content % |
|---|---|---|---|---|---|---|---|---|---|---|---|---|
| Depth (ft.) | Symbol | Description | Qp, t.s.f. | Dry Density, P.C.F. | Depth/Elev. | Number | Type | Blows/ft. | Qu, T.S.F. | | 10 20 30 40 | Wp ●──── Wl  10 20 30 40 |
| 0 | | Ground Surface | | | 0.0 | | | | | | | |
| | | Small Vane Shear Reading @ 1 ft. = 8.8 (1.84 T.S.F.) | | | | 1 | VS | | | | | |
| 2.5 | | | | | | | | | | | | |
| | | Small Vane Shear Reading @ 3 ft. = 18.5 (3.87 T.S. | | | | 2 | VS | | | | | |
| 5 | | | | | | | | | | | | |
| 7.5 | | | | | | | | | | | | |
| 10 | | | | | | | | | | | | |
| 12.5 | | | | | | | | | | | | |
| 15 | | | | | | | | | | | | |

Drill Method: **Probe rod**
Boring Started: **9/28/2022**
Boring Completed: **9/28/2022**
Tested By: **MAS**
Logging By: **MAS**

**GEOTECHNICS**
**Soil & Material Testing**

Groundwater Elev. During Drilling: ⟱
Groundwater Elev. @ Comp.: ⟱
Groundwater Elev. @          Hrs.: ⟱
Boring Location: **39.21444,-92.14469**

Sheet 1 of 1

| Project No.: **22-1064** | | Rig: **CME 55 (B-55)** |
| Project: **Hubbell 2022 Centralia MO Site** | | Location: **Centralia, MO** |
| | | Driller: **AJK** |
| Client: **University of Maine** | | |
| Boring No.: **VS-7** | | |

## SUBSURFACE PROFILE / SAMPLE

| Depth (ft.) | Symbol | Description | Qp, t.s.f. | Dry Density, P.C.F. | Depth/Elev. | Number | Type | Blows/ft. | Qu, T.S.F. | Standard Penetration Test blows/ft. 10 20 30 40 | Water Content % Wp ●—— WI 10 20 30 40 |
|---|---|---|---|---|---|---|---|---|---|---|---|
| 0 | | Ground Surface | | | 0.0 | | | | | | |
| | | Sand | | | -1.0 | | | | | | |
| | | Small Vane Shear Reading @ 1 ft. = 5.6 (1.12 T.S.F.) | | | 1.0 | 1 | VS | | | | |
| | | Small Vane Shear Reading @ 3 ft. = 6.0 (1.20 T.S.F.) | | | | 2 | VS | | | | |
| 5 | | Small Vane Shear Reading @ 5 ft. = 6.2 (1.24 T.S.F.) | | | -5.0 5.0 | 3 | VS | | | | |
| | | Small Vane Shear Reading @ 7 ft. = 9.9 (1.98 T.S.F.) End of Boring @ 7 Ft. | | | -7.0 7.0 | 4 | VS | | | | |
| 10 | | | | | | | | | | | |
| 15 | | | | | | | | | | | |
| 20 | | | | | | | | | | | |
| 25 | | | | | | | | | | | |
| 30 | | | | | | | | | | | |

Drill Method: **3 1/4" HSA with AW Rod**
Boring Started: **8/11/2022**
Boring Completed: **8/11/2022**
Tested By: **BRH**
Logging By: **BRH**

**GEOTECHNICS**
**Soil & Material Testing**

Groundwater Elev. During Drilling: ▽
Groundwater Elev. @ Comp.: ▽
Groundwater Elev. @    Hrs.: ▽
Boring Location: **See Location Sketch**
Sheet 1 of 1

| Project No.: **22-1064** | **Boring Log** | Rig: |
|---|---|---|
| Project: **Hubbell 2022 Centralia MO Site** | | Location: **Centralia, MO** |
| | | Driller: **MAS** |
| Client: **University of Maine** | | |
| Boring No.: **VS-7a** | | |

| Depth (ft.) | Symbol | SUBSURFACE PROFILE — Description | Qp, t.s.f. | Dry Density, P.C.F. | Depth/Elev. | SAMPLE Number | Type | Blows/ft. | Qu, T.S.F. | Standard Penetration Test blows/ft. 10 20 30 40 | Water Content % Wp ● Wl 10 20 30 40 |
|---|---|---|---|---|---|---|---|---|---|---|---|
| 0 | | Ground Surface | | | 0.0 | | | | | | |
| | | Small Vane Shear Reading @ 1 ft. = 10.8 (2.26 T.S.F.) | | | | 1 | VS | | | | |
| 2.5 | | | | | | | | | | | |
| 5 | | | | | | | | | | | |
| 7.5 | | | | | | | | | | | |
| 10 | | | | | | | | | | | |
| 12.5 | | | | | | | | | | | |
| 15 | | | | | | | | | | | |

Drill Method: **Probe rod**
Boring Started: **9/28/2022**
Boring Completed: **9/28/2022**
Tested By: **MAS**
Logging By: **MAS**

**GEOTECHNICS**
Soil & Material Testing

Groundwater Elev. During Drilling: ▽
Groundwater Elev. @ Comp.: ▽
Groundwater Elev. @          Hrs.: ▽
Boring Location: **39.21444,-92.14458**
**Sheet 1 of 1**

# B.3   CPT Report

| Test location name | Pre-excavated depth [ft] | Z value [ft] | Test name | Cone serial number | |
|---|---|---|---|---|---|
| Hubbell- Centralia Mo | 2.99 | 0.00 | CPT#1 | 5707 | **GEOTECHNICS** |
| **Project ID** | **Client** | **Date investigation** | **Standard/Standar...** | **Nominal surface area of...** | Soil & Material Testing |
| 22-1064 | University of Maine | 8/12/2022 | / | 10.0/150.0 | A Division of Klingner |
| **Project name** | | **Page** | **Scale** | **Net surface area quotie...** | |
| Hubbell-2022 Centralia, Mo site | | 1/1 | 1:100 | 0.830/0.000 | |
| **Remarks1** | | **Equipment operator** | | **U** | |
| | | MAS | | u2 | |

**Classification by Robertson 1986**

qc [MPa]    fs [MPa]    u2 [MPa]    Fr [%]    N60 []

Silty clay to clay

Clayey silt to silty clay

Clayey silt to silty clay
Silty clay to clay
Clayey silt to silty clay

Clayey silt to silty clay

Clayey silt to silty clay

Clayey silt to silty clay

Clayey silt to silty clay

| Test location name | | Pre-excavated depth [ft] | | Z value [ft] | | Test name | Cone serial number | |
|---|---|---|---|---|---|---|---|---|
| Hubbel, Centralia, Mo | | 0.00 | | 0.00 | | CPT1A | 5707 | |
| Project ID | | Client | | Date investigation | Standard/Standar... | | Nominal surface area of... | **GEOTECHNICS** |
| 22-1064 | | University of Maine | | 9/20/2022 | / | | 10.0/150.0 | Soil & Material Testing |
| Project name | | | | Page | Scale | | Net surface area quotie... | A Division of Klingner |
| Hubbel-2022 Centralia, Mo Site | | | | 1/1 | 1:100 | | 0.830/0.000 | |
| Remarks1 | | | | Equipment operator | | | U | |
| | | | | MAS | | | u2 | |

Classification by Robertson 1986

qc [MPa]   fs [MPa]   u2 [MPa]   Fr [%]   N60 []



Clay

215

| Test location name | Pre-excavated depth [ft] | Z value [ft] | Test name | Cone serial number | |
|---|---|---|---|---|---|
| Hubbell-Centralia, Mo | 2.99 | 0.00 | CPT#2 | 5707 | **GEOTECHNICS** |
| Project ID | Client | Date investigation | Standard/Standar... | Nominal surface area of... | Soil & Material Testing |
| 22-1064 | University of Maine | 8/12/2022 | / | 10.0/150.0 | A Division of Klingner |
| Project name | | Page | Scale | Net surface area quotie... | |
| Hubbell-2022 Centralia, Mo site | | 1/1 | 1:100 | 0.830/0.000 | |
| Remarks1 | | Equipment operator | | U | |
| | | MAS | | u2 | |

Classification by Robertson 1986

qc [MPa]   fs [MPa]   u2 [MPa]   Fr [%]   N60 []



Clay

Clay

Silty clay to clay

Silty clay to clay

Clay

Clayey silt to silty clay

Clayey silt to silty clay

216

| Test location name | Pre-excavated depth [ft] | Z value [ft] | Test name | Cone serial number | |
|---|---|---|---|---|---|
| Hubbel-Centralia ,Mo | 0.00 | 0.00 | CPT2A | 5707 | **GEOTECHNICS** |
| **Project ID** | **Client** | **Date investigation** | **Standard/Standar...** | **Nominal surface area of...** | Soil & Material Testing |
| 22-1064 | University of Maine | 9/20/2022 | / | 10.0/150.0 | A Division of Klingner |
| **Project name** | | **Page** | **Scale** | **Net surface area quotie...** | |
| Hubbel-2022 Centralia, Mo site | | 1/1 | 1:100 | 0.830/0.000 | |
| **Remarks1** | | **Equipment operator** | | **U** | |
| | | MAS | | u2 | |

Classification by Robertson 1986



qc [MPa]   fs [MPa]   u2 [MPa]   Fr [%]   N60 []

Clay

| Test location name | Pre-excavated depth [ft] | Z value [ft] | Test name | Cone serial number | |
|---|---|---|---|---|---|
| Hubbell- Centralia, Mo | 2.99 | 0.00 | CPT#3 | 5707 | **GEOTECHNICS** |
| Project ID | Client | Date investigation | Standard/Standar... | Nominal surface area of... | Soil & Material Testing |
| 22-1064 | University of Maine | 8/12/2022 | / | 10.0/150.0 | A Division of Klingner |
| Project name | | Page | Scale | Net surface area quotie... | |
| Hubbell-2022 Centralia, Mo site | | 1/1 | 1:100 | 0.830/0.000 | |
| Remarks1 | | Equipment operator | | U | |
| | | MAS | | u2 | |

### Classification by Robertson 1986

Legend: qc [MPa], fs [MPa], u2 [MPa], Fr [%], N60 []



Soil classification log (left to right by depth):
- ~3.0–6.0 ft: Clay
- ~7.0–8.0 ft: Silty clay to clay
- ~9.0–10.0 ft: Silty clay to clay
- ~12.0–13.0 ft: Silty clay to clay
- ~14.0 ft: Clayey silt to silty clay
- ~18.0 ft: Clayey silt to silty clay
- ~24.0 ft: Clayey silt to silty clay
- ~27.0 ft: Clay
- ~32.0 ft: Clayey silt to silty clay
- ~40.0 ft: Clayey silt to silty clay

| Test location name | Pre-excavated depth [ft] | Z value [ft] | Test name | Cone serial number | |
|---|---|---|---|---|---|
| Hubbel- Centralia, Mo | 0.00 | 0.00 | CPT3B | 5707 | **GEOTECHNICS** |
| Project ID | Client | Date investigation | Standard/Standar… | Nominal surface area of… | Soil & Material Testing |
| 22-1064 | University of Maine | 9/20/2022 | / | 10.0/150.0 | A Division of Klingner |
| Project name | | Page | Scale | Net surface area quotie… | |
| Hubbel-2022 Centralia, Mo site | | 1/1 | 1:100 | 0.830/0.000 | |
| Remarks1 | | Equipment operator | | U | |
| In lieu of CPT3A, o ring damaged on 3A during penetration | | MAS | | u2 | |

Classification by Robertson 1986

qc [MPa]  fs [MPa]  u2 [MPa]  Fr [%]  N60 []

Length [ft]

Sandy silt to clayey silt

Clay

219

| Test location name<br>Hubbell- Centralia, Mo | Pre-excavated depth [ft]<br>2.99 | Z value [ft]<br>0.00 | Test name<br>CPT#4 | Cone serial number<br>5707 | **GEOTECHNICS** |
|---|---|---|---|---|---|
| Project ID<br>22-1064 | Client<br>University of Maine | Date investigation<br>8/12/2022 | Standard/Standar...<br>/ | Nominal surface area of...<br>10.0/150.0 | Soil & Material Testing |
| Project name<br>Hubbell- Centralia, Mo site | | Page<br>1/1 | Scale<br>1:100 | Net surface area quotie...<br>0.830/0.000 | A Division of Klingner |
| Remarks1 | | Equipment operator<br>MAS | | U<br>u2 | |

### Classification by Robertson 1986

qc [MPa]　fs [MPa]　u2 [MPa]　Fr [%]　N60 []

Sand

Sand to silty sand

Clay

Clay

Clay

Clay

Silty clay to clay

Clayey silt to silty clay

| Test location name | Pre-excavated depth [ft] | Z value [ft] | Test name | Cone serial number | |
|---|---|---|---|---|---|
| Hubbel-Centralia, Mo | 0.00 | 0.00 | CPT4A | 5707 | **GEOTECHNICS** |
| Project ID | Client | Date investigation | Standard/Standar... | Nominal surface area of... | Soil & Material Testing |
| 22-1064 | University of Maine | 9/28/2022 | / | 10.0/150.0 | |
| Project name | | Page | Scale | Net surface area quotie... | A Division of Klingner |
| Hubbel-Centralia, Mo site | | 1/1 | 1:100 | 0.830/0.004 | |
| Remarks1 | | Equipment operator | | U | |
| | | MAS | | u2 | |

Classification by Robertson 1986

qc [MPa]   fs [MPa]   u2 [MPa]   Fr [%]   N60 []

Sand to silty sand

Sand



221

| Test location name | Pre-excavated depth [ft] | Z value [ft] | Test name | Cone serial number | |
|---|---|---|---|---|---|
| Hubbell- Centralia, Mo | 2.99 | 0.00 | CPT#5 | 5707 | **GEOTECHNICS** |
| Project ID | Client | Date investigation | Standard/Standar… | Nominal surface area of… | Soil & Material Testing |
| 22-1064 | University of Maine | 8/12/2022 | / | 10.0/150.0 | |
| Project name | | Page | Scale | Net surface area quotie… | A Division of Klingner |
| Hubbell- Centralia, Mo site | | 1/1 | 1:100 | 0.830/0.000 | |
| Remarks1 | | Equipment operator | | U | |
| | | MAS | | u2 | |

Classification by Robertson 1986

qc [MPa]  fs [MPa]  u2 [MPa]  Fr [%]  N60 []

Depth classification labels:
- Clay (≈8.5 ft)
- Clay (≈11.0 ft)
- Clay (≈13.0 ft)
- Silty clay to clay (≈19.0 ft)
- Silty clay to clay (≈21.0 ft)
- Silty clay to clay (≈22.5 ft)
- Silty clay to clay (≈24.5 ft)
- Clay (≈27.5 ft)
- Clay (≈29.0 ft)
- Silty clay to clay (≈36.5 ft)

| Test location name | Pre-excavated depth [ft] | Z value [ft] | Test name | Cone serial number | |
|---|---|---|---|---|---|
| Hubbel- Centralia, Mo | 0.00 | 0.00 | CPT5A | 5707 | **GEOTECHNICS** |
| Project ID | Client | Date investigation | Standard/Standar... | Nominal surface area of... | Soil & Material Testing |
| 22-1064 | University of Maine | 9/28/2022 | / | 10.0/150.0 | |
| Project name | | Page | Scale | Net surface area quotie... | A Division of Klingner |
| Hubbel-Centralia,mo site | | 1/1 | 1:100 | 0.830/0.004 | |
| Remarks1 | | Equipment operator | | U | |
| | | MAS | | u2 | |

## Classification by Robertson 1986

Clay



qc [MPa] · fs [MPa] · u2 [MPa] · Fr [%] · N60 []

## B.4 Atterberg Limits

# LIQUID AND PLASTIC LIMITS TEST REPORT



| | MATERIAL DESCRIPTION | LL | PL | PI | %<#40 | %<#200 | USCS |
|---|---|---|---|---|---|---|---|
| ● | Fat Clay (CH), Light Brown mottled Yellow Brown, Medium, Moist | 93 | 34 | 59 | | | CH |
| ■ | Fat Clay (CH), Light Gray mottled Yellow Brown, Stiff, Moist | 62 | 24 | 38 | | | CH |
| ▲ | Lean Clay (CL), Light Gray mottled Yellow Brown, Silty, Medium, Moist | 41 | 18 | 23 | | | CL |
| ◆ | Fat Clay (CH), Light Gray mottled Yellow Brown/Reddish Brown, Stiff, Moist | 64 | 22 | 42 | | | CH |
| | | | | | | | |

Project No.    22-1064          Client:     University of Maine

Project:      Hubbell 2022 Centralia MO Site

● Location: Boring 2          Depth: 1-2½ ft.          Sample Number: 1
■ Location: Boring 2          Depth: 3-4½ ft.          Sample Number: 2
▲ Location: Boring 2          Depth: 5-6½ ft.          Sample Number: 3
◆ Location: Boring 2          Depth: 7-8½ ft.          Sample Number: 4

Remarks:
● Natural Moisture = 33.7%
■ Natural Moisture = 26.7%
▲ Natural Moisture = 24.4%
◆ Natural Moisture = 24.4%

**GEOTECHNICS**
Soil & Material Testing
4510 Paris Gravel Road - Hannibal, MO

Figure     Boring 2

Tested By: ○ DAW   □ NPP   △ DAW   ◇ BRH      Checked By: BJS

224

# LIQUID AND PLASTIC LIMITS TEST REPORT

Dashed line indicates the approximate upper limit boundary for natural soils

CH or OH

CL or OL

CL-ML

ML or OL

MH or OH

PLASTICITY INDEX

LIQUID LIMIT

| MATERIAL DESCRIPTION | LL | PL | PI | %<#40 | %<#200 | USCS |
|---|---|---|---|---|---|---|
| ● Fat Clay (CH), Light Gray mottled Yellow Brown, Medium, Moist | 78 | 28 | 50 | | | CH |
| ■ Fat Clay (CH), Light Gray mottled Yellow Brown, Stiff, Moist | 60 | 22 | 38 | | | CH |
| ▲ Lean Clay (CL), Light Gray mottled Yellow Brown, Medium, Moist | 44 | 18 | 26 | | | CL |
| ◆ Fat Clay (CH), Light Gray mottled Yellow Brown, Medium, Moist | 61 | 20 | 41 | | | CH |
| | | | | | | |

Project No.    22-1064        Client:    University of Maine

Project:    Hubbell 2022 Centralia MO Site

● Location: Boring 5        Depth: 1-2½ ft.        Sample Number: 1
■ Location: Boring 5        Depth: 3-4½ ft.        Sample Number: 2
▲ Location: Boring 5        Depth: 5-6½ ft.        Sample Number: 3
◆ Location: Boring 5        Depth: 7-9 ft.        Sample Number: 4

Remarks:
● Natural Moisture = 21.6%
■ Natural Moisture = 25.0%
▲ Natural Moisture = 25.3%
◆ Natural Moisture = 24.9%

**GEOTECHNICS**
Soil & Material Testing
4510 Paris Gravel Road - Hannibal, MO

Figure    Boring 5

Tested By: ○ NPP    □ NPP    △ DJS    ◇ BRH

225

# APPENDIX C

# MONOTONIC LATERAL TEST RESULTS

## C.1   Helical Pile without Collar Vane
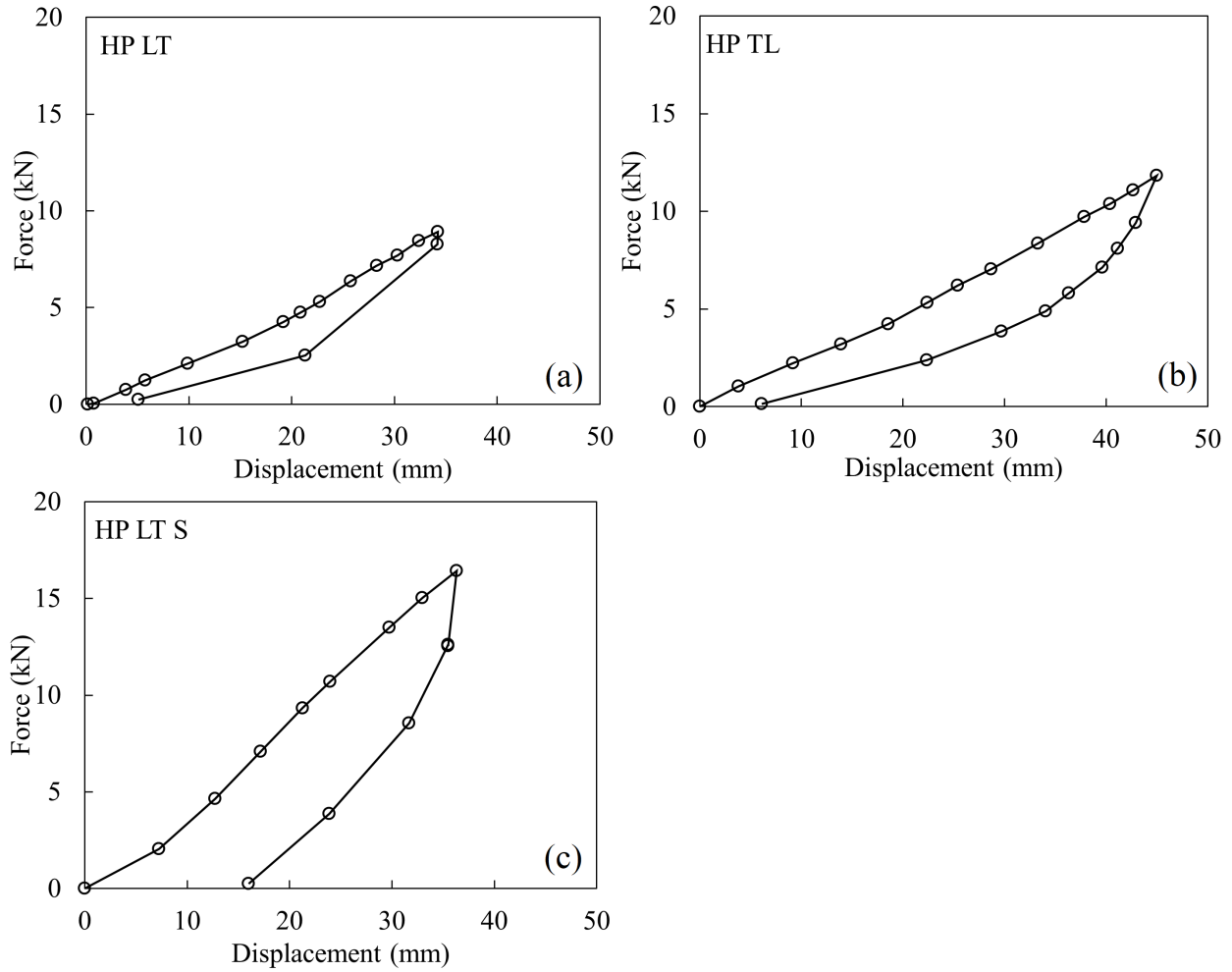


Figure C.1: Lateral response for HP without CV: (a) load sequence LT in cohesive soil; (b) load sequence TL in cohesive soil; (c) load sequence LT in granular soil.

## C.2    Collar Vane CV2 1-1
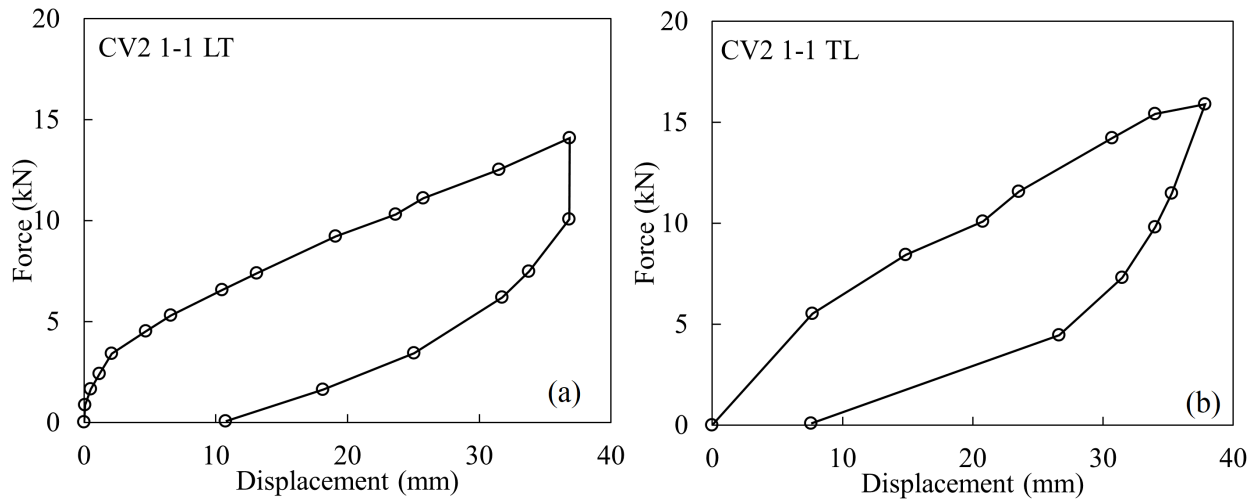


Figure C.2: Lateral response for CV2 1-1: (a) load sequence LT in cohesive soil; (b) load sequence TL in cohesive soil.

## C.3    Collar Vane CV2 1-2
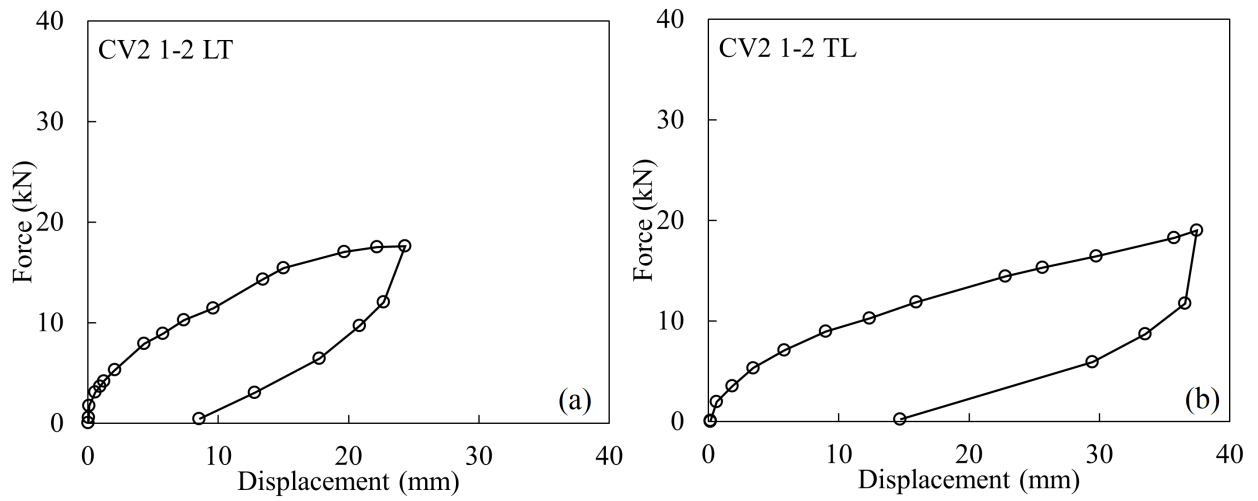


Figure C.3: Lateral response for CV2 1-2: (a) load sequence LT in cohesive soil; (b) load sequence TL in cohesive soil.

## C.4 Collar Vane CV2 1-3
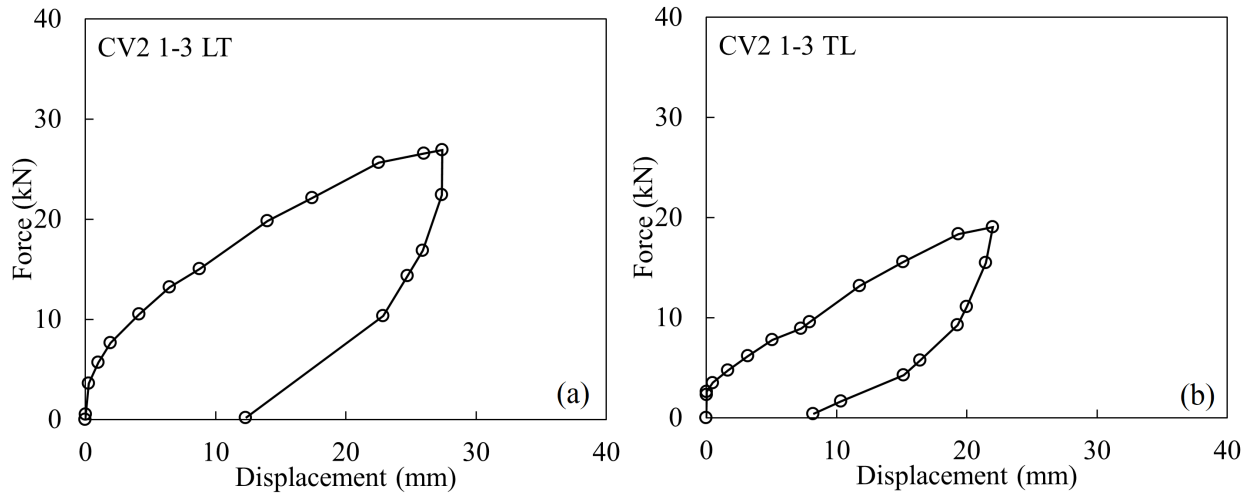


Figure C.4: Lateral response for CV2 1-3: (a) load sequence LT in cohesive soil; (b) load sequence TL in cohesive soil.

## C.5 Collar Vane CV2 2-1
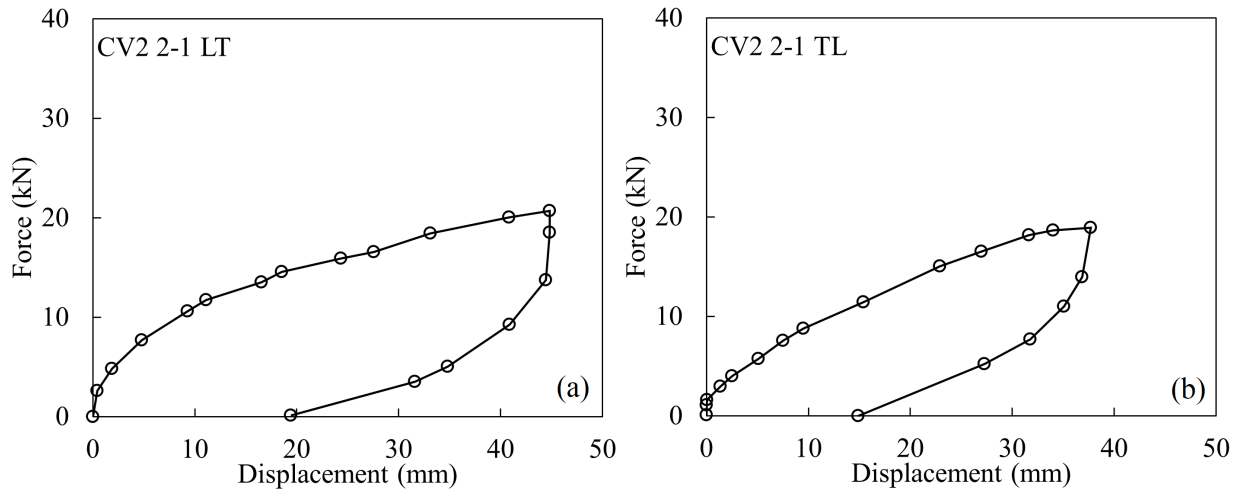


Figure C.5: Lateral response for CV2 2-1: (a) load sequence LT in cohesive soil; (b) load sequence TL in cohesive soil.

## C.6  Collar Vane CV 2-2
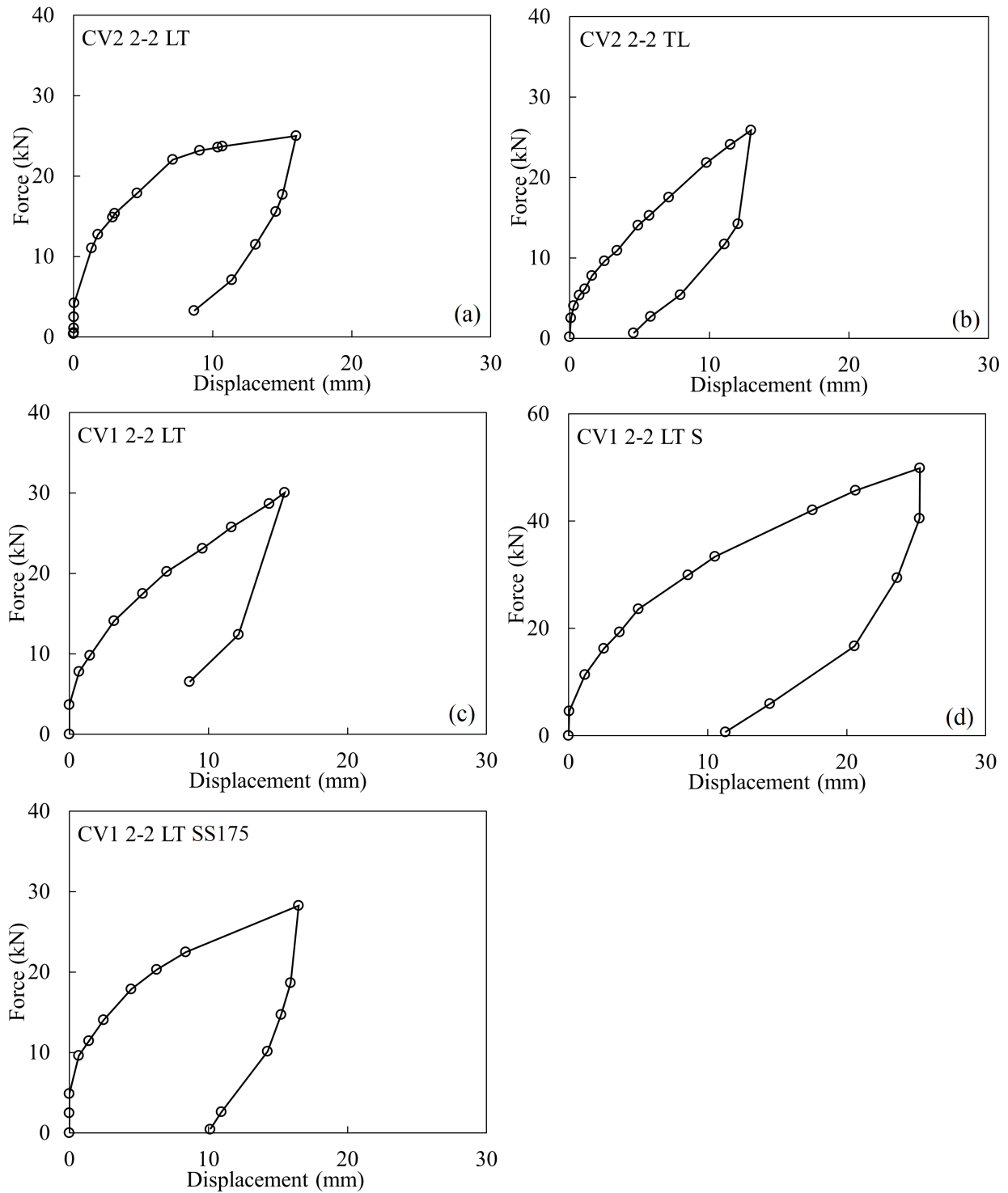


Figure C.6: Lateral response for CV 2-2: (a) two-piece CV with LT in cohesive soil; (b) two-piece CV with TL in cohesive soil; (c) one-piece CV with LT in cohesive soil; (d) one-piece CV with LT in granular soil; (e) one-piece CV with LT in cohesive soil using the square shaft.

## C.7 Collar Vane CV 2-3
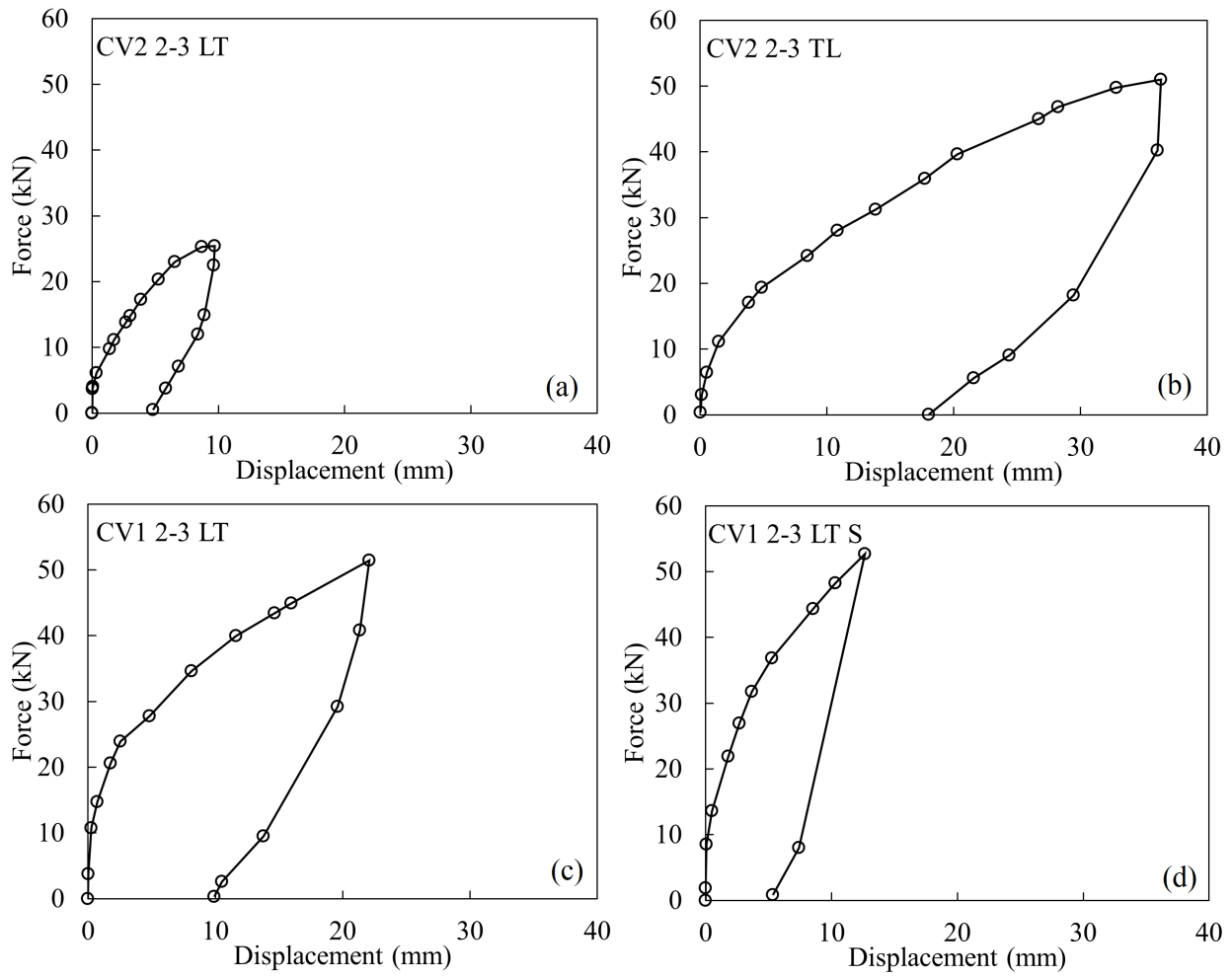


Figure C.7: Lateral response for CV 2-3: (a) two-piece CV with LT in cohesive soil; (b) two-piece CV with TL in cohesive soil; (c) one-piece CV with LT in cohesive soil; (d) one-piece CV with LT in granular soil.

## C.8 Collar Vane CV2 3-1
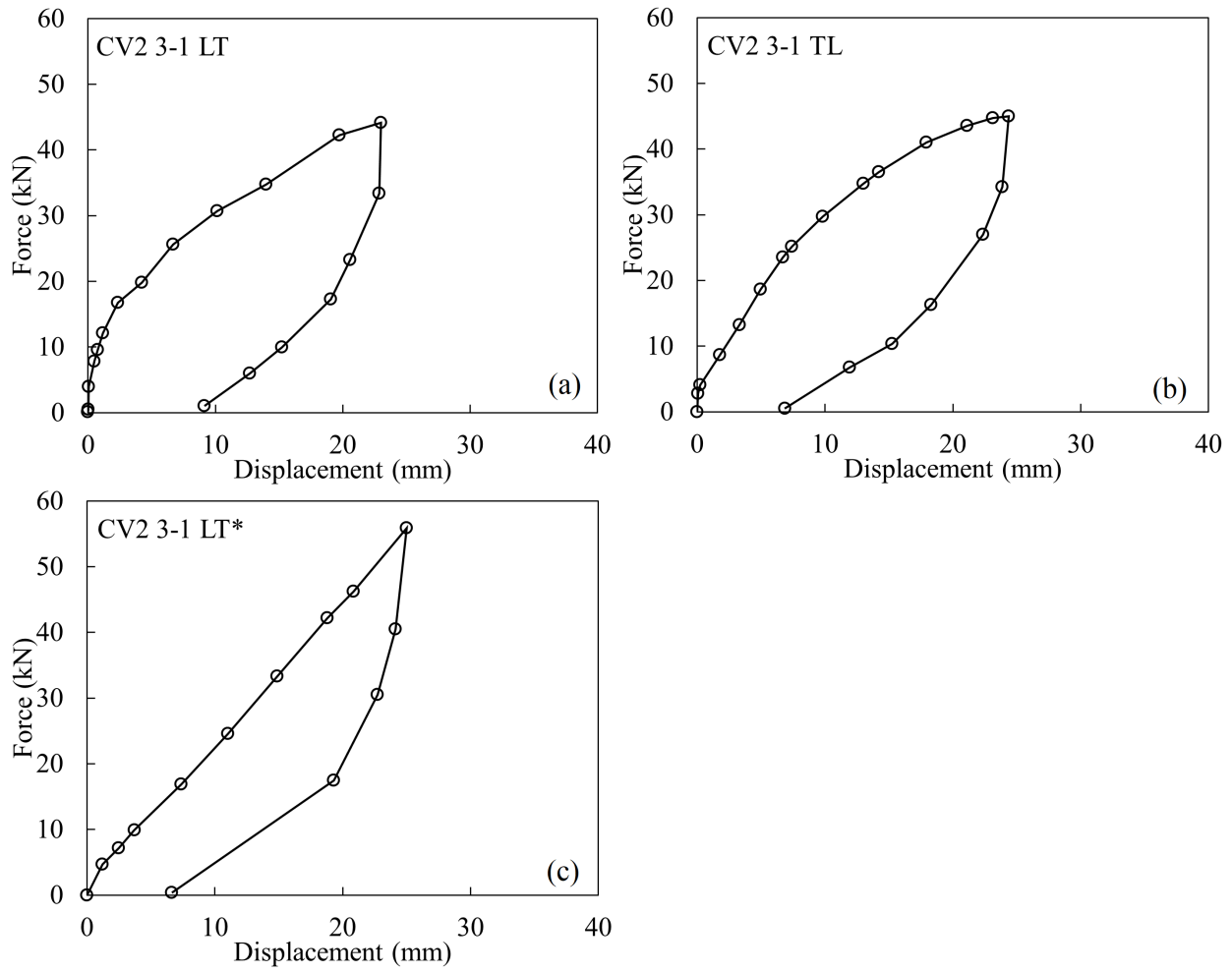


Figure C.8: Lateral response for CV2 3-1: (a) load sequence LT in cohesive soil; (b) load sequence TL in cohesive soil; (b) long-term test with load sequence LT in cohesive soil.

## C.9    Collar Vane CV 3-2
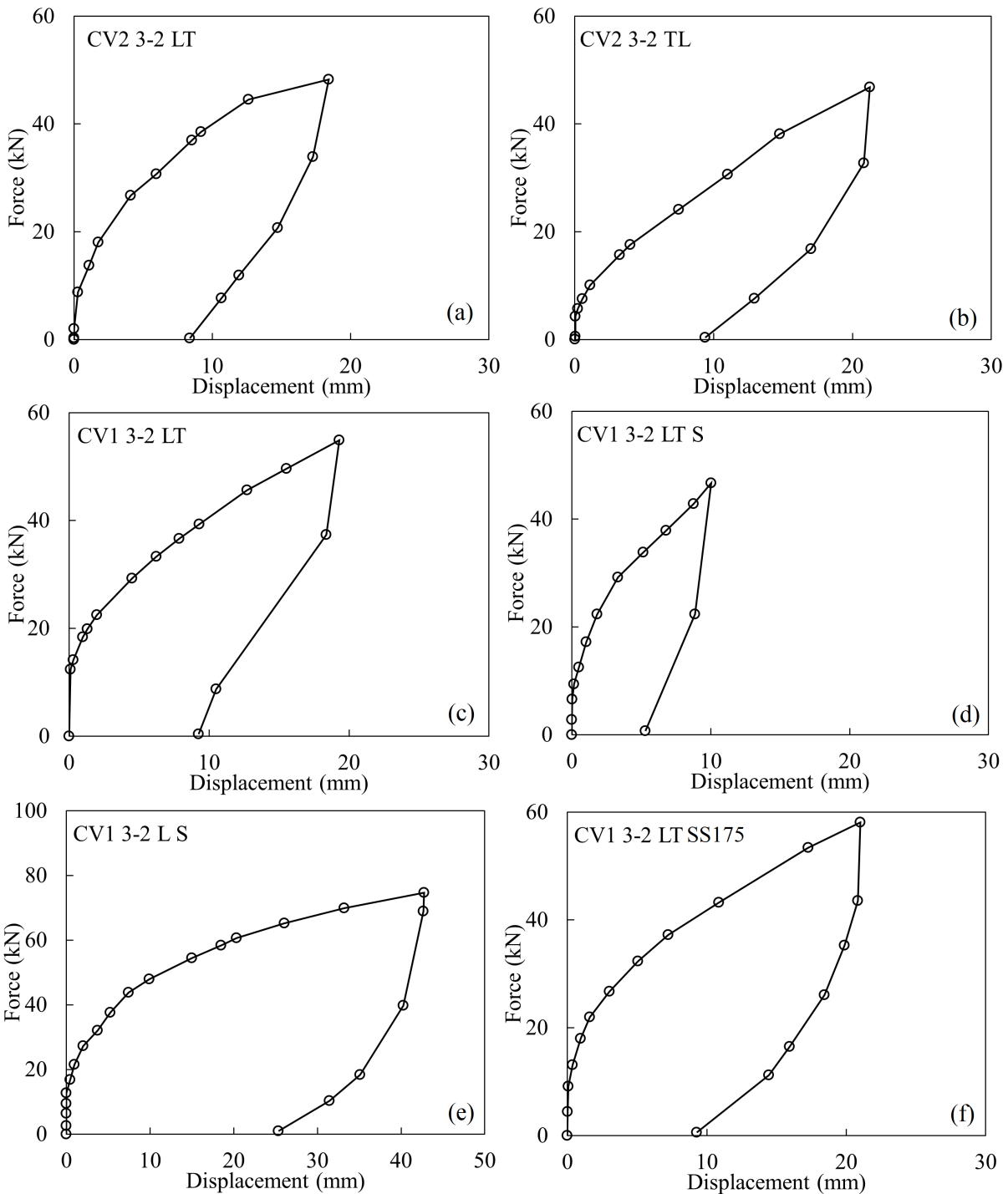


Figure C.9: Lateral response for CV 3-2: (a) two-piece with LT in cohesive soil; (b) two-piece CV with TL in cohesive soil; (c) one-piece CV with LT in cohesive soil; (d) one-piece CV with LT in granular soil; (e) one-piece CV in granular soil; (f) one-piece CV with LT in cohesive soil using square shaft.

## C.10    Collar Vane CV 3-3
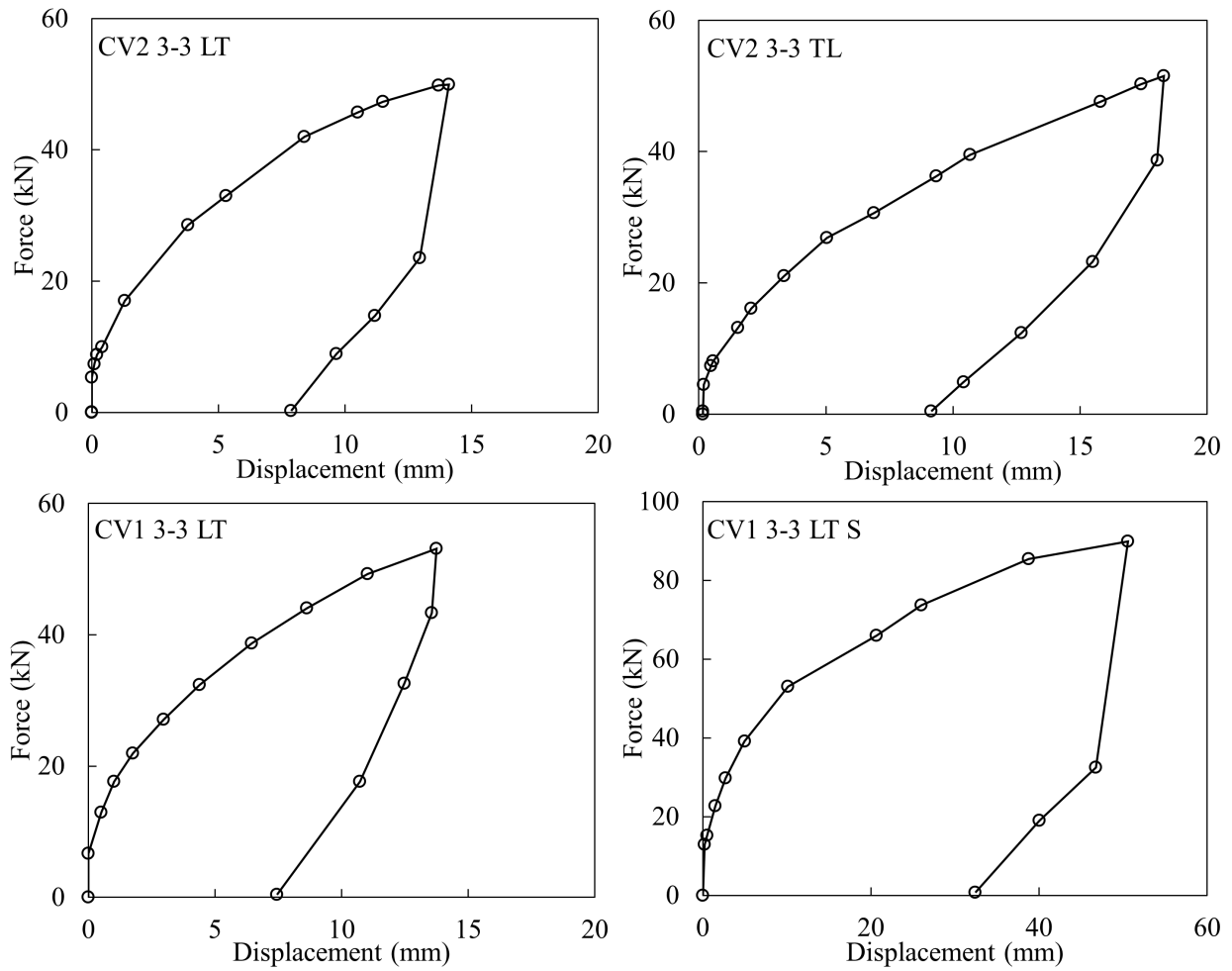


Figure C.10: Lateral response for CV 3-3: (a) two-piece with LT in cohesive soil; (b) two-piece CV with TL in cohesive soil; (c) one-piece CV with LT in cohesive soil; (d) one-piece CV with LT in granular soil.

# APPENDIX D

# MONOTONIC TORSION TEST RESULTS

## D.1 Helical Pile without Collar Vane
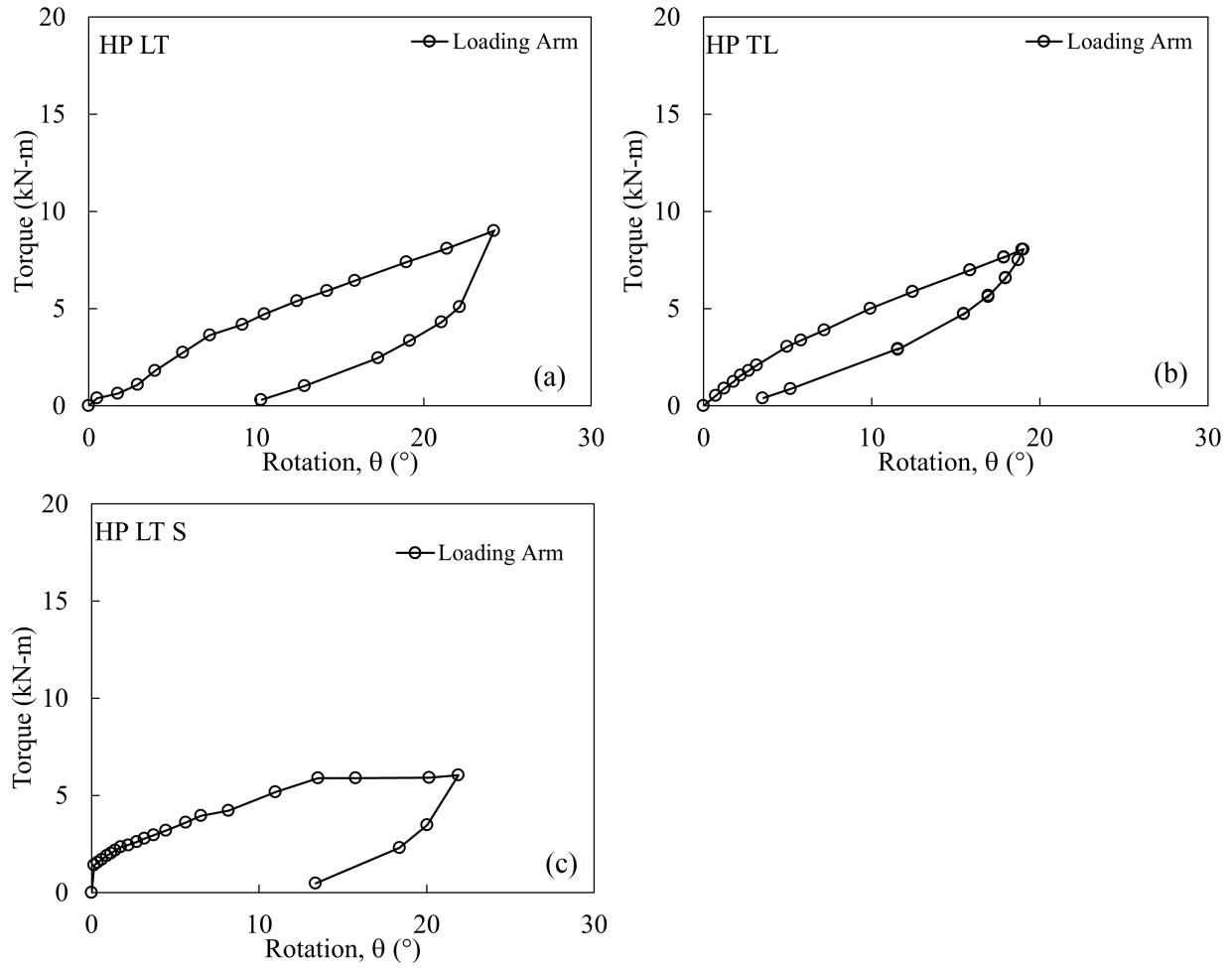


Figure D.1: Torsional response for HP without CV: (a) load sequence LT in cohesive soil; (b) load sequence TL in cohesive soil; (c) load sequence LT in granular soil.
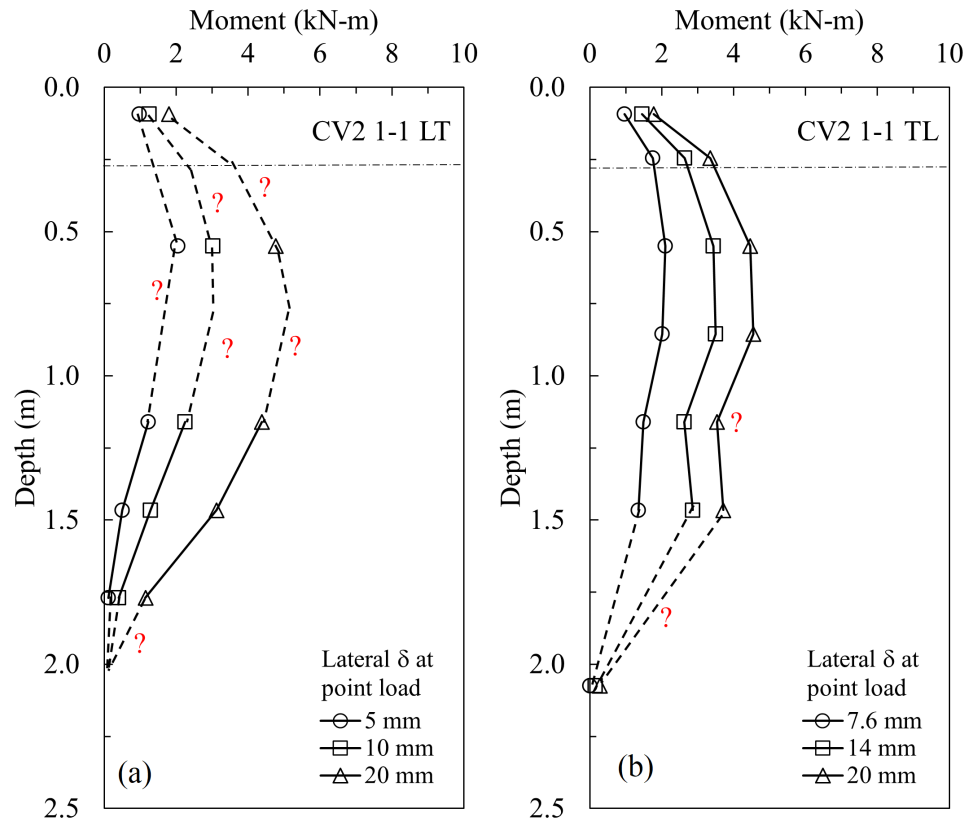
## D.2   Collar Vane CV2 1-1
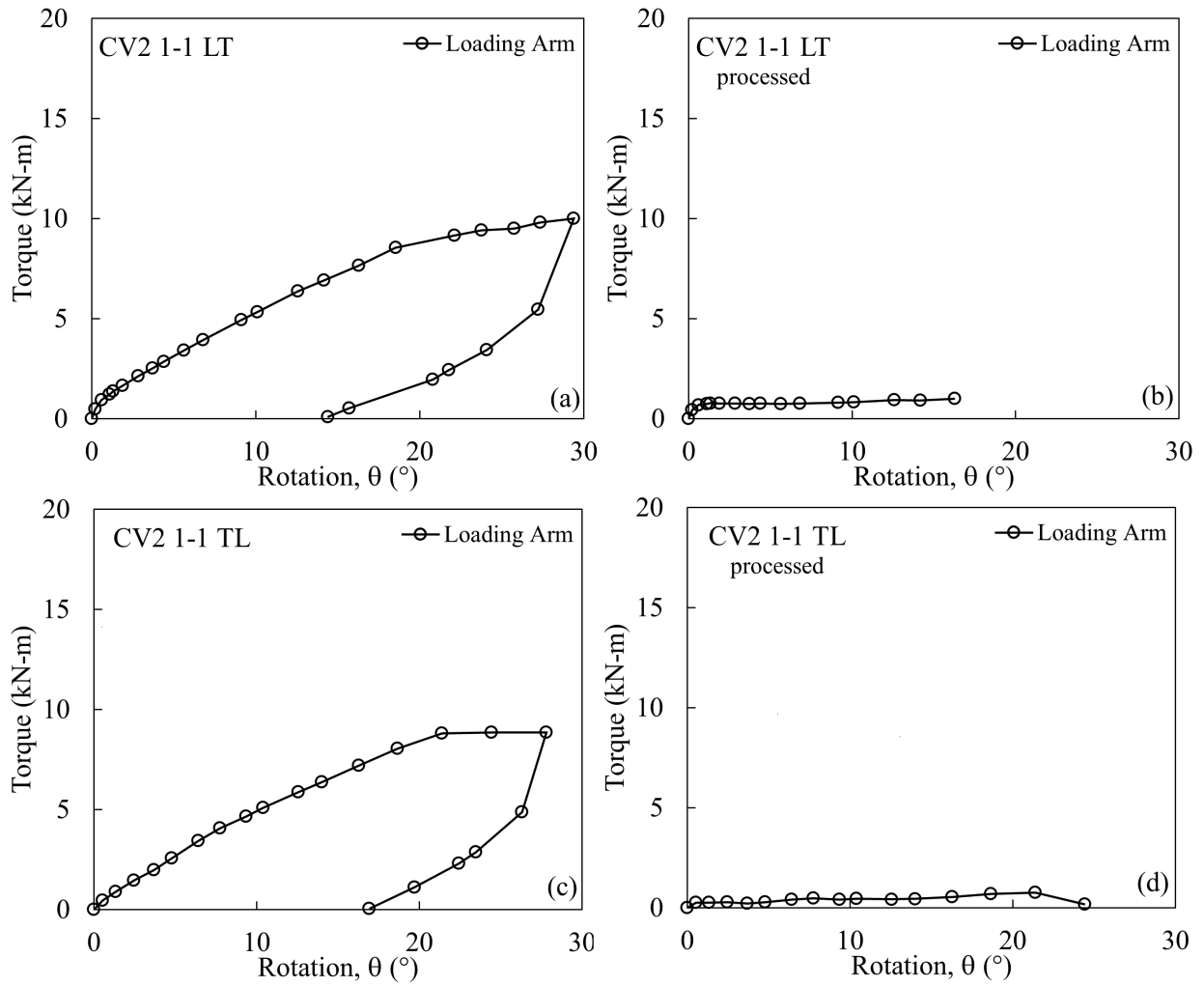


Figure D.2: Torsional response for CV2 1-1 in cohesive soil. Left side figures shows the field data, and right side only shows collar vane contribution. (a) sequence LT test; (c) sequence TL test.

## D.3 Collar Vane CV2 1-2
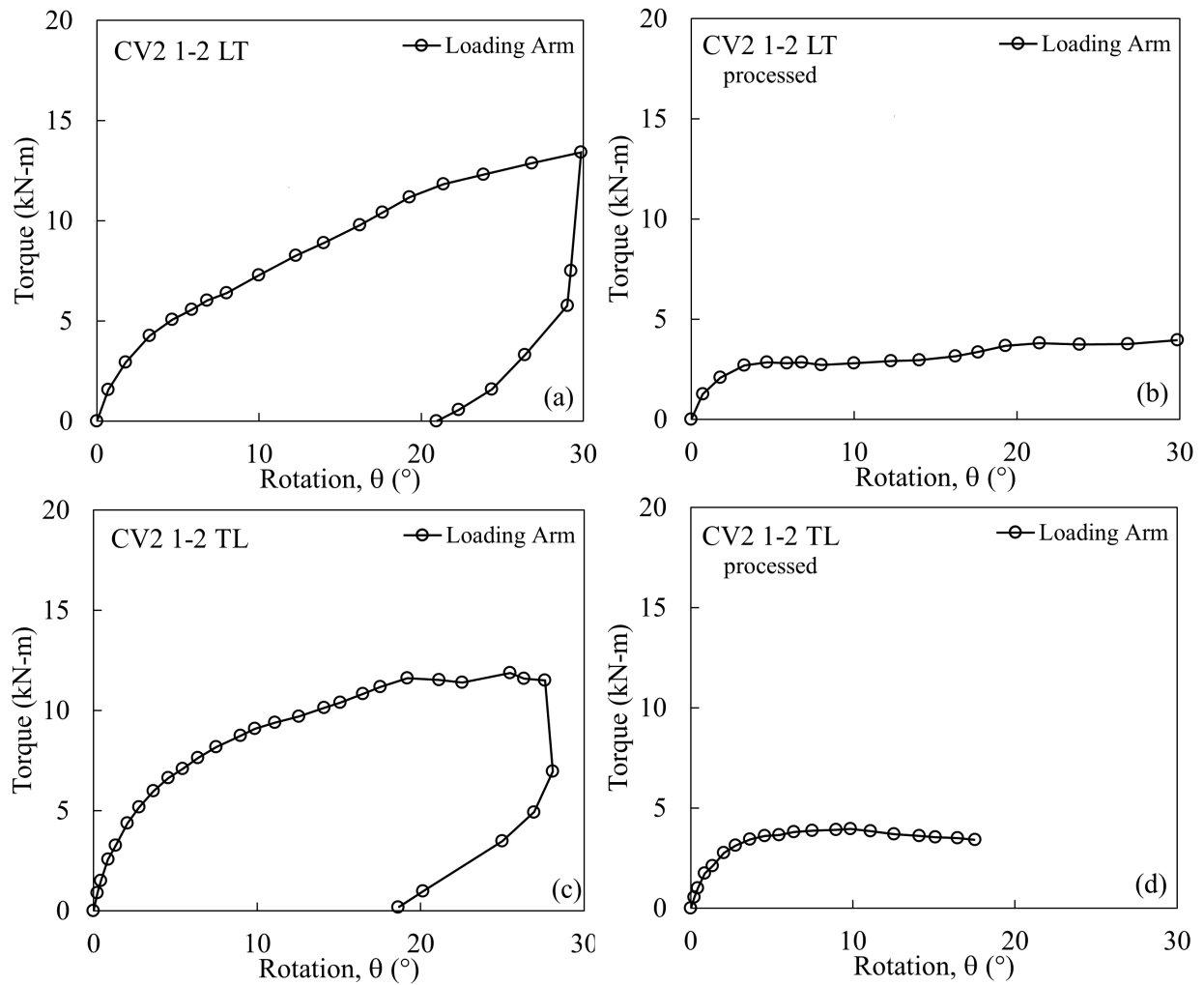


Figure D.3: Torsional response for CV2 1-2 in cohesive soil. Left side figures shows the field data, and right side only shows collar vane contribution. (a) sequence LT test; (c) sequence TL test.

## D.4 Collar Vane CV2 1-3
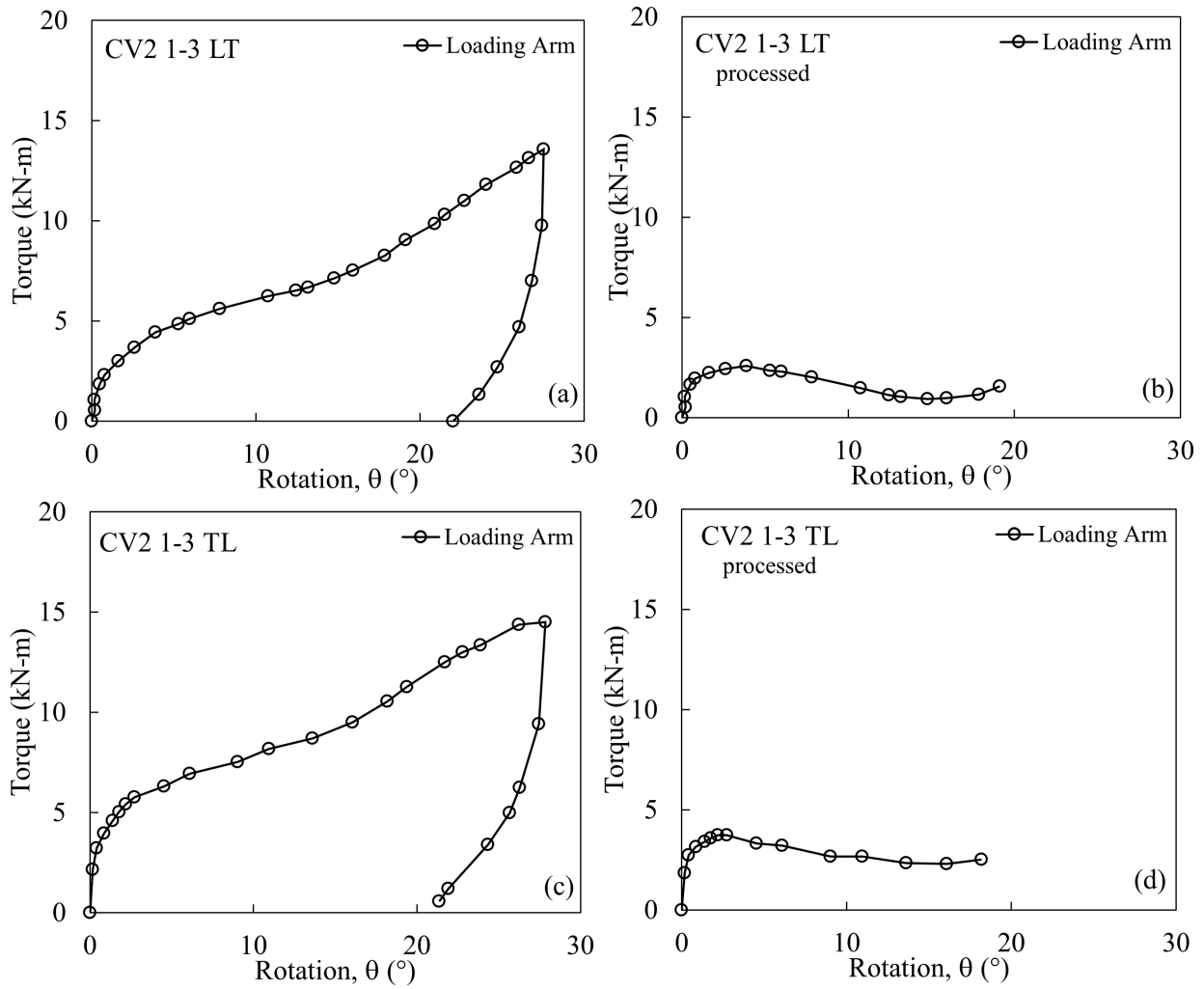


Figure D.4: Torsional response for CV2 1-3 in cohesive soil. Left side figures shows the field data, and right side only shows collar vane contribution. (a) sequence LT test; (c) sequence TL test.

## D.5 Collar Vane CV2 2-1
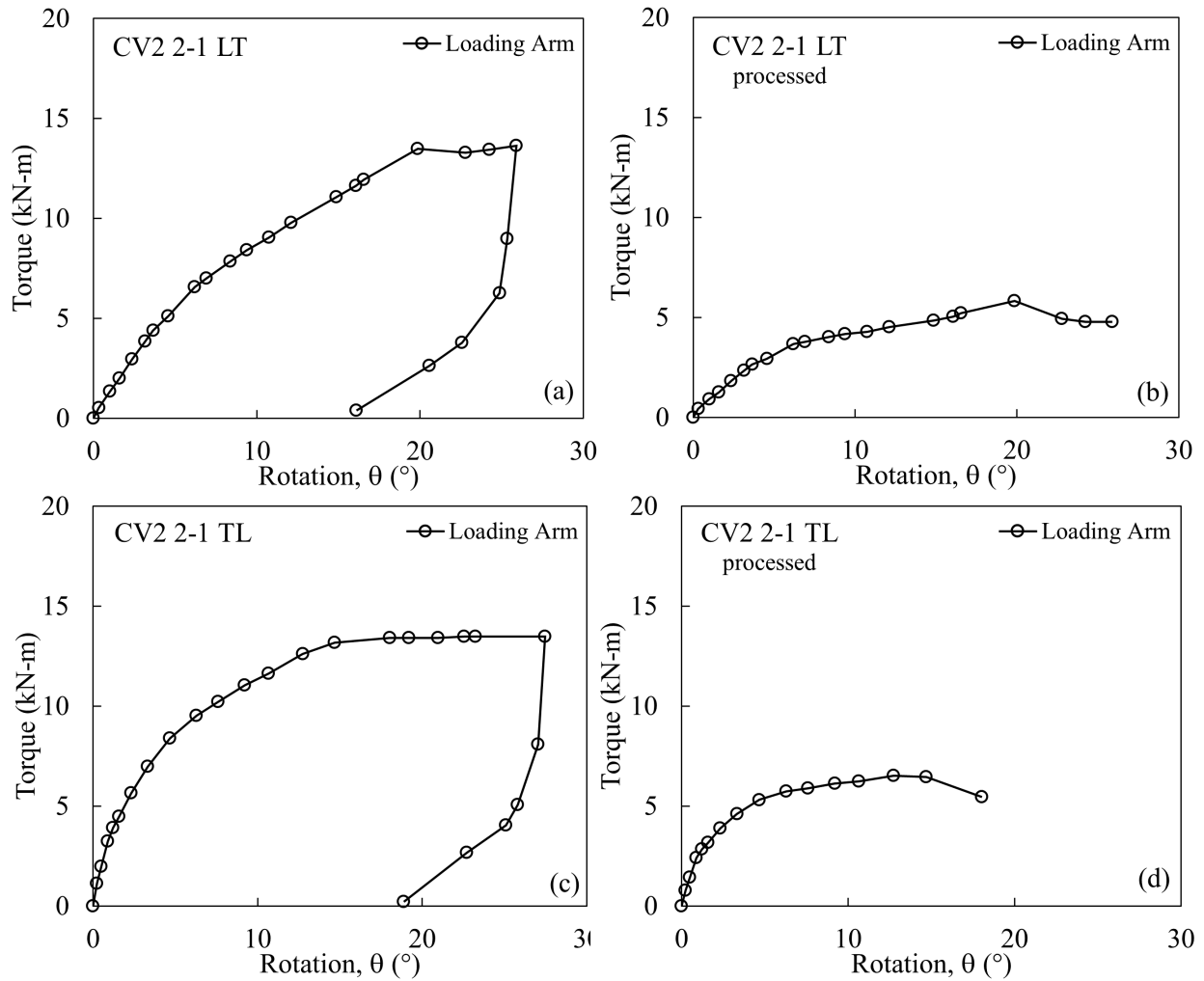


Figure D.5: Torsional response for CV2 2-1 in cohesive soil. Left side figures shows the field data, and right side only shows collar vane contribution. (a) sequence LT test; (c) sequence TL test.

## D.6   Collar Vane CV 2-2
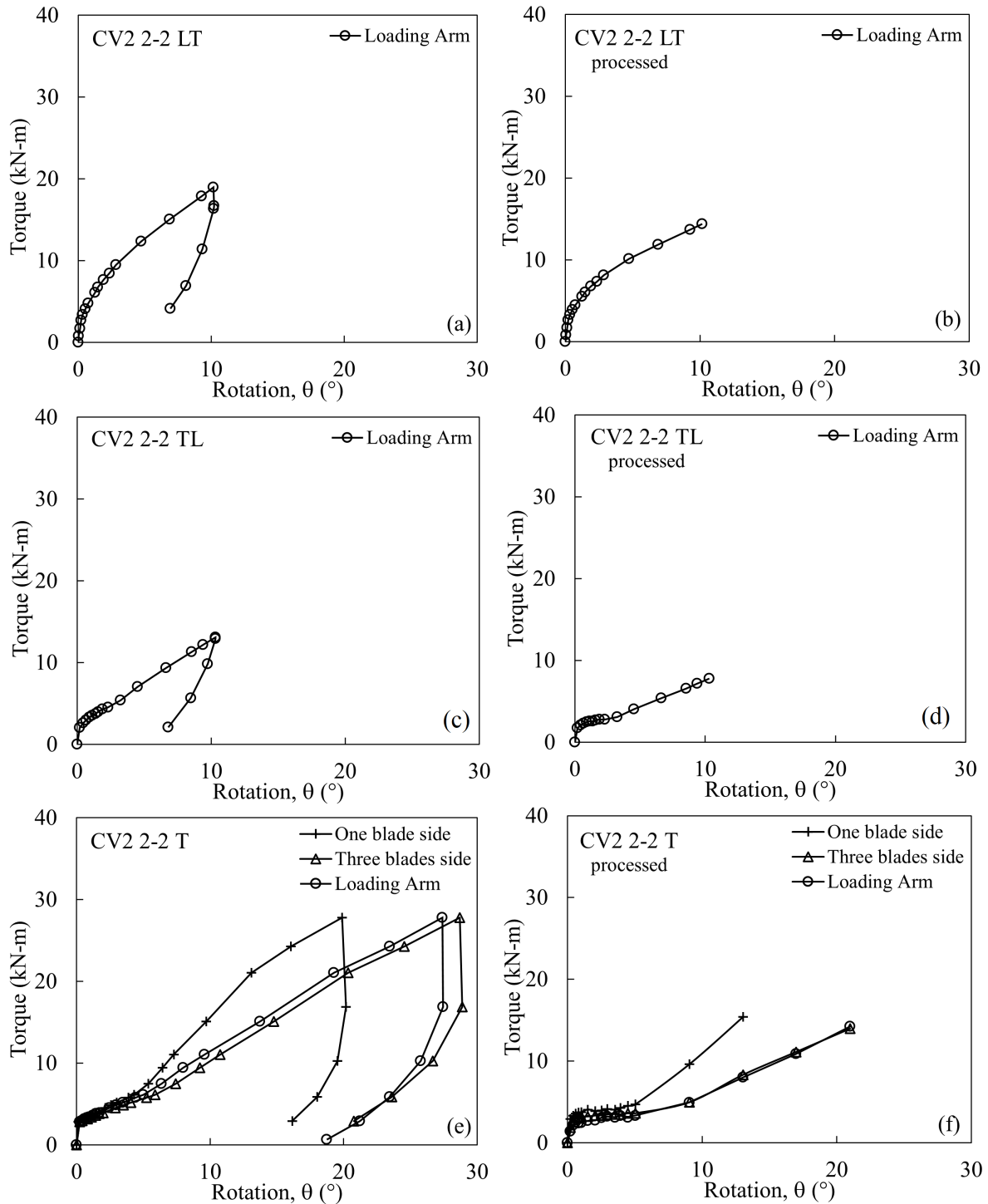


Figure D.6: Torsional response for CV2 2-2 in cohesive soil. Left side figures shows the field data, and right side only shows collar vane contribution. (a) sequence LT test; (c) sequence TL test; (e) only torsion test.
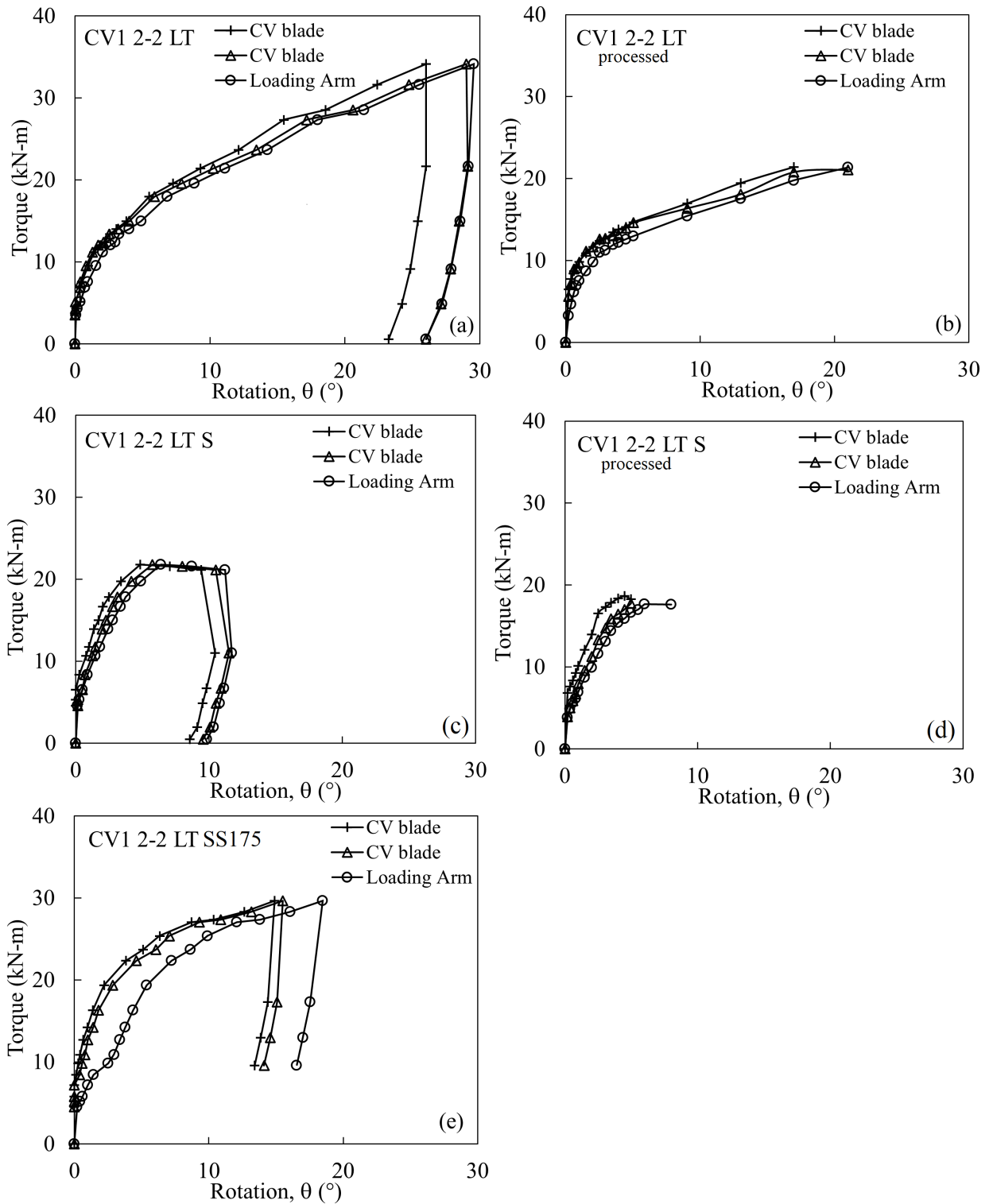
Figure D.7: Torsional response for CV1 2-2 subjected to LT sequence. Left side figures shows the field data, and right side only shows collar vane contribution. (a) test in cohesive soil; (c) test in granular soil; (e) using square shaft in cohesive soil.

## D.7   Collar Vane CV 2-3
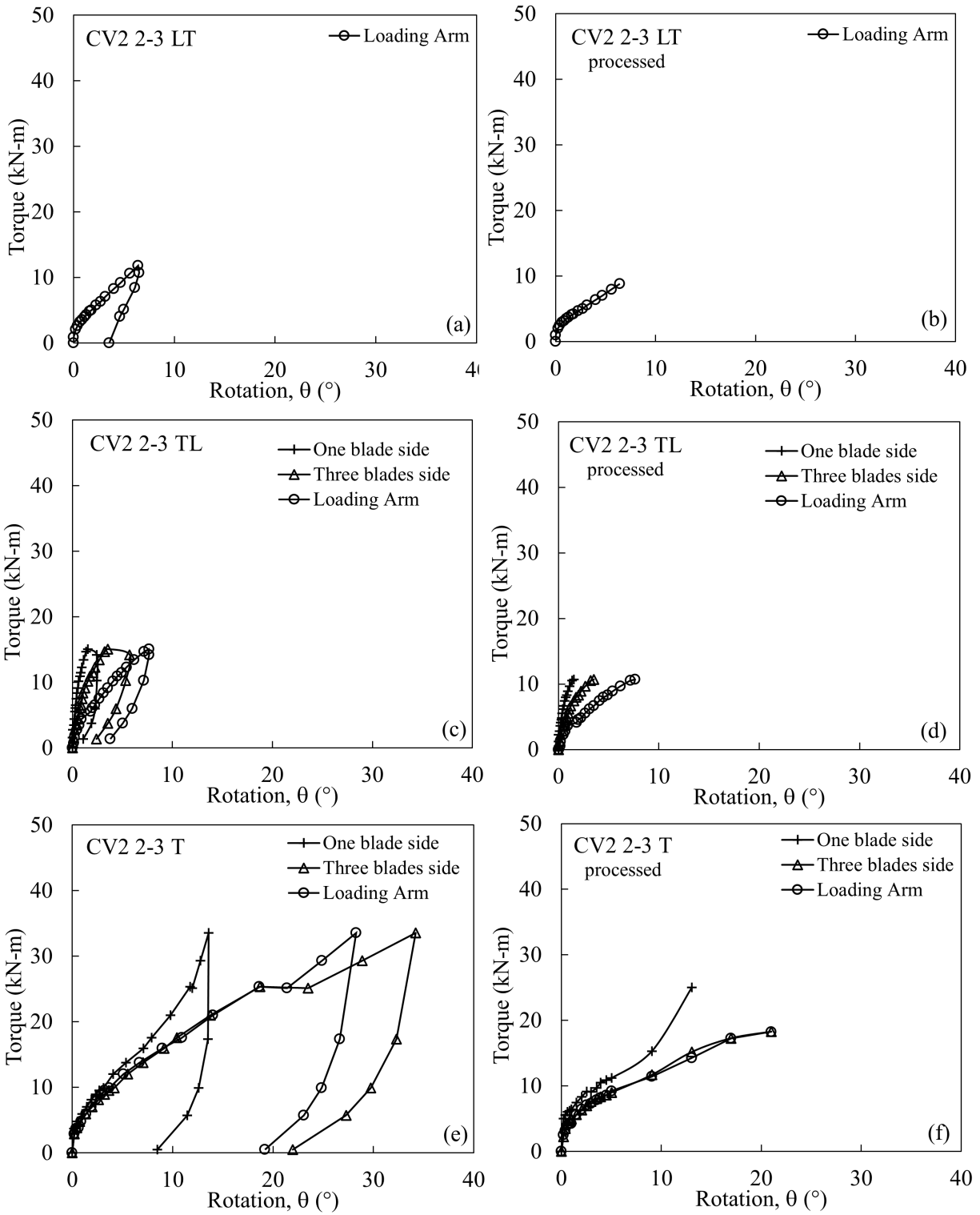


Figure D.8: Torsional response for CV2 2-3 in cohesive soil. Left side figures shows the field data, and right side only shows the contribution from collar vane.

241
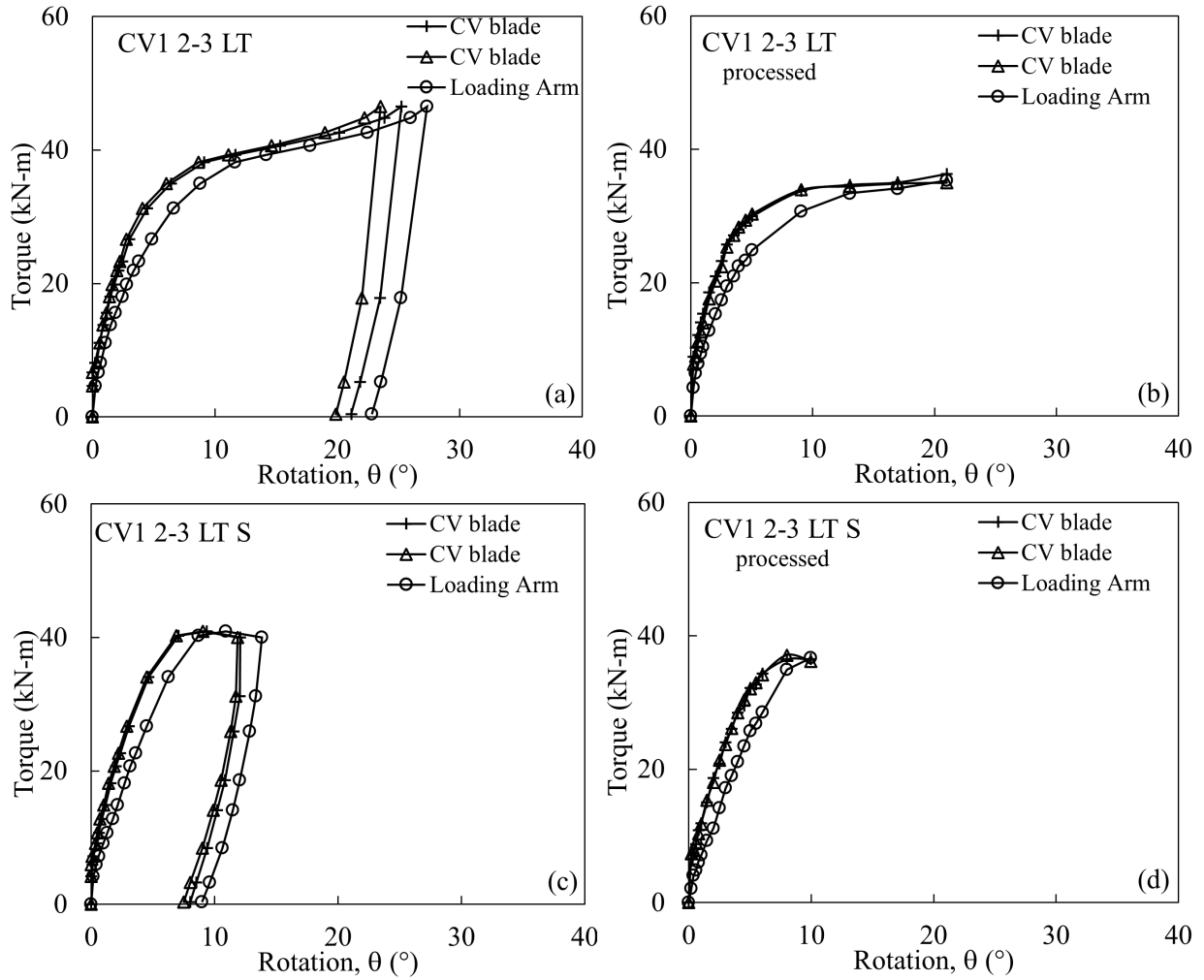
Figure D.9: Torsional response for CV1 2-3 subjected to LT sequence. Left side figures shows the field data, and right side only shows collar vane contribution. (a) test in cohesive soil; (c) test in granular soil.

## D.8   Collar Vane CV2 3-1
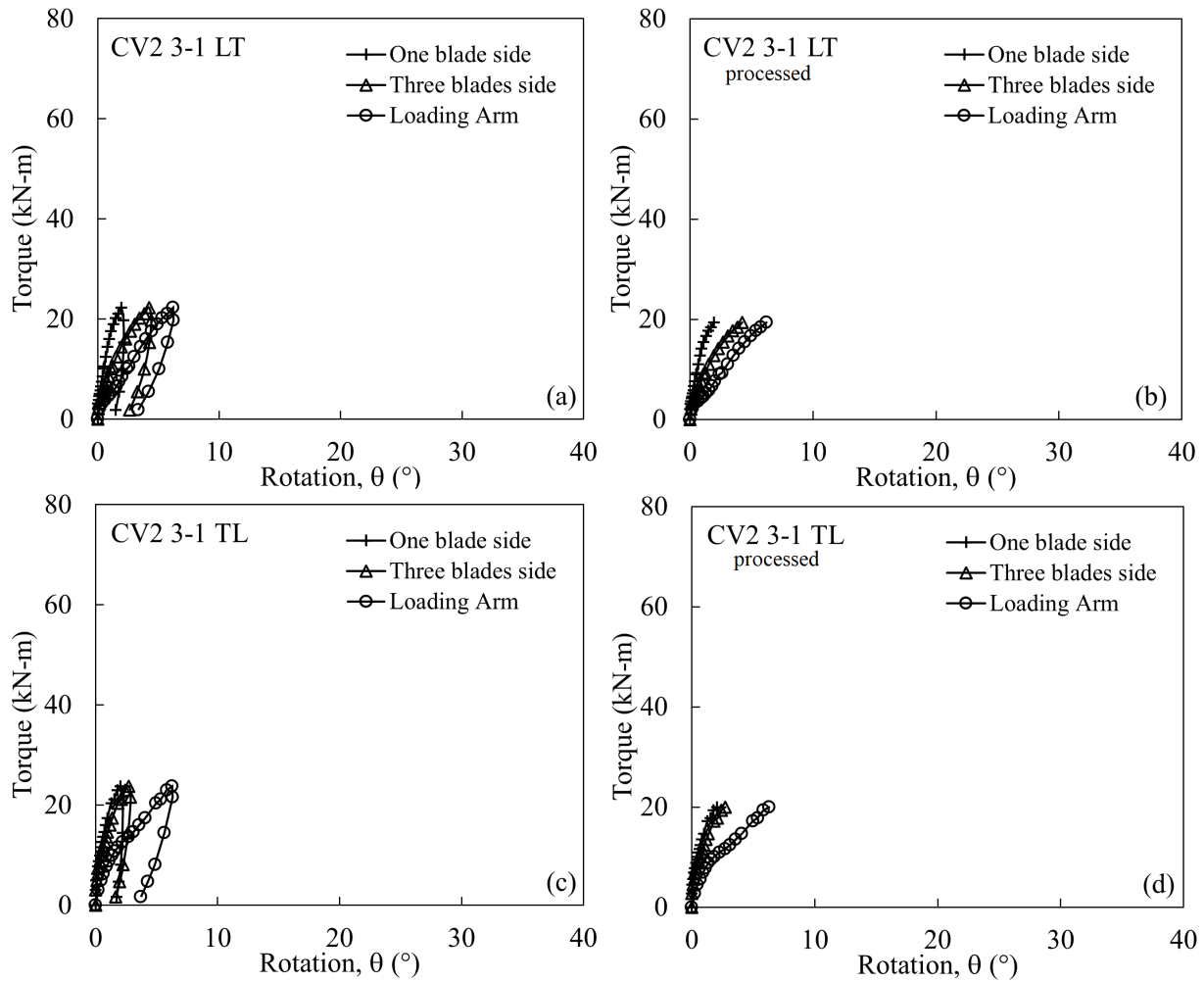


Figure D.10: Torsional response for CV2 3-1 in cohesive soil. Left side figures shows the field data, and right side only shows the contribution from collar vane. (a) sequence LT test; (c) sequence TL test.
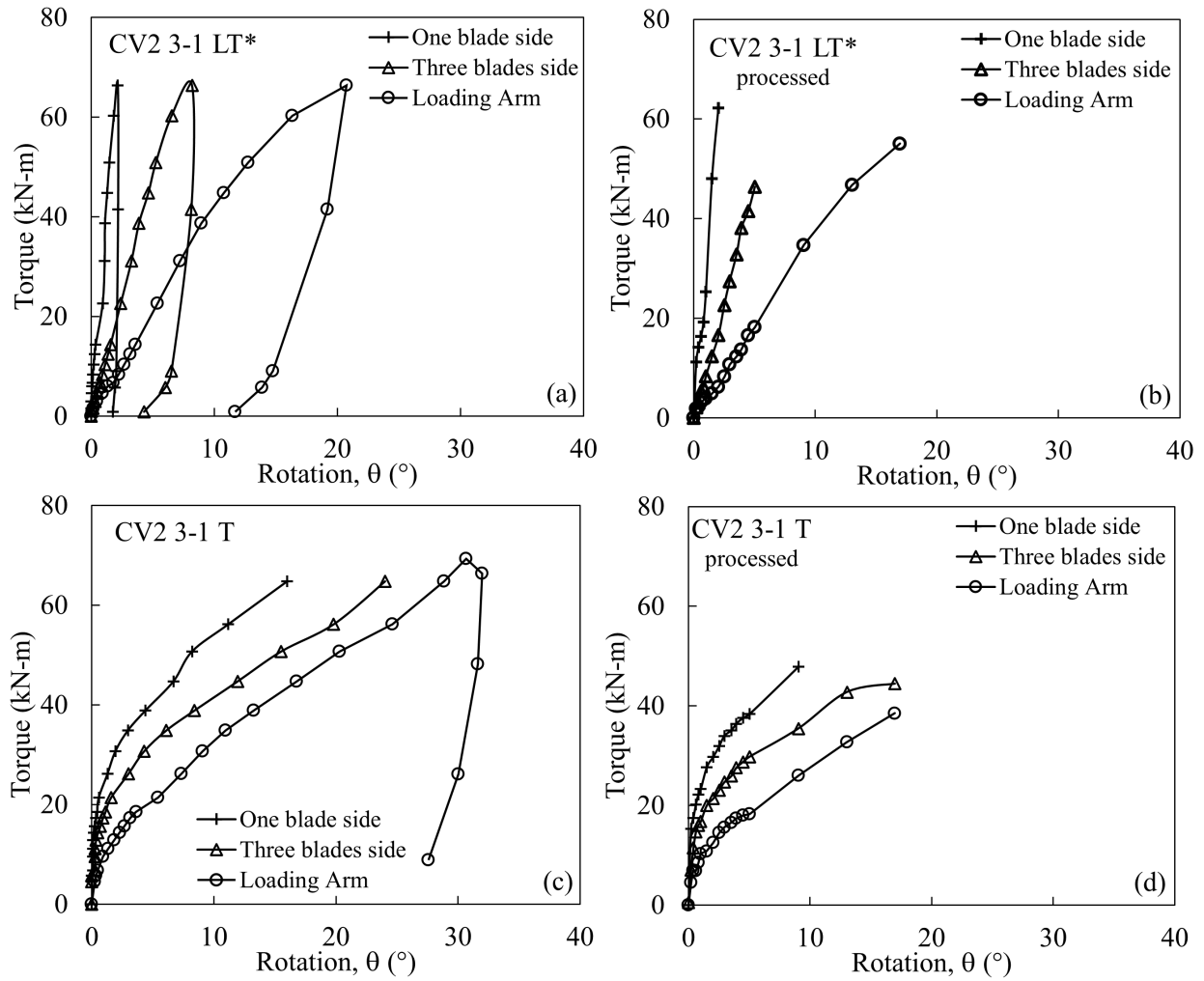
Figure D.11: Torsional response for CV2 3-1 in cohesive soil. Left side figures shows the field data, and right side only shows the contribution from collar vane. (a) Long term conditions with sequence LT; (c) only torsion test.

## D.9  Collar Vane CV 3-2
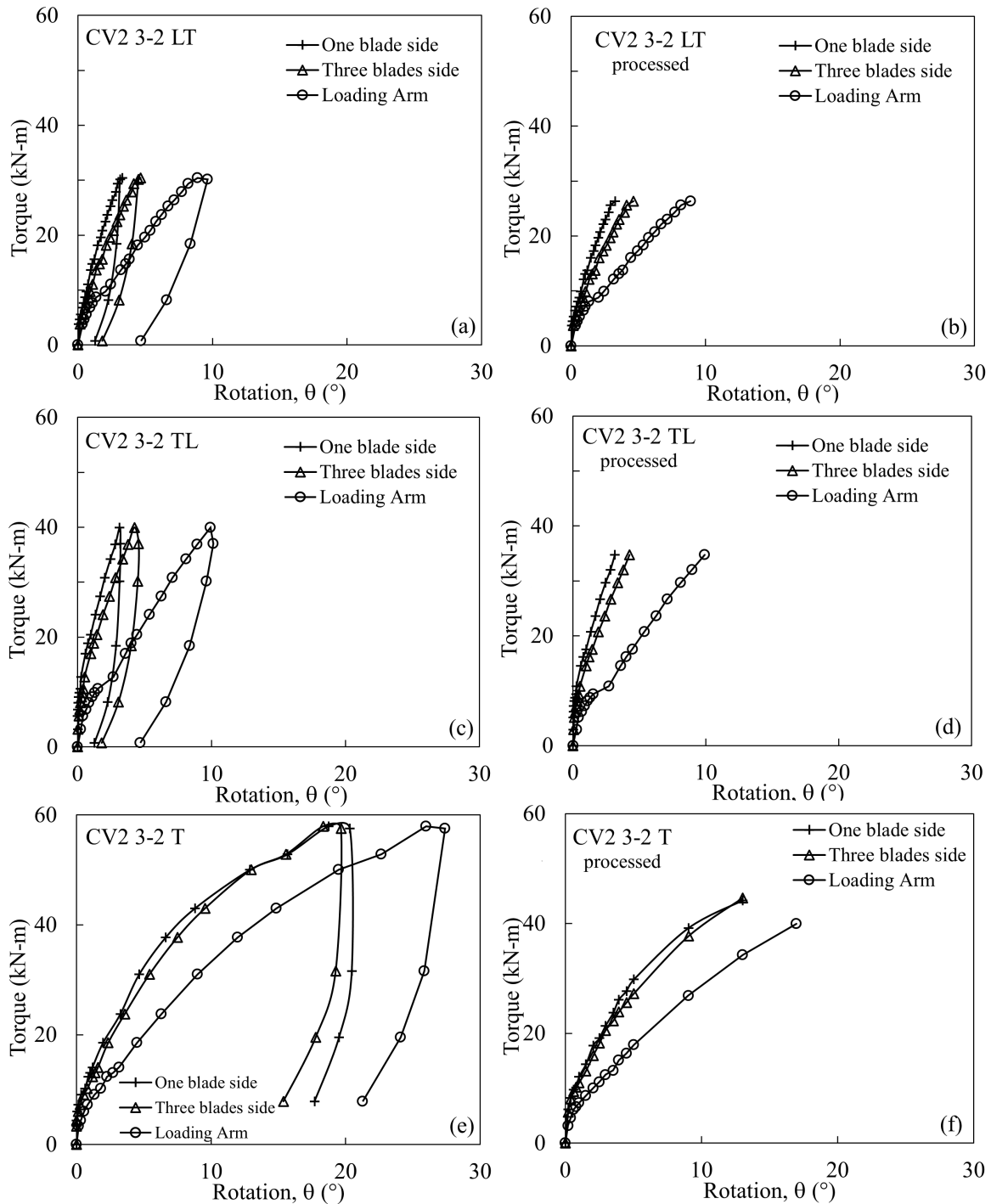


Figure D.12: Torsional response for CV2 3-2 in cohesive soil. Left side figures shows the field data, and right side only shows collar vane contribution. (a) sequence LT test; (c) sequence TL test; (e) only torsion test.
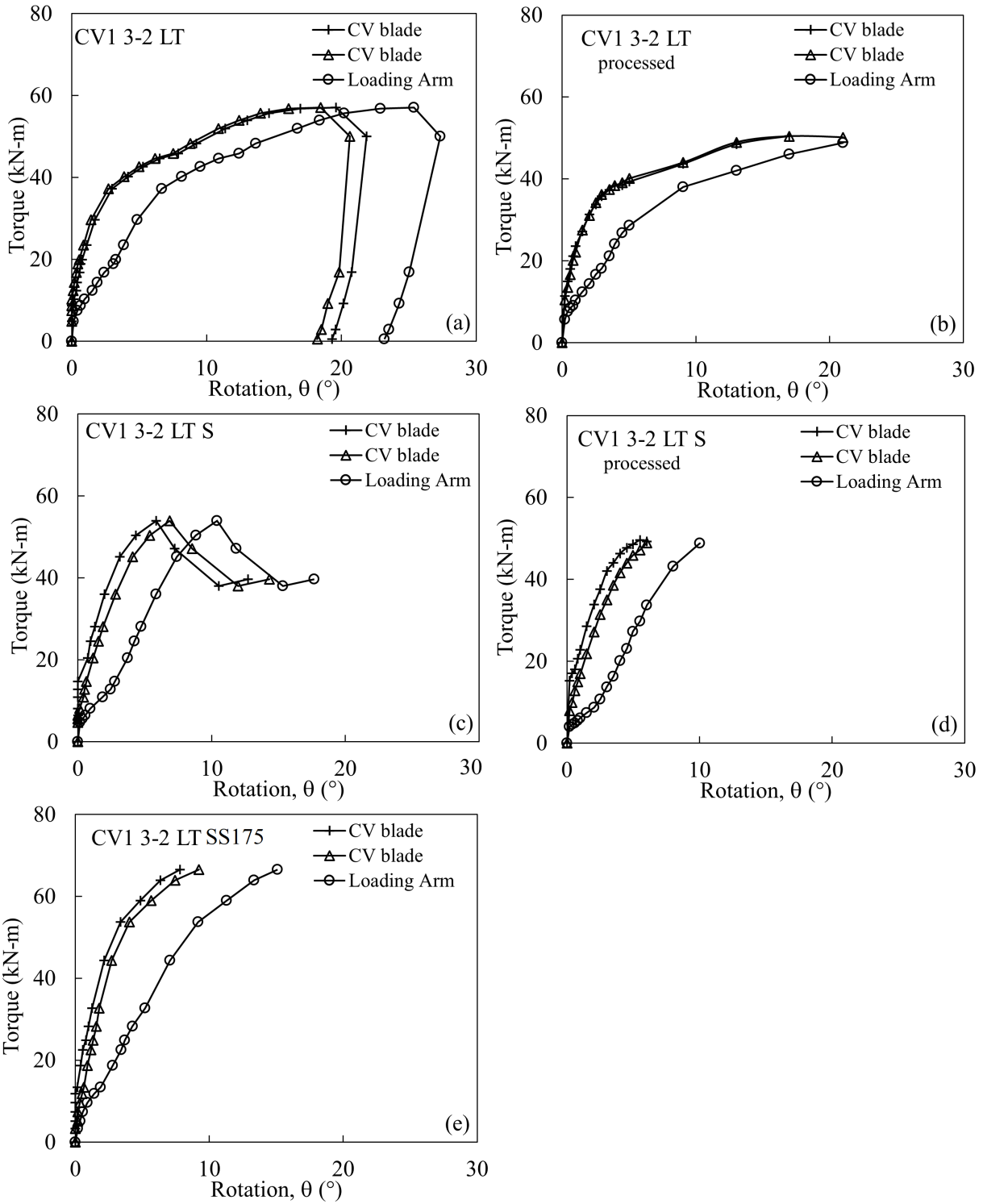
Figure D.13: Torsional response for CV1 3-2 subjected to LT sequence. Left side figures shows the field data, and right side only shows collar vane contribution. (a) test in cohesive soil; (c) test in granular soil; (e) using square shaft in cohesive soil.

## D.10 Collar Vane CV 3-3
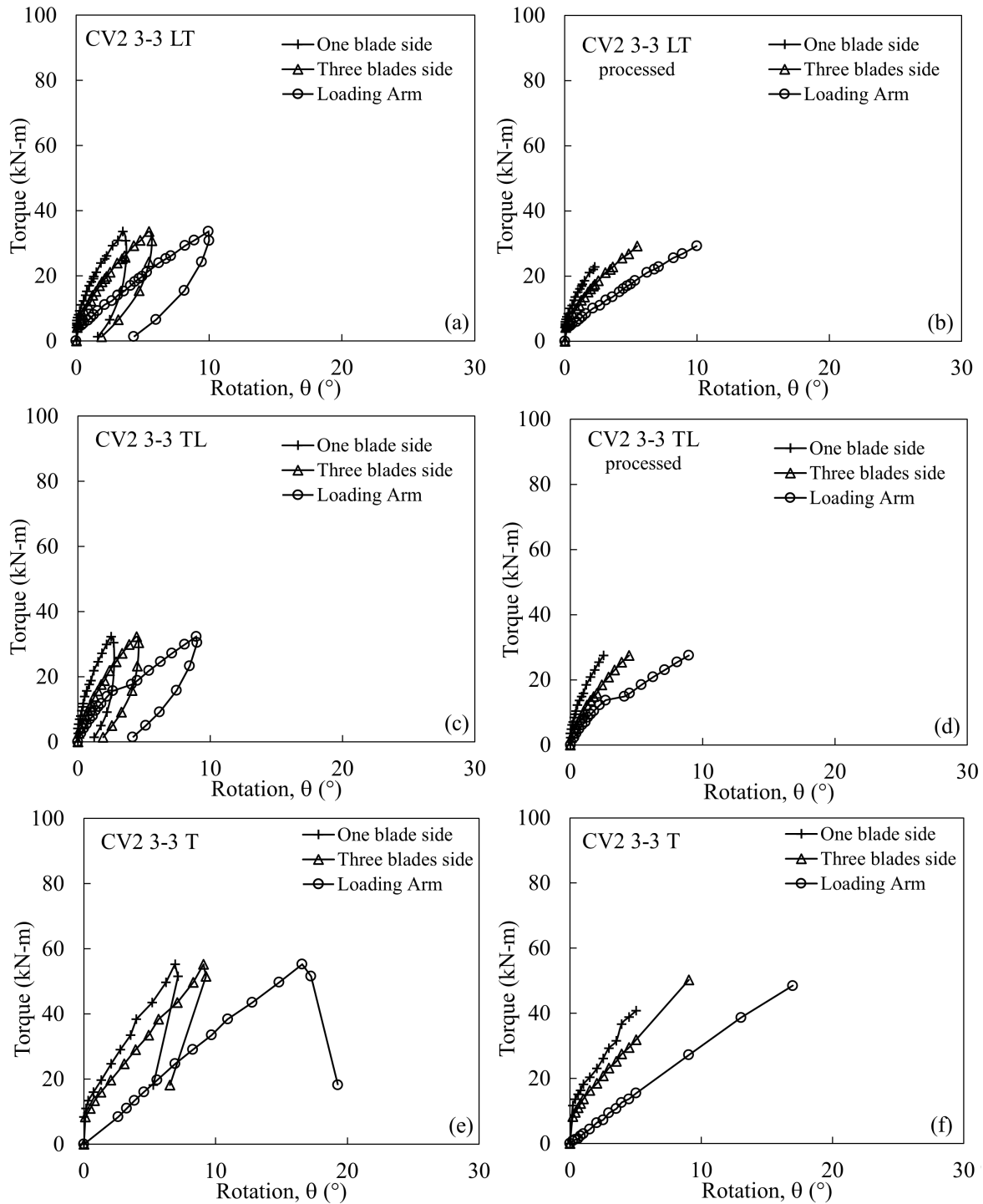


Figure D.14: Torsional response for CV2 3-3 in cohesive soil. Left side figures shows the field data, and right side only shows collar vane contribution. (a) sequence LT test; (c) sequence TL test.

247
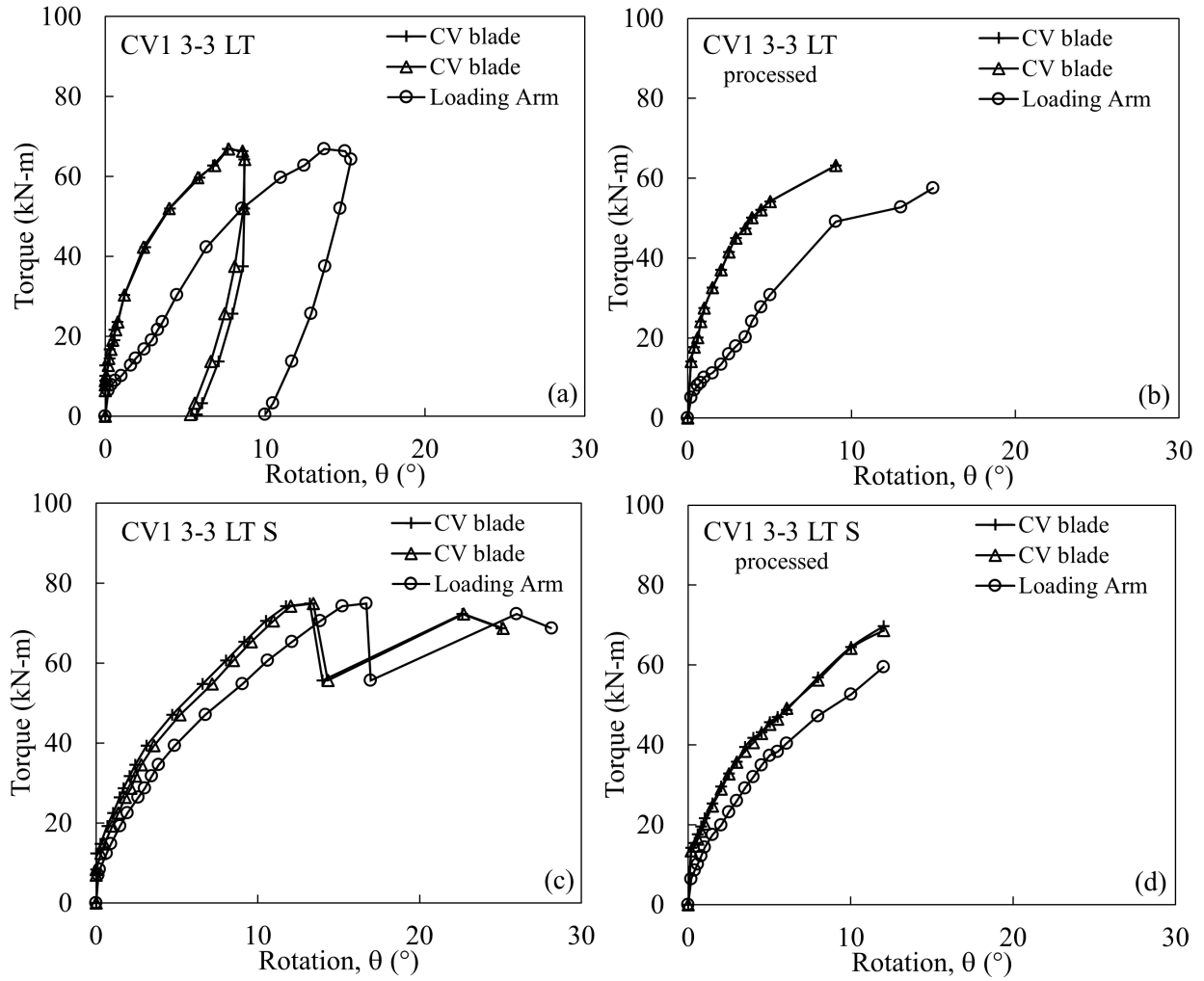
Figure D.15: Torsional response for CV1 3-3 subjected to LT sequence. Left side figures shows the field data, and right side only shows collar vane contribution. (a) test in cohesive soil; (c) test in granular soil.

# APPENDIX E

# BENDING MOMENT PROFILES

In the bending moment profiles, figures are presented with a different set of dashed lines that corresponds to: long dashed line, for missing strain gauge data or not reliable data; short dashed line, for the location where the prismatic section of the collar vane ends; and dot-dashed line, for the bottom of the collar vane. Also, the depth equal to zero corresponds to the ground surface level.

## E.1  Helical Pile without Collar Vane
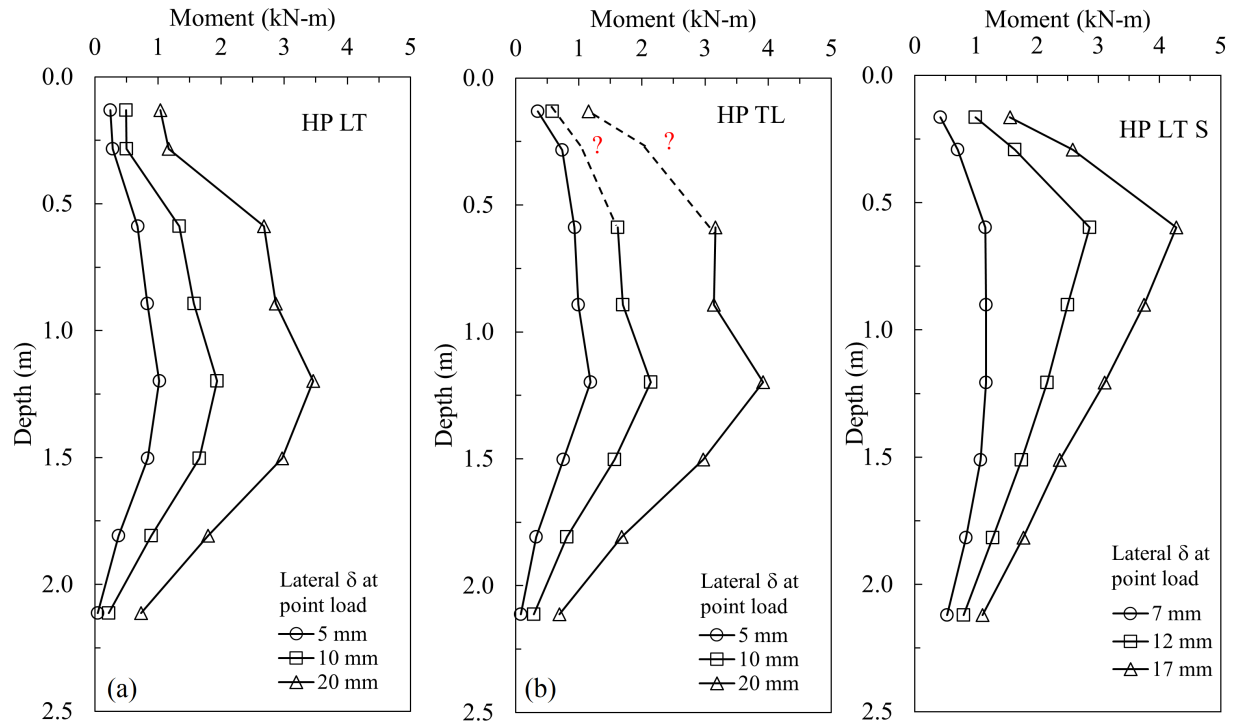


Figure E.1: Bending Moment profiles for HP without CV: (a) load sequence LT in cohesive soil; (b) load sequence TL in cohesive soil; (c) load sequence LT in granular soil.

## E.2 Collar Vane CV2 1-1



Figure E.2: Bending Moment profiles for CV2 1-1: (a) load sequence LT in cohesive soil; (b) load sequence TL in cohesive soil.

## E.3   Collar Vane CV2 1-2
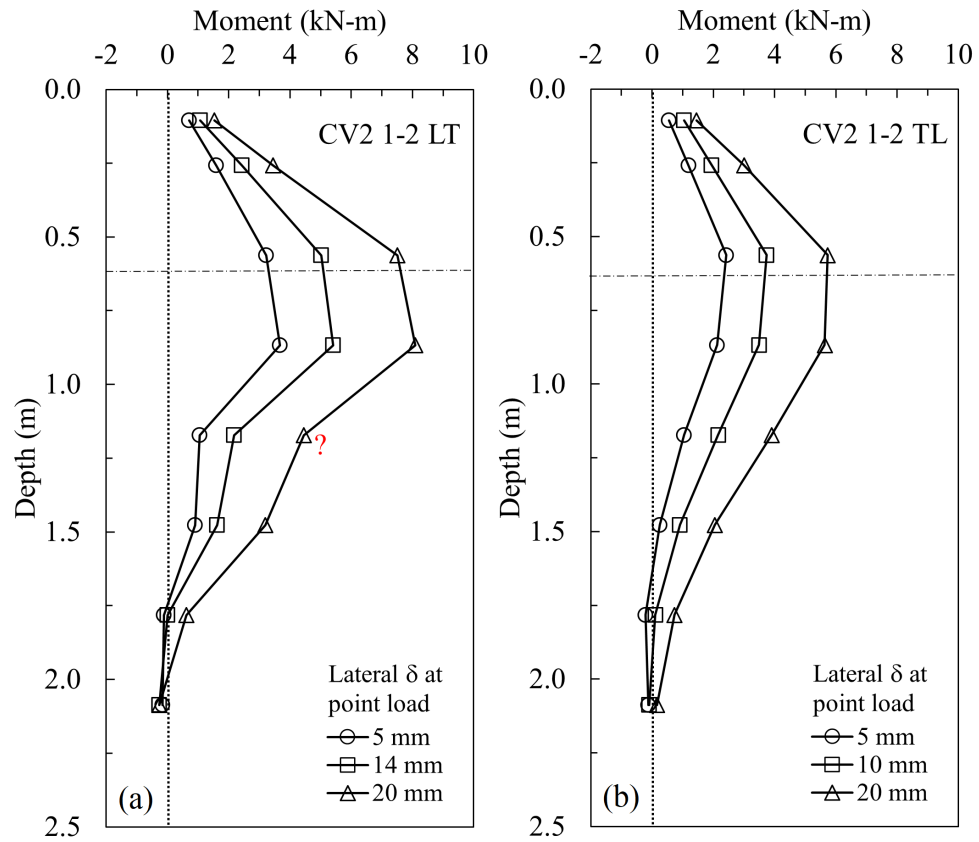


Figure E.3: Bending Moment profiles for CV2 1-2: (a) load sequence LT in cohesive soil; (b) load sequence TL in cohesive soil.

## E.4   Collar Vane CV2 1-3
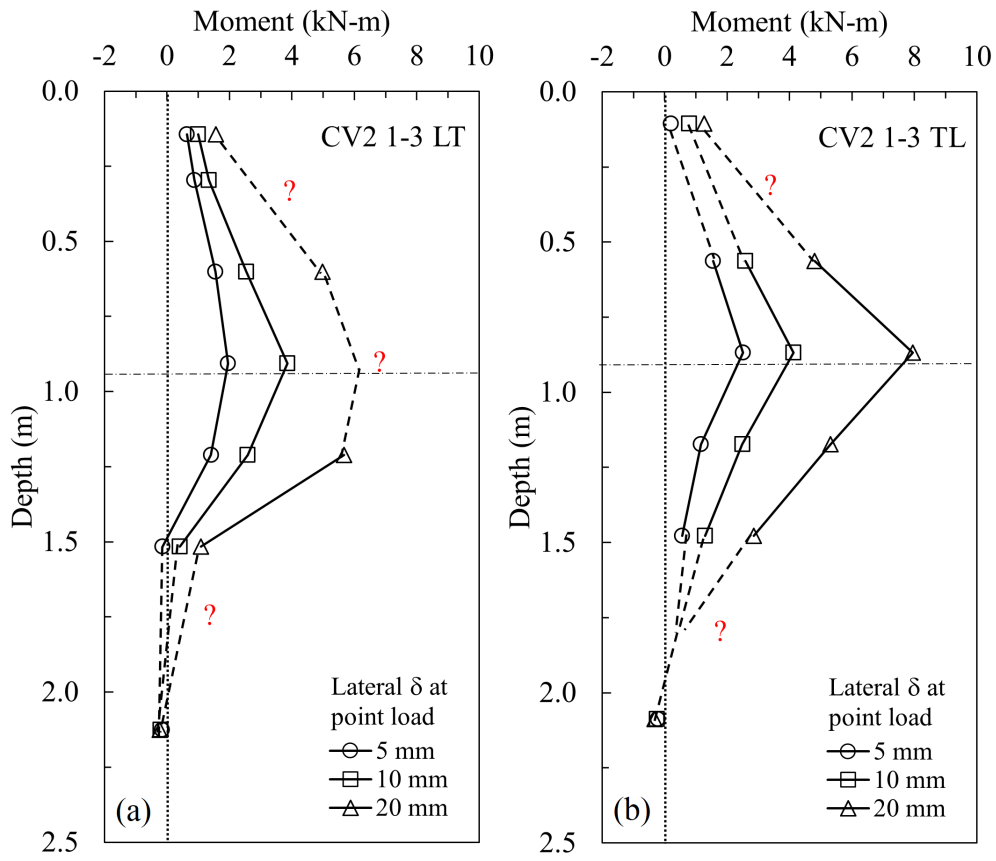


Figure E.4: Bending Moment profiles for CV2 1-3: (a) load sequence LT in cohesive soil; (b) load sequence TL in cohesive soil.

## E.5 Collar Vane CV2 2-1
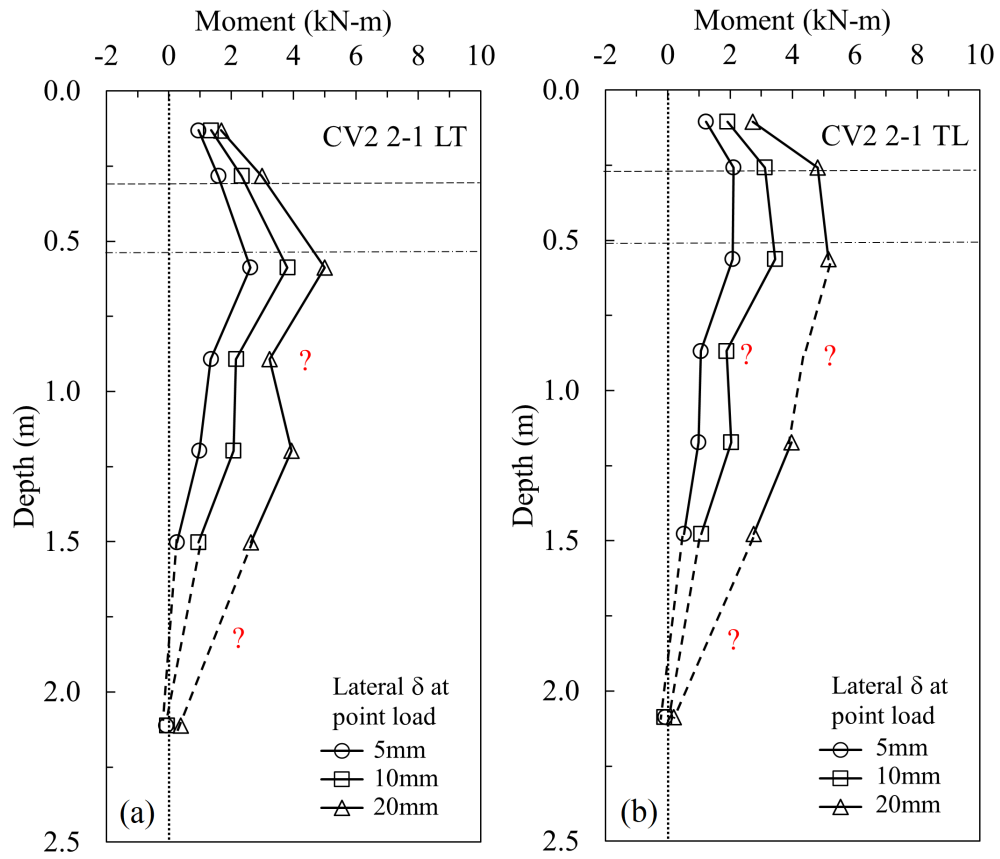


Figure E.5: Bending Moment profiles for CV2 2-1: (a) load sequence LT in cohesive soil; (b) load sequence TL in cohesive soil.

## E.6 Collar Vane CV 2-2
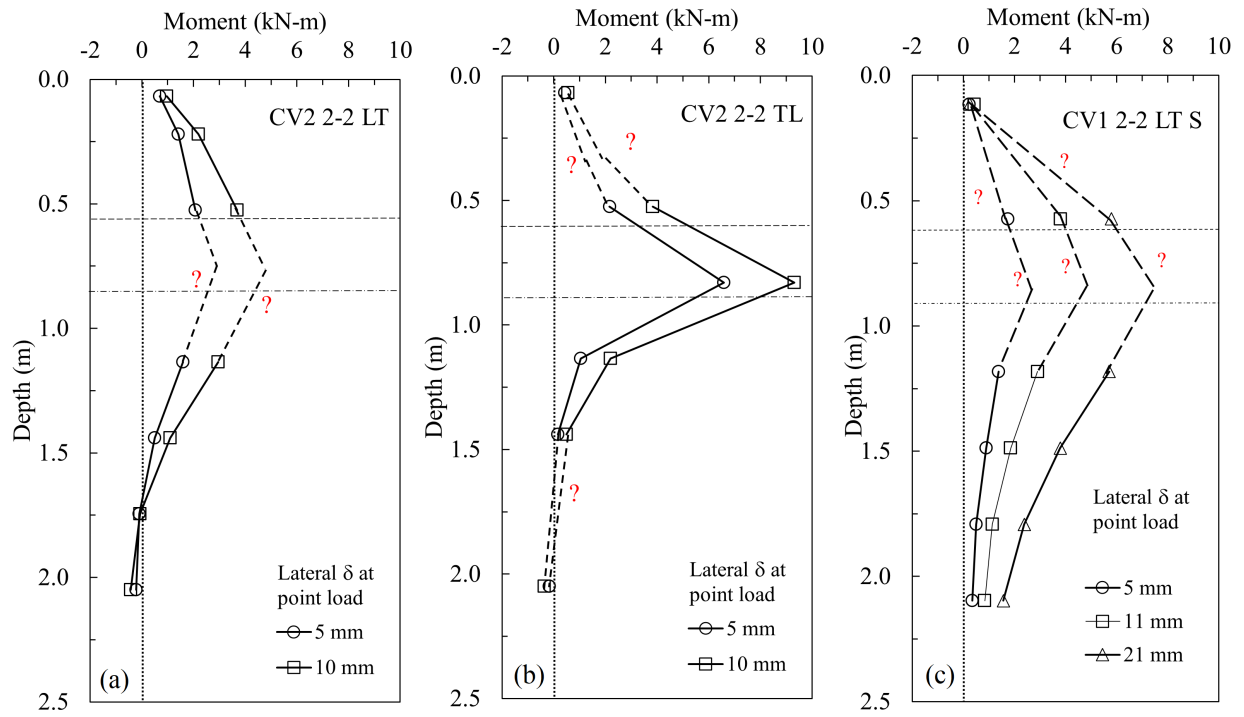


Figure E.6: Bending Moment profiles for CV 2-2: (a) two-piece CV with load sequence LT in cohesive soil; (b) two-piece CV with load sequence TL in cohesive soil; (c) one-piece CV with load sequence LT in granular soil.

## E.7   Collar Vane CV 2-3
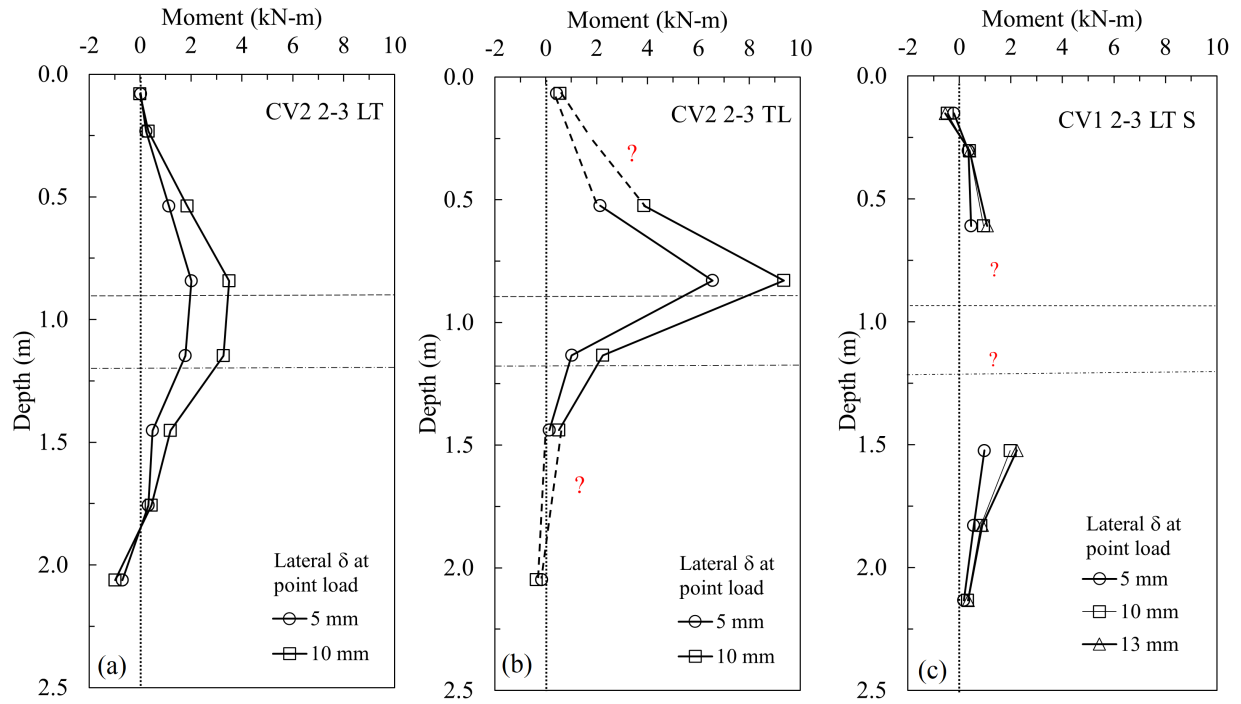


Figure E.7: Bending Moment profiles for CV 2-3: (a) two-piece CV with load sequence LT in cohesive soil; (b) two-piece CV with load sequence TL in cohesive soil; (c) one-piece CV with load sequence LT in granular soil.

## E.8   Collar Vane CV2 3-1
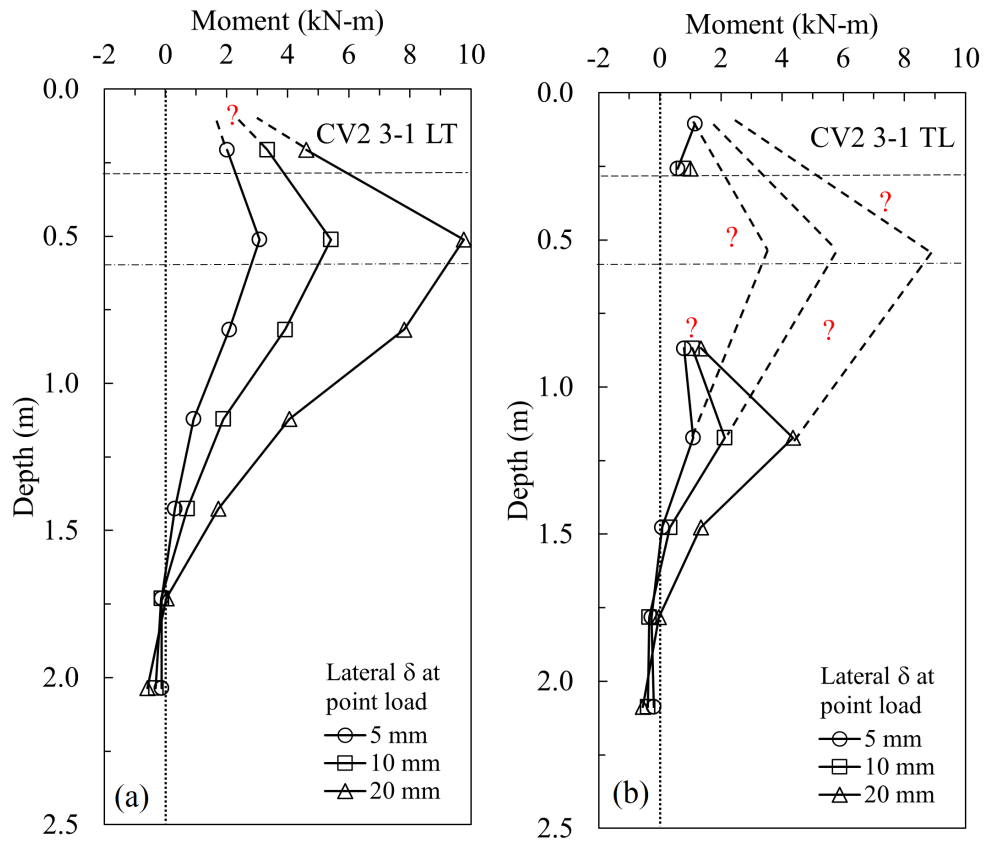


Figure E.8: Bending Moment profiles for CV2 3-1: (a) load sequence LT in cohesive soil; (b) load sequence TL in cohesive soil.

## E.9    Collar Vane CV 3-2
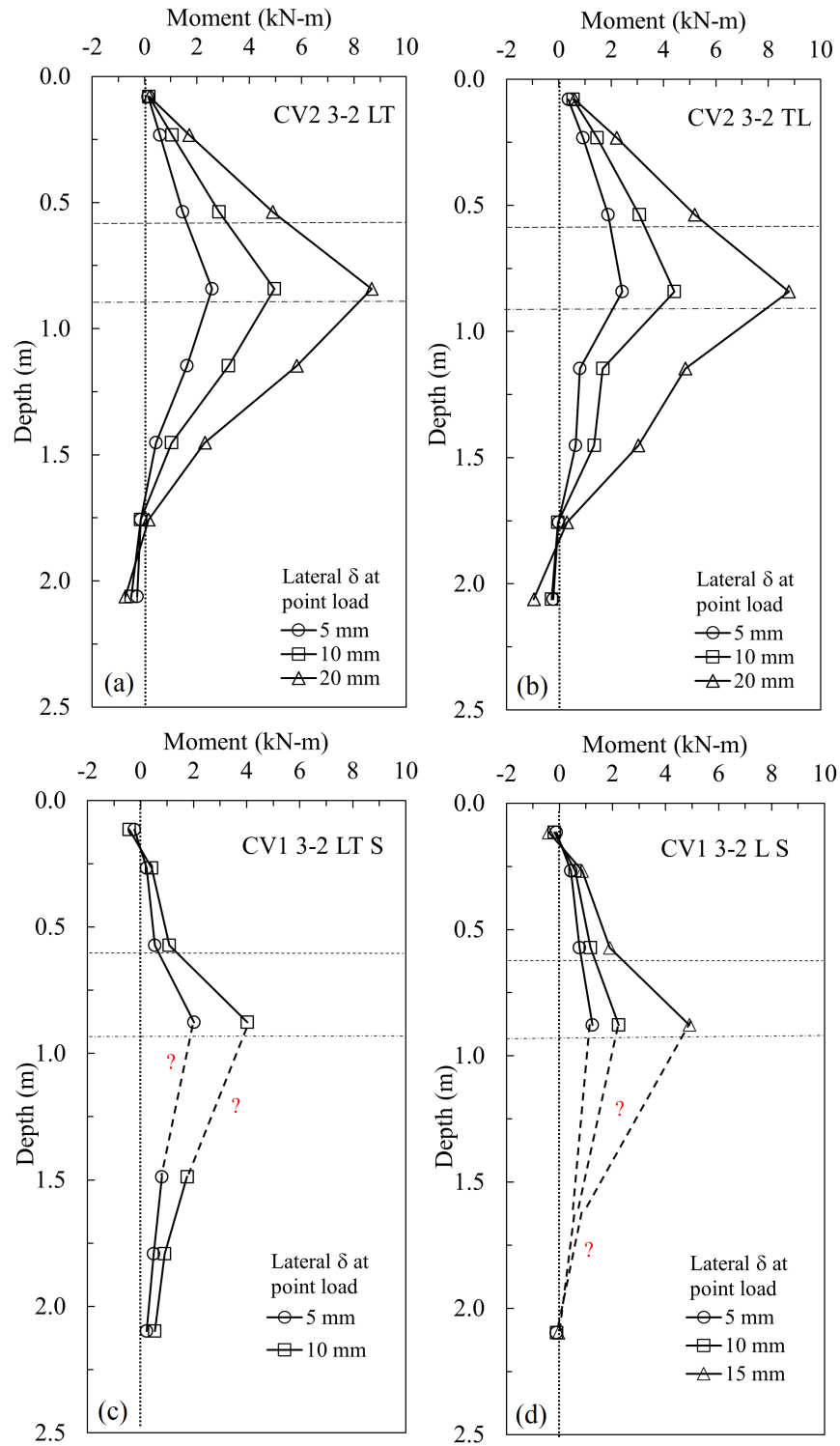


Figure E.9: Bending Moment profiles for CV 3-2: (a) two-piece CV with load sequence LT in cohesive soil; (b) two-piece CV with load sequence TL in cohesive soil; (c) one-piece CV with load sequence LT in granular soil (d) one-piece CV in granular soil.

## E.10 Collar Vane CV 3-3
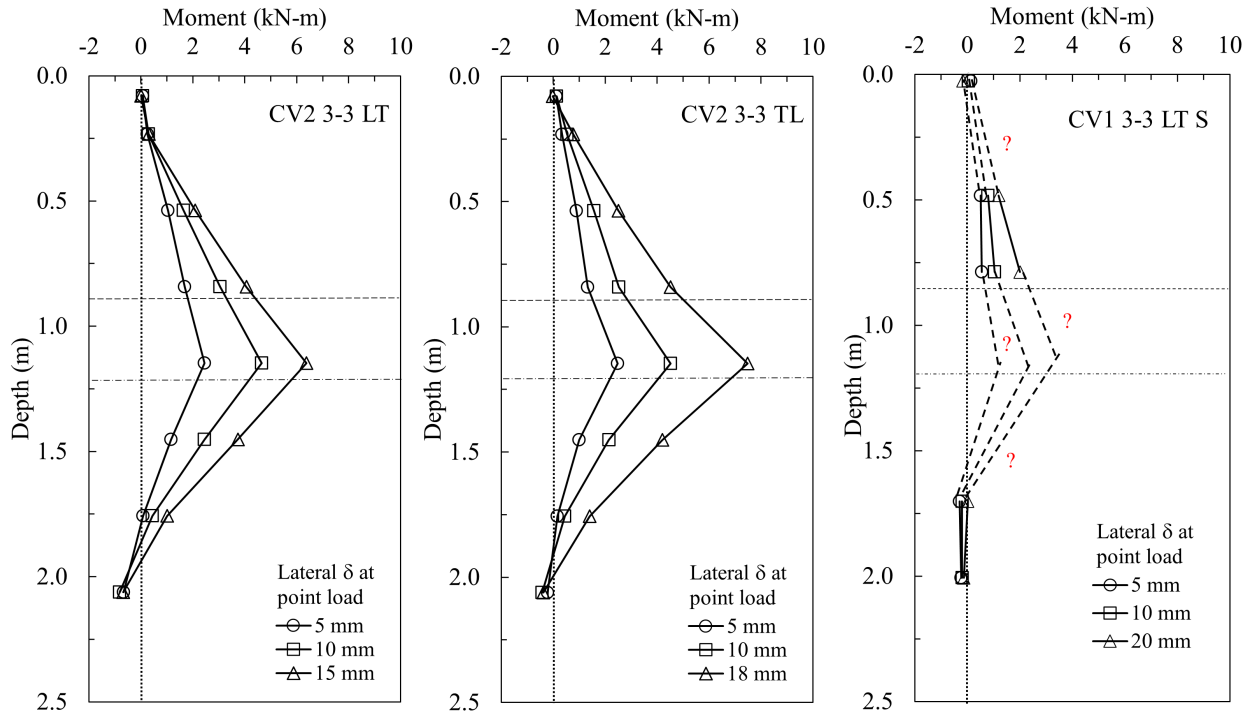


Figure E.10: Bending Moment profiles for CV 3-3: (a) two-piece CV with load sequence LT in cohesive soil; (b) two-piece CV with load sequence TL in cohesive soil; (c) one-piece CV with load sequence LT in granular soil.

# APPENDIX F

# CYCLIC LOAD TESTS RESULTS

The frequency for all cyclic tests was set to 0.125 Hz (period of 8 seconds). All the attached figures in this Appendix are plotted in terms of time. For convenience, the number of cycles transcurred in a determined amount of time is shown in Table F.1. After applying approximately 1000 loads (when possible), a quick monotonic test was performed. $P_u$ is taken as the force required to displace the pile head 12.5 mm Walker & Cox (1966) measured from the monotonic test.

Table F.1: Amount of time required to apply $N$ cycles.

| Time (s) | Number of cycles, N |
|----------|---------------------|
| 0 | 0 |
| 8 | 1 |
| 500 | 62.5 |
| 800 | 100 |
| 1000 | 125 |
| 2000 | 250 |
| 4000 | 500 |
| 6000 | 750 |
| 8000 | 1000 |

## F.1 Lateral Cyclic Load

### F.1.1 Helical Pile without Collar Vane
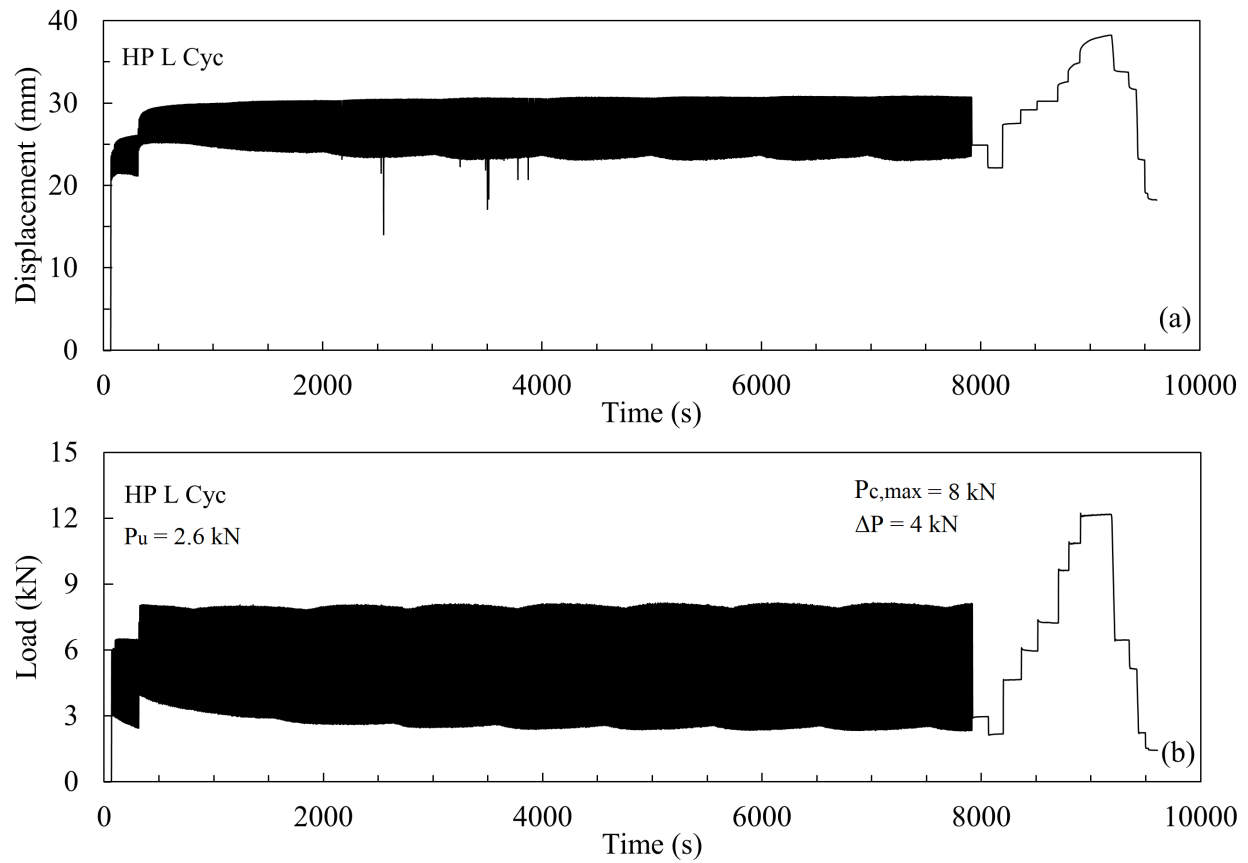


Figure F.1: Cyclic lateral load response for HP without CV in cohesive soil.

## F.1.2 Collar Vane CV2 2-1
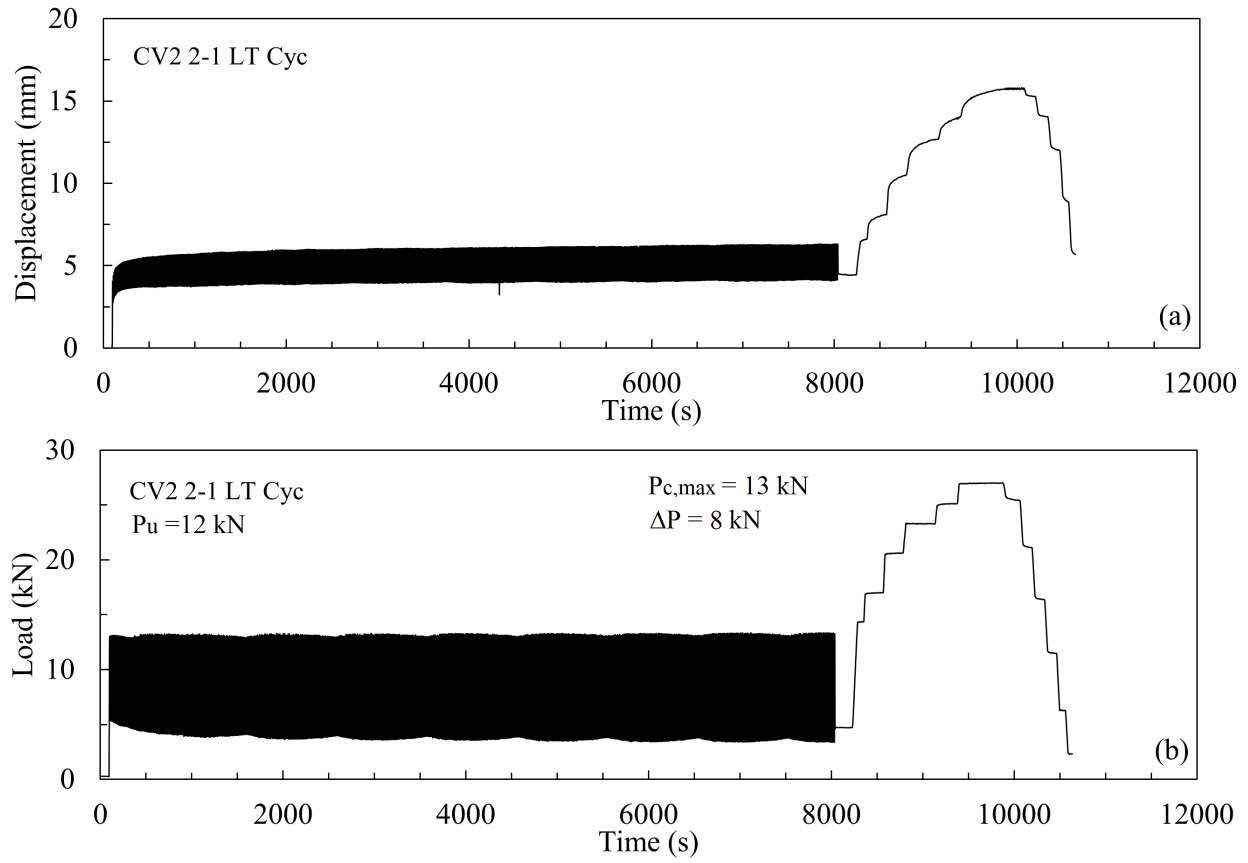


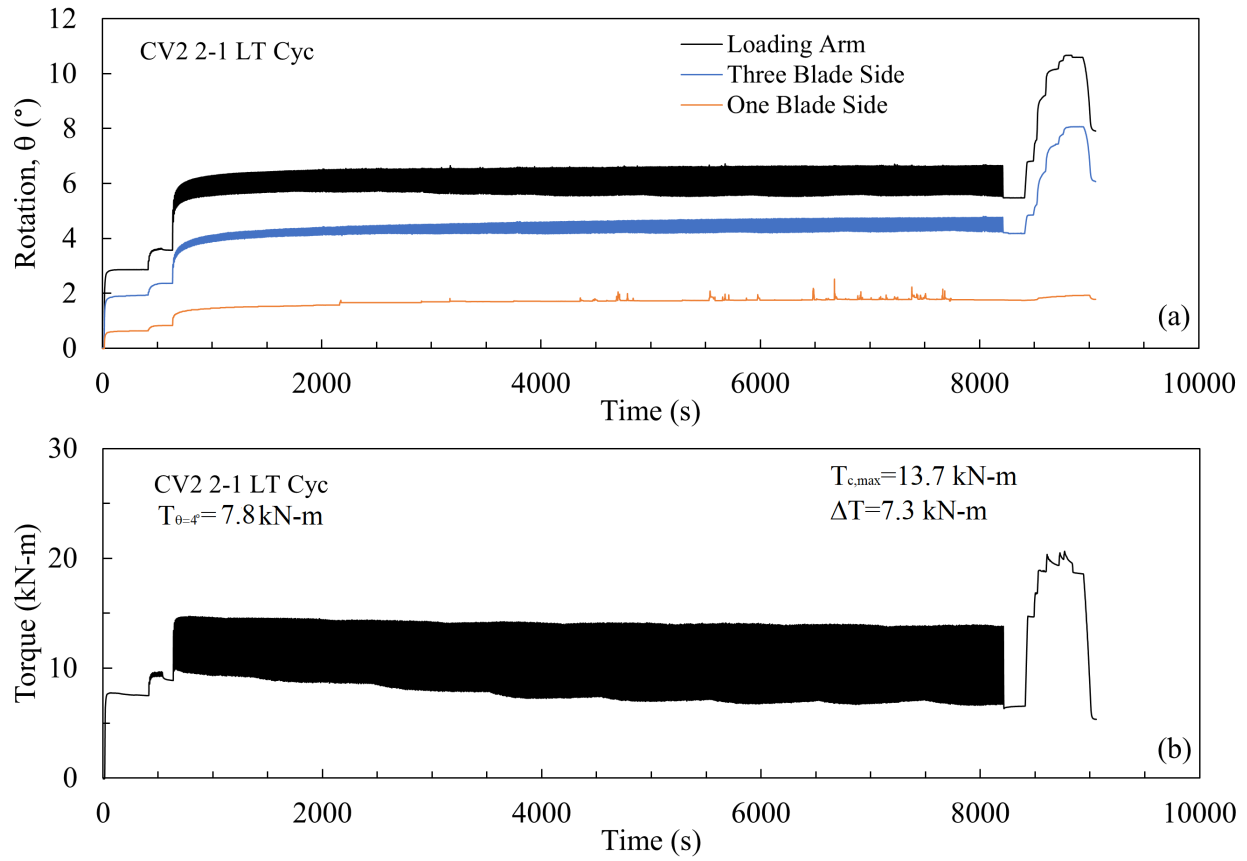Figure F.2: Cyclic lateral load response for two-piece CV2 2-1 in cohesive soil.
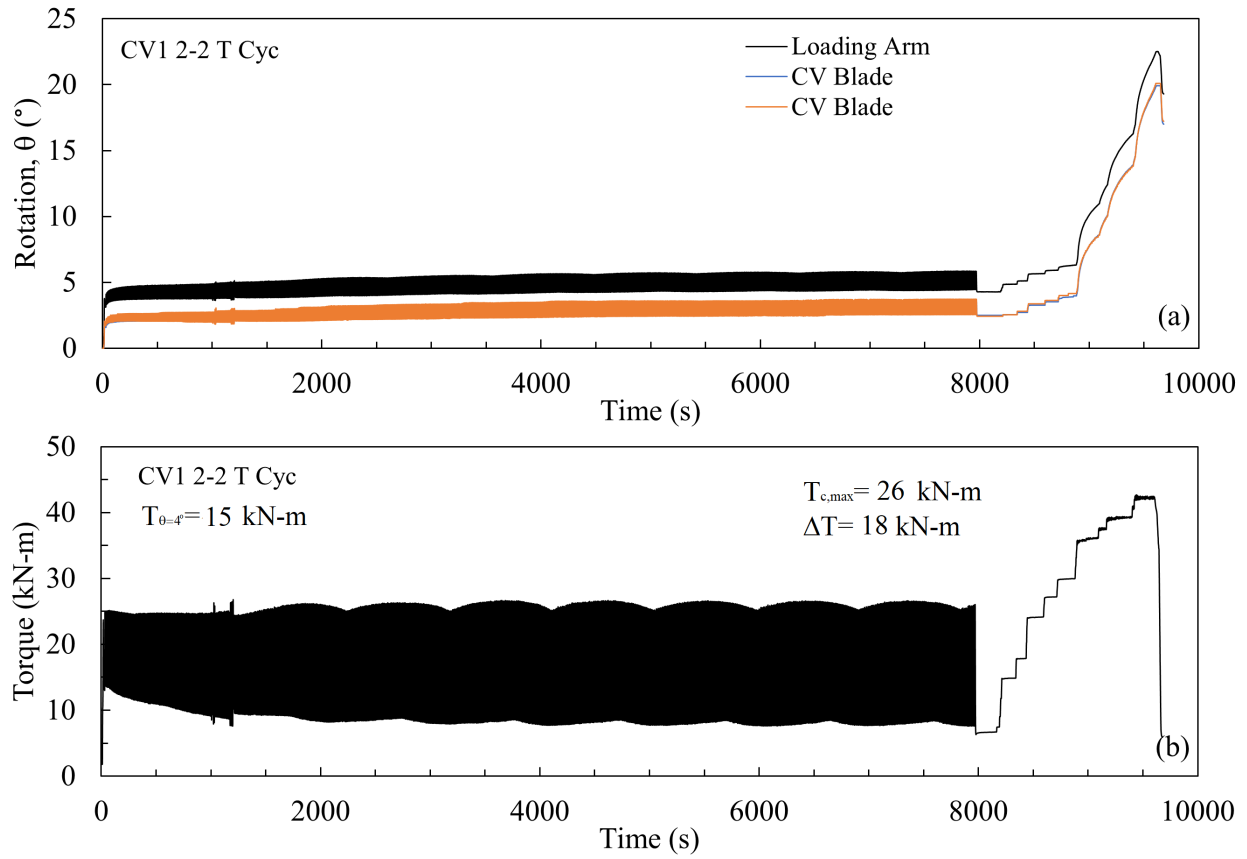
## F.1.3   Collar Vane CV1 2-2
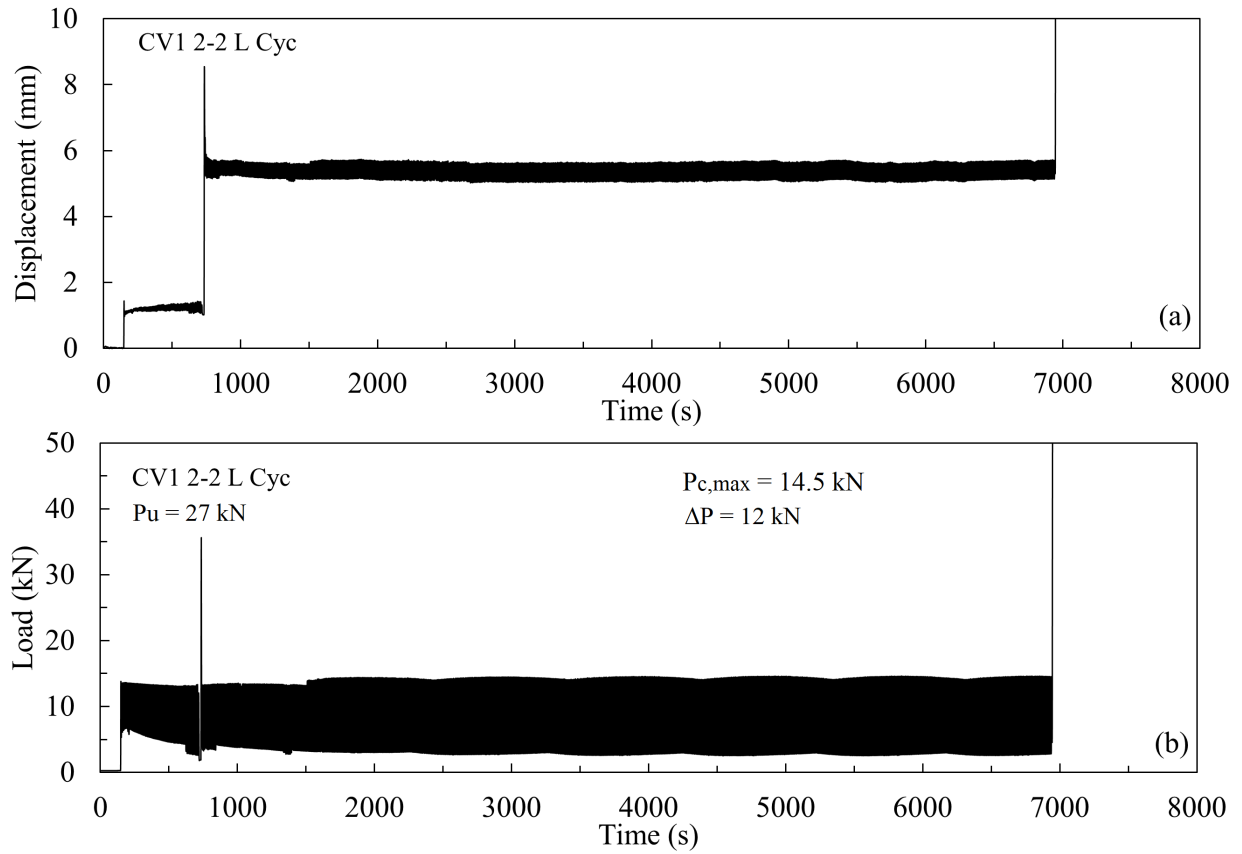


Figure F.3: Cyclic lateral load response for one-piece CV1 2-2 in cohesive soil.
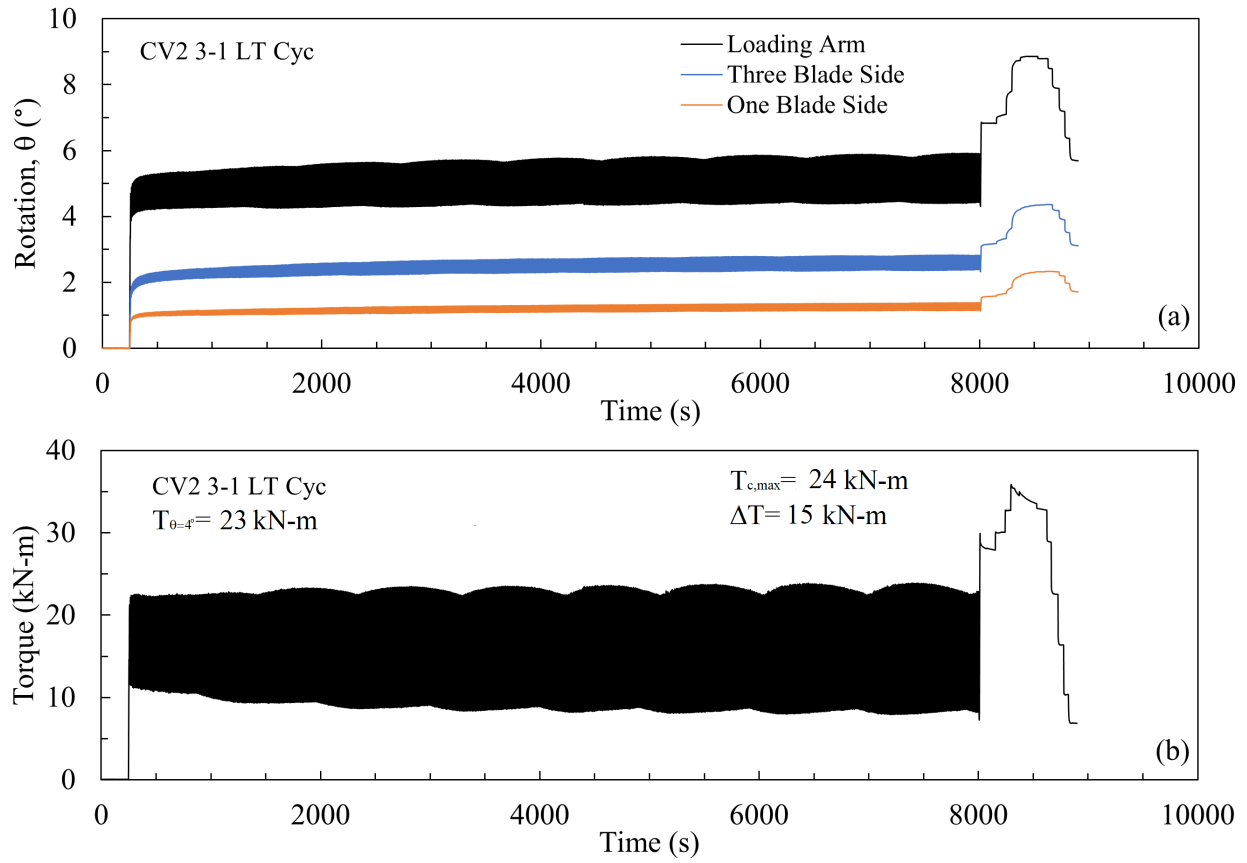
## F.1.4 Collar Vane CV2 3-1
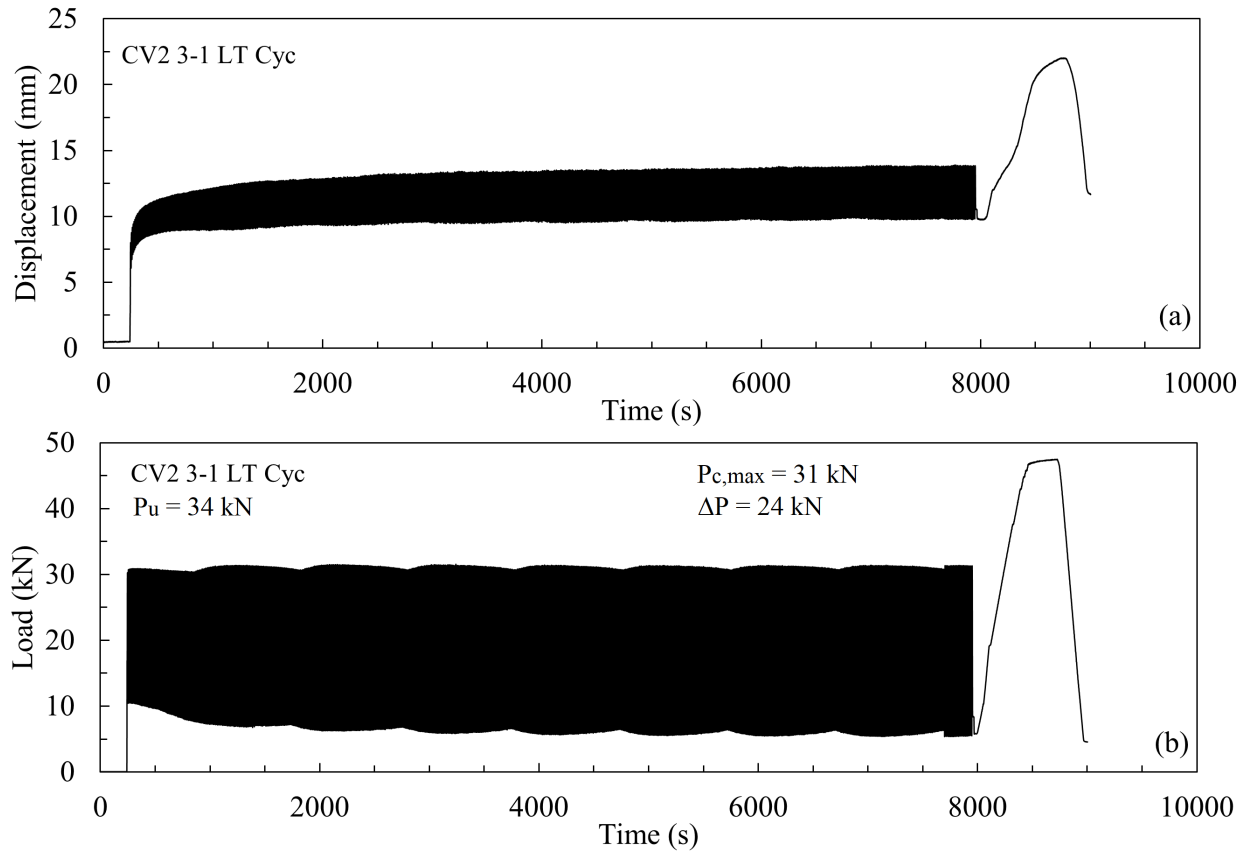


Figure F.4: Cyclic lateral load response for for two-piece CV2 3-1 in cohesive soil.
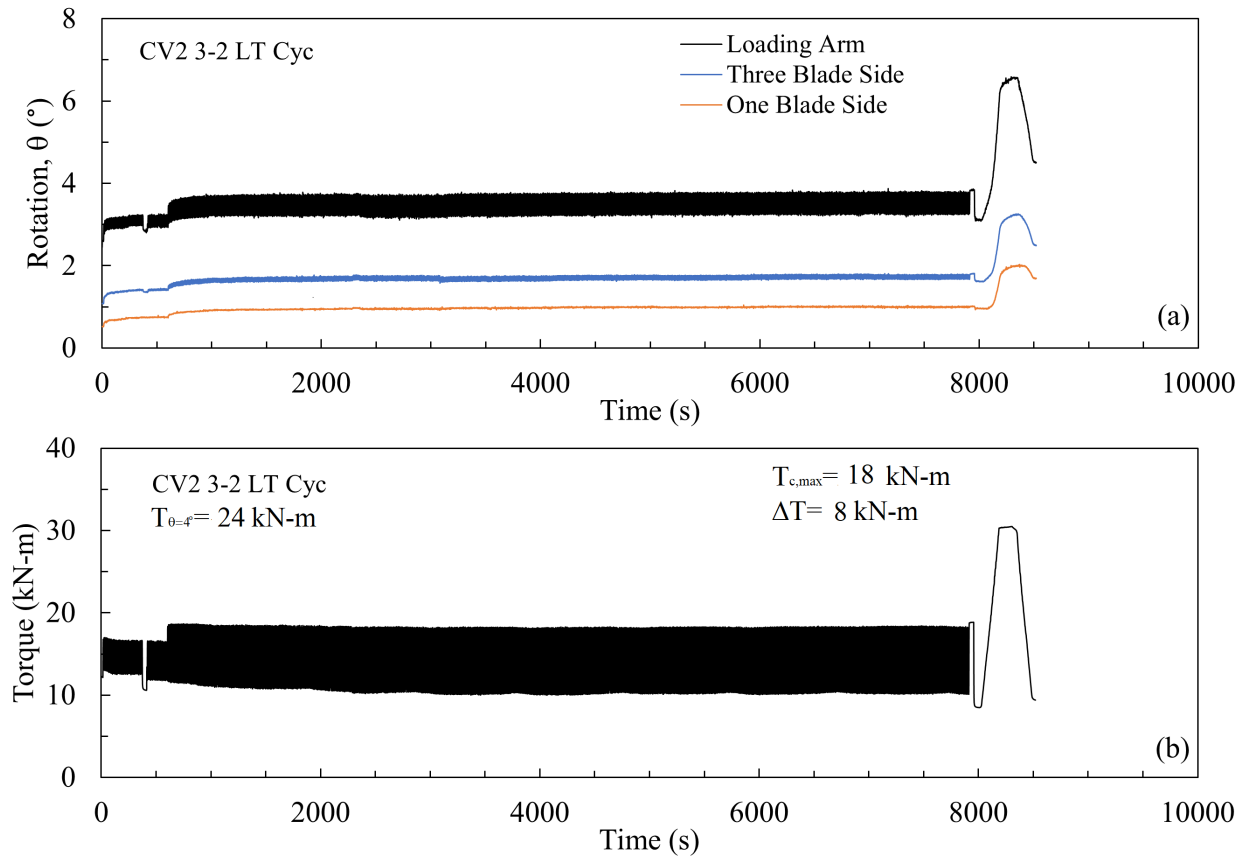
## F.1.5  Collar Vane CV 3-2
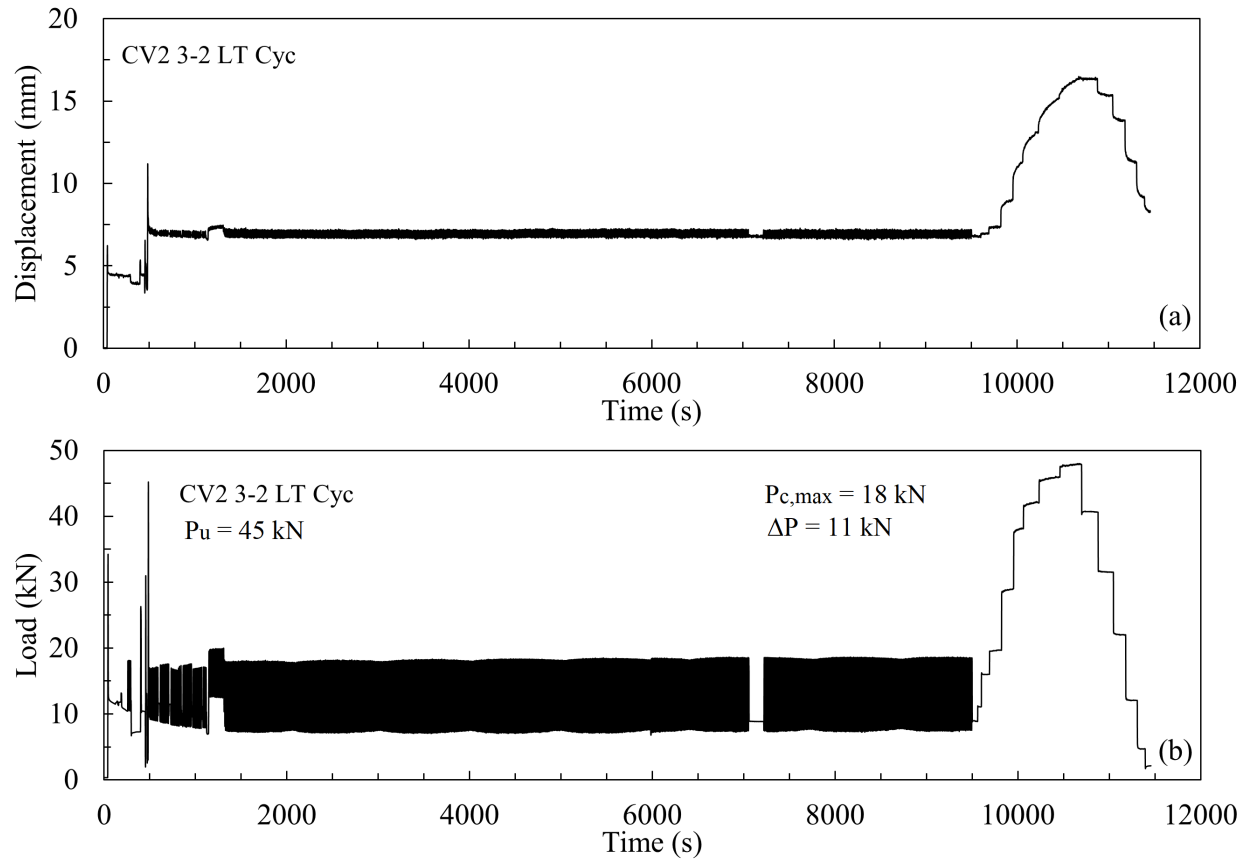


Figure F.5: Cyclic lateral load response for two-piece CV2 3-2 in cohesive soil.
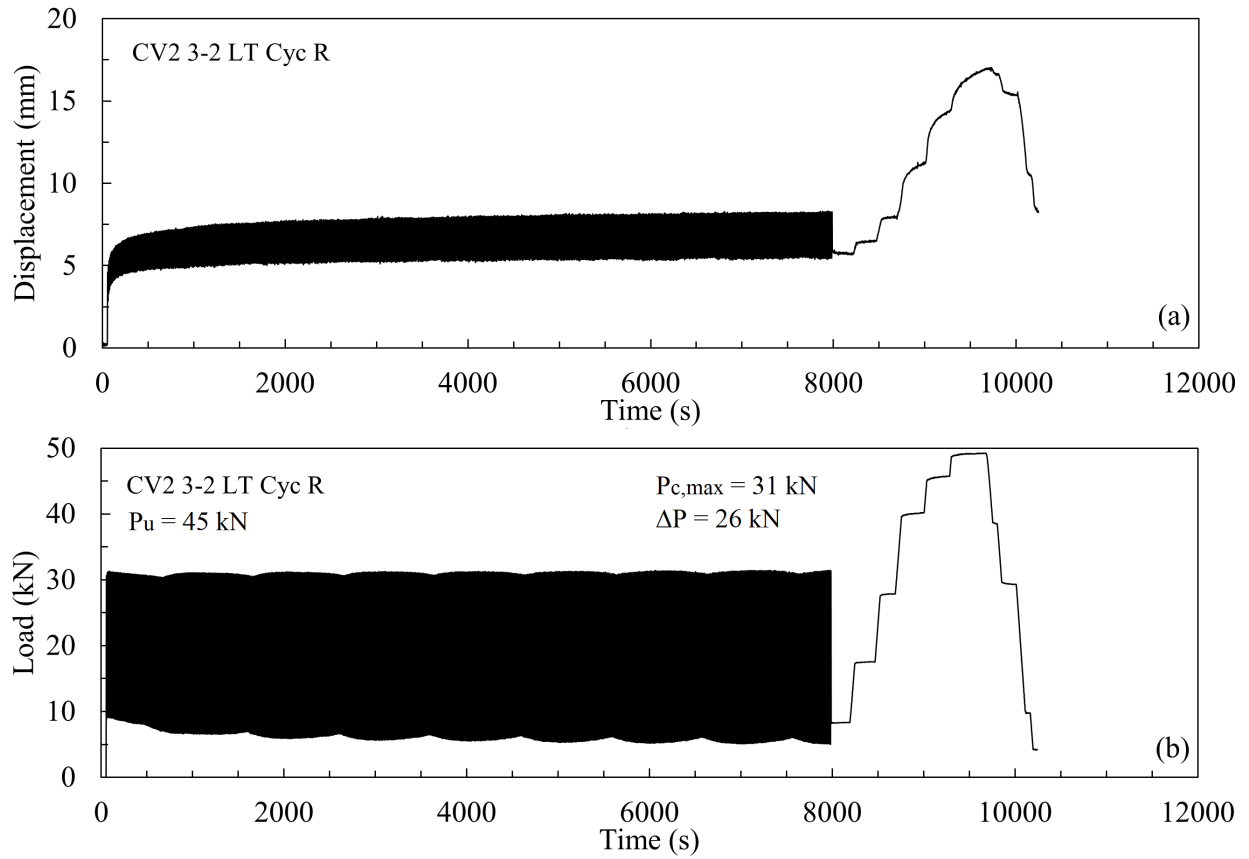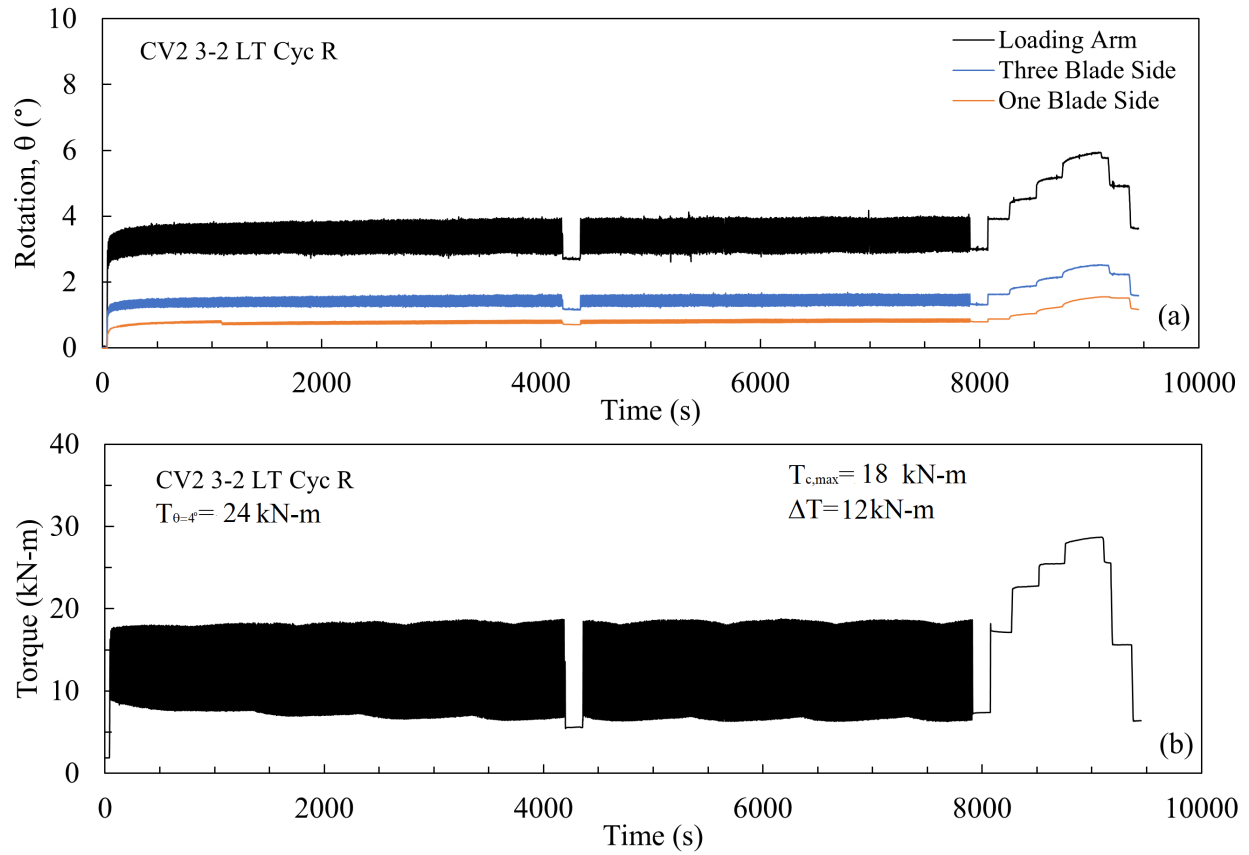
Figure F.6: Cyclic lateral load response for two-piece CV2 3-2 (with different load configuration) in cohesive soil.
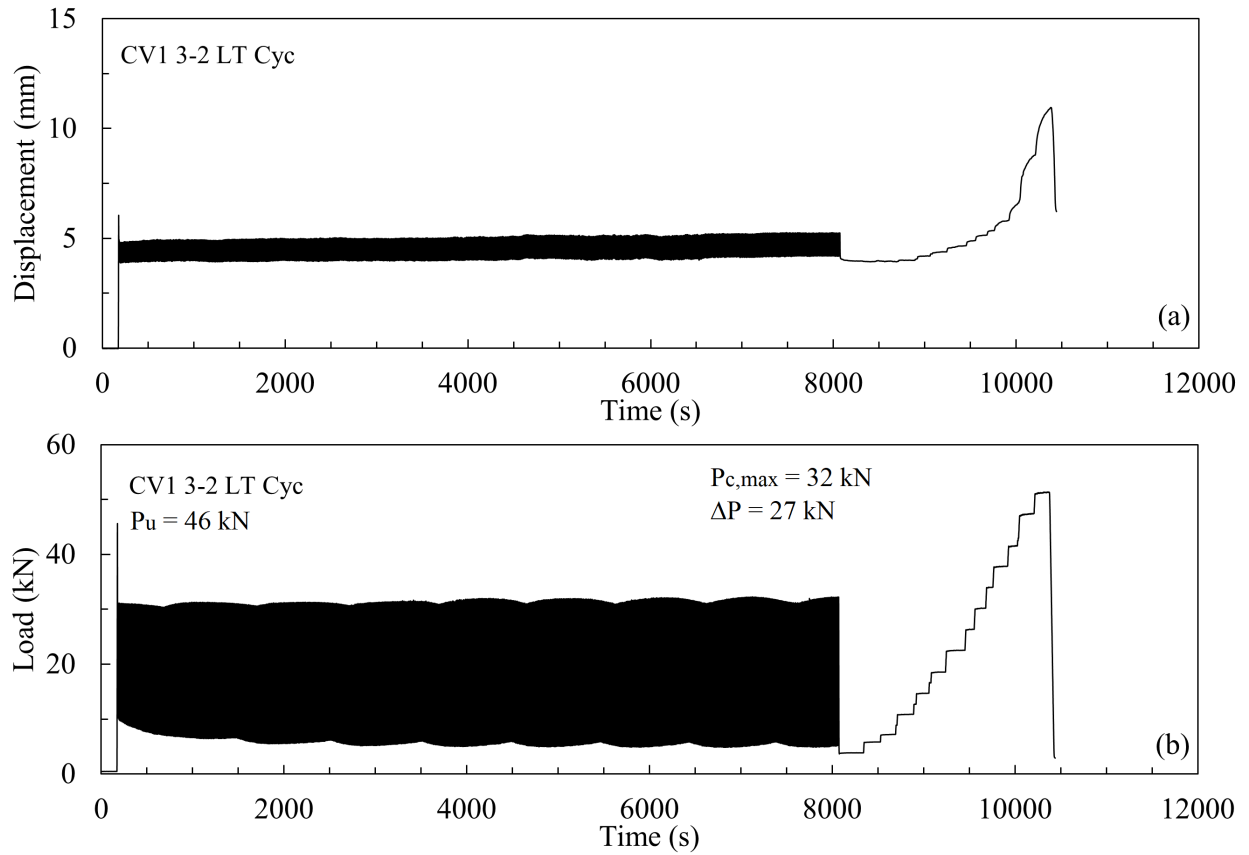
Figure F.7: Cyclic lateral load response for one-piece CV1 3-2 in cohesive soil.
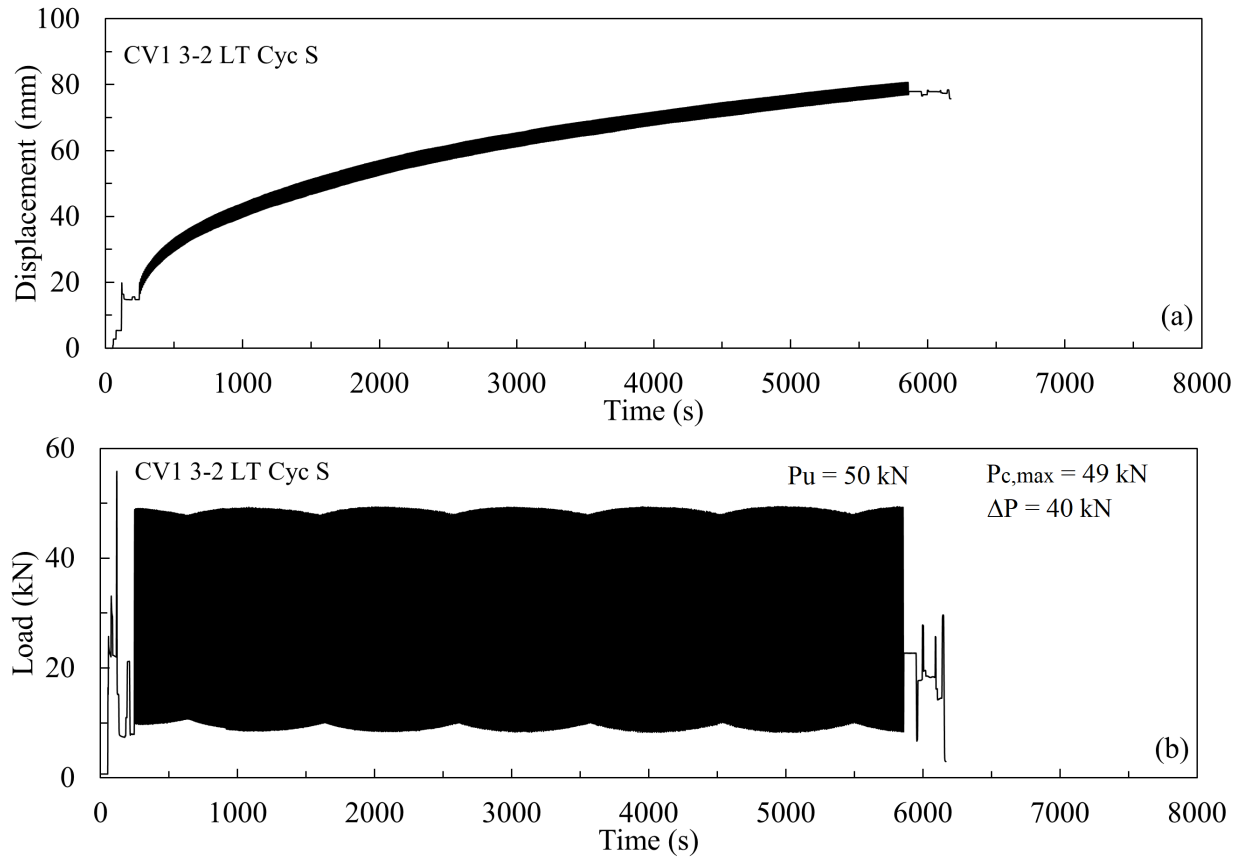
Figure F.8: Cyclic lateral load response for one-piece CV1 3-2 in granular soil.
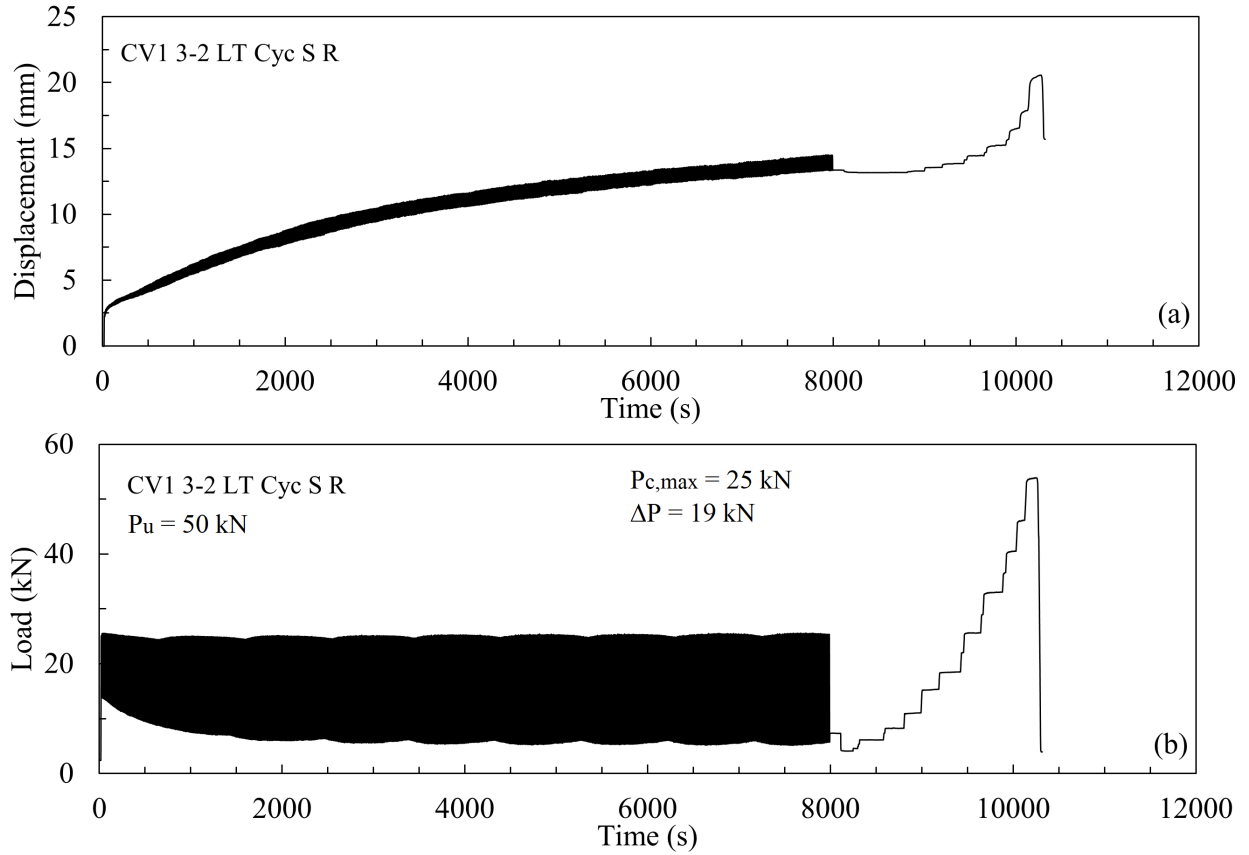
Figure F.9: Cyclic lateral load response for one-piece CV1 3-2 (with different load configuration) in granular soil.

**F.1.6  Collar Vane CV2 3-3**
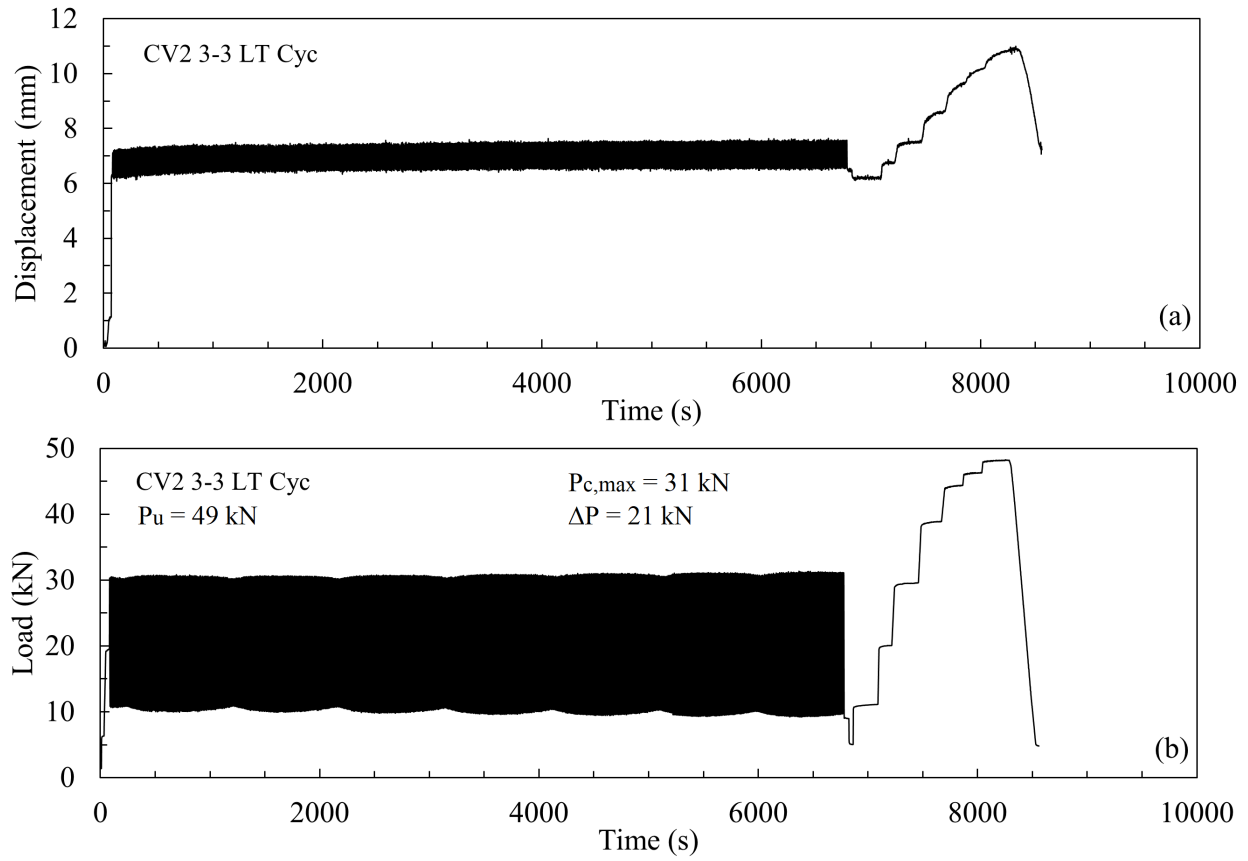


Figure F.10: Cyclic lateral load response for two-piece CV2 3-3 in cohesive soil.
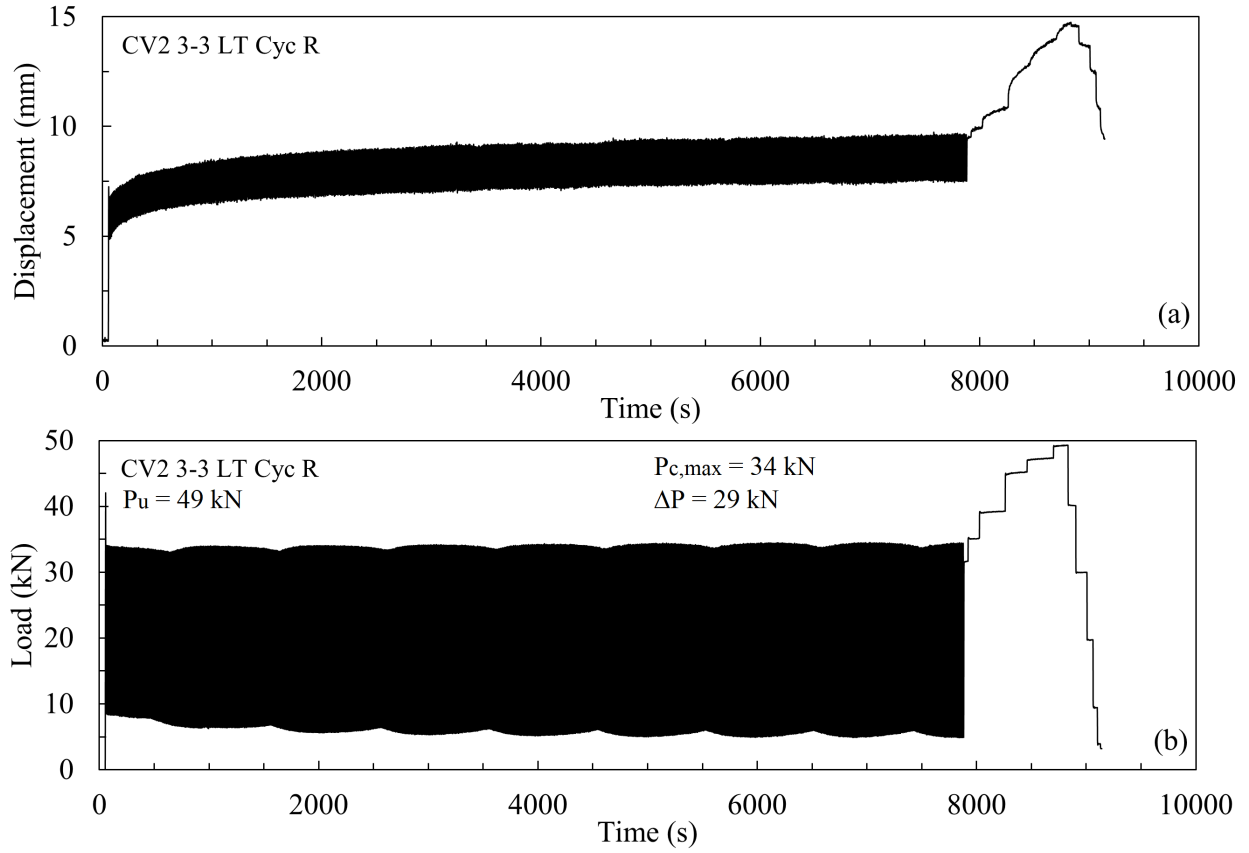
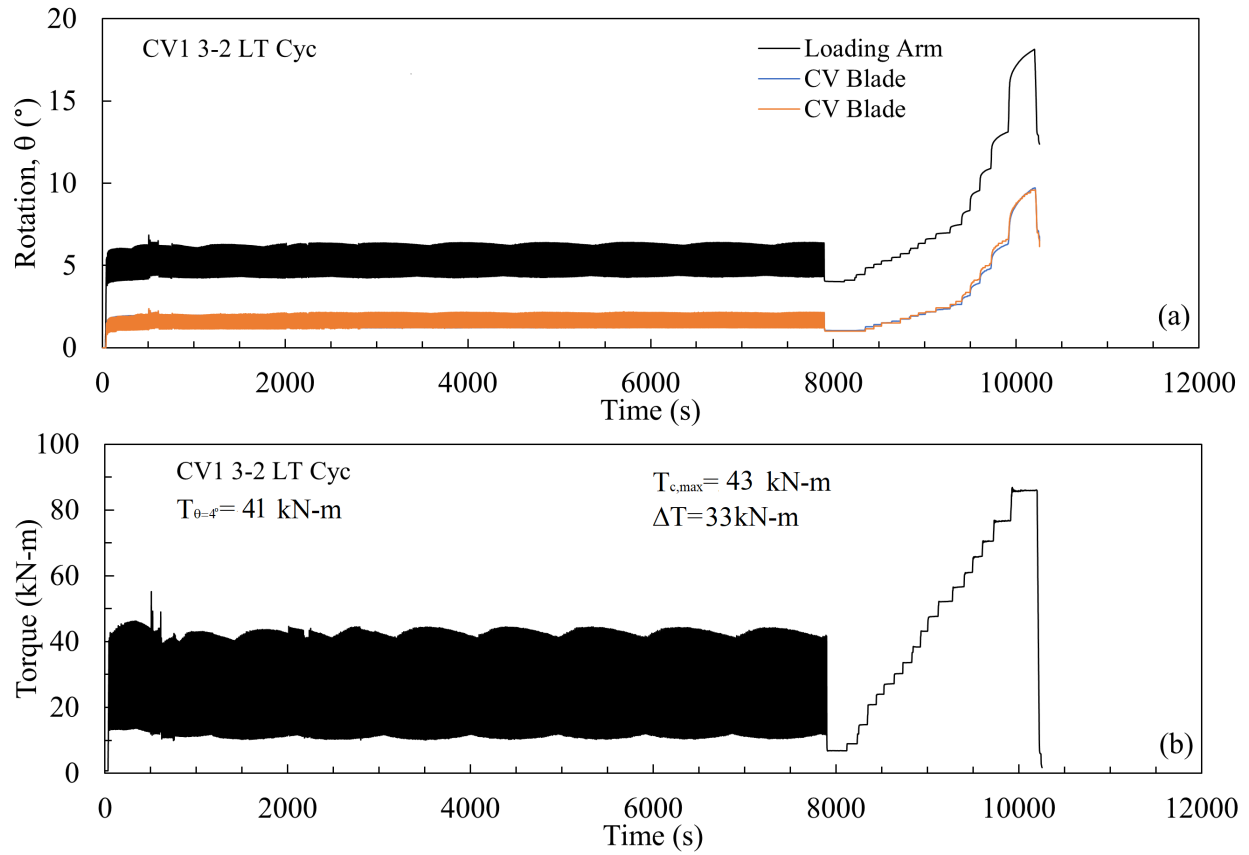Figure F.11: Cyclic lateral load response for two-piece CV2 3-3 (with different load configuration) in cohesive soil.

## F.2 Torsional Cyclic Load

### F.2.1 Collar Vane CV2 2-1



Figure F.12: Cyclic torsional load response for two-piece CV2 2-1 in cohesive soil.

## F.2.2 Collar Vane CV1 2-2



Figure F.13: Cyclic torsional load response for one-piece CV1 2-2 in cohesive soil.

### F.2.3 Collar Vane CV2 3-1



Figure F.14: Cyclic torsional load response for for two-piece CV2 3-1 in cohesive soil.
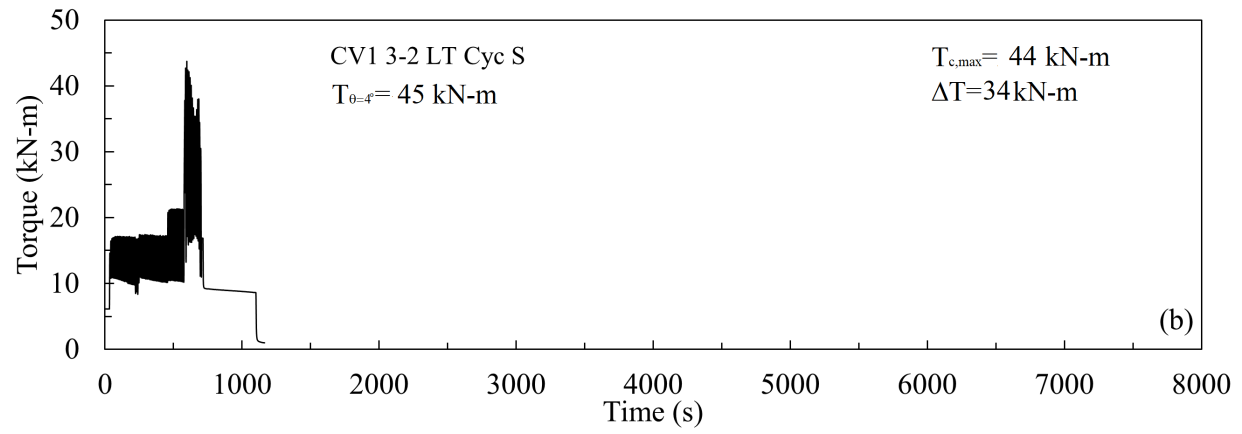
## F.2.4 Collar Vane CV 3-2



Figure F.15: Cyclic torsional load response for two-piece CV2 3-2 in cohesive soil.

Figure F.16: Cyclic torsional load response for two-piece CV2 3-2 (with different load configuration) in cohesive soil.

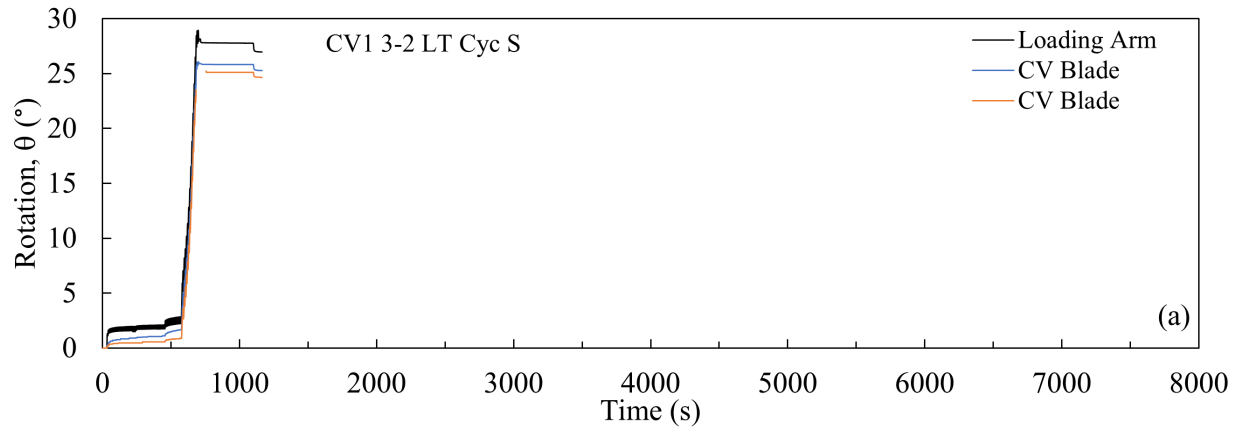Figure F.17: Cyclic torsional load response for one-piece CV1 3-2 in cohesive soil.

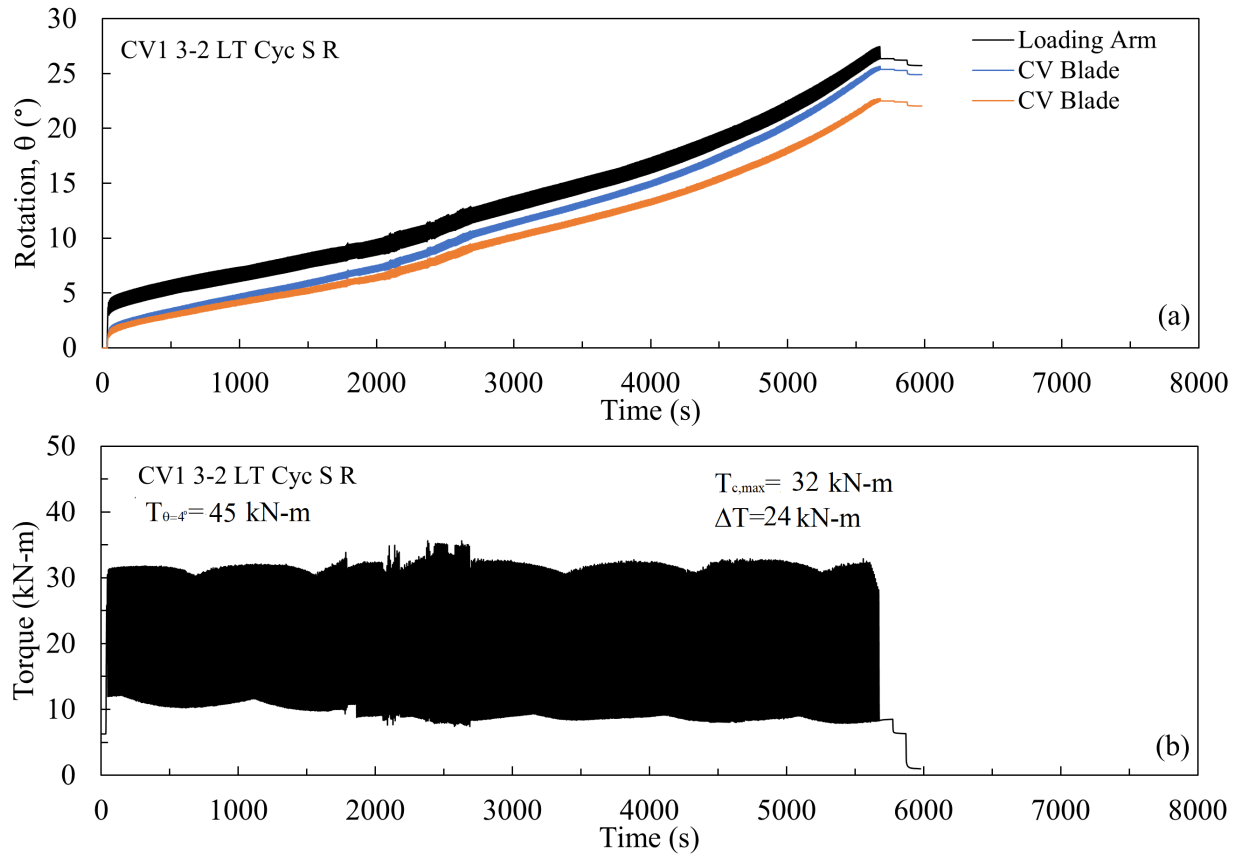Figure F.18: Cyclic torsional load response for one-piece CV1 3-2 in granular soil.

Figure F.19: Cyclic torsional load response for one-piece CV1 3-2 (with different load configuration) in granular soil.
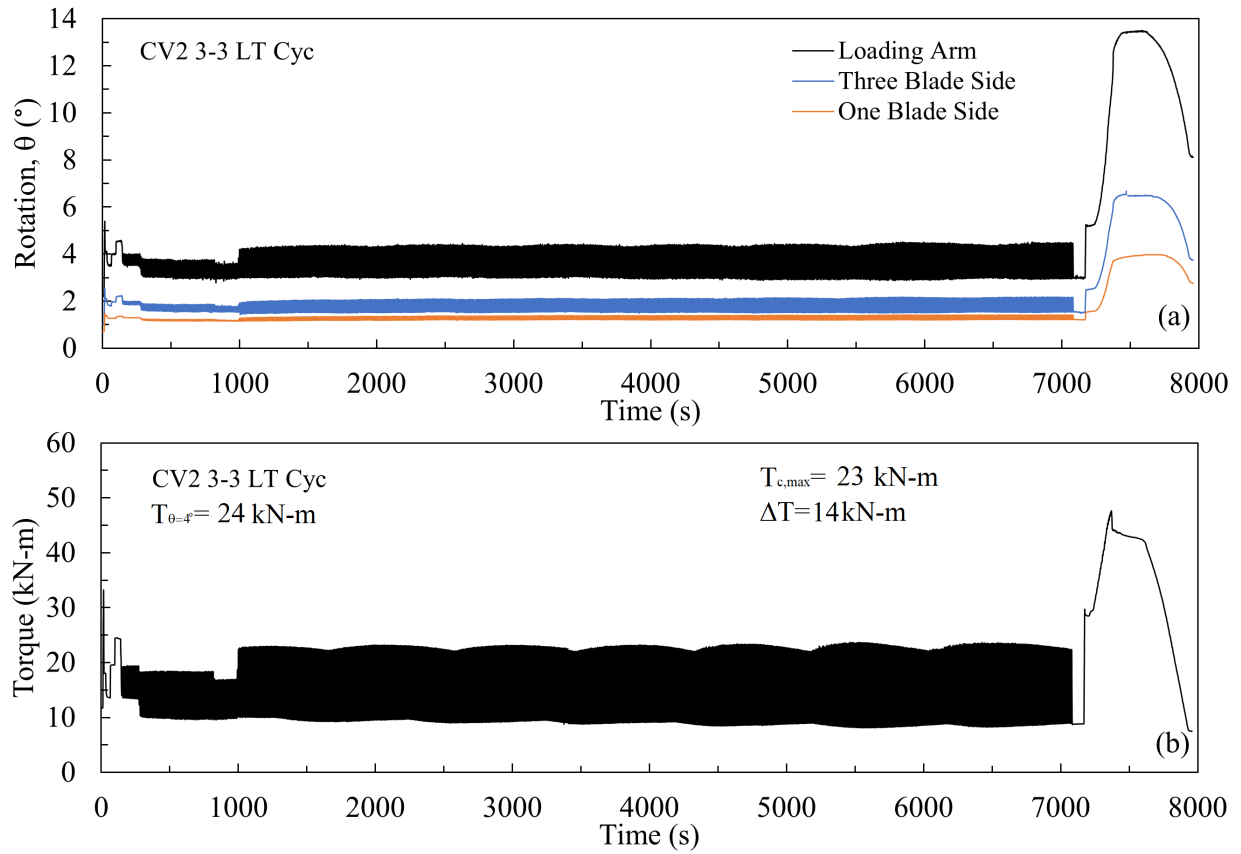
## F.2.5 Collar Vane CV2 3-3



Figure F.20: Cyclic torsional load response for two-piece CV2 3-3 in cohesive soil.
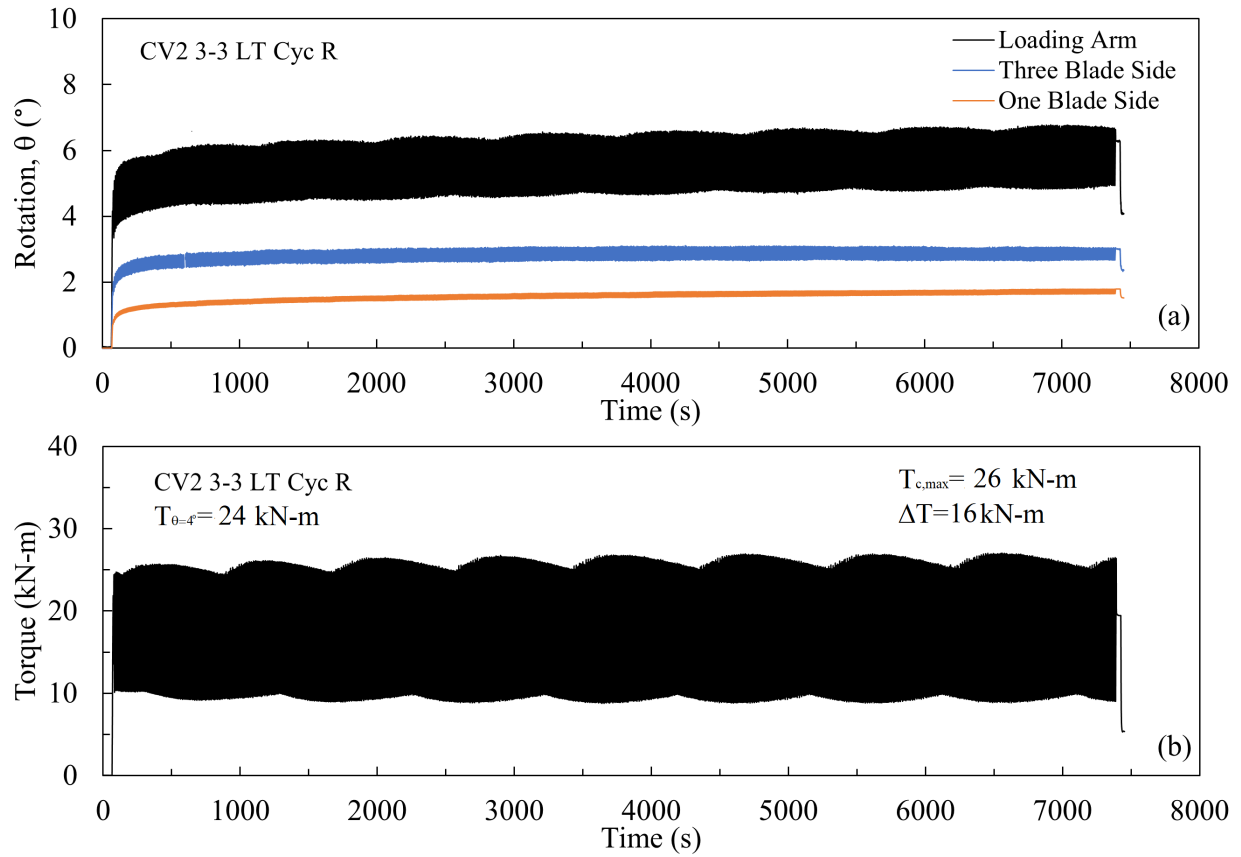
Figure F.21: Cyclic torsional load response for two-piece CV2 3-3 (with different load configuration) in cohesive soil.

# BIOGRAPHY OF THE AUTHOR

Juan Sebastián Carvajal-Muñoz was born and raised in Medellín, Colombia. He attended the University of Antioquia and graduated in 2020 with a Bachelor's degree in Civil Engineering. During his undergraduate program, Juan Sebastián found interest in Geotechnical Engineering subjects and began performing research on Soil-Structure Interaction problems with help of his former advisor, Prof. Carlos Alberto Vega-Posada. Juan Sebastián started his master's in Civil Engineering in Spring of 2021 with an emphasis in Geotechnical Engineering at the University of Maine, where he improved his research skills and obtained experience in full-scale pile instrumentation and testing. After graduation, he plans to join the industry to serve as a Geotechnical Engineer. Juan Sebastián is a candidate for the Master of Science degree in Civil Engineering from the University of Maine in May 2023.